

Dissertation

submitted to the  
Combined Faculty for the Natural Sciences and Mathematics  
of the University of Heidelberg, Germany  
for the degree of  
Doctor of Natural Sciences

**Data-driven modeling  
of the dynamic competition between  
virus infection and the antiviral interferon response**

presented by

Dipl.-Math. Melanie Rinas



# Dissertation

submitted to the  
Combined Faculty for the Natural Sciences and Mathematics  
of the University of Heidelberg, Germany  
for the degree of  
Doctor of Natural Sciences

presented by

Dipl.-Math. Melanie Rinas  
born in Bad Saulgau, Germany

Date of the oral examination: \_\_\_\_\_



Data-driven modeling  
of the dynamic competition between  
virus infection and the antiviral interferon response

Advisors: Prof. Dr. Anna Marciniak-Czochra  
Prof. Dr. Thomas Höfer



# Contents

<b>Abstract</b>	<b>i</b>
<b>Zusammenfassung</b>	<b>iii</b>
<b>1. Introduction</b>	<b>1</b>
1.1. Mathematical methods applied in this thesis . . . . .	1
1.1.1. Multi-scale stochastic modeling based on experimental data . .	1
1.1.2. Data-driven delay differential equation model of population dynamics . . . . .	3
1.2. Biological background . . . . .	5
1.2.1. What is a virus? . . . . .	5
1.2.2. Viruses studied in this thesis . . . . .	6
1.2.3. The interferon response against viral infections . . . . .	7
1.2.4. The development of vaccines . . . . .	10
1.3. Mathematical research on viral infections . . . . .	12
1.3.1. The basic concepts of mathematical modeling of viral infections	12
1.3.2. Application and contribution of mathematical models in med- ical research . . . . .	12
1.3.3. Mathematical modeling of the antiviral IFN system . . . . .	14
1.3.4. Mathematical models of the antiviral IFN system in this thesis	15
1.4. Outline of this thesis . . . . .	16
<b>2. Stochastic modeling predicts paracrine propagation of the IFN re-     sponse induced by individual sentinels</b>	<b>19</b>
2.1. Experimental study of the IFN system reveals multi-layered stochas- ticity in individual cells . . . . .	20
2.1.1. Monitoring virus-triggered IFN induction and response in sin- gle cells . . . . .	20
2.1.2. Cell-to-cell variability in IFN induction . . . . .	22
2.1.3. IFN target gene induction is an all-or-nothing switch . . . . .	28
2.2. Stochastic model of the IFN response against viral infection . . . . .	32
2.2.1. Stochastic simulation based on Gillespie's algorithm . . . . .	32
2.2.2. Model of virus-induced IFN signaling in single cells along with cell-to-cell communication through secreted IFN . . . . .	33
2.2.3. Model simulations using Gillespie's algorithm . . . . .	38
2.3. Estimation of the model parameters of the stochastic model . . . . .	42
2.3.1. Parameter determination for the virus-induced activation of the transcription factors of IFN . . . . .	42
2.3.2. Parameter determination of the IFN expression . . . . .	45
2.3.3. Parameter determination of the IFN response . . . . .	49

2.4. Stochastic modeling exposes individual IFN producers as sentinels of viral infection . . . . .	51
<b>3. Population-based modeling reveals that viral spread is mainly controlled by the autocrine effect of rapidly produced IFN</b>	<b>53</b>
3.1. Studying the dynamics of IFN-induced antiviral defense against spreading DENV in living cells . . . . .	55
3.1.1. Detection of the immediate interactions between DENV infection and the antiviral IFN response at single-cell level . . . . .	55
3.1.2. The competition between spreading DENV and IFN-induced antiviral protection . . . . .	60
3.1.3. The heterogeneous IFN response in single cells fosters the co-existence of viral spread and antiviral protection . . . . .	64
3.1.4. Examination of viral fitness by comparing DENV-wt with a DENV mutant lacking 2'-O-methyltransferase activity . . . . .	69
3.2. Population-based delay differential equation model of viral spread and IFN-induced antiviral defense . . . . .	73
3.3. Parameterization of the delay differential equation model . . . . .	81
3.3.1. Estimation of model parameters by using DENV-wt measurements . . . . .	81
3.3.2. Detection of DENV mutant specific model parameters by utilizing the knowledge from DENV-wt fitting . . . . .	89
3.4. Extension of the population-based model to elucidate the autocrine and paracrine effects of IFN . . . . .	93
3.5. Quantitative modeling predicts effective limitation of viral spread by rapid autocrine IFN action on infected cells . . . . .	100
<b>4. Discussion</b>	<b>105</b>
4.1. Stochastic modeling predicts paracrine propagation of the IFN response mediated by individual sentinels . . . . .	105
4.2. Population-based modeling predicts strong reduction of viral spread by the autocrine effect of rapidly produced IFN . . . . .	109
4.3. Using mathematical modeling to gain insight into virus-host competitions . . . . .	113
<b>A. Appendix</b>	<b>117</b>
A.1. Jacobian matrices of the delay differential equation model . . . . .	117
A.2. Jacobian matrices of the full delay differential equation model . . . . .	118
<b>Bibliography</b>	<b>119</b>
<b>Abbreviations and symbols</b>	<b>137</b>
<b>Publications and presentations</b>	<b>143</b>
<b>Acknowledgments</b>	<b>145</b>

# Abstract

The interferon system functions as a first line of defense against viral infections. The cellular recognition of viruses leads to the production of interferons (IFN) by the infected cells. Secreted IFN stimulates an antiviral response in an autocrine and paracrine manner: While autocrine IFN action inhibits virus production in infected cells, paracrine IFN signaling induces an antiviral protective state in naïve cells. Although central molecular components of the IFN system have been characterized, our quantitative understanding of its dynamics remains limited. In particular, it is not precisely known which molecular processes are decisive for the outcome of virus-host interactions.

Together with our experimental cooperation partners, we have studied virus-induced IFN signaling at single-cell resolution in communicating cell populations after infection with a non-spreading and a spreading virus. On this basis, we established two complementary mathematical models. First, we developed a stochastic multi-scale model accounting for the intracellular dynamics in individual cells and the cell-to-cell communication via secreted IFN. Second, we constructed a delay differential equation model to analyze the competition between viral spread and IFN-induced antiviral defense in a cell population. Both models were parameterized on the basis of original experimental data and the numerical analyses of the models aimed at deriving testable predictions for new experiments.

By live-cell imaging, we showed that key steps of the IFN pathway including virus-induced signaling, IFN expression, and induction of IFN-stimulated genes are stochastic events in individual cells. To relate the single-cell data after primary infection to antiviral protection at the cell-population level, we established a stochastic model which combines the heterogeneous IFN signaling in single cells with the intercellular communication through released IFN. The parameters describing the virus-induced activation of the transcription factors of the IFN gene were estimated from a distribution of observed single-cell activation times using as objective function Neyman's chi-squares statistic. The minimization of this objective function by simulated annealing revealed that virus-induced signaling is cooperative. Moreover, fitting of the measured time delays between transcription factor activation and IFN gene induction in individual cells with a gamma distribution by applying the maximum-likelihood method implies that IFN gene induction downstream of transcription factor activation is a slow multi-step process. Notably, mathematical modeling and experimental validation indicate that reliable antiviral protection in the face of multi-layered cellular stochasticity can be achieved by paracrine propagation of the IFN signal. Therefore, a few IFN-producing cells are able to protect a large number of naïve cells (Rand, Rinas et al. 2012).

To investigate the competition between viral spread and IFN-induced antiviral defense, we examined virus-host interactions after infection with spreading Dengue virus. For this purpose, our experimental partners generated data showing the antiviral response dynamics of fluorescent reporter cells after infection with a fluorescently labeled Dengue virus. Based on these kinetic data, we established a delay differential equation model with time delays for virus replication, virus production and IFN secretion. Using data-driven least-squares fitting and profile likelihood analysis, we identified the model parameters within narrow confidence bounds and found that the timing of virus production and IFN secretion after infection are almost identical. This direct competition together with the highly heterogeneous IFN response in single cells fosters the coexistence of IFN-induced protection of naïve cells and viral spread in non-protected cells. To analyze which components of the antiviral IFN system have the greatest influence on viral spread, we compared the infection dynamics of the wild-type Dengue virus with the attenuated spread of the vaccine candidate Dengue virus E217A mutant. We quantified the differences between wild-type and mutant Dengue virus infections using data-driven parameter optimization constrained by the determined wild-type virus related parameter values. In this way, we identified two mutant virus specific parameters, which explain the attenuation of the mutant through a reduced virus production rate and an accelerated IFN secretion taking place much earlier than virus production. By mathematical modeling and validation experiments, we predict that rapid IFN action curbing virus production in infected cells is critical for the attenuation of the Dengue virus E217A mutant. Thus, a fast acting autocrine IFN signal could limit viral spread in such a way that accelerated paracrine IFN response has only a minor impact on the spread of Dengue virus (Schmid, Rinas et al. submitted).

In conclusion, our work demonstrates that mathematical modeling is an essential tool to integrate data and mechanisms from the molecular to the cell-population level. The research on understanding which molecular mechanisms shape virus-host interactions might inform the development of new antiviral therapies and vaccines.

# Zusammenfassung

Das Interferon-System dient als eine der ersten Verteidigungslinien gegen virale Infektionen. Die zelluläre Erkennung von Viren führt dazu, dass infizierte Zellen Interferone (IFN) produzieren. Sezerniertes IFN stimuliert auf autokrine und parakrine Weise eine antivirale Antwort: Während die autokrine Wirkung von IFN die Virusproduktion in infizierten Zellen hemmt, induziert das parakrine IFN-Signal in naiven Zellen einen antiviralen geschützten Zustand. Obwohl die zentralen molekularen Komponenten des IFN-Systems charakterisiert sind, ist unser quantitatives Verständnis über die Dynamik dieses Systems nach wie vor begrenzt. Insbesondere ist nicht genau bekannt, welche molekularen Prozesse für den Verlauf von Virus-Wirt-Interaktionen entscheidend sind.

Zusammen mit unseren experimentellen Kooperationspartnern haben wir die durch Virus induzierte IFN-Signalübermittlung auf Einzelzellebene in kommunizierenden Zellpopulationen nach Infektion mit einem sich nicht vermehrenden und einem sich ausbreitenden Virus erforscht. Auf dieser Grundlage entwickelten wir zwei komplementäre mathematische Modelle. Zum einen erstellten wir ein stochastisches Multiskalenmodell, welches die intrazelluläre Dynamik in Einzelzellen und die Zell-Zell-Kommunikation mittels sezerniertem IFN beschreibt. Zum anderen konstruierten wir ein zeitverzögertes Differentialgleichungsmodell, um den Wettbewerb zwischen Virusausbreitung und IFN-induzierter antiviraler Abwehr in einer Zellpopulation zu analysieren. Beide Modelle wurden auf der Grundlage von neuartigen experimentellen Daten parametrisiert, wobei die numerische Analyse der Modelle auf die Erlangung von überprüfbareren Vorhersagen für neue Experimente abzielte.

Mittels Lebendzell-Mikroskopie zeigten wir, dass zentrale Teilabschnitte des IFN-Signalwegs - bestehend aus Virus-induzierter Signalübertragung, Expression von IFN und Induktion von IFN-stimulierten Genen - stochastische Ereignisse in einzelnen Zellen sind. Um die Einzelzelldaten nach primärer Infektion mit dem antiviralen Schutz der Zellpopulation in Beziehung zu setzen, haben wir ein stochastisches Modell erstellt, welches die heterogene IFN-Signaltransduktion in einzelnen Zellen mit der interzellulären Kommunikation infolge des ausgeschütteten IFN verbindet. Die Parameter, welche die Virus-induzierte Aktivierung der Transkriptionsfaktoren des IFN-Gens beschreiben, wurden anhand einer Verteilung von beobachteten Induktionszeiten in Einzelzellen geschätzt, wobei Neymans Chi-Quadrat-Statistik als Zielfunktion verwendet wurde. Die Minimierung dieser Zielfunktion mittels Simulated Annealing hat ergeben, dass die Virus-induzierte Signalübermittlung kooperativ ist. Darüber hinaus konnten die in Einzelzellen gemessenen Verzögerungszeiten zwischen der Aktivierung der Transkriptionsfaktoren und der IFN-Geninduktion unter Anwendung der Maximum-Likelihood-Methode mit einer Gammaverteilung beschrieben werden. Dies impliziert, dass die IFN-Geninduktion nach Aktivierung

der Transkriptionsfaktoren einem langsamen, mehrstufigen Prozess entspricht. Insbesondere deuten mathematische Modellierung und experimentelle Validierung darauf hin, dass ein verlässlicher antiviraler Schutz angesichts der vielschichtigen zellulären Stochastizität durch parakrine Ausbreitung des IFN-Signals erzielt werden kann. Demzufolge sind wenige IFN-produzierende Zellen dazu in der Lage, eine große Anzahl naiver Zellen zu schützen (Rand, Rinas et al. 2012).

Um den Wettbewerb zwischen viraler Ausbreitung und IFN-induzierter antiviraler Abwehr zu analysieren, untersuchten wir Virus-Wirt-Interaktionen nach Infektion mit dem sich vermehrenden Dengue-Virus. Zu diesem Zweck generierten unsere experimentellen Kooperationspartner Daten über die Dynamik der antiviralen Antwort von fluoreszierenden Reporterzellen nach Infektion mit einem fluoreszenzmarkierten Dengue-Virus. Auf der Grundlage dieser kinetischen Daten entwickelten wir ein zeitverzögertes Differentialgleichungsmodell, welches die Zeitverzögerungen der Virusreplikation, der Virusproduktion und der IFN-Ausschüttung berücksichtigt. Mittels datenbasierter Parameteroptimierung unter Verwendung der Methode der kleinsten Quadrate und der Profile-Likelihood-Methode identifizierten wir die Modellparameter innerhalb enger Konfidenzintervalle und fanden dadurch heraus, dass die Virusfreisetzung und die IFN-Sezernierung nach Infektion nahezu zeitgleich einsetzen. Dieser direkte Wettbewerb zusammen mit der äußerst heterogenen IFN-Antwort der Einzelzellen führt dazu, dass der IFN-induzierte Schutz naiver Zellen und die Virusausbreitung in nicht-geschützten Zellen nebeneinander bestehen. Um zu ermitteln, welche Komponenten des antiviralen IFN-Systems den größten Einfluss auf die virale Verbreitung haben, verglichen wir die Infektionsdynamik des Dengue-Virus-Wildtyps mit der eines sich kaum vermehrenden Impfstoffkandidaten, der Dengue-Virus E217A Mutante. Wir quantifizierten die Unterschiede zwischen Dengue-Virus Infektionen mit dem Wildtyp und der Mutante mittels datenbasierter Parameteroptimierung, welche durch die ermittelten Parameterwerte des Wildtyps beschränkt wurde. Auf diese Weise identifizierten wir zwei Mutante-spezifische Parameter, welche die Abschwächung der Dengue-Virus Mutante durch eine reduzierte Virusproduktionsrate und eine beschleunigte, deutlich vor der Virusfreisetzung einsetzende IFN-Ausschüttung erklären. Auf der Grundlage von mathematischer Modellierung und Validierungsexperimenten sagen wir voraus, dass eine rasche IFN-Wirkung, welche die Virusproduktion in infizierten Zellen eindämmt, für die Abschwächung der Dengue-Virus E217A Mutante entscheidend ist. Daher könnte ein schnelles autokrines IFN-Signal die virale Verbreitung derart einschränken, dass eine beschleunigte parakrine IFN-Antwort nur eine geringe Wirkung auf die Ausbreitung des Dengue-Virus hat (Schmid, Rinas et al. eingereicht).

Zusammenfassend veranschaulicht unsere Arbeit, dass die mathematische Modellierung ein wichtiges Instrument ist, um Daten und Mechanismen von der molekularen bis zur Ebene der Zellpopulation zusammenzuführen. Ein besseres Verständnis darüber, welche molekularen Mechanismen die Virus-Wirt-Interaktionen beeinflussen, könnte zur Entwicklung neuer antiviraler Therapien und Impfstoffe beitragen.

# 1. Introduction

Viruses have been, and continue to be, one of the major causes of global public health problems. Throughout history, viral diseases have claimed innumerable lives due to epidemic spread of infections. It is no surprise that numerous researchers from all fields of the natural sciences have for a long time contributed to the understanding and the battle against infectious diseases. This includes in particular the mathematical modeling of viral infections, which continues to play an instrumental role in improving our knowledge of virus-host interactions.

## 1.1. Mathematical methods applied in this thesis

In close collaboration with experimentalists, we perform data-driven mathematical modeling to study the competition between virus infection and the antiviral immune defense induced by secreted interferons (IFN) in communicating cell populations. In general, mathematical models are tools to describe and analyze a system in mathematical terms. In this study we use both deterministic and stochastic mathematical modeling. While the output of a deterministic model is fully determined by the parameter values and the initial conditions, a stochastic model has at least one random component causing variability, and thereby affecting the output of the model.

To account for various experimental conditions, we establish two complementary mathematical models. First, in order to link heterogeneous single-cell data after primary infection to antiviral protection at the cell-population level, we develop a multi-scale stochastic model. Second, we construct a deterministic delay differential equation model of viral spread and IFN-induced antiviral defense, which partitions the cell population into different subpopulations according to their infection state.

### 1.1.1. Multi-scale stochastic modeling based on experimental data

#### Model structure

In section 2.2, we develop a multi-scale stochastic model, which combines the observed heterogeneous intracellular dynamics of virus-induced signal transduction, IFN gene induction and IFN response in single cells with the cell-to-cell communication mediated by secreted IFN in an infected cell population (see Figure 2.9). The model is formulated as a continuous-time stochastic process in which the possible state changes of individual cells are determined through propensity functions depending on the current state of the cell and the extracellular concentration of

## 1. Introduction

secreted IFN (see section 2.2.2). Our model is thus a Markov process (see section 2.2.1). Given the high diffusion coefficient of IFN (Kreuz and Levy 1965:  $D_{\text{IFN}} = 3.42 \times 10^5 \mu\text{m}^2/\text{h}$ ; Hu et al. 2011:  $D_{\text{IFN}} = 1.08 \times 10^5 \mu\text{m}^2/\text{h}$ ), the spread of IFN on the relevant length scale of several cell diameters occurs within minutes, which is fast compared to the hour-timescale of IFN expression and IFN response. We therefore assume uniform distribution of released IFN and describe the kinetic of extracellular IFN by an ordinary differential equation (ODE) depending on the number of infected IFN-producing cells (see equation (2.11)). Corresponding to the experimental system, we consider as initial conditions that a fraction of cells is infected with virus, and that signal transduction and gene expression are inactive in all cells at the starting time.

### Model simulation

The stochastic state transitions of single cells are iterated using Gillespie’s stochastic simulation algorithm, which is a Monte Carlo procedure for the numerical simulation of stochastic kinetics (Gillespie 1976, Gillespie 1977) (see section 2.2.1 and 2.2.3). In parallel to Gillespie’s direct method, we calculate the extracellular concentration of IFN by utilizing the Euler method to integrate the corresponding differential equation numerically. Our multi-scale stochastic model is implemented and simulated in Matlab (The Mathworks Inc., Natick, MA). All model related programs are freely available as Supplementary Information for the open access paper Rand, Rinas et al. 2012 at the Molecular Systems Biology website ([www.nature.com/msb](http://www.nature.com/msb)).

### Parameter estimation

The Gillespie algorithm is a common and valuable method to simulate stochastic processes, but generating a sufficient number of realizations of extensive models with large time scale separation takes considerable time (Gillespie 2007, Cao and Samuels 2009, Banks et al. 2011). Indeed, we find that the simulation time of our model for a physiologically relevant number of cells ( $10^4$  cells) with kinetics over several hours is prohibitive of straightforward parameter optimization approaches based on experimental data. To address this limitation, we divide the parameter optimization problem into three parts with respect to the key steps of the IFN signaling pathway: (1) estimation of parameters for the virus-induced activation of the transcription factors of IFN (see section 2.3.1), (2) identification of parameters corresponding to IFN gene induction (see section 2.3.2) and (3) determination of parameters of the IFN response (see section 2.3.3).

The first two parts concern the induction of IFN expression in individual cells without intercellular communication via secreted IFN. As the simulation of isolated single-cell behavior is much less time-consuming than the full model, rigorous parameter estimation is feasible. The third part of the optimization problem regarding the IFN response depends on cell-to-cell signaling and therefore requires the simulation of a large number of communicating cells, which in turn causes impractically long calculation times. However, it turns out that we can still infer quantitative features of the IFN response from the experimental data (see section 2.3.3).

First, we estimate the parameters of the propensity function describing the virus-induced activation of the transcription factors of IFN (see section 2.3.1). This propensity function is formulated as a Hill function and its parameters are optimized from a distribution of measured single-cell activation times using as objective function Neyman’s chi-squares statistic (Baker and Cousins 1984) (see equation (2.20)). To minimize this objective function we apply the simulated annealing method (Kirkpatrick et al. 1983, Schneider and Kirkpatrick 2006). From a biological point of view, the most interesting estimate is the parameter value of the Hill coefficient, as a Hill coefficient larger than 1 implies positive cooperativity (Murray 2002). To test the goodness-of-fit with respect to the Hill coefficient, we apply the profile likelihood method (Venzon and Moolgavkar 1988) (see section 2.3.1) and consider the degree of freedom as an upper limit for good fits.

Second, we analyze if the histogram of the observed cell-to-cell variation of the time delay between transcription factor activation and IFN gene induction is stochastically compatible with a gamma distribution  $\gamma(m, z)$  (see section 2.3.2). For a positive integer  $m$ ,  $\gamma(m, z)$  describes the distribution of the sum of  $m$  independent random variables, where each random variable is exponentially distributed with rate  $z$  (Press et al. 2007). In biological terms, the gamma distribution characterizes a multi-step process consisting of  $m$  consecutive single-rate steps. Based on the measured IFN induction times after transcription factor activation monitored in single cells, we determine the parameters of the gamma distribution with the maximum-likelihood method (Myung 2003). By calculating the root of the partial derivative of the log-likelihood function  $\mathcal{L}$  with respect to  $z$ , we obtain an explicit estimator for  $z$  depending on  $m$  (see equation (2.30)). Utilizing this estimator, the parameter  $m$  is determined independently from  $z$  by numerically computing the root of the partial derivative of  $\mathcal{L}$  with respect to  $m$ .

Third, we parameterize the IFN response by describing the measured dose-response of IFN-responding cells versus external IFN with a Hill function (see section 2.3.3). The parameters of the Hill function are fitted to the dose-response data set using a least-squares method (see equation (2.35)). Restricted by the preceding parameterization, the IFN secretion rate and the IFN degradation rate are determined to match the observed time course of extracellular IFN to the proportion of IFN producing cells.

### 1.1.2. **Data-driven delay differential equation model of population dynamics**

#### **Model structure**

In section 3.2, we establish a delay differential equation (DDE) model of viral spread and IFN-induced antiviral protection in a cell population driven by experimental data. The model classifies the cell population into several subpopulations according to their infection state and is thus a modified version of the classical compartment-based SIR model, which takes into account the temporal dynamics of susceptible S, infected I and recovered R population classes (Kermack and McKendrick 1927) (see section 1.3.1). Our DDE model describes how susceptible cells can become either

## 1. Introduction

infected by extracellular virus or protected by the antiviral effect of secreted IFN (see Figure 3.16). The model is formulated as a system of 10 differential equations with three constant time delays for virus replication, virus production and IFN secretion, respectively (see system of equations (3.11)). At the starting time, only the initial number of susceptible cells and the extracellular viral load are non-zero. For variables with a delay argument, we use as history functions the constant zero function, which is compatible with the experimental protocol.

Motivated by the experimental observation that stimulation of infected cells with IFN in an early phase after infection resulted in reduced virus replication, we develop an extended version of our model. This full DDE model additionally takes into account that the recognition of secreted IFN in an early time window after viral entry inhibits virus production in infected cells (see section 3.4). The full model is described by a system of 13 differential equations with four constant time delays (see system of equations (3.37)). At the starting time only the initial number of susceptible cells as well as the extracellular viral load are non-zero. For those variables that have a delay argument, we consider as history functions the constant zero function.

### Model simulation

For the simulation of the basic DDE model (3.11) and the full DDE model (3.37) we use Matlab as a programming environment. By means of a binary Matlab executable (mex) subroutine, we set up an interface between Matlab and the freely available RADAR5 solver written in ANSI Fortran-90 (Guglielmi and Hairer 2005). The RADAR5 framework comprises an algorithm to calculate numerically the solution of stiff delay differential equations based on an adapted 3-stage Radau IIA collocation method (Hairer and Wanner 1999, Guglielmi and Hairer 2001, Guglielmi and Hairer 2008). In order to increase the accuracy of the numerical solution, we implement the time-dependent standard Jacobian matrix and the Jacobian matrix with respect to the delayed variables within the RADAR5 code. An explicit presentation of these Jacobian matrices is given in the appendix.

### Parameter estimation

In section 3.3, we perform data-driven optimization of the model parameters. For parameter estimation and computation of confidence bounds using the profile likelihood method (Venzon and Moolgavkar 1988) (see equation (3.21) and (3.22)) we employ a least-squares algorithm (see equation (3.19)). To speed up calculation, we utilize Matlab's parallel computing toolbox to run several optimization processes simultaneously on a computer cluster.

## 1.2. Biological background

### 1.2.1. What is a virus?

Science has come a long way in understanding how infectious diseases are caused. The idea that small, invisible particles might be responsible for infectious diseases goes back to writings of Aristotle (384-322 BC). The first experimental evidences of viruses has been provided by the work of Adolf Mayer and Dmitri Ivanowski (Mayer 1886, Ivanowski 1892, Artenstein 2010). Both researcher detected that the agent of the tobacco mosaic disease remained infectious after passing through a bacteria-stopping filter. Martinus Beijerinck extended the research on the tobacco mosaic virus (TMV) and established the first concept of viruses as agents that can only grow in living host cells (Beijerinck 1898).

The discovery of viruses is closely linked to the consistent progress in the area of imaging technologies. In 1677, Antonie van Leeuwenhoek developed the first microscope, which allowed him to identify microorganisms or “little animals” (Artenstein 2010). Also John Buist was not aware of his observation of “minute bodies” when he monitored in 1887 for the first time the relatively large vaccinia virus using optical microscopy (Gordon 1937). Only the invention of electron microscopes achieved through an international cooperation in the 1930s enabled the first visualization of a virus, which was published by Helmut Ruska, Gustav Kausche, and Edgar Pfankuch in 1940 (Ackermann 2011). The visual identification of viral and cellular structures using electron microscopy was a scientific milestone.

The imaging advances revealed that, the general structure of these small infectious agents is actually quite simple. A virus is made up of at least a genome and a protective capsid (Figure 1.1) (Gelderblom 1996). The genome consists of either a ribonucleic acid (RNA) or deoxyribonucleic acid (DNA), which can be single-stranded (ss), double-stranded (ds), linear or circular. Viruses with an ssRNA genome are further classified according to the polarity of the ssRNA. A viral ssRNA genome is called positive-sense, if it has the same polarity as the viral messenger RNA (mRNA) and thus can serve directly as mRNA during the replication process. A negative-sense ssRNA has the opposite polarity as the viral mRNA and must first be transcribed into a complementary strand. The viral genome together with the capsid form the nucleocapsid, which in some viruses is covered by an additional protective envelope.

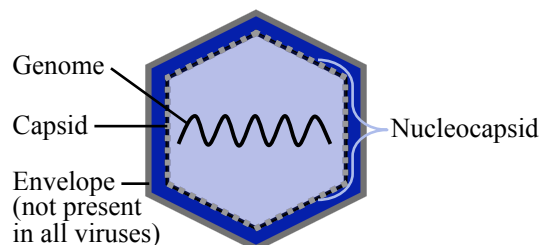


**Figure 1.1.:** Scheme of the general structure of a virus. A virus comprises at least a genome and a protective capsid. These two components form the nucleocapsid, which in some viruses is surrounded by an envelope.

## 1. Introduction

Since viruses are not able to proliferate independently, the infectious agents enter cells to utilize the cellular metabolic and biosynthetic machinery for replication.

### 1.2.2. Viruses studied in this thesis

In close collaboration with experimental partners, we investigate virus-host dynamics at single-cell level in communicating cell populations after infection with two different viruses. While we examine the dynamics of the Newcastle disease virus (NDV) in chapter 2, our work in chapter 3 is based on Dengue virus (DENV) infections.

#### **The avian Newcastle disease virus**

The first reported outbreak of Newcastle disease occurred at a farm near Newcastle upon Tyne in England in 1926 (Seal and King 2005). The Newcastle disease is a contagious bird disease, whereby the severity of the illness can range from mild to fatal (Capua and Alexander 2004). A transmission of NDV to humans is possible through a close contact with the virus or with infected birds and may cause influenza-like symptoms and even conjunctivitis.

The Newcastle disease is triggered by the avian paramyxovirus NDV, which is an enveloped, negative-sense ssRNA virus. The viral genome encodes for a nucleoprotein, phosphoprotein, matrix protein, fusion protein, haemagglutinin-neuraminidase (HN) protein and an RNA-directed RNA polymerase (Seal and King 2005). The attachment of NDV to a cell is mediated by the HN protein. For successful viral uptake into the cell during infection the HN protein interacts with the fusion protein. Subsequently, the nucleocapsid is released into the cytoplasm of the host cell, where viral replication takes place. After the synthesis of the viral proteins, genomic RNA replication starts with transcription of a positive-sense antigenome serving as a template for the negative-sense genome synthesis. The NDV genomic RNA is used for transcription as well as replication. The aggregation of viral proteins in the infected cell enables the assembly and the release of the generated virus through membrane budding. During the budding process, single copies of the NDV genome are enclosed by an outer envelope that is made from the plasma membrane of the host cell (Schirrmacher and Fournier 2009).

In experimental research, NDV is often used as a pathogen to analyze virus-host interactions. Since the avian virus cannot generate new infectious virus particles in most mammalian cell types (Rott 1979, Seal and King 2005), NDV is a suitable model to investigate primary infection without viral spread.

#### **The human Dengue virus**

The Dengue virus (DENV) is a mosquito-transmitted human pathogen widely distributed throughout tropical and subtropical regions around the world (Murray et al. 2013). The flavivirus DENV is an enveloped, positive-sense, ssRNA virus (Fischl

and Bartenschlager 2013) and includes five serotypes: DENV-1, DENV-2, DENV-3, DENV-4 and a recently discovered DENV-5 (Normile 2013). Infection with any serotype can lead to a broad spectrum of clinical manifestations, ranging from inapparent infection to flu-like Dengue fever, severe Dengue hemorrhagic fever and life-threatening Dengue shock syndrome (Díaz et al. 1988, Murphy and Whitehead 2011). The recovery from infection by one serotype can provide lifelong immunity to this specific serotype. However, subsequent secondary infection with a different serotype increases the risk of developing a serious disease. As primary infections are often asymptomatic, Dengue fever is not diagnosed and disease surveillance is inadequate, estimates of global DENV infections vary between 50 to 200 million cases per year (Murray et al. 2013). An even worse situation of annually 96 million apparent and additionally 294 million inapparent DENV infections is predicted by a cartographic modeling approach (Bhatt et al. 2013). Since approximately 50% of the world's population lives in regions with a risk of DENV infection and neither approved vaccines nor specific antiviral therapies are available, DENV is a major global health problem (Wilder-Smith et al. 2012).

The infection of a host cell by DENV starts with the binding of the virus to a cell surface receptor, which leads to the transportation of DENV into the cell via endocytosis (Lindenbach et al. 2006, Bartenschlager and Miller 2008, Welsch et al. 2009, Kumar et al. 2013, Acosta et al. 2014). The fusion of the viral envelope with the endosome membrane causes the release of the nucleocapsid into the cytoplasm. The nucleocapsid detaches and the released RNA is translated into a single viral polyprotein. This polyprotein is cleaved into 3 structural proteins, the capsid protein (C), the premembrane protein (prM) as well as the envelope protein (E) and 7 non-structural (NS) proteins (NS1, NS2A, NS2B, NS3, NS4A, NS4B, and NS5) by viral and cellular proteases (Chambers and Rice 1987, Bartenschlager and Miller 2008, Kumar et al. 2013, Acosta et al. 2014). Viral replication occurs in the cytoplasm in close association with intracellular membranes (Welsch et al. 2009, Peña and Harris 2012). Newly generated viral RNA together with capsid proteins form a nucleocapsid. The nucleocapsid associates with E and prM to form an immature virus particle inside the endoplasmic reticulum. The immature virus attains its maturity by passing through the trans-Golgi network and the mature infectious virus particle is released into the extracellular milieu.

To study the replication dynamics of DENV, our cooperation partners have generated a fully viable, fluorescent DENV reporter construct (see section 3.1.1). This DENV reporter enables us to detect both viral replication and viral spread in living host cells.

### 1.2.3. The interferon response against viral infections

Viruses can enter cells within minutes to exploit the hosts for the production of new virus particles, which are released some hours later to infect other cells. To prevent pathogen replication and spread host organisms have evolved an elaborate immune system that is able to respond in a fast, efficient and specific manner.

The immune system can be classified into an innate and an adaptive immunity.

## 1. Introduction

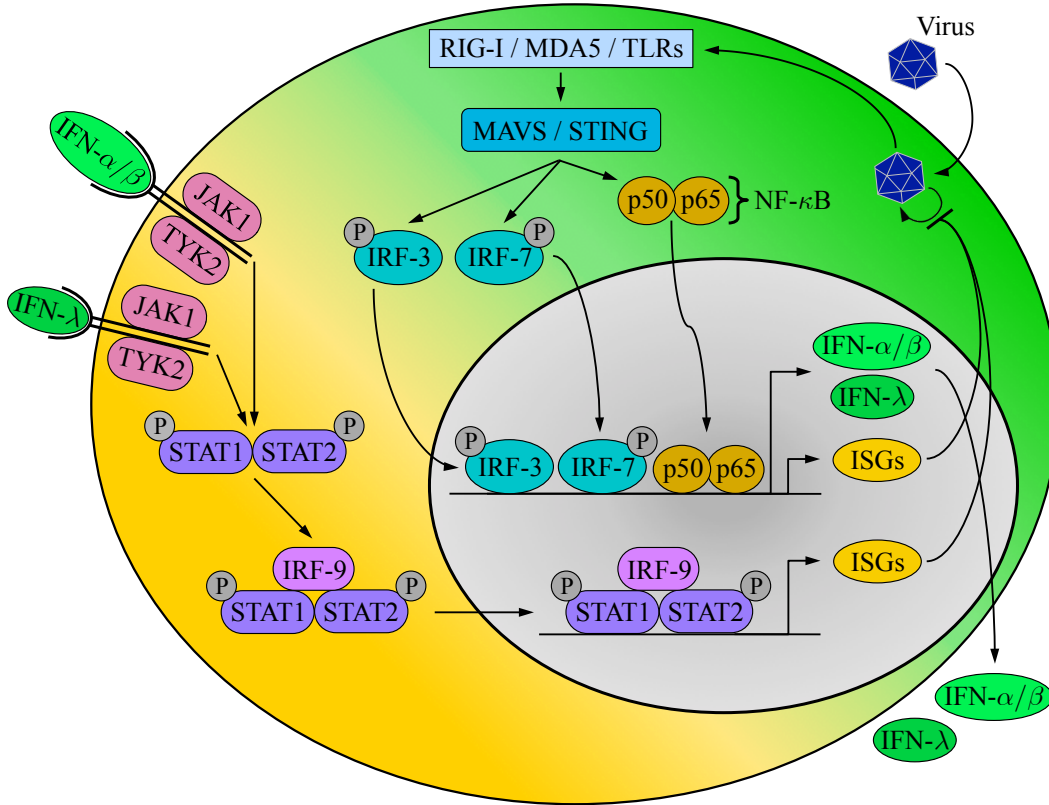


**Figure 1.2.:** Scheme of the antiviral interferon system. The cellular detection of replicating (⊙) RNA viruses by intracellular receptors activates a signaling cascade leading to the expression of interferons (IFN) as well as antiviral interferon stimulated genes (ISGs) (green background color). Secreted IFN induces the IFN response, which in turn triggers an antiviral state in the cell (yellow background color).

The discovery of these two subsystems goes back to the work of Elie Metchnikoff and Paul Ehrlich, who are considered the founders of the concepts of innate immunity and adaptive immunity, respectively (Kaufmann 2008, Artenstein 2010). Elie Metchnikoff carried out research on the innate immune response, the initial general line of defense against invading foreign pathogens, and published in 1884 his theory of cell-mediated immunity as a countermeasure against nonspecific pathogens. Complementary to this area of immunity, Paul Ehrlich studied the principles of the adaptive immune system, which comprises the defense against pathogens in the late phase of disease progression and the formation of immunological memory against specific disease agents. In the years of 1897–1901, Paul Ehrlich wrote several papers on his side-chain theory of antibody formation, which through receptor-mediated immune reactions generate a lasting infection memory (Ehrlich and Himmelweit 1956).

One central component of the innate immune response is the interferon system that provides a powerful defense against viral infections (Kunzi and Pitha 2003, Sadler and Williams 2008, Takeuchi and Akira 2009, West et al. 2011). After the infection of a host cell, intracellular pattern-recognition receptors (PRRs) are able to detect pathogen-associated molecular patterns (PAMPs) on the surface of the virus or

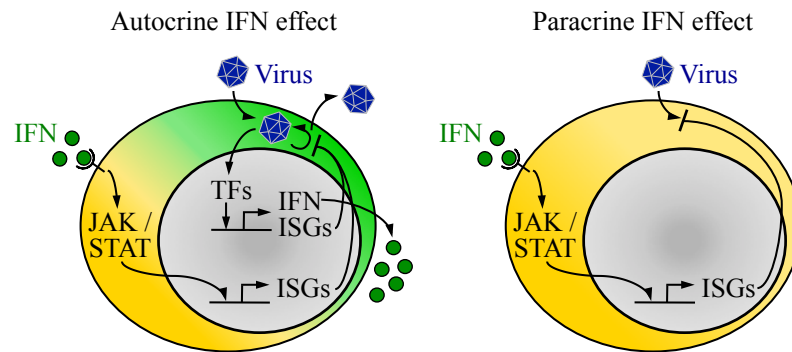


**Figure 1.3.:** Scheme of the autocrine and paracrine effect of IFN. The cellular recognition of viruses leads to the secretion of IFN (left, green background color). IFN activates in an autocrine manner in infected cells (left) the expression of antiviral ISGs (yellow background color). Moreover, the paracrine sensing of IFN by naïve cells (right) induces an antiviral protection against viral infection.

during the viral replication process. RNA viruses such as the Newcastle disease virus (see chapter 2) and Dengue virus (see chapter 3) are recognized by the RIG-I-like receptors (RLRs), including the retinoic acid-inducible gene I (RIG-I) and the melanoma differentiation-associated gene 5 (MDA5) and, in addition, by Toll-like receptors (TLRs) (Figure 1.2).

After viral sensing, RLRs associate with the mitochondrial antiviral-signaling protein (MAVS). MAVS interacts with several molecules that activate interferon regulatory factor (IRF) signaling such as the stimulator of interferon genes (STING, also known as MITA). Activation of STING leads to phosphorylation of IRF-3 as well as IRF-7. Furthermore, MAVS and different TLRs transmit the RNA virus signal to the nuclear factor  $\kappa$ B (NF- $\kappa$ B) consisting of the subunits p50 and p65. The transcription factors (TFs) IRF-3, IRF-7 as well as NF- $\kappa$ B translocate from the cytoplasm to the nucleus to induce the expression of type-I interferons (most common IFN- $\alpha$  and IFN- $\beta$ ) (Roberts et al. 1998), type-III interferons (IFN- $\lambda$ 1-4) (Wathelet et al. 1992, Takaoka and Yanai 2006, Prokunina-Olsson et al. 2013) and also some interferon stimulated genes (ISGs) (Grandvaux et al. 2002, Diamond and Farzan 2013, Chen et al. 2013). These ISGs can prevent further viral entry or inhibit viral replication in the infected host cell (Jiang et al. 2010, Brass et al. 2009).

Moreover, secreted interferons (IFN) induce the Janus activated kinase / signal transducer and activator of transcription (JAK/STAT) signaling pathway in an autocrine and paracrine manner (Figure 1.3) (Hall and Rosen 2010). The term autocrine IFN signaling stands for the action of IFN on already infected cells. Whereas paracrine IFN signaling is a form of cell-to-cell communication and describes the effect of IFN on naïve cells. While the IFN- $\alpha$  receptor recognizes secreted type-I IFN, type-III IFN is sensed through the IFN- $\lambda$  receptor (Takaoka and Yanai 2006, Sadler and Williams 2008). Stimulation of the specific IFN receptors activates JAK1 as well as tyrosine kinase 2 (TYK2) and these kinases phosphorylate STAT1 and STAT2. Phosphorylated STAT1/STAT2 together with IRF-9 form the IFN-stimulated gene factor 3 (ISGF3). The nuclear translocation of ISGF3 results in the expression of ISGs, which in turn block viral activity in infected cells and trigger an antiviral

## 1. Introduction

protective state in naïve cells.

While central molecular components of the IFN system have been characterized, it is not precisely known which processes of the antiviral IFN defense are essential for the outcome of viral infections. In the present work, we address this question by means of data-driven mathematical modeling in an IFN-competent cell system after primary infection with non-spreading NDV (see chapter 2) and, additionally, post infection with spreading DENV (see chapter 3).

### 1.2.4. The development of vaccines

In addition to researching viruses and the antiviral immune response, scientists tried intensively to develop a method for preventing infections. The first tool to protect from viral infection was variolation, which has been initially carried out in China around the 17th century in the fight against smallpox (Leung 2011). The idea of this ancient attempt was to expose a healthy person with material taken from a smallpox patient to trigger an attenuated but lifelong protective infection. In most cases variolation was effective, but about 1 to 14 percent of the recipients contracted severe smallpox and died (Gross and Sepkowitz 1998, Mishra 2012).

Based on the preparatory work of countless scientists, Edward Jenner achieved a medical breakthrough in 1796 by demonstrating in a systematic clinical study that preinoculation with cowpox virus protects humans against smallpox. This finding is widely regarded as the beginning of the science of vaccinology (Jenner 1801, Hilleman 2000 Artenstein 2010). After a long lasting global vaccination campaign against smallpox starting in the early 1800s, an international commission in 1979 certified the global eradication of a human disease for the first time in history (Mishra 2012).

The principle of vaccination is to generate a specific immune memory that facilitates early viral recognition and a fast response upon infection with a certain virus. Immune memory is achieved by challenging the host with a mimick of the virus that induces a virus specific immune response without causing the disease. Nowadays, there are three basic types of vaccines: subunit vaccines, inactivated vaccines, and live-attenuated vaccines (Cann 2005, Artenstein 2010, Pulendran and Ahmed 2011). Subunit vaccines contain only some components of the virus that are just sufficient to trigger a protective immune response but not enough to initiate a dangerous infection. Prominent examples for subunit vaccines are hepatitis B and human papillomavirus vaccines. The second group, the inactivated vaccines, are produced by growing virus in cell culture and subsequently damaging the virus particles in such a way that virus replication cannot occur, but the virus capsid proteins are recognized by the immune system. Current examples include the inactivated hepatitis A, polio and influenza vaccines. The third category, the live-attenuated vaccines, are replication-competent viruses with reduced pathogenicity to elicit an immune response without leading to disease. The used vaccine strain can originate from a natural virus as was the case for smallpox vaccines or from an artificially attenuated virus like the licensed vaccine YF-17D against yellow fever.

In the case of DENV, there are currently several vaccine candidates in clinical tri-

als (Pierson and Diamond 2014). In addition, the DENV-E217A mutant, which barely spreads, evokes strong immune responses and is therefore regarded as a novel live-attenuated vaccine candidate (Züst et al. 2013). Since the design of effective vaccines depends on the understanding which antiviral factors are decisive to generate a strong immune response while limiting viral spread, we analyze the underlying mechanisms responsible for the differences between DENV wild-type and attenuated DENV-E217A mutant infections by means of a data-driven mathematical model in chapter 3.

## 1.3. Mathematical research on viral infections

### 1.3.1. The basic concepts of mathematical modeling of viral infections

Early mathematical work on viral infections was mainly focused on better understanding the spread of the infection between hosts. William Heaton Hamer established a discrete model concerning measles epidemics, in which he assumed that the net rate of spread of infection is proportional to the product of the densities of susceptible and infectious individuals (Hamer 1906). This notion is one of the basic concepts in mathematical epidemiology and known as the “mass-action” principle of transmission for directly transmitted infections (Anderson and May 1991). Few years later, the scientists Anderson McKendrick as well as Ronald Ross derived the law of mass-action for differential equations in a diverse and independent manner. While Ronald Ross formulated mass-action from an original chemical perspective, Anderson McKendrick recognized the universal use of the mass-action principle (Heesterbeek 2005).

The classical epidemic model known as SIR model developed by William Kermack and Anderson McKendrick takes into account the temporal dynamics of susceptible  $S$ , infected  $I$  and recovered  $R$  population classes (Kermack and McKendrick 1927). This basic compartment model can be used to derive an epidemic threshold result, which states that an epidemic outbreak occurs if the basic reproduction number  $R_0$  is larger than 1 (Hethcote 2000). Since  $R_0$  is defined as the average number of secondary infections caused by one infected individual in an entirely susceptible population, a significant reduction of susceptible individuals through widespread vaccination can prevent epidemics. Moreover, the threshold result allows to identify viral diseases, which might be possible to eradicate. The data-based estimates of the basic reproduction number for smallpox  $R_{0,\text{smallpox}} = 5$  and for measles  $R_{0,\text{measles}} = 16$  (Hethcote 1989, Anderson and May 1991) successfully demonstrate that it is easier to eliminate smallpox through vaccination as achieved in 1979 than to combat the still ongoing but declining transmission of measles (World Health Organization, WHO 2014, Liu et al. 2014). Over time, the classical epidemic model has been utilized as a basis for more complex and virus specific models. Such extended models include additions like dividing the population into further compartments, integrating additional biological factors, incorporating age structures and considering spatial spread (Anderson and May 1991, Hethcote 2000, Getto et al. 2008, Labadie and Marciniak-Czochra 2011).

### 1.3.2. Application and contribution of mathematical models in medical research

Mathematical models have been recognized as essential tools for providing new insights into the understanding of viral dynamics in human diseases (Moghadas 2006). Prominent examples that mathematical modeling based on patient data can successfully guide the development of new antiviral therapies include research on acquired

immunodeficiency syndrome (AIDS) and hepatitis C.

Since the first reported cases of AIDS around 1962–1972 (Gilbert et al. 2007), the spread of its causative agent, the human immunodeficiency virus (HIV), triggered a dreadful pandemic that cost the lives of more than 24 million people worldwide (Feldmann et al. 2002). Each year the number of HIV-infected individuals rises dramatically with around 2.3 million new HIV infections in 2012 (WHO 2014), while the creation of a vaccine against AIDS is an ongoing challenge. To restrain the propagation of HIV in the patient, in 1987 scientists started to generate specific inhibitors of the viral enzymes (Montagnier 2010). Mathematical modeling based on clinical data of patients treated with such an inhibitor, revealed that following an initial exponential decline of HIV levels post treatment, HIV is sustained primarily by a continuous and highly productive virus replication (Ho et al. 1995, Wei et al. 1995). Thus, Ho et al. assumed that treatment of HIV as early as possible after infection could have a massive clinical impact. Based on the rapid HIV replication rate, a large mutation rate of the HIV genome was computed (Coffin 1995, Perelson et al. 1997). Importantly, mathematical modeling indicated that the high mutation ability of HIV can result in a fast resistance to any single drug and especially to those for which one mutation is sufficient to overcome the antiviral effects (Perelson et al. 1997, Perelson 2002). By this means, mathematical analysis guided the design of an immediate and prolonged combination therapy consisting of three and more inhibitors also known as highly active antiretroviral therapy (HAART). In most cases, the treatment of HIV patients with HAART prevents the onset of a lethal infection (Zuniga et al. 2008), which in turn results in an higher number of people living with HIV (~ 35.3 million people were living with HIV in 2012, WHO 2014).

Another example of the interdisciplinary cooperation between mathematical modeling and medical science is the field of hepatitis C research. Hepatitis C is a severe liver disease caused by the hepatitis C virus (HCV). The infection with HCV is initially asymptomatic, but becomes chronic in about 80% of the infected individuals and can lead to serious liver diseases (Lauer and Walker 2001). With about 170 million chronically infected people worldwide and an annual number of 3–4 million new infections, hepatitis C is a major global health problem (Rantala and Van de Laar 2008). Apart from the challenge to generate a protective vaccine, scientists work intensively on the improvement of the pharmacological treatment of HCV. Mathematical modeling of viral kinetics under therapy has contributed to a better understanding of the HCV pathogenesis and continuously supported the development of antiviral drugs. A seminal model describing the dynamics of uninfected target cells, infected cells and extracellular HCV could be parameterized with time course data of patients treated with IFN and thus allowed to uncover the rapid dynamics of HCV (Neumann et al. 1998). Moreover, the model indicated that the major initial effect of IFN is to inhibit virus production or release rather than preventing new infections. In consideration of new pharmaceuticals, this standard HCV model has been extended over the years (Guedj and Neumann 2010, Rong et al. 2010, Adiwijaya et al. 2010, Chatterjee et al. 2012). In particular, a multi-scale model of HCV infection and treatment, which includes both intracellular and extracellular HCV kinetics has proven to be an efficient tool to analyze the mode of action of different antiviral drugs including IFN (Guedj et al. 2013). This multi-scale model

## 1. Introduction

demonstrated the antiviral effect of IFN in constraining HCV replication and to a much lesser extent also HCV secretion. Furthermore, mathematical models comprising all relevant molecular processes of HCV replication have been established using steady-state measurements (Dahari et al. 2007) and additionally based on time course data (Binder et al. 2013). These comprehensive models provide a more precise understanding of the determinants of HCV replication that could be targeted by pharmacological therapies.

### 1.3.3. Mathematical modeling of the antiviral IFN system

Mathematical modeling of viral infections has a rich tradition. While much work has focused on the adaptive immunity generating a specific and lasting response (Anderson and May 1991, Nowak and May 2000), relatively few models described the initial phase of infection.

The key elements of the IFN-induced defense against viral infections have been examined using a mathematical model, which describes the temporal dynamics of susceptible, infected and resistant cells along with extracellular virus and protective IFN (Getto et al. 2008). Getto et al. have shown that in the case of a virus mortality rate larger than zero the virus will become eventually extinct and uninfected cells persist. If the virus mortality rate is zero, the kinetics may lead to the extinction of susceptible cells. Getto et al. compared this basic model with an extended variant in which the density of the infected cells is structured according to the infection age. The infection-age structured model allows to study the impact of heterogeneous intracellular processes like infection age dependent production of virus, secretion of IFN as well as cell mortality. This model predicts that viral infection can be defeated by both prolonging and shortening the time period of virus production. In addition, the basic model was expanded to investigate the spatial effects of diffusing virus, IFN and cells (Labadie and Marciniak-Czochra 2011). Labadie and Marciniak-Czochra demonstrated that susceptible cells cannot coexist with extracellular virus in the long run and that the spatial structure has a negative influence on the proliferation of viruses that have a mortality rate larger than zero. Moreover, the comprehensive mathematical analysis of the basic, infection-age structured and reaction diffusion model revealed conclusions concerning existence, asymptotic behavior and stability of the model solutions, which strongly depend on the initial conditions.

Systems biology approaches have also been successfully applied to explore the molecular mechanisms shaping the antiviral immune response (Gottschalk et al. 2013). In the case of the IFN system, mathematical models not only supported the characterization of virus-induced activation of IFN expression (Zou et al. 2010, Cheng et al. 2011) but also contributed to uncover the regulation of antiviral signaling mediated by IFN (Smieja et al. 2008, Maiwald et al. 2010).

Given the central role of the IFN system in the antiviral immune defense, it is astonishing that only a fraction of virus-infected cells express IFN (Zawatzky et al. 1985). Experimental studies suggested that the cell-to-cell variability of IFN expression is influenced by the cell-cycle state (Zawatzky et al. 1985), the limited availability of transcription factors (Apostolou and Thanos 2008) or due to viral

countermeasures (Chen et al. 2010, Killip et al. 2011). Based on single-cell data, Tay et al. (2010) established a hybrid stochastic-deterministic model to investigate the observed heterogeneous activation of NF- $\kappa$ B, which is one essential transcription factor of IFN. This model was able to reproduce both the measured digital activation and the analogue information processing of single-cell NF- $\kappa$ B dynamics. Moreover, the heterogeneous IFN induction was associated with the formation of the IFN- $\beta$  enhanceosome, a higher-order protein complex that initiates transcription from the IFN- $\beta$  promoter. Stochastic modeling and experimental validation showed that the sequential assembly of the multicomponent IFN- $\beta$  enhanceosome represents a major source of the detected heterogeneous IFN expression (Hu et al. 2007).

#### **1.3.4. Mathematical models of the antiviral IFN system in this thesis**

In order to study both the molecular key components of the IFN pathway in individual cells and the population dynamics after viral infection, we establish an integrative stochastic model that links virus-induced heterogeneous single-cell behavior with the cell-to-cell communication via secreted IFN (see chapter 2). The model is based on measurements in which a murine cell line was infected with NDV. While replication of NDV induces the expression of IFN in infected mouse cells (Kato et al. 2005, Childs et al. 2007), NDV is unable to produce new infectious virus particles in the murine NIH3T3 fibroblasts used in this study (Rott 1979). This system is thus a suitable tool to examine IFN induction elicited by primary infection only without influences by secondary infections. To adapt the mathematical model to the experimental conditions, we neglect viral spread in the stochastic model. Mathematical modeling and experimental validation indicate that few IFN-producing cells might act as sentinels of viral infection to protect a large number of naïve cells through powerful propagation of the IFN signal (Rand, Rinas et al. 2012).

Driven by the question, which factors of the antiviral IFN system are essential for limiting viral spread, we move to a system where viral spread is possible (see chapter 3). Based on time-resolved data of spreading DENV-infected cells, we establish a mathematical model of viral spread and IFN-induced antiviral protection. The model is a modified version of the classical SIR model (Kermack and McKendrick 1927). Apart from susceptible, infected and protected cells, our model also comprises extracellular virus as well as secreted IFN. To study which antiviral factors of the IFN system have the greatest influence on viral spread, we compare the infection dynamics of DENV wild-type with the attenuated spread of a DENV mutant. Using mathematical modeling and validation experiments, we find that the attenuation of the mutant is mainly due to the effect of accelerated IFN secretion to inhibit virus production during the early stages of viral replication, whereas faster protection of naïve cells by IFN has only a minor impact on spreading DENV (Schmid, Rinas et al. submitted).

## 1.4. Outline of this thesis

In this thesis we study the antiviral IFN system by means of data-driven mathematical modeling in intense collaboration with our experimental partners. Our work focuses on the question, which components of the IFN system are decisive to successfully combat viral infections.

In chapter 2, we investigate the relation between single-cell behavior and cell-to-cell communication via secreted IFN after primary infection with the Newcastle disease virus (NDV). By live-cell imaging, we show that the key steps of the IFN system comprising virus-induced signal transduction, IFN expression and IFN response are stochastic events in individual cells (see section 2.1).

To link the single-cell data to antiviral protection at the cell-population level, we establish a stochastic model, which combines the virus-induced IFN signaling in individual cells with the intercellular communication through released IFN (see section 2.2). For the parameter estimation we utilize our extensive data regarding high-dose infections (see section 2.3). Fitting of observed distributions of single-cell switching-on times reveals two mechanistically relevant conclusions. First, the induction of RIG-I-mediated signaling by virus is cooperative and, second, IFN gene induction downstream of transcription factor activation is a slow multi-step process. Mathematical modeling and experimental validation indicate that reliable antiviral response in the face of multi-layered cellular stochasticity is achieved by paracrine propagation of the IFN signal (see section 2.4) (Rand, Rinas et al. 2012).

To analyze which factors of the antiviral IFN pathway play a pivotal role in limiting viral spread, we examine the dynamics of spreading Dengue virus (DENV) in an IFN-competent cell system in chapter 3. Using fluorescent reporter cells and a fully viable DENV wild-type (DENV-wt) reporter construct, we demonstrate that IFN efficiently protects naïve cells from productive DENV infection and, if given early after infection, reduces viral replication in infected cells (see section 3.1.1 and 3.1.2). However, since antiviral IFN response is highly heterogeneous in single cells, viral spread and protection of cells by IFN occur in parallel - and compete - following DENV infection (see section 3.1.3). To examine which antiviral factors are able to control viral spread, we compare DENV-wt with the vaccine candidate DENV-E217A mutant, which induces a stronger IFN response and barely spreads (see section 3.1.4).

As the data concerning DENV infection suggest that the timing of IFN expression and virus production play an important role, we study the competition between viral spread and IFN-induced antiviral defense by means of a population-based delay differential equation model (see section 3.2). We first parameterize the model using DENV-wt infection data exclusively (see section 3.3.1). Then, we utilize this DENV-wt specific parameter set to discover DENV-E217A mutant specific parameters. The parameter optimization based on DENV-E217A mutant data demonstrates that the attenuation of the mutant can be explained by a reduced virus production rate and an accelerated IFN secretion (see section 3.3.2). To identify the relative importance of the two DENV-E217A mutant specific parameters on viral spread, we develop

an extended version of our delay differential equation model, which in addition to the paracrine effect of IFN on naïve cells also explicitly describes the autocrine IFN action on infected cells (see section 3.4). By analyses performed with this full model and validation experiments, we find that the attenuation of the mutant can primarily be attributed to accelerated IFN secretion triggered by DENV-E217A mutant infection (see section 3.5). This rapid IFN signal limits virus production during early phases of viral replication in infected cells, whereas accelerated protection of naïve cells by paracrine IFN action has only a low impact on the spread of DENV. The outcome of infection is thus primarily determined by the relative dynamics of DENV replication and the autocrine effect of IFN on infected cells (Schmid, Rinas et al. submitted).

In chapter 4, we discuss our findings separately for each model system (see section 4.1 and 4.2) and subsequently in overall terms (see section 4.3). In this regard, we assess our results, compare them with previous reports and draw biological conclusions.



## 2. Stochastic modeling predicts paracrine propagation of the IFN response induced by individual sentinels

The interferon system, as a first line of defense against viral infections, has a central antiviral function (see section 1.2.3) (Kunzi and Pitha 2003, Sadler and Williams 2008, Takeuchi and Akira 2009, West et al. 2011). Since the expression of interferons (IFN) is crucial to initiate an antiviral protective state, it is quite surprising that only a fraction of cells in a virus-infected cell population induces IFN (Zawatzky et al. 1985).

The literature suggests various reasons for the observed cell-to-cell heterogeneity in IFN expression. Some studies have concluded that host cell-intrinsic causes, such as a mechanism of IFN gene induction (Hu et al. 2007, Apostolou and Thanos 2008) or cellular variance in expression of the viral sensor protein retinoic acid-inducible gene I (RIG-I) (Hu et al. 2011) lead to heterogeneous IFN production. Alternatively, the stochasticity in IFN induction has been linked to the infecting virus due to its ability to antagonize the IFN system (Chen et al. 2010, Killip et al. 2011). According to the involved cell type or virus it could be that multiple factors contribute to the heterogeneity in IFN induction.

To study cell-to-cell variability of the IFN system, our experimental cooperation partners Ulfert Rand, Mario Köster and Hansjörg Hauser from the Department of Gene Regulation and Differentiation at the Helmholtz Centre for Infection Research (HZI) in Braunschweig generated a set of reporter constructs to monitor successive steps of IFN induction and IFN response in individual cells (see section 2.1.1, Rand 2010). The live-cell imaging data demonstrate that all key steps of the IFN system - the virus-induced signal transduction, the IFN expression (see section 2.1.2), and the induction of IFN-stimulated genes (ISGs) (see section 2.1.3) - are stochastic events in single cells. Additional experiments reveal that cell-intrinsic variability largely contributes to the detected heterogeneity in IFN induction (see section 2.1.2). Moreover, the examination of the response to IFN shows a dose-dependent binary pattern of two distinct subpopulations (see section 2.1.3). While the IFN-responding subpopulation is protected against viral infection, virus can still replicate in the non-responding cell fraction.

Based on the observed stochastic dynamics of the IFN network we establish a multi-scale mathematical model accounting for the stochastic intracellular dynamics in individual cells and the cell-to-cell communication via released IFN (see section

## 2. Stochastic modeling predicts paracrine propagation of the IFN response

2.2). The model is formulated as a continuous-time stochastic process in which the possible state changes of individual cells are specified through propensity functions depending on the current state of the cell and the extracellular concentration of secreted IFN. The kinetic of extracellular IFN is described by an ordinary differential equation and depends on the number of infected IFN-producing cells. The stochastic state transitions of individual cells with respect to virus replication, expression of IFN and induction of ISGs are simulated using Gillespie’s stochastic simulation algorithm, while the intercellular communication via IFN is calculated in parallel with a deterministic Euler method.

To determine the model parameters from the experimental data, we utilize our extensive measurements for high-dose infections (see section 2.3). The parameters describing the virus-induced activation of the transcription factors of IFN are estimated from a distribution of observed single-cell activation times using as objective function Neyman’s chi-squares statistic (Baker and Cousins 1984) (see section 2.3.1). For the minimization of this objective function we apply the simulated annealing algorithm (Kirkpatrick et al. 1983, Schneider and Kirkpatrick 2006). The resulting parameter estimates indicate that the initiation of RIG-I-mediated signaling by virus is cooperative.

Moreover, we find that the measured histogram of the time delay between transcription factor activation and IFN gene induction in individual cells can be fitted with a gamma distribution by using the maximum-likelihood method (Myung 2003) (see section 2.3.2). The parameter optimization reveals that IFN gene induction downstream of transcription factor activation corresponds to a slow multi-step process consisting of six consecutive and exponentially distributed steps.

Importantly, mathematical modeling and validation experiments predict that a small fraction of IFN-producing cells are sufficient to induce IFN target genes in the other, non-producing cells of the population (see section 2.4). Thus, we expect that stochastic sensing of viral infections by the innate immune system together with paracrine signal propagation provide an efficient and viral load-sensitive mechanism to achieve a reliable antiviral protection of the cell population (Rand, Rinas et al. 2012).

### **2.1. Experimental study of the IFN system reveals multi-layered stochasticity in individual cells**

#### **2.1.1. Monitoring virus-triggered IFN induction and response in single cells**

The finding that only a fraction of infected cells induces IFN (Zawatzky et al. 1985, Hu et al. 2007) demonstrates the necessity to investigate the IFN system at single-cell level. A valuable method to monitor the dynamics and variability of individual cells in real time is provided by live-cell imaging (Spiller et al. 2010). The first live-cell analysis for the IFN system was realized by our experimental collaboration partners Ulfert Rand, Mario Köster and Hansjörg Hauser (Rand 2010, Rand et al.

## 2.1. Experimental study of the IFN system reveals multi-layered stochasticity

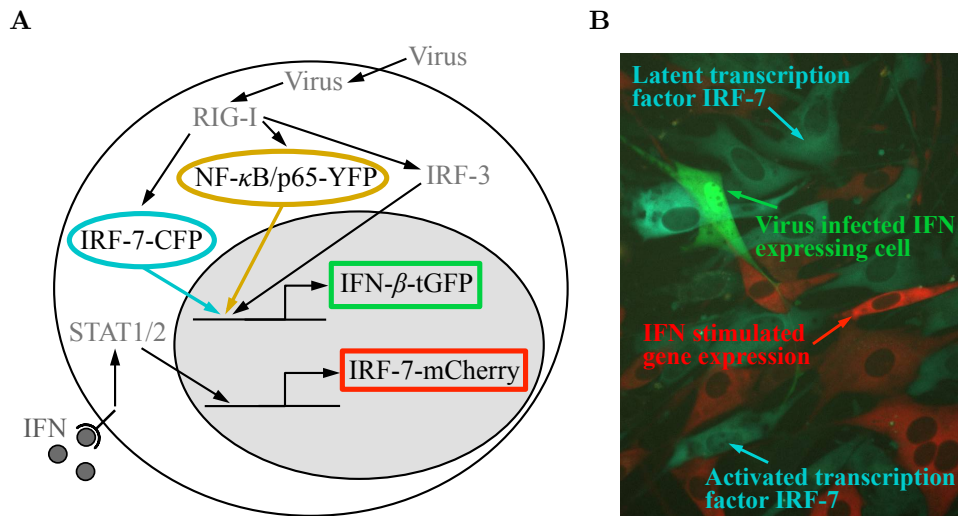


**Figure 2.1.:** Visualization of the key steps of the IFN pathway with fluorescent reporter cells. (A) Scheme of the established intracellular reporters. Virus recognition by RIG-I causes the nuclear translocation of the fusion proteins IRF-7-CFP (cyan cytoplasm → cyan nucleus) and NF- $\kappa$ B/p65-YFP (yellow cytoplasm → yellow nucleus). Subsequent IFN- $\beta$  expression becomes visible through the BAC reporter IFN- $\beta$ -tGFP (green cytoplasm) and induces the expression of ISGs illustrated by the BAC construct IRF-7-mCherry (red cytoplasm). (B) Fluorescence picture of the generated intracellular reporters. The virus-induced activation of the latent transcription factor IRF-7 (cyan cytoplasm) lead to its nuclear translocation (cyan nucleus). The following expression of IFN (green cytoplasm) results in the induction of the ISG IRF-7 (red cytoplasm). (Experiments by U. Rand, M. Köster and H. Hauser)

2012).

Hauser and colleagues developed fluorescent reporter cells to visualize successive key steps of the IFN system consisting of (i) virus-induced signal transduction, (ii) IFN expression and (iii) IFN response (Figure 2.1, Table 2.1). The signal transduction after the recognition of viruses by intracellular receptors like RIG-I results in the nuclear translocation of the nuclear factor  $\kappa$ B (NF- $\kappa$ B) and the IFN regulatory factors (IRFs) 3 as well as 7 (Brennan and Bowie 2010). To observe the nuclear translocation of the transcription factors, the scientists at the HZI designed dual reporter cells which were labeled with the fluorescent markers NF- $\kappa$ B/p65-YFP (yellow fluorescent protein) and IRF-7-CFP (cyan fluorescent protein), respectively. The presence of the transcription factors IRF-3/7 and NF- $\kappa$ B in the nucleus induces the expression of IFN including IFN- $\beta$  (Theofilopoulos et al. 2005). The induction of IFN- $\beta$  was monitored by transfecting murine fibroblasts with a bacterial artificial chromosome (BAC) encoded reporter expressing TurboGFP (green fluorescent protein) under the control of the IFN- $\beta$  promoter (IFN- $\beta$ -tGFP). In addition, a dual reporter cell line expressing both IRF-7-CFP and IFN- $\beta$ -tGFP was generated. Another BAC-based reporter construct in which the mCherry gene is linked to the C-terminal end of the genomic IRF-7 sequence (IRF-7-mCherry, monomeric cherry red fluorescent protein) enables the investigation of the prototypical ISG IRF-7 in response to secreted IFN (Honda et al. 2005).

## 2. Stochastic modeling predicts paracrine propagation of the IFN response

Reporter cell line	Visualization	Color
IRF-7-CFP - NF- $\kappa$ B/p65-YFP	Activation of IRF-7 and NF- $\kappa$ B	cyan/yellow
IRF-7-CFP - IFN- $\beta$ -tGFP	IRF-7 activation, IFN expression	cyan/green
IFN- $\beta$ -tGFP	IFN expression	green
IRF-7-mCherry	IFN response	red

**Table 2.1.:** Overview of the used fluorescent reporter cell lines in chapter 2. Our collaboration partners developed 4 fluorescent reporter cell lines to monitor (1) the activation of the transcription factors IRF-7 and NF- $\kappa$ B in a given cell, (2) the relation between IRF-7 activation and IFN- $\beta$  expression in a certain cell, (3) single-cell IFN- $\beta$  expression as well as (4) IFN-induced IRF-7 response in individual cells.

All reporter constructs were transfected into murine NIH3T3 fibroblasts and representative stable cell clones were utilized for the studies (Rand, Rinas et al. 2012; Supplementary Figure S2 and Supplementary Figure S8, Rand 2010).

### 2.1.2. Cell-to-cell variability in IFN induction

In order to examine the properties of the virus-induced IFN system, we use the Newcastle Disease Virus (NDV), which is an enveloped, negative-sense single-stranded (ss) RNA virus (cf. section 1.2.2). After infection, NDV replicates and induces IFN expression in the murine NIH3T3 fibroblasts via the viral RNA sensor RIG-I (Kato et al. 2005, Kato et al. 2006, Childs et al. 2007), but the avian NDV virus cannot generate new infectious virus particles in the mouse cells (Rott 1979). Therefore the experimental setup allows us to examine the properties of the IFN pathway after primary infection.

As we are primarily interested in the single-cell behavior of IFN expression, we first monitored IFN- $\beta$ -tGFP reporter cells by time-lapse microscopy (cf. section 2.1.1) after infection with different doses of NDV given in haemagglutinating unit per milliliter (HAU/ml) (Figure 2.2A left and Rand, Rinas et al. 2012: Supplementary Movie S1). The IFN- $\beta$ -producing cells started at various times to express IFN- $\beta$  with cell-to-cell differences of up to 20 h. Although we detected earlier onset of IFN- $\beta$ -tGFP induction after infection with higher viral loads, the relative variability or “noise” (Swain et al. 2002, Elowitz et al. 2002, Kærn et al. 2005) which can be quantified with the coefficient of variation ( $CV$ ; standard deviation divided by mean) varied only slightly (Figure 2.2A top left).

Moreover, we analyzed if the temporal heterogeneity in IFN- $\beta$  expression is determined by varying times of infection or due to intrinsic features of the host cell. For this purpose, viral infection was bypassed by using the polyinosinic-polycytidylic acid (poly I:C) stimuli. Poly I:C is a synthetic double-stranded RNA mimicking viral infections. This viral-surrogate serves as a non-replicating inducer control as it is recognized by the intracellular virus sensors RIG-I, MDA5 and TLR3 (Alexopoulou et al. 2001, Yoneyama et al. 2004, Kato et al. 2006). Poly I:C was introduced into IFN- $\beta$ -tGFP reporter cells through liposome-mediated transfection, which allows a synchronization of the viral stimuli (Figure 2.2A right, B and C). Also after transfec-

## 2.1. Experimental study of the IFN system reveals multi-layered stochasticity

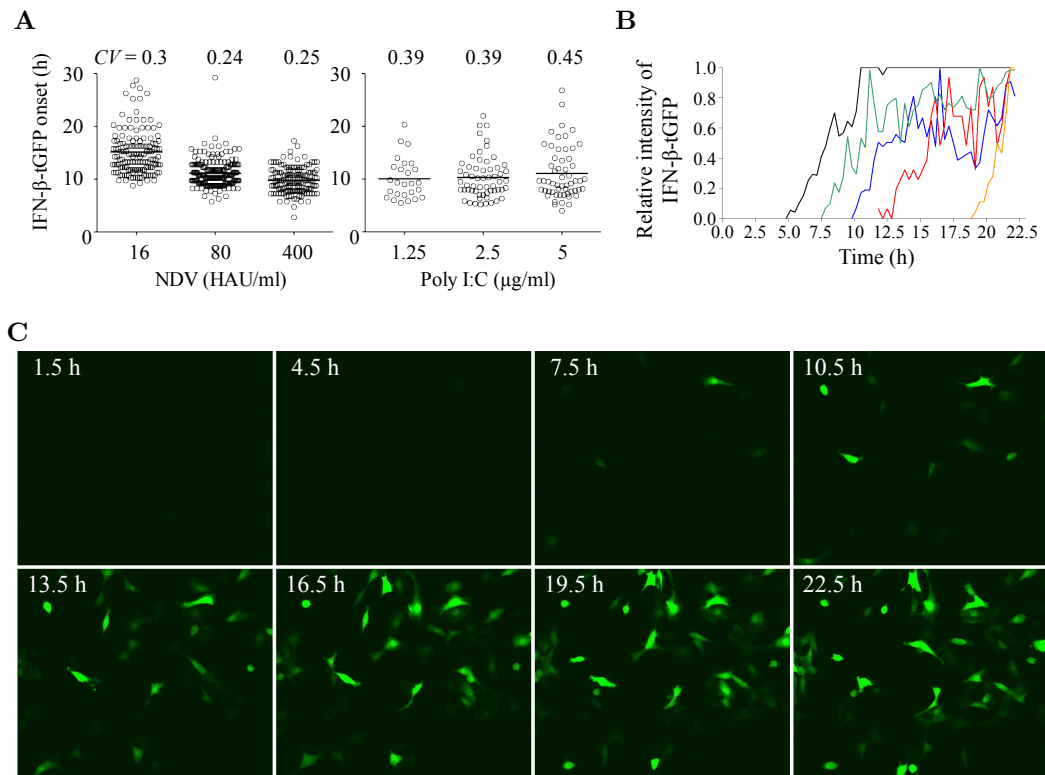


**Figure 2.2.:** Cell-to-cell heterogeneity in onset of IFN- $\beta$  expression. (A) Single-cell variability in IFN- $\beta$  induction is not caused by varying infection times. IFN- $\beta$ -tGFP reporter cells were infected for 1 h with different doses of NDV (left, x-axis) or transfected with varying concentrations of poly I:C (right, x-axis). Onset of IFN- $\beta$ -tGFP expression (y-axis) was detected by time-lapse microscopy at 15 min intervals. The scatter plots show the distribution of 456 NDV-infected cells or 140 poly I:C transfected cells, respectively. Experiment-related coefficient of variation ( $CV$ ) is given at the top. (B, C) Live imaging illustrates heterogeneous IFN- $\beta$  induction in individual cells. IFN- $\beta$ -tGFP reporter cells were stimulated with 32  $\mu$ g/ml poly I:C and subsequently monitored via time-lapse microscopy every 20 min. Selected single-cell kinetics in (B) and fluorescence pictures at indicated time post stimulation in (C) are presented. (Experiments by U. Rand, M. Köster and H. Hauser)

tion with different poly I:C concentrations we observed an extremely heterogeneous onset of IFN- $\beta$  expression in individual cells, which was quantitatively comparable to viral infection as seen by the same order of magnitude of the  $CV$ s (Figure 2.2A top right). These data reveal that the cell-to-cell variance in IFN- $\beta$  expression originates not from variable infection times.

To quantitatively determine viral replication and IFN induction in single cells, IFN- $\beta$ -tGFP reporter cells were infected with NDV and subjected to flow cytometry. At several time points post infection (p.i.) we measured simultaneously the viral hemagglutinin-neuraminidase (HN) protein and the IFN- $\beta$ -tGFP intensity (Figure 2.3A and B). The increasing fraction of virus replicating cells over time was followed by an about 12 h delayed rising number of IFN- $\beta$ -tGFP positive cells. As in other studies (Kumagai et al. 2009, Rehwinkel et al. 2010), we detected IFN- $\beta$ -tGFP expression only in cells with replicating virus. However, a remarkable number of in-

## 2. Stochastic modeling predicts paracrine propagation of the IFN response

ected cells did not express IFN. To analyze this phenomenon further, we divided the amount of infected cells into cells with low or high viral load, respectively (Rand, Rinas et al. 2012: Supplementary Figure S3). Since both subpopulations contained nearly the same fraction of IFN- $\beta$ -tGFP positive cells, we found no correlation between the level of viral replication and the expression of IFN- $\beta$ -tGFP.

In the literature it was discussed that the absence of IFN-inducing viral RNA may be responsible for the heterogeneity in IFN expression (Killip et al. 2011). Thus, we infected IFN- $\beta$ -tGFP reporter cells with NDV and subsequently transfected intracellular RNA of IFN-producing and non-producing cells into naïve IFN- $\beta$ -tGFP reporter cells (Rand, Rinas et al. 2012: Figure 2C and Supplementary Figure S4). As both RNA transfections activated a comparable fraction of IFN- $\beta$ -tGFP positive cells, heterogeneous IFN induction appears despite the presence of IFN-inducing viral RNA. These results demonstrate that viral replication is necessary to induce IFN but not sufficient.

Furthermore, we investigated the properties of IFN- $\beta$ -tGFP expression after infection with different virus doses (Figure 2.3C). The fraction of IFN- $\beta$ -tGFP positive cells increased almost linearly with higher virus concentrations and a multiplicity of infection (MOI; number of infectious virus particles divided by the number of potential host cells) of 1 induced IFN expression in less than half of the IFN- $\beta$ -tGFP reporter cells. In contrast, the mean fluorescence intensity (MFI) of the IFN- $\beta$  expressing subpopulation reached  $\sim 70\%$  of its maximum already at very low virus titer (5 HAU/ml NDV). Therefore, virus-induced IFN- $\beta$  production is dominated by the fraction of IFN- $\beta$  expressing cells.

Taken together, we observed stochastic IFN- $\beta$  expression after infection with NDV and after transfection with the viral-surrogate poly I:C. The data show strong cell-to-cell heterogeneity in IFN- $\beta$  induction, which is not caused by varying infection times, the level of viral replication or the absence of IFN-inducing viral RNA. Therefore we conclude that the stochasticity in IFN- $\beta$  expression is predominantly of cellular origin.

To examine mechanistically how cell-to-cell variability in IFN expression arises, we had a closer look on the IFN induction pathway. We analyzed the virus-induced activation of the key transcription factors NF- $\kappa$ B and IRF-7 by utilizing the dual reporter cells expressing NF- $\kappa$ B/p65-YFP and IRF-7-CFP (cf. section 2.1.1). After infection with NDV, latent transcription factors NF- $\kappa$ B and IRF-7 located initially in the cytoplasm, translocated into the nucleus (Figure 2.4A). The nuclear translocation of both transcription factors happened simultaneously in a single cell, but this joint translocation time varied strongly between different cells from 7 to 20 h post infection (Figure 2.4B). We also observed a simultaneous translocation of the transcription factors NF- $\kappa$ B/p65 and IRF-3 in individual cells by antibody staining of endogenous NF- $\kappa$ B/p65 as well as IRF-3 after infection with NDV or transfection with poly I:C (Rand, Rinas et al. 2012: Supplementary Figure S6). The discovery of a single cell specific but at population level varying translocation time of the key transcription factors of IFN demonstrates that strong cell-to-cell heterogeneity in IFN induction originates already in the shared upstream activation pathway of NF- $\kappa$ B and IRF-7.

## 2.1. Experimental study of the IFN system reveals multi-layered stochasticity

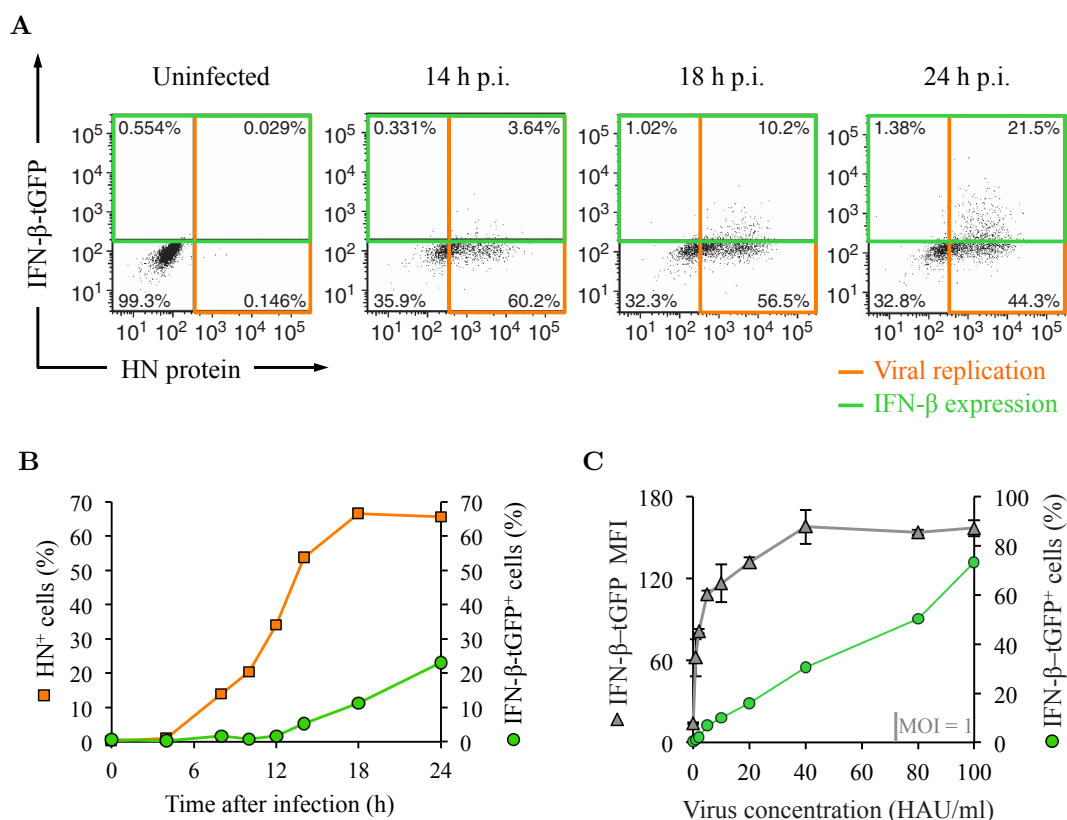


**Figure 2.3.:** Quantitative and temporal heterogeneity in IFN- $\beta$  expression. (A, B) Viral replication is necessary but not sufficient to activate IFN- $\beta$  expression. IFN- $\beta$ -tGFP reporter cells infected with 40 HAU/ml NDV for 1 h were subjected to flow cytometry at the indicated time points post infection (p.i.). Representative dot plots in (A) illustrate the jointly measured viral HN protein (x-axis) as well as IFN- $\beta$ -tGFP (y-axis) of individual cells. The corresponding kinetics of virus replicating cells (HN<sup>+</sup>, orange color) and IFN- $\beta$  expressing cells (IFN- $\beta$ -tGFP<sup>+</sup>, green color) are shown in (B). (C) Secreted IFN is determined by the fraction of IFN-producing cells. IFN- $\beta$ -tGFP reporter cells were infected with 1, 2, 5, 10, 20, 40, 80 or 100 HAU/ml NDV and analyzed by flow cytometry 24 h after infection. Illustrated are the fraction of IFN- $\beta$  positive cells (IFN- $\beta$ -tGFP<sup>+</sup>, green color) and the respective geometric mean of the fluorescence intensity (MFI) of the IFN- $\beta$  expressing subpopulation (gray color, mean of triplicate measurements and error bars). (Experiments by U. Rand, M. Köster and H. Hauser)

Additionally, we studied the relation between transcription factor activation and IFN induction using dual reporter cells expressing IRF-7-CFP together with IFN- $\beta$ -tGFP (Figure 2.4C as well as Rand, Rinas et al. 2012: Supplementary Figure S7). Most of the cells (91% at 80 HAU/ml NDV) with activated transcription factor IRF-7 also expressed IFN afterwards (Figure 2.4D). The few cells (9% at 80 HAU/ml NDV) which exhibited no IFN- $\beta$  expression after transcription factor activation showed similar distributed IRF-7 nuclear translocation times as the IFN- $\beta$  producing cells (Figure 2.4D bottom part). Since we found no IFN- $\beta$ -tGFP induction without prior nuclear translocation of IRF-7, activation of IRF-7 is necessary for IFN- $\beta$  production. It is also almost (in 91% of the cells) sufficient. Thus, we suggest that the decision to express IFN is primarily taken upstream of transcription factor

## 2. Stochastic modeling predicts paracrine propagation of the IFN response

activation.

The signaling delay from viral infection to IRF-7 nuclear translocation  $T_{\text{sig}}$  (mean value  $\bar{T}_{\text{sig}} = 11.7 \pm 4.0$  h) was comparably broadly distributed among individual cells as already detected with the dual reporter cells expressing the fusion proteins NF- $\kappa$ B/p65-YFP and IRF-7-CFP (Figure 2.4B;  $\bar{T}_{\text{sig}} = 11.9 \pm 3.4$  h). Furthermore, also the time delay between nuclear translocation of IRF-7 and onset of IFN- $\beta$ -tGFP expression  $T_{\text{gen}}$  (mean value  $\bar{T}_{\text{gen}} = 3.4 \pm 1.5$  h) varied remarkably from cell-to-cell. The similar  $CV$ s of  $T_{\text{sig}}$  ( $CV_{\text{sig}} = 0.34$ ) and  $T_{\text{gen}}$  ( $CV_{\text{gen}} = 0.44$ ) indicate a comparable variability of virus-induced signal transduction and subsequent IFN- $\beta$ -tGFP gene expression. These quantitative data thus reveal that both transcription factor activation and IFN- $\beta$  expression are sources of heterogeneity in single cells.

The phenomenon of cellular variability is widely studied in many different research areas. Cellular noise is classified into intrinsic noise arising from inherent stochastic biochemical reactions observed in equal elements and extrinsic noise, which results from extrinsic factors varying from one cell to another like differences in cell-cycle stage or cellular environment (Elowitz et al. 2002, Swain et al. 2002, Raser and O’Shea 2005, Maheshri and O’Shea 2007, Raj and van Oudenaarden 2008, Snijder and Pelkmans 2011). To analyze the origin of the single-cell heterogeneity more closely, we reduced extrinsic cell-to-cell differences through examining sister cells which divided during the first hour post infection (Spencer et al. 2009). The experiments show that the virus-induced nuclear translocation of IRF-7 happened mainly asynchronously in sister cells with a temporal difference larger than 2 h in  $\sim 50\%$  of the cell pairs (Figure 2.5A). An even weaker relation between sister cells was found for the time of IFN- $\beta$ -tGFP expression after transcription factor activation (Figure 2.5B), which agrees with the previously described stochastic transcription of the IFN- $\beta$  gene (Apostolou and Thanos 2008). To quantify the relation of sister cells we used the correlation coefficient  $r$  and the coefficient of determination  $r^2$ . The value of the coefficient of determination can be interpreted as the percentage of the variation that is explained through the correlation between the sister cells (Taylor 1990). The corresponding coefficient of determination was 0.6 for  $T_{\text{sig}}$  and 0.34 for  $T_{\text{gen}}$ , which in turn means that 40% of the variability in signaling and 66% of the variability in IFN- $\beta$ -tGFP expression are uncorrelated between sister cells and thus provide an estimate for the cell-intrinsic heterogeneity.

In order to verify whether different viral replication kinetics in sister-cell pairs are a source of stochasticity, we repeated the sister cell analysis with poly I:C stimulated reporter cells. Even after transfection with poly I:C the sister cells showed a largely uncorrelated behavior in IRF-7 activation as well as IFN- $\beta$ -tGFP expression (Figure 2.5E and F), with similar coefficients of determination ( $r^2 = 0.54$  for  $T_{\text{sig}}$  and  $r^2 = 0.11$  for  $T_{\text{gen}}$ ) as after viral infection. In addition, we tested if the time of cell division  $T_{\text{div}}$  influences the variation between sister cells in terms of transcription factor activation or IFN- $\beta$  induction. For this purpose, we determined the time elapsed since cell division versus the time difference between sister cells regarding IRF-7 signaling  $\Delta T_{\text{sig}}$  and IFN- $\beta$ -tGFP expression  $\Delta T_{\text{gen}}$  (Figure 2.5C and D for NDV infection; Figure 2.5G and H for poly I:C stimulation). The consideration of cell division yielded very weak correlations which argues against strong impact of the cell cycle on the stochasticity in IFN induction.

## 2.1. Experimental study of the IFN system reveals multi-layered stochasticity

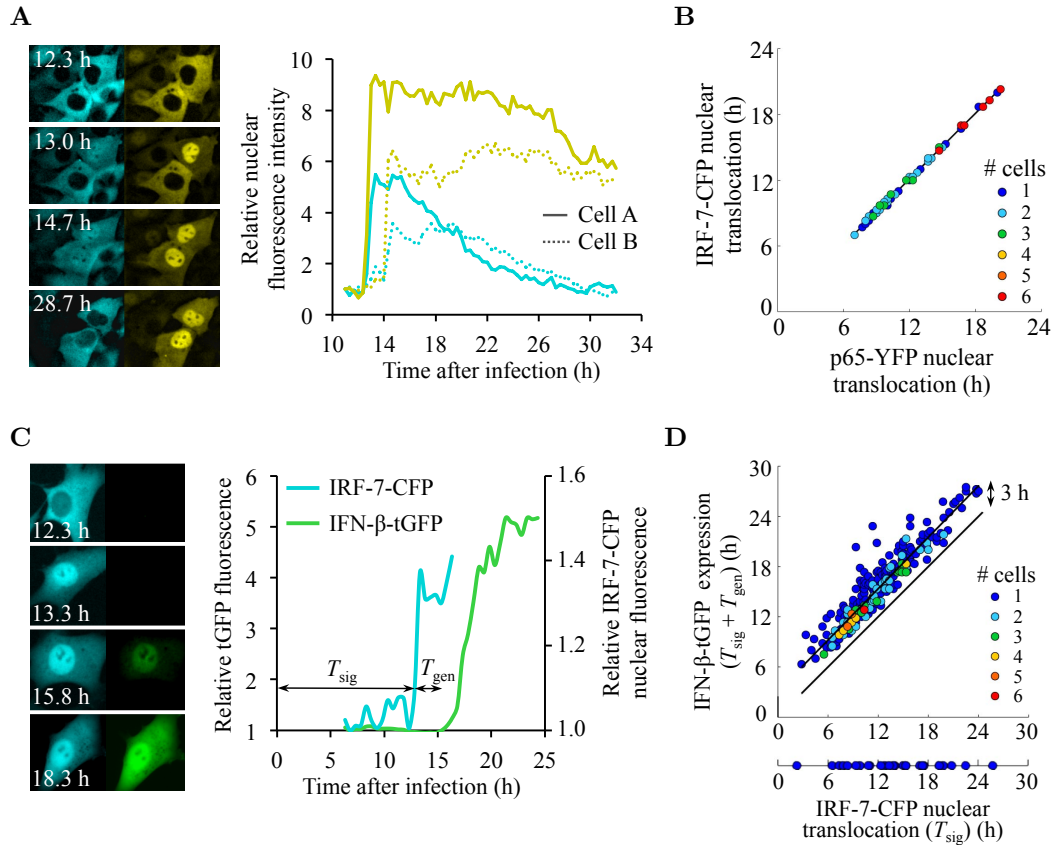


**Figure 2.4.:** Both virus-induced signal transduction and IFN expression are sources of heterogeneity. (A, B) Synchronous translocation time of transcription factors in single cells varies at cell population level. Dual reporter cells expressing the fusion proteins NF- $\kappa$ B/p65-YFP and IRF-7-CFP were infected with 80 HAU/ml NDV for 1 h and monitored by time-lapse microscopy every 20 min. (A) Fluorescence images of subcellular localization of IRF-7-CFP (left column) and p65-YFP (right column) at denoted time post infection. The kinetics show relative nuclear fluorescence for IRF-7-CFP (cyan) and p65-YFP (yellow) of two different cells. (B) Initial nuclear translocation of p65-YFP and IRF-7-CFP were determined in 65 individual cells and plotted against each other. Colored dots represent the frequency of data points. (C, D) Heterogeneous transcription factor activation and IFN expression in single cells. Dual reporter cells expressing IRF-7-CFP together with IFN- $\beta$ -tGFP were infected with 80 HAU/ml NDV and monitored by time-lapse microscopy at 20 min intervals. (C) Fluorescence images of subcellular localization of IRF-7-CFP (left column) and IFN- $\beta$ -tGFP (right column) at given time post infection. The kinetics show relative fluorescence intensity for nuclear IRF-7-CFP (cyan) as well as tGFP (green) of one cell.  $T_{sig}$  indicates the signaling delay from viral infection to IRF-7 nuclear translocation and  $T_{gen}$  defines the period of time between nuclear translocation of IRF-7 and onset of IFN- $\beta$ -tGFP expression. (D) Initial nuclear translocation of IRF-7-CFP ( $T_{sig}$ ) and IFN- $\beta$ -tGFP expression ( $T_{sig} + T_{gen}$ ) were determined in 315 individual cells and plotted against each other. Colored dots represent the frequency of data points. (Experiments by U. Rand, M. Köster and H. Hauser)

In summary, the data revealed two sources of cell-to-cell heterogeneity in IFN induction, namely the virus-induced signal transduction and the subsequent IFN expression (cf. Figure 2.4). According to the sister-cell analysis, approximately half of the

## 2. Stochastic modeling predicts paracrine propagation of the IFN response

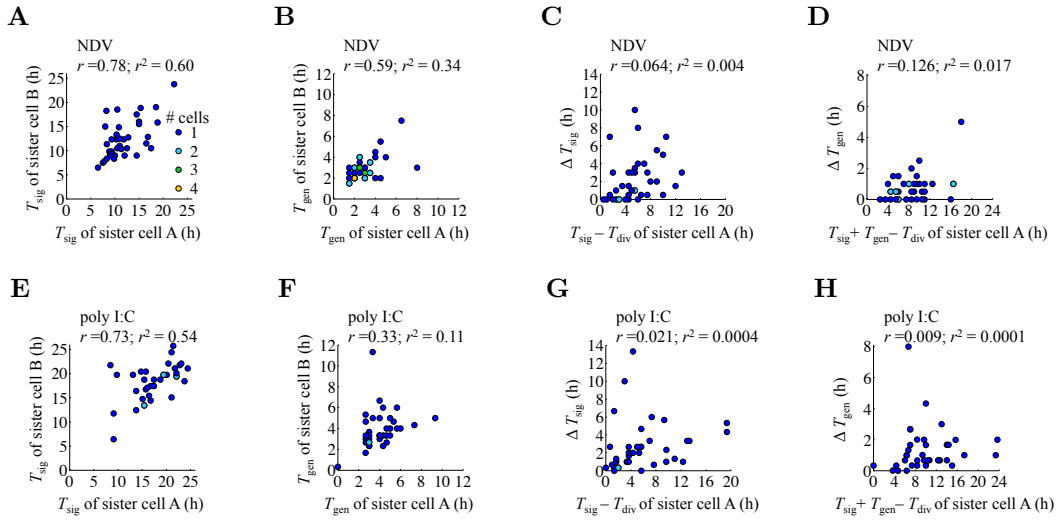


**Figure 2.5.:** Heterogeneous IFN induction in sister cells. (A-H) Dual reporter cells expressing IRF-7-CFP or IRF-7-TagRFP (red fluorescent protein tag) together with IFN- $\beta$ -tGFP were infected with 80 HAU/ml NDV for 1 h (A-D, 38 sister-cell pairs) or transfected with 5 mg/ml poly I:C (E-H, 36 sister-cell pairs) and monitored by time-lapse microscopy every 20 min. Colored dots represent the frequency of data points. Experiment-related correlation coefficient  $r$  and the coefficient of determination  $r^2$  are given at the top. (A, E) Delay from viral infection to IRF-7 nuclear translocation  $T_{\text{sig}}$  of sister cell A versus sister cell B. (B, F) Time interval between IRF-7 nuclear translocation and IFN- $\beta$ -tGFP expression  $T_{\text{gen}}$  of sister-cell pairs. (C, G) Time elapsed from cell division  $T_{\text{div}}$  to IRF-7 nuclear translocation ( $T_{\text{sig}} - T_{\text{div}}$ ) of one sister cell versus time difference between sister cells regarding IRF-7 signaling  $\Delta T_{\text{sig}}$ . (D, H) Time elapsed from cell division to IFN- $\beta$ -tGFP expression ( $T_{\text{sig}} + T_{\text{gen}} - T_{\text{div}}$ ) of one sister cell versus time difference between sister cells regarding IFN- $\beta$ -tGFP expression  $\Delta T_{\text{gen}}$ . (Experiments by U. Rand, M. Köster and H. Hauser)

stochasticity in both sources can be attributed to cell-intrinsic variability (cf. Figure 2.5). This intrinsic stochasticity provides a rationale for the lack of correlation of viral replication and IFN- $\beta$  expression (cf. Figure 2.3A).

### 2.1.3. IFN target gene induction is an all-or-nothing switch

The observation that many cells with replicating virus do not express IFN- $\beta$  or do so only very late after infection demonstrates that virus-induced IFN- $\beta$  expression is incomplete (cf. Figure 2.3). To understand the functional consequences of this stochastic and occasional IFN induction, the cellular antiviral response to IFN in terms of ISG expression should also be considered. Thus, we stimulated the IRF-7-mCherry reporter cells (cf. section 2.1.1) with IFN- $\beta$  (given in units per milliliter (U/ml)) and monitored IRF-7 expression by time-lapse microscopy (Figure 2.6 and Rand, Rinas et al. 2012: Supplementary Movie S2). Individual cells responded very heterogeneously at various time points to IFN- $\beta$  stimulation. So, not only IFN induction but also IFN response is a stochastic event in single cells.

To quantify the observed heterogeneous response to IFN, IRF-7-mCherry reporter

## 2.1. Experimental study of the IFN system reveals multi-layered stochasticity

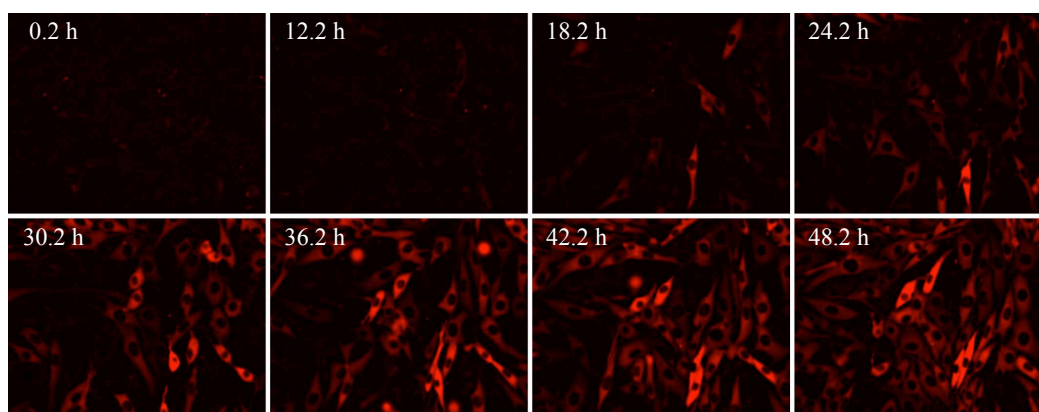


**Figure 2.6.:** Single-cell heterogeneity of IRF-7 expression in response to IFN- $\beta$ . IRF-7-mCherry reporter cells were stimulated with 500 U/ml IFN- $\beta$  and detected by time-lapse microscopy at 30 min intervals. Selected fluorescence pictures at indicated time post stimulation are presented. (Experiments by U. Rand, M. Köster and H. Hauser)

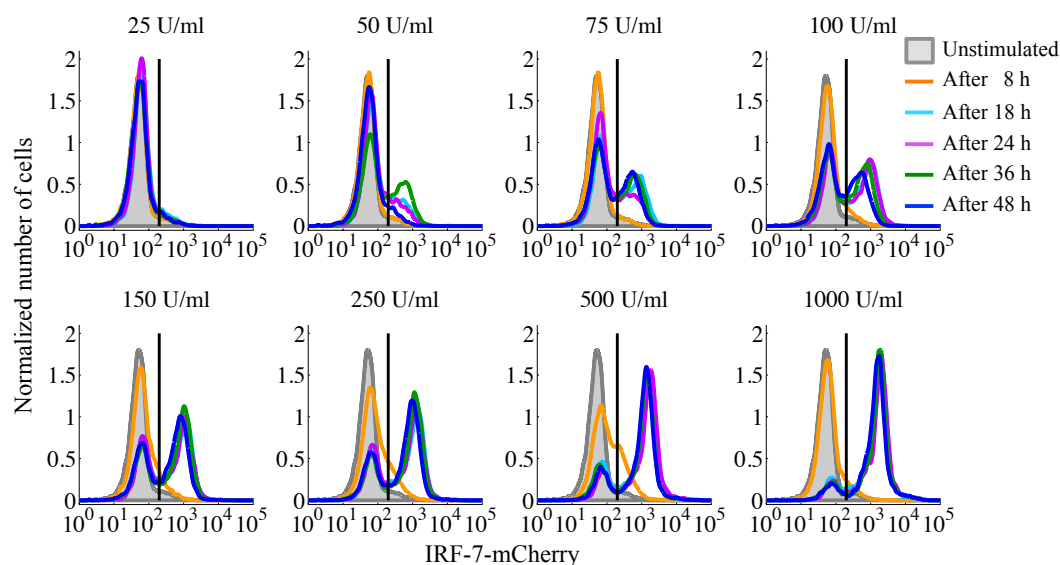


**Figure 2.7.:** Binary time- and dose-dependent IRF-7-mCherry response towards IFN- $\beta$ . IRF-7-mCherry reporter cells were stimulated with increasing concentrations of IFN- $\beta$  indicated at the top of each panel. The intensity of IRF-7-mCherry expression was measured by flow cytometry at multiple time points after stimulation, which is represented through different colors. Normalized distributions are shown to enable the comparison of individual measurements with each other. (Experiments by U. Rand, M. Köster and H. Hauser)

cells were stimulated with different concentrations of IFN- $\beta$  and analyzed by flow cytometry at several times after stimulation (Figure 2.7). The distributions of IRF-7-mCherry levels from individual cells showed a bimodal pattern with distinct IRF-7 expressing and non-expressing subpopulations. The IRF-7 expressing subpopulation increased with the passage of time and with higher amounts of extracellular IFN- $\beta$ , which implies a time- and dose-dependent response to IFN. We also measured the IFN response in several IRF-7-mCherry clones and detected consistently a binary IRF-7 expression (Rand, Rinas et al. 2012: Supplementary Figure S8). Moreover,

## 2. Stochastic modeling predicts paracrine propagation of the IFN response

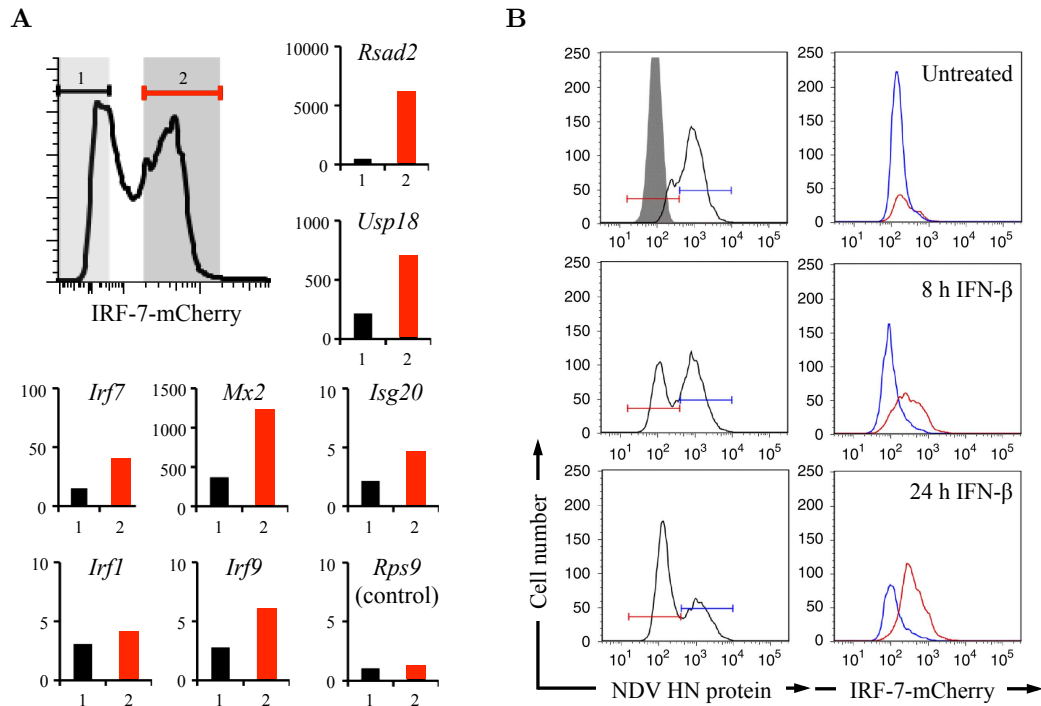


**Figure 2.8.:** Bimodality of IRF-7 expression is reflected in ISG transcription and antiviral protection. (A) IRF-7 expression represents production of ISGs. IRF-7-mCherry reporter cells were stimulated with 500 U/ml IFN- $\beta$  for 16 h and subjected to FACS. IRF-7-mCherry negative (1, black) as well as positive (2, red) cells illustrated by the shaded areas were separated. RNA was isolated from both subpopulations and analyzed by qPCR for the expression of indicated ISGs and Rps9 as a control. The bar charts show the fold RNA increase in relation to untreated reporter cells after normalization to  $\beta$ -actin mRNA. (B) IRF-7 expression correlates with antiviral protection. IRF-7-mCherry reporter cells were left untreated (upper row), pre-treated for 8 h (middle row) or 24 h (lower row) with 500 U/ml IFN- $\beta$  and subsequently infected with 80 HAU/ml NDV. After an infection period of 20 h, we measured simultaneously in each single cell the NDV HN intracellular antibody level and IRF-7-mCherry fluorescence intensity by flow cytometry. The NDV HN positive (colored in blue) as well as negative cells (colored in red) were identified (left column) and examined for their respective IRF-7-mCherry expression (right column). (Experiments by U. Rand, M. Köster and H. Hauser)

the unresponsiveness was not influenced by competition of cells for available IFN- $\beta$ , since IFN- $\beta$  was still detectable in the supernatant for more than 30 h (Rand, Rinas et al. 2012: Supplementary Figure S9).

To test whether induction of IRF-7-mCherry correlates with the expression of endogenous ISGs, we separated IRF-7-mCherry negative and positive cells by fluorescence-activated cell sorting (FACS) and analyzed isolated RNA from these cells by quantitative polymerase chain reaction (qPCR) for the expression of common ISGs (Figure 2.8A). All tested ISGs showed enhanced mRNA levels in IRF-7-mCherry expressing cells (Figure 2.8A red bars, whereby the 40S ribosomal protein S9 (RPS9) serves as control). These measurements suggest that a distinct subpopulation of cells which can be identified by IRF-7-mCherry expression coordinately activates an antiviral gene program. To examine this further, we pre-treated IRF-7-mCherry

### *2.1. Experimental study of the IFN system reveals multi-layered stochasticity*

reporter cells with IFN- $\beta$  for 8 or 24 h to allow induction of ISGs and subsequently infected the cells with NDV (Figure 2.8B). Virus replicated in IRF-7-mCherry negative cells (Figure 2.8B in blue color) but not in the IRF-7-mCherry positive cells (Figure 2.8B in red color). Thus, only IRF-7-mCherry expressing cells have been protected by IFN-induced antiviral ISG expression.

Taken together, the data demonstrate that IFN response is a stochastic, IFN- $\beta$  concentration-dependent, switch in individual cells. This switch is characterized by an all-or-nothing principle, in which virus can replicate in the non-responding subpopulation and the responding subpopulation is protected against viral replication.

## 2.2. Stochastic model of the IFN response against viral infection

The experimental study of the IFN system revealed a remarkably strong cell-to-cell heterogeneity of both IFN induction (cf. section 2.1.2) and antiviral IFN response (cf. section 2.1.3). To understand the stochastic dynamics of the IFN network we develop a multi-scale mathematical model that combines the virus-induced IFN signaling in individual cells with the extracellular cell-to-cell communication via secreted IFN in an infected cell population (Figure 2.9). The stochastic state transitions of individual cells with respect to virus replication, IFN induction and IFN response are iterated using Gillespie's algorithm, while the intercellular communication via IFN is calculated in parallel with a deterministic Euler method.

### 2.2.1. Stochastic simulation based on Gillespie's algorithm

The stochastic simulation algorithm (SSA) by Daniel T. Gillespie is a Monte Carlo procedure to simulate numerically stochastic kinetics (Gillespie 1976, Gillespie 1977). It has been proven that the SSA is fully equivalent to the master equation approach, which in turn is the fundamental description of stochastic processes (McQuarrie 1967, Matheson et al. 1975). Using Gillespie's algorithm enables the realization of a continuous-time Markov process (Gillespie 1976, Banks et al. 2011, Gillespie 2007).

A continuous-time stochastic process  $\{X(t), t \geq 0\}$  is a set of random variables  $X$  at time  $t$  on a countable state space  $Q$ , where  $X$  can be in a state  $s \in Q$ . The process  $\{X(t), t \geq 0\}$  is called a Markov process, if the Markov property

$$\begin{aligned} \mathcal{P}(X(t_{n+1}) = s_{n+1} \mid X(t_0) = s_0, X(t_1) = s_1, \dots, X(t_n) = s_n) \\ = \mathcal{P}(X(t_{n+1}) = s_{n+1} \mid X(t_n) = s_n) \end{aligned} \quad (2.1)$$

is fulfilled for all  $n \in \mathbb{N}_0$ , successive times  $t_0 \leq t_1 \leq \dots \leq t_n \leq t_{n+1}$  and states  $s_0, s_1, \dots, s_{n+1} \in Q$  (Waldmann and Stocker 2004). The notation  $\mathcal{P}(A \mid B)$  designates the conditional probability of  $A$  under the condition  $B$ . The Markov property therefore requires a memoryless system in which a state change depends only on the current state and not on the past history.

In our model, the Gillespie algorithm is applied to simulate the dynamic process of a heterogeneous cell population comprising  $N$  cells. A single cell  $i$  with  $i = 1, \dots, N$  can be in  $K$  different states  $S_{k,i}$ ,  $k \in \{1, \dots, K\}$ . The transitions between these states of an individual cell are specified through  $M$  state dependent propensity functions  $\{W_1, \dots, W_M\}$ . The whole system is characterized by the state vector of the cell population

$$X(t) = (S_{k,1}(t), \dots, S_{k,N}(t)) = x, \quad (2.2)$$

at time  $t \in \mathbb{R}_{\geq 0}$ . The full system with respect of the  $K$  different subpopulations is given by

$$Y(t) = (Y_1(t), \dots, Y_K(t)) = y, \quad (2.3)$$

## 2.2. Stochastic model of the IFN response against viral infection

where  $Y_k(t)$  denotes the number of individuals in the state  $S_k$ . The goal is to determine the dynamic of  $X(t)$ , given that the system was in state  $X(t_0) = x_0$  at the starting time  $t_0$ .

In the following section 2.2.2, we establish a stochastic model that describes key steps of the IFN system at single-cell level along with intercellular communication through expressed IFN. To simulate a time step  $X(t) \rightarrow X(t + dt)$  of the population dynamic, we consider at time  $t$  all possible state changes of the individual cells of the population and compute the time interval  $dt$  and the state change to be realized in accordance with Gillespie's direct method (see section 2.2.3) (Gillespie 2007, Cao and Samuels 2009).

### 2.2.2. Model of virus-induced IFN signaling in single cells along with cell-to-cell communication through secreted IFN

To analyze the heterogeneous single-cell dynamics of the antiviral IFN network, we develop a stochastic model for an ensemble of  $N$  individual cells communicating via released IFN.

Since the experimentally used virus cannot spread (cf. section 2.1.2 page 22), we restrict the viral activity in our model to the initial infection with subsequent virus replication and neglect reinfection. Depending on the initial infection dose, we set a fraction of cells as infected. A certain percentage of these infected cells will eventually express IFN- $\beta$  corresponding to the measured number of IFN- $\beta$ -tGFP<sup>+</sup> cells (cf. Figure 2.3). Since the MOIs used in the experiments are approximately unity or below, the number of infecting virus particles per cell is low. At the starting time  $t_0 = 0$ , we therefore randomly assign each cell  $i = 1, \dots, N$  a number of intracellular virus particles  $V_i$  according to

$$V_i(0) = \begin{cases} 0 & , \text{ if cell } i \text{ is uninfected;} \\ 1, 2 \text{ or } 3 & , \text{ if cell } i \text{ is infected.} \end{cases} \quad (2.4)$$

The state  $S_{k,i}(t)$  of a cell  $i$  at time  $t \in \mathbb{R}_{\geq 0}$  is defined by the intracellular viral load  $V_i(t)$  and the phenomenological state  $Z_{l,i}(t)$  representing the signal transduction in single cells after viral infection. To count the number of all possible single-cell states  $K$ , we utilize the index  $k = 1, \dots, K$ .

The initial condition of the model is given by the states of the individual cells at time zero  $S_{k,i}(0) = (Z_{l,i}(0), V_i(0))$ , whereby only the following two phenomenological states are possible at time  $t_0 = 0$ :

(Z0)  $Z_{0,i} \hat{=}$  cell  $i$  is uninfected

(Z1)  $Z_{1,i} \hat{=}$  cell  $i$  is infected and virus replication is recognizable by receptors.

After the initial infection, the cells change their current states  $S_{k,i}(t) = (Z_{l,i}(t), V_i(t))$  and the number of cells in a state  $S_k$  at time  $t \in \mathbb{R}_{\geq 0}$ , denoted as  $Y_k(t)$ , varies over time. For a compact computational description of the system that can be compared

## 2. Stochastic modeling predicts paracrine propagation of the IFN response

with the live-cell imaging data (cf. section 2.1.2 and 2.1.3), we choose additional phenomenological states  $Z_{l,i}$  as illustrated in Figure 2.9 and outlined under (Z2)–(Z9) below.

Experiments of the virus-induced IFN expression revealed two sources of single-cell variability, first, the activation of latent transcription factors NF- $\kappa$ B and IRF-7 downstream of viral sensing by RIG-I (cf. Figure 2.4A and B) and, second, induction of the IFN- $\beta$  gene by intranuclear NF- $\kappa$ B and IRF-7 (cf. Figure 2.4C and D). Based on the sister-cell analysis, both of these sources arise substantially from cell-intrinsic noise (cf. Figure 2.5). In the model, we thus attributed the cell-to-cell variability in IFN induction and IFN response to intrinsic stochasticity. On the one hand, both the onset of transcription factor activation and IFN- $\beta$  expression are broadly distributed among the cell population (cf. Figure 2.4D). On the other hand, the examination of single-cell kinetics in terms of nuclear fluorescence intensity of the transcription factors NF- $\kappa$ B as well as IRF-7 (cf. sample trajectories in Figure 2.4A) and IFN- $\beta$  fluorescence (cf. sample kinetics in Figure 2.4C) show a quantitatively step rise once nuclear translocation and gene induction, respectively, have been triggered. To account for the switch-like activation of the transcription factors and subsequent IFN- $\beta$  expression, we describe the dynamics of these events in an individual cell  $i = 1, \dots, N$  as stochastic transitions between the following discrete states (Z1)–(Z3) shown along the first column in Figure 2.9 (Mariani et al. 2010):

(Z1)  $Z_{1,i} \hat{=}$  cell  $i$  is infected and virus replication is recognizable by receptors

(Z2)  $Z_{2,i} \hat{=}$  NF- $\kappa$ B/IRF is activated in cell  $i$

(Z3)  $Z_{3,i} \hat{=}$  cell  $i$  secretes IFN- $\beta$ .

Furthermore, our studies expose the IFN response as an IFN- $\beta$  concentration dependent all-or-nothing switch in individual cells (cf. Figure 2.7 and Figure 2.8). To model the switch-like induction of antiviral ISGs, we simulate the IFN response as two stochastic transitions between discrete states consisting of the IFN-dependent nuclear translocation of STAT1/2 (Lillemeier et al. 2001, Vinkemeier 2004) and the subsequent expression of ISGs, such as IRF-7. With regard to the possible combinations of the cell properties we consider the states (Z4)–(Z9) as follows (cf. middle and last column in Figure 2.9):

(Z4)  $Z_{4,i} \hat{=}$  STAT1/2 is activated in cell  $i$

(Z5)  $Z_{5,i} \hat{=}$  NF- $\kappa$ B/IRF and STAT1/2 are activated in cell  $i$

(Z6)  $Z_{6,i} \hat{=}$  cell  $i$  secretes IFN- $\beta$  and STAT1/2 is activated

(Z7)  $Z_{7,i} \hat{=}$  cell  $i$  expresses ISGs

(Z8)  $Z_{8,i} \hat{=}$  cell  $i$  expresses ISGs and NF- $\kappa$ B/IRF is activated

(Z9)  $Z_{9,i} \hat{=}$  cell  $i$  expresses IFN- $\beta$  and ISGs.

The transitions between the states  $S_{k,i}(t) = (Z_{l,i}(t), V_i(t))$  with  $k \in \{1, \dots, K\}$  and  $l \in \{0, \dots, 9\}$  are defined by state-dependent propensity functions  $W_m$  for

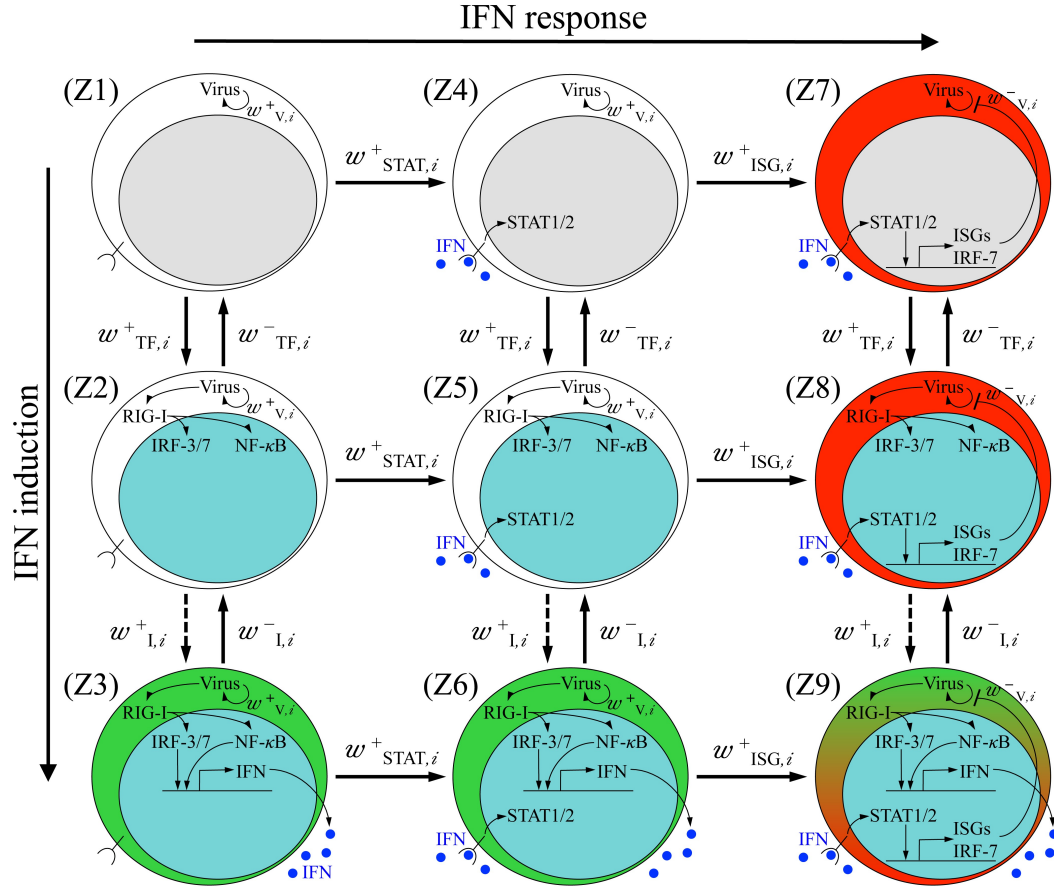


**Figure 2.9.:** A multi-scale mathematical model of IFN induction and response. The model describes an infected cell population with state transitions of individual cells according to (i) virus replication ( $\odot$ ), (ii) virus-induced nuclear translocation of the transcription factors IRFs/NF- $\kappa$ B (cyan nucleus), (iii) IFN- $\beta$  gene induction (green cytoplasm), (iv) nuclear translocation of STAT1/2 induced by extracellular IFN and (v) expression of antiviral ISGs including IRF-7 (red cytoplasm), in combination with the cell-to-cell communication via secreted IFN. Possible state changes of an individual cell  $i \in \{1, \dots, N\}$  between the discrete states (Z1)–(Z9) depend on the propensity functions  $w_{s,i}^{\pm}$  with  $s \in \{V, TF, I, STAT, ISG\}$ . The color code corresponds to the experimentally used fluorescent reporter cells (cf. section 2.1.1). Induction of IFN- $\beta$  (dashed arrow) is explicitly modeled as a multi-step process to fit the available experimental data (cf. section 2.3.2); all other state transitions are described as single steps (solid arrows).

$m = 1, \dots, M$ . In order to make a reference to the occurring state transition, we specify the propensity functions of an individual cell  $i$  as  $w_{s,i}^{\pm}$ , which in turn depend on the current state of the cell  $S_{k,i}(t)$ . For the description of our system, we choose the following propensity functions (cf. Figure 2.9):

- (1) After the initial infection the virus starts to replicate in the host cells. We simulate the replication of virus particles in the model as a birth-death process (Kendall 1949) with the rate constant of virus replication  $r_V$  and the rate constant of virus decay  $d_V$  (Figure 2.10). The associated propensity function

## 2. Stochastic modeling predicts paracrine propagation of the IFN response

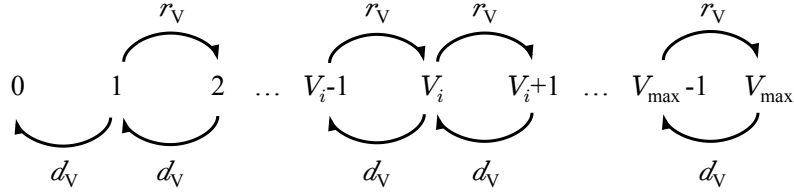


**Figure 2.10.:** Scheme of the used birth-death process to simulate virus replication. Intracellular virus particles  $V_i$  replicate in an infected cell  $i \in \{1, \dots, N\}$  with the rate constant of virus replication  $r_V$ . The maximal number of virus particles which an intact cell can harbor is defined by  $V_{\max}$ . The antiviral effect of ISG expression inhibits further viral replication and decreases the intracellular viral load with the rate constant of virus decay  $d_V$ .

of virus replication is specified through

$$w_{V,i}^+ = r_V V_i(t) \mathcal{H}(V_{\max} - V_i(t)), \quad (2.5)$$

where the Heaviside step function

$$\mathcal{H}(V_{\max} - V_i(t)) = \begin{cases} 0 & , \text{ if } V_i(t) \geq V_{\max}; \\ 1 & , \text{ if } V_i(t) < V_{\max} \end{cases} \quad (2.6)$$

is taken into account for the limited capacity of an intact cell to harbor maximal  $V_{\max}$  virus particles.

- (2) The presence of virus induces the activation of the transcription factors NF- $\kappa$ B as well as IRF-7. In dependence of the intracellular viral load  $V_i$ , we describe the propensity function of transcription factor (TF) activation by the Hill function

$$w_{\text{TF},i}^+ = k_{\text{RIG-I}} \frac{V_i(t)^{h_V}}{K_V^{h_V} + V_i(t)^{h_V}}, \quad (2.7)$$

with the half-saturation constant  $K_V$ , the Hill coefficient  $h_V$  and the rate  $k_{\text{RIG-I}}$  of RIG-I pathway activation by virus (Alon 2006). This formulation enables a threshold response of the RIG-I pathway with saturation regarding the number of intracellular virus particle  $V_i$ . Since some reporter cells demonstrated that IRF-7 accumulated in the nucleus also returns to the cytoplasm (cf. left column in Figure 2.4A, Rand 2010), we allow in our model the inactivation of the RIG-I pathway with propensity

$$w_{\text{TF},i}^- = l_{\text{RIG-I}}. \quad (2.8)$$

- (3) The nuclear translocation of the transcription factors NF- $\kappa$ B as well as IRF-7 leads to IFN- $\beta$  gene induction according to the propensity

$$w_{\text{I},i}^+ = k_{\text{IFN}}, \quad (2.9)$$

whereby IFN- $\beta$  expression can also terminate with propensity

$$w_{\text{I},i}^- = l_{\text{IFN}}. \quad (2.10)$$

## 2.2. Stochastic model of the IFN response against viral infection

- (4) The experimental data show that the fraction of IFN- $\beta$  expressing cells determines the extracellular concentration of IFN- $\beta$  (cf. Figure 2.3C). Although extracellular IFN- $\beta$  decreases through the cellular uptake and degradation in the medium, IFN- $\beta$  was always detectable in the supernatant (cf. Rand, Rinas et al. 2012: Supplementary Figure S9) indicating the presence of a large number of IFN- $\beta$  molecules in the cell culture. Regarding the high diffusion coefficient of IFN (Kreuz and Levy 1965:  $D_{\text{IFN}} = 3.42 \times 10^5 \mu\text{m}^2/\text{h}$ ; Hu et al. 2011:  $D_{\text{IFN}} = 1.08 \times 10^5 \mu\text{m}^2/\text{h}$ ), diffusion on the relevant length scale of several cell diameters occurs fast (within minutes) compared to the hour-timescale of IFN and ISG expression. For these reasons, we consider a uniform distribution of secreted IFN in our model and calculate the instantaneously equilibrating extracellular concentration of IFN- $\beta$  in parallel with the Gillespie algorithm. We assume that IFN- $\beta$  producing cells secrete IFN- $\beta$  with the rate constant  $k_S$  and take into account a degradation of extracellular IFN- $\beta$  according to the rate constant  $d_{\text{IFN}}$ . The corresponding differential equation of the extracellular concentration of IFN- $\beta$   $I$  over time is given by

$$\dot{I}(t) = k_S N_{\text{IFN}}(t) - d_{\text{IFN}} I(t), \quad (2.11)$$

where  $N_{\text{IFN}}(t)$  stands for the number of IFN- $\beta$  expressing cells at time  $t$ .

- (5) The activation of STAT1/2 by autocrine or paracrine recognition of extracellular IFN- $\beta$   $I$  (cf. Figure 1.3) is formulated with the propensity function

$$w_{\text{STAT},i}^+ = k_{\text{STAT}} \frac{I^{h_{\text{IFN}}}}{K_{\text{IFN}}^{h_{\text{IFN}}} + I^{h_{\text{IFN}}}}, \quad (2.12)$$

where  $k_{\text{STAT}}$ ,  $K_{\text{IFN}}$  and  $h_{\text{IFN}}$  denote the rate, the half-saturation constant and the Hill coefficient of STAT1/2 pathway activation by IFN, respectively.

- (6) Activated STAT1/2 in turn cause the expression of ISGs, including IRF-7, with propensity

$$w_{\text{ISG},i}^+ = k_{\text{ISG}}. \quad (2.13)$$

As the observed number of IRF-7 expressing cells remained high within the observation period of 48 h post infection (cf. Figure 2.11B (4)), we ignore both a termination of ISG expression and an inactivation of STAT1/2.

- (7) To characterize the induction of an antiviral state through IFN response, we assume that in an ISG expressing cell  $i \in \{1, \dots, N\}$  viral replication is inhibited and the intracellular viral load  $V_i$  declines according to the propensity function

$$w_{V,i}^- = d_V V_i(t), \quad (2.14)$$

where  $d_V$  denotes the rate constant of virus decay (cf. Figure 2.10).

An additional overall decline of viral load can be attributed to the death of virus-infected cells (cf. decrease of  $\text{HN}^+$  cells in Figure 2.3A and B, orange color). To keep the model as simple as possible we have neglected cell death and also cell proliferation by simulating a constant cell population. The consideration of a non-growing cell population is justified since we did not detect obvious differences in

## 2. Stochastic modeling predicts paracrine propagation of the IFN response

heterogeneous IFN- $\beta$  induction between the cell fraction dividing during the time of observation (cf. Figure 2.5A and B) and the whole cell population which contains a sizable proportion of non-dividing cells (cf. Figure 2.4B and D).

### 2.2.3. Model simulations using Gillespie's algorithm

Our cell population model, which couples the stochastic state changes of individual cells according to the propensity functions  $w_{s,i}^{\pm}$  with the intercellular communication via secreted IFN- $\beta$  (cf. section 2.2.2), is implemented and simulated in Matlab (The Mathworks Inc., Natick, MA) using Gillespie's direct method (Gillespie 2007, Cao and Samuels 2009).

To execute a time step of the dynamics, we consider at time  $t \in \mathbb{R}_{\geq 0}$  all possible state changes of each cell  $i = 1, \dots, N$  and calculate the time interval  $dt$  after which the next stochastic switching event takes place by

$$dt = -\frac{\ln(u_1)}{w_0}, \quad (2.15)$$

where  $u_1$  denotes a random number drawn from the unit-interval uniform distribution. The denominator in (2.15) is defined as

$$w_0 = \sum_{s \in \mathcal{S}^+} \sum_{i=1}^N w_{s,i}^+ + \sum_{s \in \mathcal{S}^-} \sum_{i=1}^N w_{s,i}^- = \sum_{m=1}^M W_m \quad (2.16)$$

with  $\mathcal{S}^+ = \{V, TF, I, STAT, ISG\}$  as well as  $\mathcal{S}^- = \{V, TF, I\}$ . The term  $w_0$  represents the sum of all propensity functions  $W_m$  for  $m = 1, \dots, M$  that "lead away" from the current state of the system.

The propensity function  $W_j$  of the actually occurring state transition at time  $t + dt$  has to fulfill the condition

$$\sum_{m=1}^{j-1} W_m < u_2 w_0 \leq \sum_{m=1}^j W_m, \quad (2.17)$$

where  $u_2$  denotes a second random number drawn from the uniform distribution in the unit-interval.

In parallel to the Gillespie algorithm, we compute the extracellular IFN- $\beta$  concentration  $I$  by utilizing the Euler discretization of the differential equation (2.11):

$$\begin{aligned} \dot{I}(t) &= k_S N_{\text{IFN}}(t) - d_{\text{IFN}} I(t) \\ \Leftrightarrow \frac{I(t+dt) - I(t)}{dt} &= k_S N_{\text{IFN}}(t) - d_{\text{IFN}} I(t) \\ \Leftrightarrow I(t+dt) &= I(t) + dt[k_S N_{\text{IFN}}(t) - d_{\text{IFN}} I(t)]. \end{aligned} \quad (2.18)$$

The application of the Euler method requires a sufficiently small time step  $dt$  that satisfies  $dt \ll d_{\text{IFN}}^{-1}$ . We found the latter condition to be guaranteed with the parameter choices for our model (cf. Table 2.2). After every Gillespie step, we update the system in accordance with the current states of the individual cells. To compare the model simulations with the experimental data (Figure 2.11), we take into account the following readouts (ROs):

## 2.2. Stochastic model of the IFN response against viral infection

(RO1) The total viral load of the cell population computed by

$$V(t) = \sum_{i=1}^N V_i(t) \quad (2.19)$$

is compared with the measured mean fluorescence intensity of the viral hemagglutinin-neuraminidase (HN) protein staining by using a scaling factor (cf. Figure 2.3A and Figure 2.11B (1)).

(RO2) During simulation, we extract the modeled initial nuclear translocation times of the transcription factors NF- $\kappa$ B and IRF-7 after infection  $\mathcal{T}_{\text{sig},i}, i = 1, \dots, N$  through storing the time point a cell  $i$  changes for the first time its state from  $Z_{1,i}$  to  $Z_{2,i}$ , from  $Z_{4,i}$  to  $Z_{5,i}$  or from  $Z_{7,i}$  to  $Z_{8,i}$  (cf. Figure 2.9 upper and middle row). These simulated times  $\mathcal{T}_{\text{sig},i}$  are used to fit the distribution of the imaged activation times of the transcription factors  $T_{\text{sig}}$  (cf. Figure 2.4D and Figure 2.11A upper panel).

(RO3) The simulated time delays between transcription factor activation and onset of IFN- $\beta$  expression  $\mathcal{T}_{\text{gen},i}, i = 1, \dots, N$  are calculated by storing the time point a cell  $i$  with activated transcription factor starts to express IFN- $\beta$  (cf. Figure 2.9 middle and last row). The modeled times  $\mathcal{T}_{\text{gen},i}$  are utilized for the estimation of the observed time spans  $T_{\text{gen}}$  of IFN- $\beta$ -tGFP switching-on times after activation of the transcription factors (cf. Figure 2.4D and Figure 2.11A lower panel).

(RO4) The simulated number of IFN- $\beta$  expressing cells at time  $t$   $N_{\text{IFN}}(t)$  is related to the monitored IFN- $\beta$ -tGFP<sup>+</sup> reporter cells (cf. Figure 2.3B and Figure 2.11B (2)).

(RO5) The computed extracellular IFN- $\beta$  concentration over time  $I(t)$  is compared with the experimentally quantified amount of released IFN- $\beta$  (Figure 2.11B (3)).

(RO6) The modeled number of ISG expressing cells at time  $t$   $N_{\text{ISG}}(t)$  represents the investigated IRF-7-mCherry<sup>+</sup> reporter cells (cf. Figure 2.7 and Figure 2.11B (4)).

The determination of the model parameters is explained briefly in the following and described in more detail in the next section 2.3. The resulting parameter values are listed in Table 2.2 and lead to the simulations shown in Figure 2.11.

For the parameterization of our model, we focus on the extensive data for high-dose infections with 40 and 80 HAU/ml NDV (Figure 2.11). Fitting of the observed distributions regarding the NF- $\kappa$ B/IRF-7 nuclear translocation times ( $T_{\text{sig}}$ ) and the IFN- $\beta$ -tGFP switching-on times ( $T_{\text{sig}} + T_{\text{gen}}$ ) results in a good approximation of the data (Figure 2.11A) and enables the description of the measured kinetic of IFN- $\beta$ -tGFP<sup>+</sup> cells (Figure 2.11B (2)). The fits require that (i) the activation of the RIG-I-mediated signaling by virus is cooperative (cf. section 2.3.1) and (ii) IFN- $\beta$  gene induction is modeled as a multi-step process (cf. section 2.3.2). These two conclusions drawn from the parameter estimation correspond well with previously

## 2. Stochastic modeling predicts paracrine propagation of the IFN response

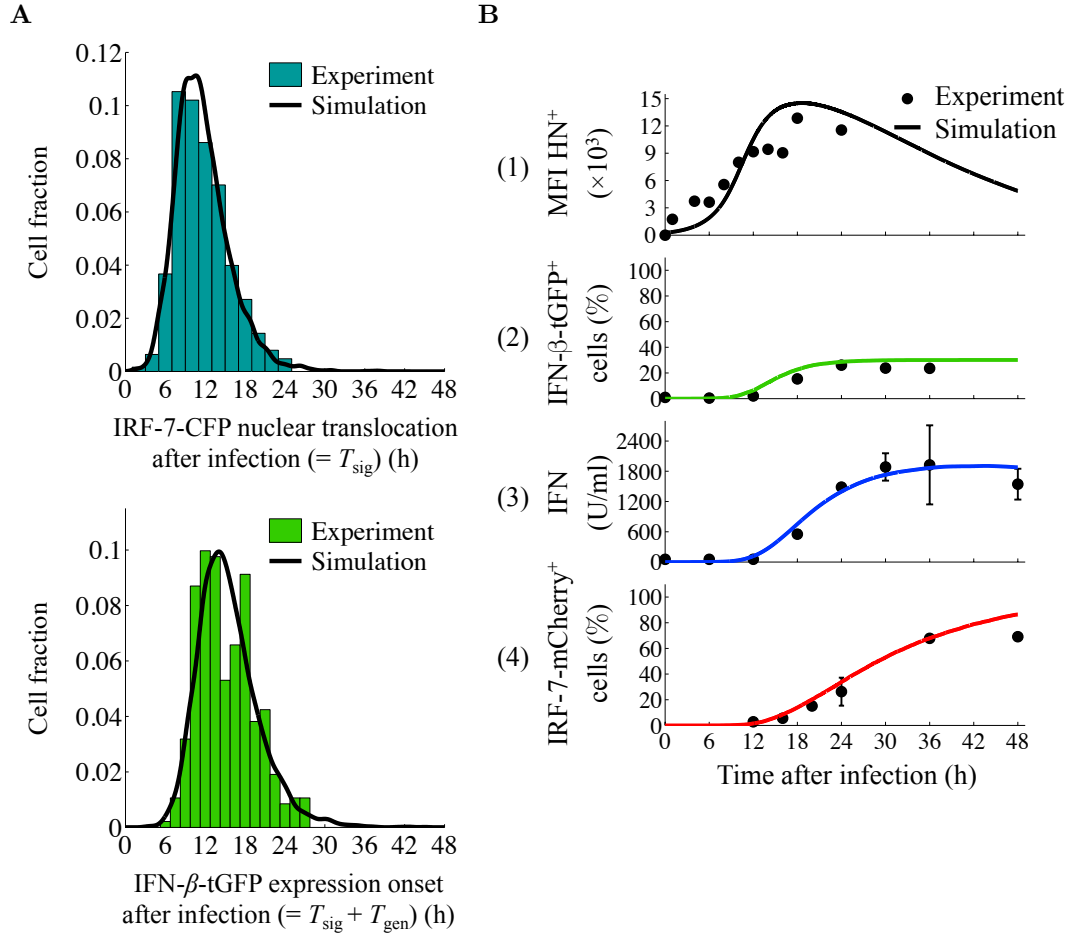


**Figure 2.11.:** Simulating the multi-layered cell-to-cell heterogeneity of the IFN system results in predictable populations dynamics. (A) Model simulations of NF- $\kappa$ B/IRF nuclear translocation time points and IFN- $\beta$ -tGFP onset times versus experimental data. With the stochastic model computed distributions (black lines) match the data of IRF-7-CFP nuclear translocation times ( $T_{\text{sig}}$ , cyan histogram) and IFN- $\beta$ -tGFP expression onset ( $T_{\text{sig}} + T_{\text{gen}}$ , green histogram) monitored in single cells after infection with 80 HAU/ml NDV (cf. Figure 2.4D for a representation of individual time points). (B) Comparison between simulated and measured cell population dynamics. The stochastic model (solid lines) reproduces the observed kinetics (dots) of (1) viral load (as measured by HN expression), (2) IFN- $\beta$ -tGFP induction, (3) extracellular IFN titre and (4) IRF-7-mCherry expression after infection with 40 HAU/ml NDV. The smooth model curves in (A) and (B) are mean values obtained by simulating  $10^4$  cells. Time course data in (B)(2)–(4) represent the mean and standard deviation of triplicate measurements. (Experiments by U. Rand, M. Köster and H. Hauser)

described findings (Hu et al. 2007, Ford and Thanos 2010, Onoguchi et al. 2010, Binder et al. 2011).

To estimate the parameters of the IFN response, we initially scale our model to the measuring unit of IFN by fitting the dose-response curve of IRF-7-expressing cells depending on external IFN- $\beta$  (cf. Figure 2.14). Restricted through this calibration and the already specified dynamics of IFN- $\beta$  producing cells (cf. Figure 2.11B (2), green curve), we determine the IFN- $\beta$  secretion rate per cell to match the observed

## 2.2. Stochastic model of the IFN response against viral infection

Model parameter		Value
Intracellular virus dynamics		
Maximum viral load per cell	$V_{\max}$	130
Rate constant of virus replication	$r_V$	0.34/h
Rate constant of virus decay	$d_V$	0.1/h
IFN induction		
Rate of RIG-I pathway activation by virus	$k_{\text{RIG-I}}$	0.48/h
Half-saturation constant of RIG-I pathway activation by virus	$K_V$	43
Hill coefficient of RIG-I pathway activation by virus	$h_V$	3
Rate of RIG-I pathway inactivation	$l_{\text{RIG-I}}$	0.4/h
Rate constant of IFN- $\beta$ gene induction	$k_{\text{IFN}}$	1.79/h
Rate of termination of IFN- $\beta$ expression	$l_{\text{IFN}}$	0.08/h
IFN response		
Half-saturation constant of STAT1/2 pathway activation by IFN- $\beta$	$K_{\text{IFN}}$	100 U/ml
Hill coefficient of STAT1/2 pathway activation by IFN- $\beta$	$h_{\text{IFN}}$	1
Rate of STAT1/2 pathway activation	$k_{\text{STAT}}$	0.1/h
Rate constant of ISG (IRF-7) induction by STAT1/2 pathway	$k_{\text{ISG}}$	0.1/h
Rate constant of IFN- $\beta$ secretion	$k_S$	0.13 U/h/ml/cell
Rate constant of IFN- $\beta$ degradation	$d_{\text{IFN}}$	0.15/h

**Table 2.2.:** Model parameters of the stochastic model. Based on the biological meaning of the model parameters (cf. section 2.2.2), we determined the parameter values as depicted in section 2.3. All model simulations in section 2.2.3 and 2.4 refer to this parameter set.

time course of extracellular IFN (cf. Figure 2.11B (3)). With these parameters (cf. Table 2.2), the simulated kinetic of IRF-7-expressing cells agrees with the data (cf. Figure 2.11B (4)).

Importantly, the model simulations demonstrate that the single-cell heterogeneity of transcription factor activation, IFN- $\beta$  gene induction as well as ISG expression translates into predictable dynamics of IFN-secreting and protected cell fractions at the population level.

### 2.3. Estimation of the model parameters of the stochastic model

The Gillespie algorithm is a prevalent and valuable method to simulate stochastic processes. Nevertheless, the long computation time of this algorithm for extensive models with large time scale separation is a serious disadvantage (Gillespie 2007, Cao and Samuels 2009, Banks et al. 2011). Also the simulation of our full model for a sufficient number of cells ( $N = 10^4$  cells) with dynamics over several hours is very time consuming and practically excludes straightforward optimization approaches for parameter estimation. Therefore we divide the parameter estimation problem into three parts: (1) determination of parameters for the virus-induced activation of the transcription factors IRFs/NF- $\kappa$ B (cf. section 2.3.1), (2) identification of parameters with respect to IFN- $\beta$  expression (cf. section 2.3.2) and (3) estimation of parameters concerning the IFN response (cf. section 2.3.3).

The first two parts consider the induction of IFN in individual cells without cell-to-cell communication via secreted IFN- $\beta$ . As the simulation of isolated single-cell behavior is much faster than the complete model, rigorous parameter estimation is applicable and several mechanistically relevant conclusions will be drawn from the parameter optimization.

The third part regarding ISG induction depends on the intercellular signaling between cells, which implies the need for simulating large numbers of cells and thus having impractically long calculation times. However, it turns out that we can still derive quantitative features of ISG expression from the experimental data.

An overview of the determined parameter values in this section is provided in Table 2.2 and serves as a reference for the used parameter set of all model simulations in section 2.2.3 and 2.4.

#### 2.3.1. Parameter determination for the virus-induced activation of the transcription factors of IFN

In our model, we describe the activation of the transcription factors of IFN in an infected cell  $i \in \{1, \dots, N\}$  as a state change from virus-infected to NF- $\kappa$ B/IRF-activated according to the propensity function (2.7) given by

$$w_{\text{TF},i}^+ = k_{\text{RIG-I}} \frac{V_i(t)^{h_V}}{K_V^{h_V} + V_i(t)^{h_V}},$$

with the rate constant  $k_{\text{RIG-I}}$ , the half-saturation constant  $K_V$ , the Hill coefficient  $h_V$  of RIG-I pathway activation and the intracellular viral load  $V_i(t)$  at time  $t \in \mathbb{R}_{\geq 0}$  (cf. Figure 2.9). A perfectly suited experiment to determine the parameters of  $w_{\text{TF},i}^+$  is the single-cell analysis of the nuclear translocation time of NF- $\kappa$ B and IRF-7 after infection  $T_{\text{sig}}$  monitored by live-cell imaging (cf. Figure 2.4D explicit for IRF-7 and also for NF- $\kappa$ B, since both transcription factors synchronously translocate into the nucleus as illustrated in Figure 2.4B). To describe this measured histogram of

### 2.3. Estimation of the model parameters of the stochastic model

nuclear translocation times of the transcription factors (Figure 2.12A), we utilize a submodel comprising viral replication and subsequent NF- $\kappa$ B/IRF-7 activation.

For the simulation of the submodel we initially characterize viral reproduction by comparing the model with the measured time course of viral replication after high-dose infection (cf. Figure 2.11B (1)). By setting the rate constant of virus replication  $r_V = 0.34/\text{h}$ , the maximum viral load per cell  $V_{\max} = 130$  and the rate constant of virus termination  $d_V = 0.1/\text{h}$ , we receive a satisfactory match of the model with the data.

Next, we compute the distribution of NF- $\kappa$ B/IRF translocation times by simulating the submodel consisting of viral replication and subsequent NF- $\kappa$ B/IRF-7 activation sufficiently often using Gillespie's algorithm. To adjust this computed distribution to the experimentally measured histogram, we allow the parameters of the RIG-I pathway activation by virus ( $k_{\text{RIG-I}}$ ,  $K_V$  and  $h_V$ ) to vary while keeping the previously determined viral replication parameters ( $r_V$ ,  $V_{\max}$  and  $d_V$ ) fixed. As objective function we use Neyman's chi-squares statistic (Baker and Cousins 1984), which considers the squared difference between the binned observed and simulated events weighted by the inverse binned experimental data as a measure for the sample variance:

$$\chi^2_{\text{Neyman}} = \sum_{b=1}^B \frac{(D_b - E_b)^2}{D_b}, \quad (2.20)$$

where  $B$  denotes the number of bins of the histogram,  $D_b$  stands for the number of observed events in the  $b$ th bin and  $E_b$  represents the number of simulated events in the  $b$ th bin for  $b \in \{1, \dots, B\}$ , under the condition

$$\sum_{b=1}^B D_b = \sum_{b=1}^B E_b. \quad (2.21)$$

In order to satisfy the condition (2.21) and to ensure accuracy by simulating many more events ( $5 \times 10^4$  runs) than experimentally measured (315 cells), we utilize the the cumulative distribution function (CDF) for normalization. We calculate  $E_b$  using the cumulative distribution function of the simulations for transcription factor activation at time  $t \in \mathbb{R}_{\geq 0}$  given by

$$CDF_{\text{TF}}(t) = \frac{1}{N_s} \sum_{i=1}^{N_s} \mathbb{1}_{[0;t]}(\mathcal{T}_{\text{sig},i}), \quad (2.22)$$

with the number of simulated events  $N_s$ , the simulated nuclear translocation times of the transcription factors  $\mathcal{T}_{\text{sig},i}$ ,  $i = 1, \dots, N_s$  and the characteristic function  $\mathbb{1}$  of the interval  $[0; t]$

$$\mathbb{1}_{[0;t]}(\mathcal{T}_{\text{sig},i}) = \begin{cases} 1 & , \text{ for } \mathcal{T}_{\text{sig},i} \in [0; t]; \\ 0 & , \text{ for } \mathcal{T}_{\text{sig},i} \notin [0; t]. \end{cases} \quad (2.23)$$

After simulating the submodel  $N_s$  times, we compute the number of simulated events in the  $b$ th bin according to

$$E_b = N_{\text{data}}(CDF_{\text{TF}}(t_b^{j+1}) - CDF_{\text{TF}}(t_b^j)), \quad (2.24)$$

## 2. Stochastic modeling predicts paracrine propagation of the IFN response

where  $N_{\text{data}}$  defines the number of observed data points, while  $t_b^j$  and  $t_b^{j+1}$  designate the left and the right bin edge of the  $b$ th bin for  $j \in \{1, \dots, B\}$ , respectively.

For the minimization of the objective function (2.20) we apply the simulated annealing method, which is a heuristic optimization technique (Kirkpatrick et al. 1983, Schneider and Kirkpatrick 2006). The idea of simulated annealing is based on the thermodynamic concept that slow cooling of a system allows to find the minimum energy state (Press et al. 2007). In the initial phase of the algorithm (high temperature), it is more likely that large changes in the objective function occur and that slightly worse solutions are permitted. With increasing computation time (falling temperatures), changes in the objective function become progressively smaller and the temperature-dependent probability to accept a worse solution tends to zero. The opportunity to enable slightly worse solutions, i.e. controlled uphill steps, prevents to get stuck in a local optimum and therefore makes it possible to find the global minimum. To minimize our objective function (2.20), we use the simulated annealing algorithm implemented by Joachim Vandekerckhove, which is freely available at the Mathworks File Exchange library. The resulting parameter values ( $k_{\text{RIG-I}} = 0.48/\text{h}$ ,  $K_V = 43$  and  $h_V = 3.0$ ) yield a good match of computed and measured distributions of nuclear translocation times of the transcription factors (cf. Figure 2.12A).

From a biological point of view, the most interesting feature of this parameter set is the high Hill coefficient  $h_V$ , since a Hill coefficient larger than 1 implies positive cooperativity (Murray 2002). To analyze how robust the estimation of the Hill coefficient  $h_V$  is, we utilize the profile likelihood method (Venzon and Moolgavkar 1988). Thus, we fix  $h_V$  systematically to different values around the estimated optimum of  $h_V = 3.0$  and refit  $k_{\text{RIG-I}}$  as well as  $K_V$  by simulated annealing. To ensure that the obtained values of the objective function (2.20) are unaffected by the inherent stochasticity of the submodel, we repeat the calculation for each fixed value of  $h_V$   $10^4$  times. The profile likelihood (Figure 2.12B) shows the corresponding mean values of Neyman’s chi-squares statistic for each fixed  $h_V$ . A measure for the goodness of the fit is the degree of freedom ( $DF$ ), which defines an upper limit for good fits (Press et al. 2007). In the present case, the degree of freedom is calculated by

$$\begin{aligned} DF &= B - \text{normalization constraint} - \text{number of fit parameters} \\ &= 12 - 1 - 3 \\ &= 8. \end{aligned} \tag{2.25}$$

A non-cooperative activation of the RIG-I pathway ( $h_V = 1$ ) far exceeds the degree of freedom, whereby a Hill coefficient  $h_V \geq 3$  leads to a very good fit of the translocation-time distribution. Based on these findings we conclude that the activation of the RIG-I pathway by virus is cooperative, while the available data are insufficient to estimate the precise degree of cooperativity.

After the nuclear translocation of the transcription factor IRF-7 we monitored in some reporter cells a relocation of IRF-7 back to the cytoplasm and after a while again an accumulation in the cytoplasm (cf. left column in Figure 2.4A, Rand 2010). To account for this nucleocytoplasmic transport of IRF-7 we allow in our model the inactivation of the RIG-I pathway with the rate  $l_{\text{RIG-I}}$ , which consequently prevents

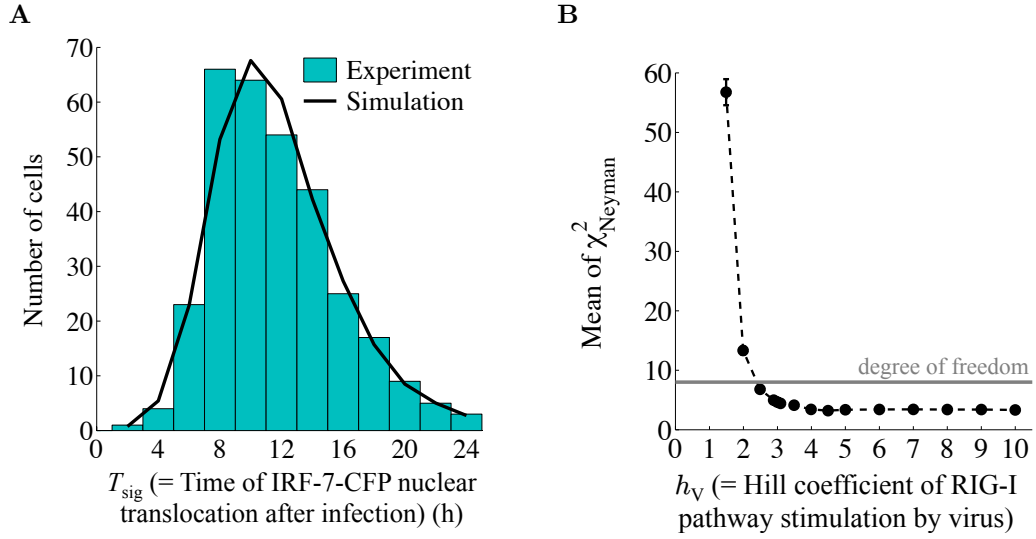


**Figure 2.12.:** Parameter determination demonstrates a cooperative induction of RIG-I mediated signaling by virus. (A) Parameter estimation of virus-induced transcription factor activation. As basis for the parameter determination serves the initial nuclear translocation time of IRF-7 monitored by live-cell imaging in 315 IRF-7-CFP reporter cells after infection with 80 HAU/ml NDV (cyan histogram, cf. Figure 2.4D for a representation of individual time points). The computed distribution (black line) is obtained by simulating  $5 \times 10^4$  runs of the mathematical submodel comprising viral replication and subsequent NF- $\kappa$ B/IRF-7 activation. A match of the computed with the measured distribution is achieved by applying the simulated annealing algorithm. (B) Profile likelihood with respect to the Hill coefficient of virus-induced RIG-I signaling  $h_V$ . The profile likelihood calculation is repeated  $10^4$  times for each fixed value of  $h_V$ . Shown are the resulting mean values and standard deviations of Neyman’s chi-squares statistic. The upper limit for a good fit is defined by the degree of freedom ( $DF = 8$ , cf. (2.25)). (Experiments by U. Rand, M. Köster and H. Hauser)

or at least delays a subsequent IFN- $\beta$  gene induction. For the adaptation of the parameter  $l_{\text{RIG-I}}$ , it is therefore necessary to simulate the whole IFN induction pathway with the determined parameter values for viral replication and RIG-I pathway activation discussed in this section and the results from the parameter estimation of IFN- $\beta$  gene induction outlined in the following section 2.3.2. After simulation of the IFN induction, we compare the arising distribution of IFN- $\beta$  switching-on times with the measured histogram (cf. Figure 2.11A, lower graph) and find an improved match by setting  $l_{\text{RIG-I}} = 0.4/\text{h}$ .

### 2.3.2. Parameter determination of the IFN expression

After the virus-induced nuclear translocation of the transcription factors NF- $\kappa$ B and IRF-7 we detected that the majority of the cells (91% at 80 HAU/ml NDV) also induces the IFN- $\beta$  gene (cf. Figure 2.4D). The time delay between nuclear translocation of IRF-7 and onset of IFN- $\beta$ -tGFP expression  $T_{\text{gen}}$  varied considerably in individual cells and resulted in a broad distribution (Figure 2.13). To simulate the heterogeneous onset of IFN- $\beta$  expression after transcription factor activation using Gillespie’s algorithm, we have to formulate this state transition as a Markov process

## 2. Stochastic modeling predicts paracrine propagation of the IFN response

(cf. section 2.2 page 32). The only continuous distribution fulfilling the Markov property (2.1) is the memoryless exponential distribution (cf. Waldmann and Stocker 2004). However, according to the shape of the experimentally measured histogram of  $T_{\text{gen}}$  (cf. Figure 2.13) a single exponentially distributed rate cannot generate the distinct time delay between transcription factor activation and IFN- $\beta$  gene induction. In this context it should be noted that the distribution of the transcription factor translocation times  $T_{\text{sig}}$  (cf. Figure 2.12A) can neither be modeled with a single exponential rate (cf. section 2.3.1). In the case of transcription factor activation, the time delay between infection and virus-induced signaling is explained by the viral replication process (cf. Figure 2.10).

A possible explanation for the observed time delay between the nuclear translocation of the transcription factors NF- $\kappa$ B/IRF-7 and IFN- $\beta$  expression is the multi-step assembly of the IFN- $\beta$  enhanceosome that activates transcription from the IFN- $\beta$  promoter (Hu et al. 2007, Ford and Thanos 2010). Therefore we analyze if the measured histogram of  $T_{\text{gen}}$  can be fitted with a gamma distribution  $\gamma(m, z)$ . For a positive integer  $m$ ,  $\gamma(m, z)$  describes the distribution of the sum of  $m$  independent random variables, where each random variable is exponentially distributed with rate  $z$  (Press et al. 2007). Based on the measured onset times of IFN- $\beta$ -tGFP expression after transcription factor activation  $T_{\text{gen},i}$  for  $i = 1, \dots, N_{\text{data}}$  monitored in  $N_{\text{data}} = 315$  individual cells (cf. Figure 2.13), we estimate the parameters of the gamma distribution  $m$  and  $z$  with the maximum-likelihood method (Myung 2003). For this purpose, we have to maximize the likelihood function  $L$  of the sample  $T_{\text{gen},i}$ ,  $i = 1, \dots, N_{\text{data}}$ , which is described as

$$L(p_1, \dots, p_{N_p} | T_{\text{gen},1}; \dots; T_{\text{gen},N_{\text{data}}}) = f(T_{\text{gen},1}; \dots; T_{\text{gen},N_{\text{data}}} | p_1, \dots, p_{N_p}) \quad (2.26)$$

using the assumed common density function  $f(t | p_1, \dots, p_{N_p})$  with the parameters  $p_1, \dots, p_{N_p}$  and  $t \in \mathbb{R}$ . The density function of the considered gamma distribution  $f_\gamma$  is given  $\forall m, z > 0$  by

$$f_\gamma(t | m, z) = \begin{cases} \frac{z^m}{\Gamma(m)} t^{m-1} e^{-z t} & , \text{ for } t > 0; \\ 0 & , \text{ for } t \leq 0, \end{cases} \quad (2.27)$$

with the gamma function  $\Gamma(m)$ . According to Euler's integral representation, the gamma function is defined for  $m > 0$  as

$$\Gamma(m) = \int_0^\infty t^{m-1} e^{-t} dt. \quad (2.28)$$

Instead of maximizing  $L$ , we prefer to maximize the log-likelihood function  $\mathcal{L}$  of the independent and identically distributed (i.i.d.) sample  $T_{\text{gen},i}$ ,  $i = 1, \dots, N_{\text{data}}$ :

### 2.3. Estimation of the model parameters of the stochastic model

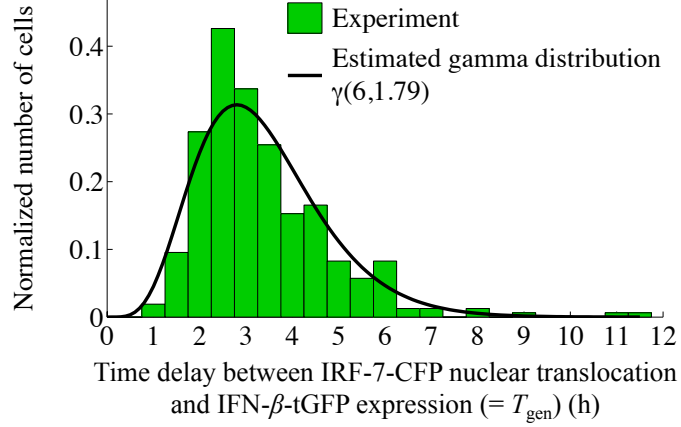


**Figure 2.13.:** Parameter estimation characterizes IFN- $\beta$  gene induction as a multi-step process. The parameter determination of IFN- $\beta$  gene induction is based on the time delay between IRF-7-CFP nuclear translocation and IFN- $\beta$ -tGFP expression ( $T_{\text{gen}}$ ) monitored by live-cell imaging in 315 dual reporter cells after infection with 80 HAU/ml NDV (green histogram, cf. Figure 2.4D for a representation of individual time points). The observed histogram can be approximated by the gamma distribution  $\gamma(6, 1.79)$  (black line), which represents a stochastic process consisting of 6 consecutive and with rate 1.79/h exponentially distributed steps. (Experiments by U. Rand, M. Köster and H. Hauser)

$$\begin{aligned}
 & \mathcal{L}(m, z \mid T_{\text{gen},1}; \dots; T_{\text{gen},N_{\text{data}}}) \\
 &= \ln(L(m, z \mid T_{\text{gen},1}; \dots; T_{\text{gen},N_{\text{data}}})) \\
 (2.26) \quad & \stackrel{=}{=} \ln(f_{\gamma}(T_{\text{gen},1}; \dots; T_{\text{gen},N_{\text{data}}} \mid m, z)) \\
 & \stackrel{T_{\text{gen},i} \text{ i.i.d.}}{=} \ln\left(\prod_{i=1}^{N_{\text{data}}} f_{\gamma}(T_{\text{gen},i} \mid m, z)\right) \\
 (2.27) \quad & \stackrel{=}{=} \ln\left(\prod_{i=1}^{N_{\text{data}}} \left[\frac{z^m}{\Gamma(m)} T_{\text{gen},i}^{m-1} e^{-z T_{\text{gen},i}}\right]\right) \\
 &= N_{\text{data}} \ln\left(\frac{z^m}{\Gamma(m)}\right) + \sum_{i=1}^{N_{\text{data}}} \ln(T_{\text{gen},i}^{m-1} e^{-z T_{\text{gen},i}}) \\
 &= N_{\text{data}} m \ln(z) - N_{\text{data}} \ln(\Gamma(m)) \\
 & \quad + (m-1) \sum_{i=1}^{N_{\text{data}}} \ln(T_{\text{gen},i}) - z \sum_{i=1}^{N_{\text{data}}} T_{\text{gen},i}.
 \end{aligned} \tag{2.29}$$

To find a maximum of the likelihood function, we first calculate the root of the partial derivative of  $\mathcal{L}$  with respect to  $z$

$$\begin{aligned}
 & \frac{\partial}{\partial z} \mathcal{L}(m, z \mid T_{\text{gen},1}; \dots; T_{\text{gen},N_{\text{data}}}) = 0 \\
 (2.29) \quad & \iff N_{\text{data}} m \frac{1}{z^*} - \sum_{i=1}^{N_{\text{data}}} T_{\text{gen},i} = 0 \\
 & \iff z^* = \left(\frac{1}{N_{\text{data}} m} \sum_{i=1}^{N_{\text{data}}} T_{\text{gen},i}\right)^{-1}, \tag{2.30}
 \end{aligned}$$

## 2. Stochastic modeling predicts paracrine propagation of the IFN response

which results in an explicit estimator for  $z$  depending on  $m$  and allows to reformulate  $\mathcal{L}$  as follows:

$$\begin{aligned}
& \mathcal{L}(m, z | T_{\text{gen},1}; \dots; T_{\text{gen},N_{\text{data}}}) \Big|_{z=z^*} \\
\stackrel{(2.30)}{=} & -N_{\text{data}} m \ln \left( \frac{1}{N_{\text{data}} m} \sum_{i=1}^{N_{\text{data}}} T_{\text{gen},i} \right) - N_{\text{data}} \ln(\Gamma(m)) \\
& + (m-1) \sum_{i=1}^{N_{\text{data}}} \ln(T_{\text{gen},i}) - m N_{\text{data}} \\
= & N_{\text{data}} \left[ m \ln(N_{\text{data}} m) - m \ln \left( \sum_{i=1}^{N_{\text{data}}} T_{\text{gen},i} \right) - \ln(\Gamma(m)) - m \right] \\
& + (m-1) \sum_{i=1}^{N_{\text{data}}} \ln(T_{\text{gen},i}).
\end{aligned} \tag{2.31}$$

Utilizing this new formulation (2.31), the partial derivative of  $\mathcal{L}$  with respect to  $m$  is given by

$$\begin{aligned}
& \frac{\partial}{\partial m} \mathcal{L}(m, z | T_{\text{gen},1}; \dots; T_{\text{gen},N_{\text{data}}}) \Big|_{z=z^*} \\
\stackrel{(2.31)}{=} & N_{\text{data}} \left[ \ln(N_{\text{data}} m) + 1 - \ln \left( \sum_{i=1}^{N_{\text{data}}} T_{\text{gen},i} \right) - \frac{\Gamma'(m)}{\Gamma(m)} - 1 \right] + \sum_{i=1}^{N_{\text{data}}} \ln(T_{\text{gen},i}) \\
= & N_{\text{data}} \left[ \ln(N_{\text{data}} m) - \ln \left( \sum_{i=1}^{N_{\text{data}}} T_{\text{gen},i} \right) - \frac{\Gamma'(m)}{\Gamma(m)} \right] + \sum_{i=1}^{N_{\text{data}}} \ln(T_{\text{gen},i}) \\
=: & \mathcal{M}(m | T_{\text{gen},1}; \dots; T_{\text{gen},N_{\text{data}}}).
\end{aligned} \tag{2.32}$$

Fulfilling the necessary condition for a maximum of the likelihood function concerning the partial derivative of  $\mathcal{L}$  with respect to  $m$  supplies an implicit estimate of  $m$ :

$$\begin{aligned}
& \frac{\partial}{\partial m} \mathcal{L}(m, z | T_{\text{gen},1}; \dots; T_{\text{gen},N_{\text{data}}}) = 0 \\
\stackrel{(2.32)}{\iff} & \mathcal{M}(m | T_{\text{gen},1}; \dots; T_{\text{gen},N_{\text{data}}}) = 0.
\end{aligned} \tag{2.33}$$

We determine  $m$  independently from  $z$  through solving the nonlinear equation (2.33) with the trust-region-dogleg algorithm of Matlab's optimization toolbox (Coleman and Zhang 2003). Using the measured data points  $T_{\text{gen},i}$  we obtain  $m = 6.4$ . Since in the present case  $m$  is interpreted as the number of exponentially distributed steps in a stochastic process, we round  $m$  to the nearest integer. Inserting  $m = 6$  in (2.30) yields directly  $z = 1.79/\text{h}$ . The resulting gamma distribution  $\gamma(6, 1.79)$  provides a good approximation of the measured histogram of  $T_{\text{gen}}$  (cf. Figure 2.13). Therefore we conclude that IFN- $\beta$  expression after transcription factor activation can be described through 6 consecutive and exponentially distributed steps with rate  $k_{\text{IFN}} = 1.79/\text{h}$ . Consequently, each of these first-order processes has a half-life of  $\ln(2)/k_{\text{IFN}} = 23$  min. The estimated number of steps and the half-life correspond

### 2.3. Estimation of the model parameters of the stochastic model

well with the mechanistic knowledge about the multi-step formation of the IFN- $\beta$  enhanceosome (Hu et al. 2007, Ford and Thanos 2010), although transcription and translation might also contribute relevant steps.

In addition, we have observed that the activated transcription factors NF- $\kappa$ B and IRF-7 stay in average for  $\sim 13$  h in the nucleus (Rand 2010). This mean duration provides an upper limit for the average time span of IFN production, since IFN expression requires the presence of transcription factors in the nucleus. Accordingly, we fix the rate of termination of IFN- $\beta$  expression to  $l_{\text{IFN}} = 0.08/\text{h}$ .

#### 2.3.3. Parameter determination of the IFN response

With the intention to obtain quantitative insight into IFN-induced ISG regulation, we have a closer look on the IRF-7 response experiment, in which the IRF-7-mCherry reporter cells were stimulated with increasing units of IFN- $\beta$  and subjected to flow cytometry at different times after stimulation (cf. Figure 2.7). On the basis of this experiment, we derive a dose-response data set by recording the maximal fraction of IRF-7-mCherry<sup>+</sup> cells for each applied IFN- $\beta$  concentration (Figure 2.14). The hyperbolic shape of the derived data set indicates that the dose-response to the extracellular concentration of IFN- $\beta$   $I$  can be characterized by a Hill function

$$R(I) = \frac{I^{h_{\text{IFN}}}}{K_{\text{IFN}}^{h_{\text{IFN}}} + I^{h_{\text{IFN}}}}, \quad (2.34)$$

where  $K_{\text{IFN}}$  and  $h_{\text{IFN}}$  denote the half-saturation constant and the Hill coefficient of STAT1/2 pathway activation by IFN- $\beta$ , respectively.

To fit the parameters of the Hill function to the dose-response data set, we utilize the trust-region-reflective least-squares algorithm of Matlab's optimization toolbox (Coleman and Zhang 2003). The least-squares method is based on the chi-squares statistic

$$\chi^2 = \sum_{i=1}^{N_{\text{data}}} \left( \frac{d_i - y(x_i | p_1, \dots, p_M)}{\sigma_i} \right)^2, \quad (2.35)$$

with the number of observed data points  $N_{\text{data}}$ , the measured data set  $(x_i, d_i)$ , the corresponding measurement error  $\sigma_i$  for  $i = 1, \dots, N_{\text{data}}$  and the objective function  $y(x_i | p_1, \dots, p_M)$  at  $x_i$  with  $M$  adjustable parameters  $p_j$  for  $j = 1, \dots, M$  (Press et al. 2007). In order to find the best fit parameter values, the chi-squares statistic  $\chi^2$  has to be minimized.

In the present optimization problem, we consider (2.34) as objective function to describe the derived dose-response data set by assuming a measurement error of 10%. The resulting parameter values  $K_{\text{IFN}} = 100.8$  U/ml and  $h_{\text{IFN}} = 1.08$  yield a satisfying fit to the data (cf. Figure 2.14, black curve). For simulations of the full model we use non-negative integer numbers and set  $K_{\text{IFN}} = 100$  U/ml as well as  $h_{\text{IFN}} = 1$  (cf. Figure 2.14, red curve). The description of the IFN-induced response data by a Hill coefficient with value 1 implies a non-cooperative IRF-7 induction through extracellular IFN- $\beta$  (Murray 2002).

## 2. Stochastic modeling predicts paracrine propagation of the IFN response

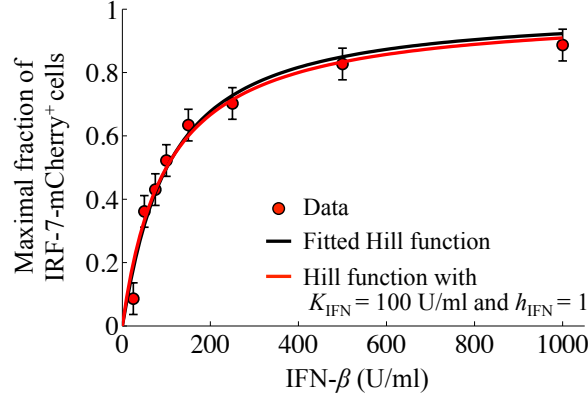


**Figure 2.14.:** Parameter estimation reveals a non-cooperative induction of IRF-7 by extracellular IFN- $\beta$ . Based on the IRF-7 response measurement (cf. Figure 2.7), we derive a dose-response data set (red dots) by considering the maximal fraction of IRF-7-mCherry<sup>+</sup> cells (y-axis) for each applied IFN- $\beta$  concentration (x-axis). The data set was fitted with a Hill function (black curve) by applying a trust-region-reflective least-squares algorithm and assuming the indicated 10% measurement error (black error bars). For further simulations we round the fitted parameter values to the nearest integers  $K_{\text{IFN}} = 100$  U/ml and  $h_{\text{IFN}} = 1$  (red curve). (Experiments by U. Rand, M. Köster and H. Hauser)

In contrast to the dose-response parameters  $K_{\text{IFN}}$  and  $h_{\text{IFN}}$ , the rate constants for STAT1/2 activation  $k_{\text{STAT}}$  and ISG induction  $k_{\text{ISG}}$  cannot be rigorously fitted from the available data. By comparing the simulated kinetic of ISG expression to the experimentally measured one at high viral load (cf. Figure 2.11B (4)), we detect that  $k_{\text{STAT}} = k_{\text{ISG}} = 0.1/\text{h}$  leads to a good match between model and data.

For the determination of the IFN- $\beta$  secretion rate  $k_{\text{S}}$  and the IFN- $\beta$  degradation rate  $d_{\text{IFN}}$ , we use the measured kinetics of IFN- $\beta$ -tGFP expressing cells and the amount of released IFN after high-dose infection (cf. Figure 2.11B (2) and (3)). Using the preceding parameterization of the IFN- $\beta$  induction (cf. section 2.3.1 and 2.3.2) enables the description of the IFN- $\beta$ -tGFP<sup>+</sup> cell fraction over time. Restricted by the kinetic of the IFN- $\beta$ -producing cells and the already adjusted measurement unit of IFN through fitting  $K_{\text{IFN}} = 100$  U/ml, we find that  $k_{\text{S}} = 0.13$  U/(h ml cell) and  $d_{\text{IFN}} = 0.15/\text{h}$  lead to a good agreement between the measured and simulated dynamic of extracellular IFN (cf. Figure 2.11B (3)).

## 2.4. Stochastic modeling exposes individual IFN producers as sentinels of viral infection

The temporal dynamics of IFN- $\beta$ -tGFP expressing cells and IRF-7-mCherry responding cells after infection with high viral load (cf. Figure 2.11 (2) and (4)) suggest that IFN- $\beta$  secreted by a single cell can induce antiviral ISG production in several cells. To analyze this presumption more closely, we simulate the stochastic model for a range of low-dose infections, where IFN- $\beta$ -producing cells are rare. The subsequent comparison of the predicted kinetics of IFN-responding cells with the measured fraction of ISG-expressing cells shows a good match with the associated data (Figure 2.15A).

In addition, we consider the proportion of IFN responding cells to IFN producing cells after infection with different virus titers (Figure 2.15B). For low-dose infections, the model predicts a strong paracrine propagation of antiviral protection through secreted IFN, with up to 40 times as many ISG-expressing cells than IFN-secreting cells. This model prediction proved remarkably accurate when tested experimentally, given that the model is calibrated only for high dose infections (cf. Figure 2.15B blue square and Figure 2.11).

To further examine the relation between IFN expressing and IFN responding cells, we cultivated IFN- $\beta$ -tGFP reporter cells together with IRF-7-mCherry cells (Fig-

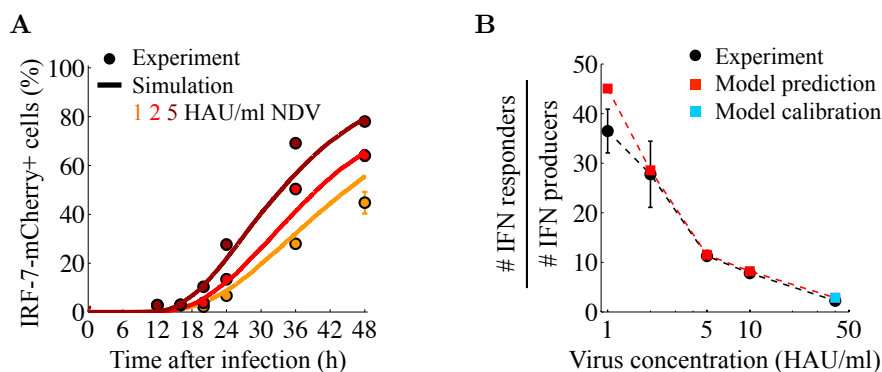


**Figure 2.15.:** Paracrine propagation of the IFN response is predicted by the model and verified experimentally. (A, B) After the model parameterization based on experimental data concerning high dose infections, we simulate the model for low dose infections by taking into account a population of  $10^4$  cells. (A) The model predicts IFN response dynamics after low-dose infections. The simulated kinetics of ISG expressing cells (solid curves) can be confirmed by the measured dynamics of IRF-7-mCherry<sup>+</sup> cells (dots) for sparse infections with 1, 2 and 5 HAU/ml NDV. (B) Predicted paracrine propagation of the IFN response induced by individual sentinels. Shown is the proportion of IFN responding cells to IFN producing cells (y-axis) after infection with different viral doses (x-axis) for an infection period of 48 h. The blue square denotes the model calibration (cf. Figure 2.11), while the red squares represent the predictions of the model regarding low-dose infections. The subsequent verification of the model predictions by experimental data is marked by the black dots. The data correspond to the mean and standard deviation of triplicate measurements. (Experiments by U. Rand, M. Köster and H. Hauser)

## 2. Stochastic modeling predicts paracrine propagation of the IFN response

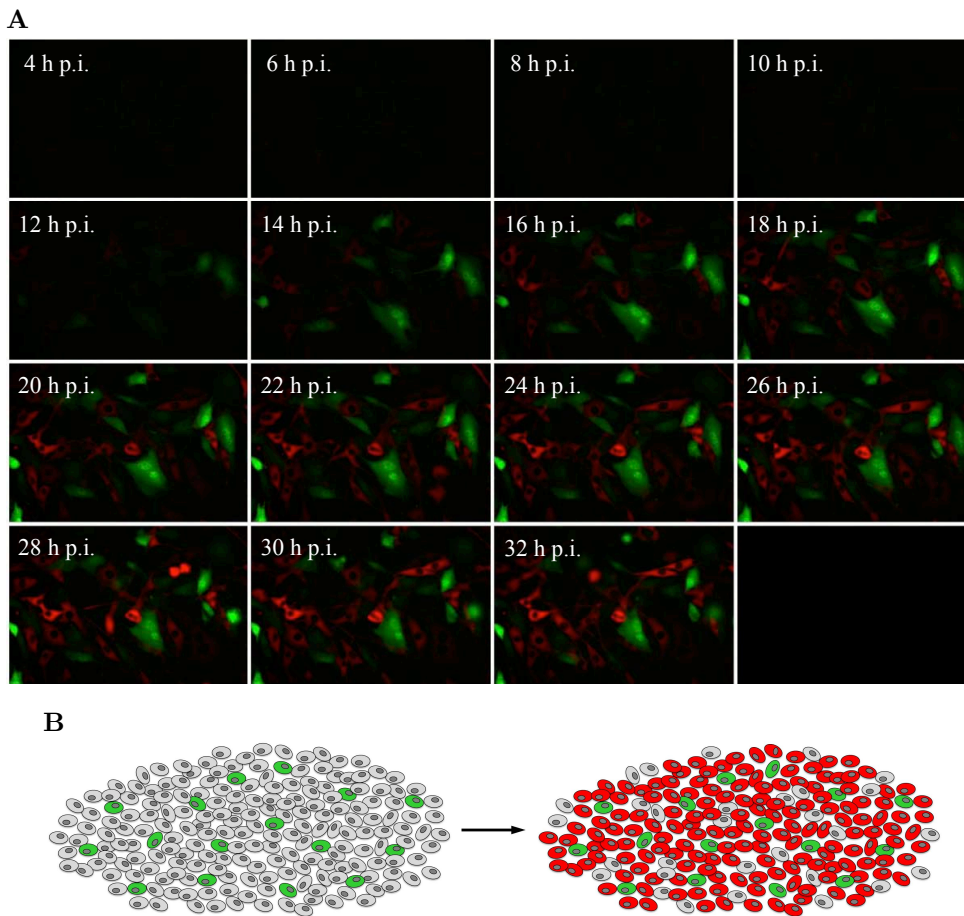


**Figure 2.16.:** Illustrations of the predicted paracrine response communication based on our analysis of the antiviral IFN system with respect to primary infections. (A) Co-culturing of IFN- $\beta$ -tGFP and IRF-7-mCherry reporter cells illustrates paracrine communication. IFN- $\beta$ -tGFP reporter cells (green cells) were infected with 40 HAU/ml NDV for 1 h. After this infection period IRF-7-mCherry cells (red cells) were added at same density and cells were subjected to time-lapse microscopy. Merged fluorescence pictures for IFN- $\beta$ -tGFP and IRF-7-mCherry at indicated time points post infection (p.i.) are shown. (B) Scheme of the assumed protective function of IFN-producing cells. In consideration of our study of the IFN network, we speculate that few IFN- $\beta$  expressing cells (green cells) can induce an antiviral gene program in a large number of cells (red cells) to curb viral infection. (Experiments by U. Rand, M. Köster and H. Hauser)

ure 2.16A). Indeed, we detected that few IFN- $\beta$ -tGFP expressing cells can induce ISG expression in many IRF-7-mCherry cells. This observation corroborates the predicted paracrine amplification of the IFN signal (Figure 2.16B).

Based on our study of the antiviral IFN system regarding primary infections we suggest that the paracrine propagation of the IFN response transforms stochastic single-cell behavior into efficient and predictable antiviral protection of the cell population. If this is the case, a few IFN-producing cells might suffice as sentinels of viral infection to protect a large number of naïve cells (Rand, Rinas et al. 2012).

### 3. Population-based modeling reveals that viral spread is mainly controlled by the autocrine effect of rapidly produced IFN

Driven by the question, which components of the antiviral IFN system play a decisive role in limiting viral spread, we move to a system where viral spread is possible. Together with our experimental collaboration partners Bianca Schmid and Ralf Bartenschlager from the Department of Infectious Diseases at the University of Heidelberg, we study the dynamics of spreading Dengue virus (DENV) in an IFN-competent cell system.

DENV elicits a strong IFN response in host cells and, at the same time, counteracts both IFN induction and IFN response (Figure 3.1). Several studies (Aguirre et al. 2012, Yu et al. 2012) demonstrate that DENV restrains IFN expression by cleaving the stimulator of IFN genes (STING, also known as MITA), which in turn mediates the activation of the transcription factors IRF-3 as well as IRF-7 (cf. Figure 1.2) (Zhong et al. 2008, Ishikawa and Barber 2008, West et al. 2011, Acosta et al. 2014). Further findings from the literature illustrate a DENV-induced inhibition of STAT1 (Muñoz-Jordán et al. 2003, Muñoz-Jordán et al. 2005) and degradation of STAT2 (Jones et al. 2005, Ashour et al. 2009, Mazzon et al. 2009, Morrison et al. 2013) resulting in an disruption of the antiviral IFN response. In addition, DENV can modify its RNA genome by 2'-O-methylation (Egloff et al. 2002, Ray et al. 2006, Dong et al. 2014). It is reported that 2'-O methylation of the viral genome prevents the viral recognition by the intracellular receptor melanoma differentiation-associated gene 5 (MDA5) (Züst et al. 2011) and supports evasion from the antiviral response (Daffis et al. 2010, Züst et al. 2011, Szretter et al. 2012, Kimura et al. 2013).

Despite the countermeasures taken by DENV to disturb the antiviral IFN pathway, DENV strongly induces the expression of IFN and antiviral ISGs (Kurane and Ennis 1987, Jiang et al. 2010, Schoggins et al. 2012, Pan et al. 2012). It was shown that pre-stimulation with IFN protects cells against DENV (Diamond et al. 2000, Diamond and Harris 2001) and some ISGs inhibit viral entry or impede the early replication of DENV (Jiang et al. 2010, Chan et al. 2012).

Quantitative approaches to analyze this competition between DENV and the antiviral IFN system have been lacking and it remains poorly understood why DENV is at all able to spread in an IFN-competent cell systems. To investigate the direct interactions between DENV infection and the antiviral IFN response in living cells, our cooperation partners have generated a fully viable DENV wild-type (DENV-wt)

### 3. Viral spread is mainly controlled by the autocrine effect of rapidly produced IFN

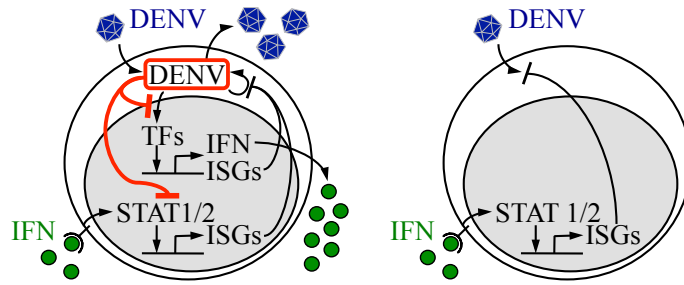


**Figure 3.1.:** Scheme of the competition between spreading DENV and the antiviral IFN system. After infection of a host cell, DENV can on the one hand interfere the induction of IFN by cleaving the transcription factor (TF) activator STING and, on the other hand, suppress the IFN response through inhibition of STAT1 and degradation of STAT2 (red inhibition links). In addition, DENV modifies its RNA genome by 2'-O-methylation (indicated by the red frame), which further negatively impacts the IFN network. Despite these impairments of the IFN pathway, the recognition of DENV replication ( $\odot$ ) through intracellular receptors strongly induces the expression of IFN and also some ISGs. Secreted IFN activates in an autocrine manner in infected cells (left) the expression of antiviral ISGs, which in turn inhibit the early replication of DENV. Moreover, the paracrine sensing of IFN by naïve cells (right) results in an antiviral protection against DENV infection.

reporter construct and fluorescent reporter cells to monitor viral replication, virus-induced signal transduction and ISG expression (see section 3.1.1, Schmid 2014). The data indicate that IFN efficiently protects naïve cells against productive DENV infection and, if given early after infection, reduces viral replication in infected cells (see section 3.1.2). In agreement with the results regarding primary infection with NDV (see section 2.1.2 and 2.1.3), we also detected strong cell-to-cell heterogeneity in IFN induction as well as IFN response after DENV infection (see section 3.1.3). Importantly, this implies that protection of naïve cells by secreted IFN and viral spread in unprotected cells occur simultaneously. To examine which antiviral factors have the greatest influence on viral spread, we compare DENV-wt with the vaccine candidate DENV-E217A mutant, which lacks 2'-O-methylation of the viral RNA genome, induces a stronger IFN response and barely spreads (see section 3.1.4).

In consideration of the experimental findings, we establish a delay differential equation model of viral spread and IFN-induced antiviral protection in a cell population (see section 3.2). At first, we parameterize the model from measurements concerning DENV-wt infection (see section 3.3.1). By utilizing this DENV-wt specific parameter set, we are able to identify two DENV-E217A mutant specific parameters, which explain the attenuation of the mutant through a reduced virus production rate and an accelerated IFN expression (see section 3.3.2). To determine the relative importance of the two DENV-E217A mutant specific parameters on viral spread, we develop an extended version of the model, which in addition to the paracrine effect of IFN on naïve cells also explicitly considers the autocrine effect of IFN on infected cells (see section 3.4). By analyses performed with this full model and validation experiments, we demonstrate that the attenuation of the DENV-E217A mutant is mainly due to the effect of a rapid IFN signal to limit virus production in infected cells during the early stages of viral replication, whereby faster paracrine protection

### 3.1. Studying the dynamics of IFN-induced antiviral defense against DENV

of naïve cells by IFN has only a weak impact on spreading DENV (see section 3.5). Our results thus indicate that the outcome of infection is primarily determined by the relative dynamics of DENV replication and autocrine IFN action on already infected cells (Schmid, Rinas et al. submitted).

## 3.1. Studying the dynamics of IFN-induced antiviral defense against spreading DENV in living cells

### 3.1.1. Detection of the immediate interactions between DENV infection and the antiviral IFN response at single-cell level

Previous studies on DENV have described the viral replication process (Lindenbach et al. 2006, Bartenschlager and Miller 2008, Welsch et al. 2009, Kumar et al. 2013), the propagation properties under the influence of IFN stimulation (Diamond et al. 2000, Diamond and Harris 2001, Jones et al. 2005) and the antiviral effect of IFN target genes against DENV (Chan et al. 2012, Schoggins et al. 2012) primarily under steady-state conditions. However, a kinetic analysis of the direct interactions between DENV infection and the antiviral IFN response in individual cells has been missing. To address the lack of a single-cell system enabling such investigation, our experimental cooperation partners Bianca Schmid and Ralf Bartenschlager have established both a fully viable DENV wild-type (DENV-wt) reporter and IFN-competent fluorescent reporter cells (Schmid 2014).

For the visualization of DENV replication and spread our collaboration partners constructed a genetically modified DENV reporter virus expressing the far red fluorescent protein TurboFP635 “faR” (Figure 3.2A). This DENV-faR-wt reporter construct is based on the DENV serotype 2 (isolate 16681), which is an enveloped, positive-sense, single-stranded (ss) RNA virus (Fischl and Bartenschlager 2013). The DENV genome encodes 3 structural proteins, the capsid protein (C), the pre-membrane protein (prM) as well as the envelope protein (E) and 7 non-structural (NS) proteins (NS1, NS2A, NS2B, NS3, NS4A, NS4B, and NS5) (Chambers and Rice 1987, Bartenschlager and Miller 2008, Kumar et al. 2013, Acosta et al. 2014). While the structural proteins and the RNA genome form the infectious virus particle, the non-structural proteins are required for RNA replication, which takes place in the cytoplasm in close association with intracellular membranes (cf. section 1.2.2) (Welsch et al. 2009, Peña and Harris 2012). During the replication process of the DENV-faR-wt construct, the integrated faR fluorescent protein accumulates in the nucleus as the capsid sequence contains a nuclear localization signal (NLS) (Figure 3.2B and C).

In order to study the interplay of DENV infection with the IFN system in real time at single-cell level, the biologists generated IFN-competent fluorescent reporter cell lines to monitor the virus-triggered signal transduction and the induction of distinct ISGs (Figure 3.2B and C, Table 3.1). After infection, the sensing of the RNA virus by the intracellular receptors RIG-I, the melanoma differentiation-associated gene 5 (MDA5) and the Toll-like receptor 3 (TLR3) leads to the nuclear translocation

### 3. Viral spread is mainly controlled by the autocrine effect of rapidly produced IFN

Reporter cell line	Visualization	Color
IRF-3-eGFP	Activation of IRF-3	green, plotted in cyan
IFIT1-deGFP	IFIT1 expression	green
Mx1-deGFP	Mx1 expression	green, plotted in yellow

**Table 3.1.:** Overview of the used fluorescent reporter cell lines in chapter 3. Our cooperation partners developed 3 fluorescent reporter cell lines to monitor at single-cell level (1) the activation of the transcription factor IRF-3, (2) the induction of IFIT1 and (3) the expression of Mx1.

of the transcription factors NF- $\kappa$ B, IRF-3 as well as IRF-7 (Bustos-Arriaga et al. 2011, Nasirudeen et al. 2011, da Conceição et al. 2013, Acosta et al. 2014). For the detection of transcription factor activation, reporter cells were tagged with the fluorescent marker IRF-3-eGFP using the enhanced green fluorescent protein (eGFP) (cf. Figure 3.2B and C, in cyan color to clearly distinguish IRF-3-eGFP from other GFP markers). Transcription factors located in the nucleus result in the expression of IFN- $\alpha$ , IFN- $\beta$  as well as IFN- $\lambda$  (Wathelet et al. 1992, Pichlmair and Reis e Sousa 2007, Thompson and Locarnini 2007, Thompson et al. 2011, Prokunina-Olsson et al. 2013) and some ISGs including the IFN-induced protein with tetratricopeptide repeats 1 (IFIT1, also known as ISG56) (Grandvaux et al. 2002, Diamond and Farzan 2013, Chen et al. 2013). The recognition of extracellular IFN causes the phosphorylation of STAT1 and STAT2, which in turn induce the expression of ISGs such as IFIT1 as well as MX dynamin-like GTPase 1 (Mx1) (Darnell et al. 1994, Onoguchi et al. 2007, Stark and Darnell Jr. 2012). To visualize the expression of the subset of ISGs that are expressed together with IFN as well as in response to IFN, the virologists transfected cells with a bacterial artificial chromosome (BAC) encoding for a fusion protein composed of IFIT1 and a destabilized version of the enhanced green fluorescent protein (deGFP) (cf. Figure 3.2B and C, green color). Another BAC-based reporter construct Mx1-deGFP was created to detect the expression of Mx1 which exclusively occurs in response to extracellular IFN (Bandyopadhyay et al. 1995) (cf. Figure 3.2B and C, in yellow color for a better comparison of Mx1-deGFP with other GFP markers).

All reporter constructs were stably transfected into carcinomic human alveolar epithelial cells (A549), since A549 cells are permissive for DENV, able to produce IFN and capable to induce an IFN-stimulated antiviral gene program (Schmid 2014). While IFIT1 as well as Mx1 proteins are very stable, e.g. mouse MxA has a half-life of  $\sim 2.3$  days (Ronni et al. 1993) and human IFIT1 has a half-life of  $> 24$  h (Andreas Pichlmair, personal communication), we observed for the deGFP reporter cells short half-lives of  $\sim 2$  h for IFIT1-deGFP and  $\sim 4$  h for Mx1-deGFP (Schmid 2014). The reduction of the half-lives due to destabilized reporter proteins enables a more precise characterization of the dynamics of the IFN response. Therefore, infection of the reporter cell lines IFIT1-deGFP or Mx1-deGFP with the generated DENV-faR-wt is an ideal model system for live-cell dual-color imaging of virus replication indicated by the red nucleus and IFIT1 or Mx1 expression appearing in the cytoplasm of individual cells over time.

To examine how accurate the constructed DENV reporter reflects viral replica-

### 3.1. Studying the dynamics of IFN-induced antiviral defense against DENV

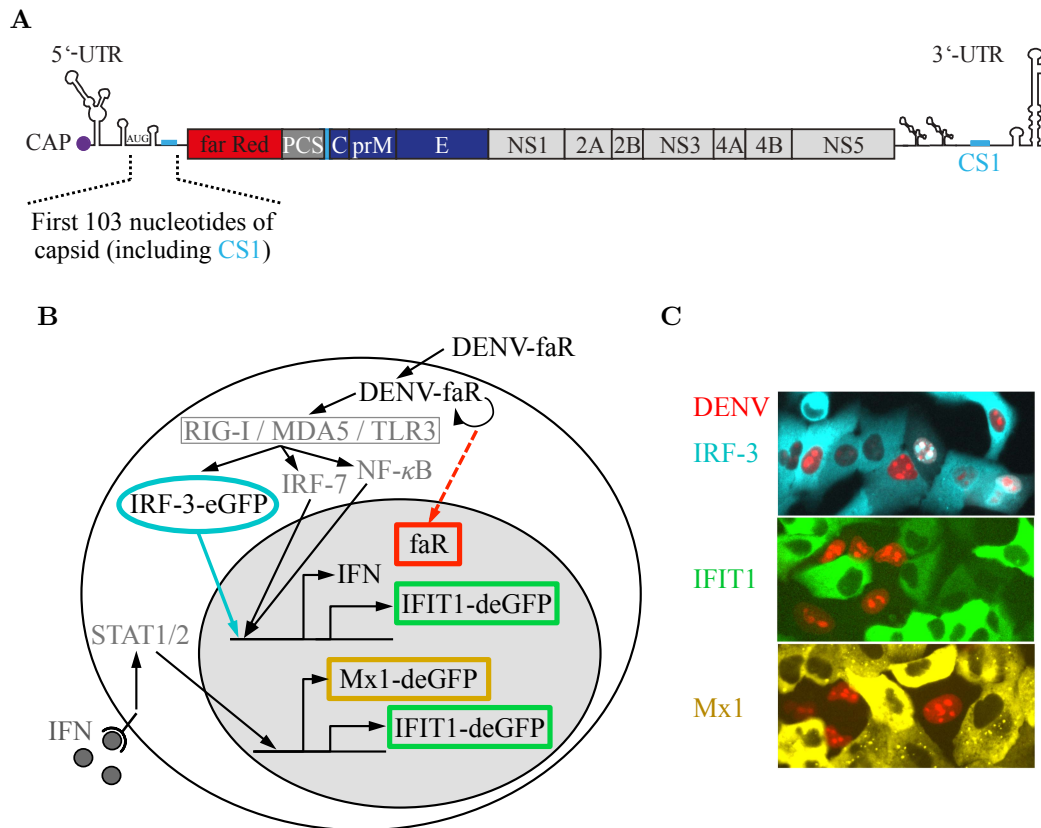


**Figure 3.2.:** The immediate interactions between DENV infection and the antiviral IFN response can be monitored in real time with generated fluorescent reporter constructs. (A) Scheme of the established DENV-faR-wt reporter virus genome. The first 103 nucleotides of the capsid coding sequence of DENV-wt contain the circularization sequence 1 (CS1), which is essential for DENV RNA replication. The virologists duplicated the first 103 nucleotides of the capsid sequence and inserted them at the 5' end of the reporter gene. The far red reporter is fused N-terminally with amino acid residues of the capsid protein containing a NLS, and C-terminally with the sequence encoding for the 2A cleavage factor of the *Thossea asigna* virus (PCS) to generate the authentic N-terminus of the capsid protein. The adjacent polyprotein can be cleaved into 3 structural proteins (capsid protein (C), premembrane protein (prM) as well as envelope protein (E)) and 7 non-structural (NS) proteins (NS1, NS2A, NS2B, NS3, NS4A, NS4B, and NS5) by viral and cellular proteases during the viral replication process. (B, C) Scheme and fluorescence pictures of the created intracellular reporter constructs. Infection with DENV-faR becomes visible through the nuclear accumulation of the faR fluorescent protein in virus replicating cells ( $\odot$ , red nucleus). Subsequent viral sensing through the receptors RIG-I, MDA5 and TLR3 causes the translocation of the latent fusion protein IRF-3-eGFP (plotted in cyan) into the nucleus (cyan nucleus). Activated transcription factors induce the expression of IFN and some ISGs including IFIT1. The recognition of extracellular IFN stimulates the production of further ISGs such as IFIT1 and Mx1. ISG expression is illustrated by the BAC constructs IFIT1-deGFP (green cytoplasm) and Mx1-deGFP (plotted in yellow). (Experiments by B. Schmid and R. Bartenschlager)

tion, we directly compared the faR protein marker with the well-established DENV double-stranded (ds) RNA indicator for active virus replication in the same cell after infection with a high dose of DENV-faR-wt (Figure 3.3). The subsequent im-

### 3. Viral spread is mainly controlled by the autocrine effect of rapidly produced IFN

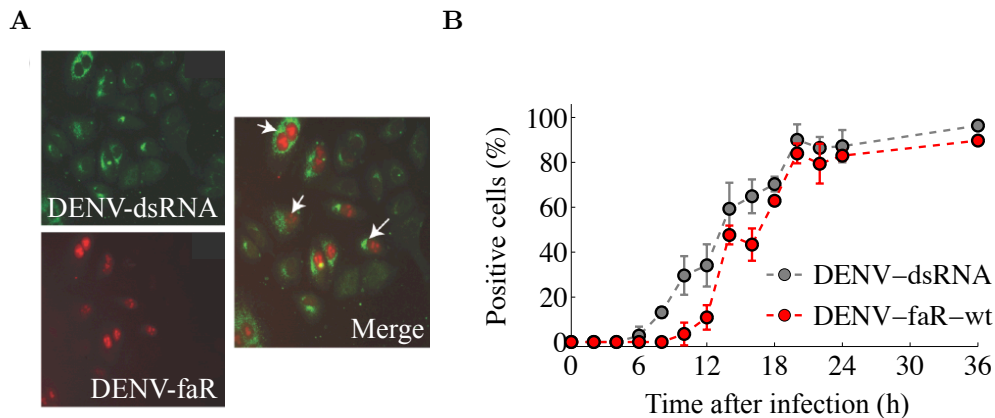


**Figure 3.3.:** The generated DENV-faR-wt reporter is a reliable marker to detect DENV replication dynamics in individual cells. (A, B) A549 cells were infected with DENV-faR-wt at a MOI of 10 and analyzed by immunofluorescence assay using the faR fluorescent protein or dsRNA-specific antibodies. (A) Strong correlation between faR fluorescent protein and dsRNA in a given host cell. Selected immunofluorescence pictures of DENV-dsRNA (top left in green color) and DENV-faR (bottom left in red color) individually or combined (right) at 14 h post infection demonstrate correlated presence of both markers in a given host cell. (B) Similar dynamics of faR protein and dsRNA expression. The fraction of dsRNA (gray color) or faR protein (red color) positive cells was determined after infection via ImageJ cell counter plugin. Shown are the mean values and standard deviations of two independent measurements. (Experiments by B. Schmid and R. Bartenschlager)

munofluorescence analysis showed a strong correlation between the appearance of the faR fluorescent protein and the production of dsRNA in a given host cell (cf. Figure 3.3A). Following the heavily infected cell population over time resulted in similar kinetics of faR protein and dsRNA expression with only a slightly delayed detection of the faR protein marker (cf. Figure 3.3B). These data demonstrate that the DENV reporter is a reliable marker to study the dynamics of DENV replication at single-cell level.

Apart from verifying the reliability of the created DENV-faR-wt reporter to monitor viral replication we also characterized the propagation properties of the DENV reporter construct. First we investigated whether DENV-faR-wt infected cells produce a comparable amount of infectious virus particles as DENV-wt infected cells. The release of infectious virus particles was quantified by performing a limiting dilution assay to determine the tissue culture infectious dose 50 (TCID<sub>50</sub>) per milliliter (ml), where TCID<sub>50</sub> is the dilution which infects 50% of replicate cell cultures (Lindenschbach et al. 2005). The corresponding TCID<sub>50</sub> titers were calculated by applying the widely used method of Spearman and Kärber (Hierholzer and Killington 1996). The resulting extracellular virus titers over time after infection with DENV-faR-wt were only marginally lower as compared to DENV-wt (Figure 3.4A). DENV-faR-wt is thus well suited to analyze the release of new viral particles.

Moreover, we examined if the DENV reporter efficiently spreads in IFN-competent human A549 cells by comparing DENV-faR-wt with DENV-faR trans-complementation particle (TCP) infection. TCPs are particles which contain no genetic informa-

### 3.1. Studying the dynamics of IFN-induced antiviral defense against DENV

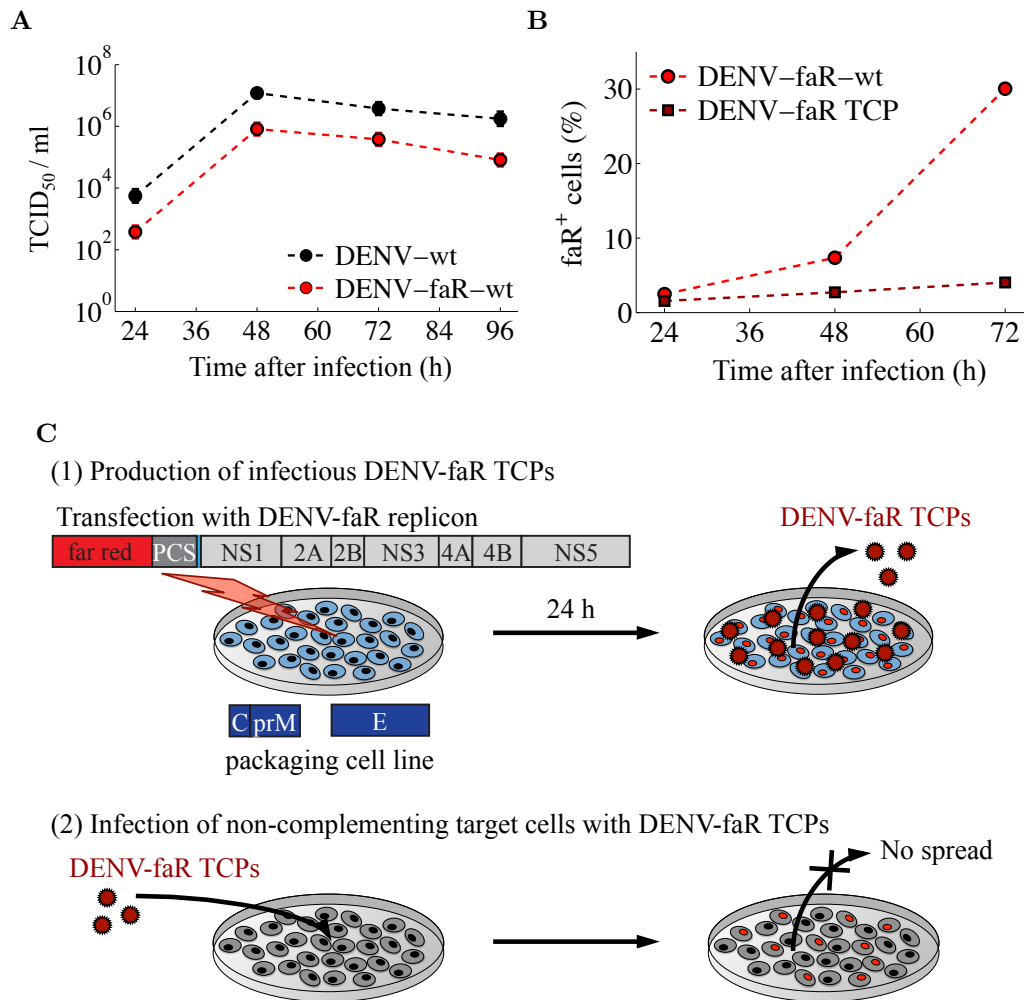


**Figure 3.4.:** The established DENV-faR reporter efficiently spreads in IFN-competent cells. (A) Virus production of DENV-faR-wt complies with the viral release of DENV-wt. A549 cells were infected with DENV-wt (black color) or DENV-faR-wt (red color) at a MOI of 1. At the indicated time points after infection we measured the virus titers in the supernatant by performing a limiting dilution assay to determine the tissue culture infectious dose 50 (TCID<sub>50</sub>) per milliliter (ml). (B) DENV-faR-wt propagates successfully in an IFN-competent cell system. A549 cells were infected with virus producing DENV-faR-wt (red color; virus production shown in (A)) or with non-spreading DENV-faR TCP (dark red color; cf. TCP system in (C)) at a MOI of 0.1. The fraction of faR positive cells was detected at three time points after infection by flow cytometry. (C) Scheme of the TCP system. (1) Infectious DENV-faR TCPs were produced by transfecting cells that stably express the structural proteins C, prM as well as E with a subgenomic DENV-faR reporter replicon RNA. This replicon contains the faR reporter gene and lacks C, prM and E that are provided in trans in the engineered helper cell line. DENV-faR TCPs (dark red circles) released into the cell culture supernatant were harvested 24 h after transfection. (2) DENV-faR TCPs are unable to spread in cell cultures that do not express the structural proteins C, prM and E, as DENV-faR TCPs cannot encode the required structural proteins by themselves. Thus, infection of naïve target cells with DENV-faR TCPs only leads to infection and replication, but not to virus particle production and viral spread. (Experiments by B. Schmid and R. Bartenschlager)

### 3. *Viral spread is mainly controlled by the autocrine effect of rapidly produced IFN*

tion to encode the structural proteins C, prM and E. While TCPs are able to enter host cells and replicate the viral genome, they cannot spread as the missing structural proteins are necessary to form infectious virus particles (Lai et al. 2008). To produce infectious DENV-faR TCPs the biologists transfected a helper cell line stably expressing the structural proteins C, prM as well as E with a subgenomic DENV-faR reporter replicon RNA that contains the faR reporter gene and lacks the structural proteins (Figure 3.4C (1)). The subsequent infection of non-complementing target cells with the non-spreading DENV-faR TCPs enables the investigation of a single round of infection (Figure 3.4C (2)). The comparison of DENV-faR TCP and DENV-faR-wt infected cells showed an almost constant fraction of DENV-faR TCP positive cells over time, whereby the number of DENV-faR-wt positive cells grew steadily (Figure 3.4B). These data demonstrate that the DENV-faR-wt reporter efficiently spreads in an IFN-competent cell system.

Taken together, the established DENV-faR-wt reporter is a reliable tool to observe the dynamics of viral replication, virus production and viral spread. Additionally, the infection of the reporter cell lines IRF-3-eGFP, IFIT1-deGFP or Mx1-deGFP with DENV-faR-wt allows us to investigate the immediate interactions between DENV infection and the antiviral IFN response at single-cell level.

#### **3.1.2. The competition between spreading DENV and IFN-induced antiviral protection**

The competition between DENV and the antiviral IFN system is characterized, on the one hand, by the virus-induced IFN expression followed by strong antiviral IFN response. But on the other hand, DENV is able to proliferate, to spread and to counteract IFN production as well as IFN-induced signaling (cf. Figure 3.1). To analyze the strength of the IFN-induced antiviral protection, we stimulated IFN-competent human A549 cells prior, at or post DENV infection with IFN. We used a high viral dose to ensure a large number of primary infected cells and measured the fraction of DENV-wt positive cells 24 h post infection (Figure 3.5A and B). IFN pre-treatment enables initiation of the antiviral IFN response in advance and resulted in a remarkable decrease of infected cells compared to the control experiment without IFN stimulation (cf. Figure 3.5B black horizontal line). The IFN pre-stimulation experiments demonstrate a protective effect of IFN against DENV infection. In comparison with no IFN treatment, IFN stimulation at or post infection still yielded a significantly reduced number of infected cells for delays up to 6 h after infection. As we expect that secondary infections are rare at the used viral titer, the IFN post-treatment measurements indicate a reduction of viral replication and, consequently, virus production in infected cells through recognition of IFN in a certain time window post infection.

Findings from the literature describe that DENV is able to disturb IFN-induced signaling by STAT2 degradation (Jones et al. 2005, Ashour et al. 2009, Mazzon et al. 2009, Morrison et al. 2013). To examine this proposed countermeasure of DENV in our system, we related the dynamics of DENV replication directly with STAT2 expression. For this purpose, we infected human A549 cells with DENV-wt

### 3.1. Studying the dynamics of IFN-induced antiviral defense against DENV

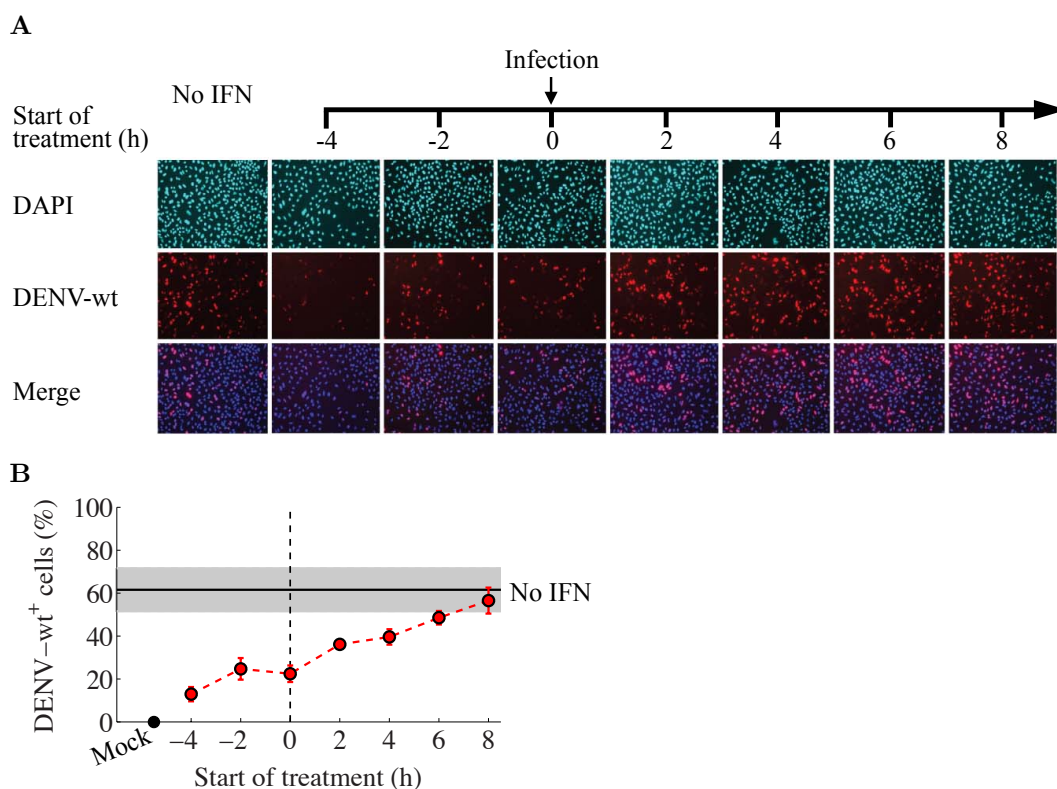


**Figure 3.5.:** IFN can protect naïve cells against DENV infection and, if given early after infection, reduces viral replication in infected cells. (A, B) IFN-competent A549 cells were left untreated (no IFN) or treated with 100 international units per milliliter (IU/ml) IFN- $\alpha$  prior (-4 h, -2 h), at (0 h) or post (2 h, 4 h, 6 h, 8 h) infection with DENV-wt at a MOI of 10. (A) After an infection period of 24 h we performed an immunofluorescence assay to highlight nuclear DNA by 4',6-diamidino-2-phenylindole (DAPI) staining (upper row, cyan color) and simultaneously visualized DENV-wt using a NS5-specific antiserum (middle row, red color). Merged images of DAPI and DENV-wt staining are shown in the last row. (B) Quantification of DENV-wt positive cells in (A) by analyzing 500-1000 cells in two view fields for each column in (A). The error bar diagram illustrates the mean values and standard deviations for treated cells, while the mean value and standard deviation for the measurement without treatment is specified by the black line and the shaded gray area, respectively. The dashed vertical line indicates the experiment in which cells were stimulated and infected at the same time. Mock-treated cells served as control. (Experiments by B. Schmid and R. Bartenschlager)

and quantified simultaneously the DENV envelope and STAT2 protein levels over time by Western blot analysis (Figure 3.6). In agreement with other reports (Jones et al. 2005), the Western blot analysis showed already after 6 h post infection a rapid decrease of the ISG STAT2. From 26 h after infection onwards, STAT2 levels increased again, which might be due to STAT2 expression in response to secreted IFN, continued growth of some uninfected cells or limitation of viral spread by IFN-induced protection of some remaining naïve cells in the meantime. In any case, the dynamic of STAT2 expression after infection illustrates the impairment of the IFN response by DENV replication.

In order to obtain more insight in the properties of DENV with respect to viral

### 3. Viral spread is mainly controlled by the autocrine effect of rapidly produced IFN

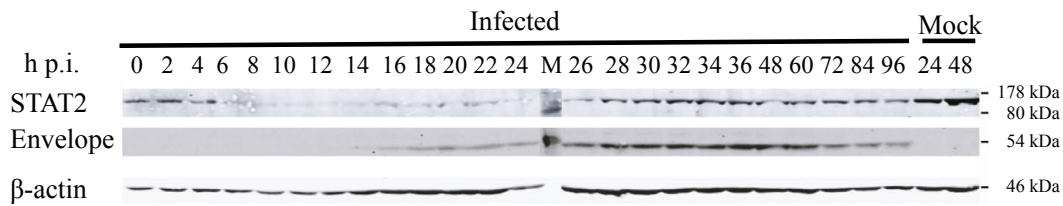


**Figure 3.6.:** DENV counteracts the IFN response by STAT2 degradation. IFN-competent A549 cells were infected with DENV-wt at a MOI of 10. At the given time points post infection (p.i.), STAT2 (upper strip), DENV envelope (middle strip) and  $\beta$ -actin (last strip, as loading control) protein levels were detected simultaneously by Western blot analyze using the respective specific antibodies. Mock-infected cells (last two columns) serves as reference. Numbers at the right refer to the positions of molecular weight standards in kilodalton (kDa). A representative immunoblot out of three independent experiments is shown. (Experiments by B. Schmid and R. Bartenschlager)

replication, virus production and immune activation, we utilized the classical method for the determination of single-step growth curves (Ellis and Delbrück 1939, Gong et al. 1996). Therefore, we infected A549 cells with the DENV-faR reporter (cf. Figure 3.2) at a high viral dose and measured in short time intervals viral RNA, virus release, IFIT1 mRNA expression and IFN- $\lambda$  production (Figure 3.7). The initial high level of detected viral RNA and extracellular virus is due to added DENV particles which stick to the cell surface and remained in spite of thoroughly performed multiple washing steps. Disregarding the residual DENV particles bound on the cells, the first RNA replication occurred roughly 8 h post infection (p.i.) and increasing viral RNA levels saturated 48 h p.i. New infectious virus particles were released approximately between 14-36 h after infection. The subsequent decrease of extracellular virus can probably be attributed to exhausted or dying infected cells and virus degradation in the medium. In agreement with the dynamics of viral replication and virus production, we found an increase of IFIT1 mRNA (coding for IFIT1) starting 12 h p.i. followed by an delayed release of IFN- $\lambda$  from 18 h p.i. onwards.

Furthermore, the data in Figure 3.7 demonstrate that DENV replication leads to IFN production in A549 cells. To investigate the antiviral effect of secreted IFN to induce ISG expression in our system, we treated the IFIT1-deGFP and Mx1-deGFP reporter cells (cf. Figure 3.2) with IFN- $\alpha$  and measured for several ISGs the mRNA expression levels in deGFP positive as well as negative cells (Figure 3.8A for IFIT1-deGFP reporter cells; similar results for Mx1-deGFP reporter cells, Schmid 2014). IFN-treated and deGFP positive cells expressed a higher amount of ISG mRNAs than IFN-stimulated deGFP negative cells. We also monitored the induction kinetics of the IFIT1-deGFP and Mx1-deGFP reporter cells after stimulation with biologically equipotent concentrations (Bauhofer et al. 2012) of IFN- $\alpha$  or IFN- $\lambda$  (Figure 3.8B for IFN- $\lambda$  treatment; similar results after IFN- $\alpha$  stimulation, Schmid 2014). The fraction of IFIT1-deGFP<sup>+</sup> and Mx1-deGFP<sup>+</sup> was almost identical over time for both types of IFN. In addition, we studied the dose response of IFIT1-deGFP and Mx1-deGFP reporter cells to IFN- $\alpha$  and IFN- $\lambda$  (Figure 3.8C and D for IFN- $\lambda$ ; similar results for IFN- $\alpha$ , Schmid 2014). The mean fluorescence intensity (MFI) (Figure 3.8C) as well as the number of IFN-responding cells (Figure 3.8D) increased with

### 3.1. Studying the dynamics of IFN-induced antiviral defense against DENV

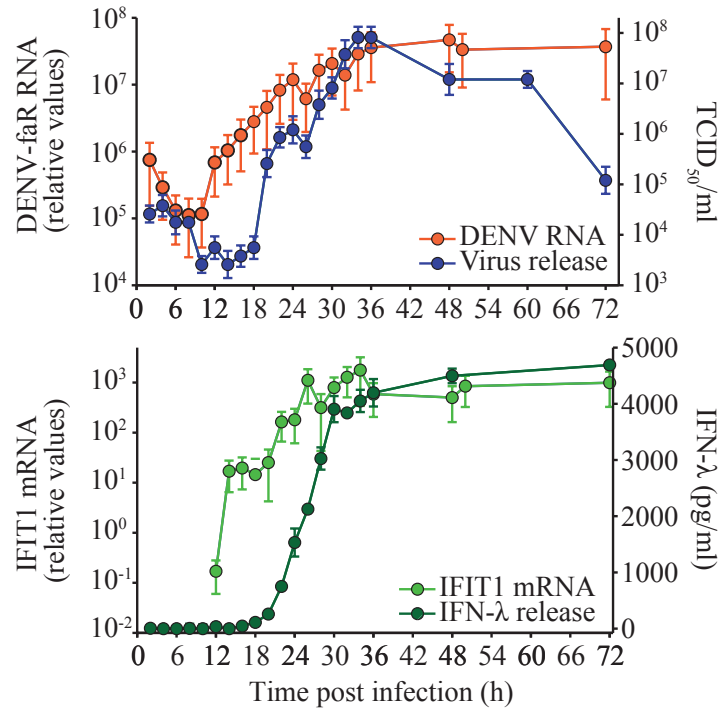


**Figure 3.7.:** Temporally resolved dynamics of viral replication, virus production and immune activation after DENV infection. IFN-competent A549 cells were infected with DENV-faR-wt at a MOI of 10 and analyzed at the indicated time points post infection. Upper panel: Viral RNA (orange color) was evaluated by quantitative real time reverse polymerase chain reaction (qRT-PCR). In addition, we measured extracellular virus (blue color) by performing a limiting dilution assay to determine the tissue culture infectious dose 50 (TCID<sub>50</sub>) per milliliter (ml). Lower panel: IFIT1 mRNA (light green color) was quantified using qRT-PCR. Moreover, we detected the amount of extracellular IFN-λ (dark green color) by enzyme-linked immunosorbent assay (ELISA). Viral RNA and IFIT1 mRNA were normalized to glyceraldehyde 3-phosphate dehydrogenase (GAPDH) mRNA (Schmid 2014). The virus release data is a representative result out of three independent experiments. All other values correspond to the mean and standard deviation of independent triplicate measurements. (Experiments by B. Schmid and R. Bartenschlager)

higher IFN concentrations. With the exception of the MFI values after stimulation with  $10^4$  ng/ml IFN-λ, we detected a substantial agreement of the dose-dependent IFN response between IFIT1 and Mx1 reporter cells. These data show that the IFIT1 and Mx1 reporter cells are comparable to each other and respond in a time and dose-dependent way to IFN-α as well as IFN-λ with the expression of different ISGs.

In summary, DENV efficiently spreads in IFN-competent cells, but at the same time also elicits a strong IFN response. Our data revealed that extracellular IFN efficiently protects naïve cells against DENV infection and, if given early after infection, inhibits viral replication in infected cells.

### 3. Viral spread is mainly controlled by the autocrine effect of rapidly produced IFN

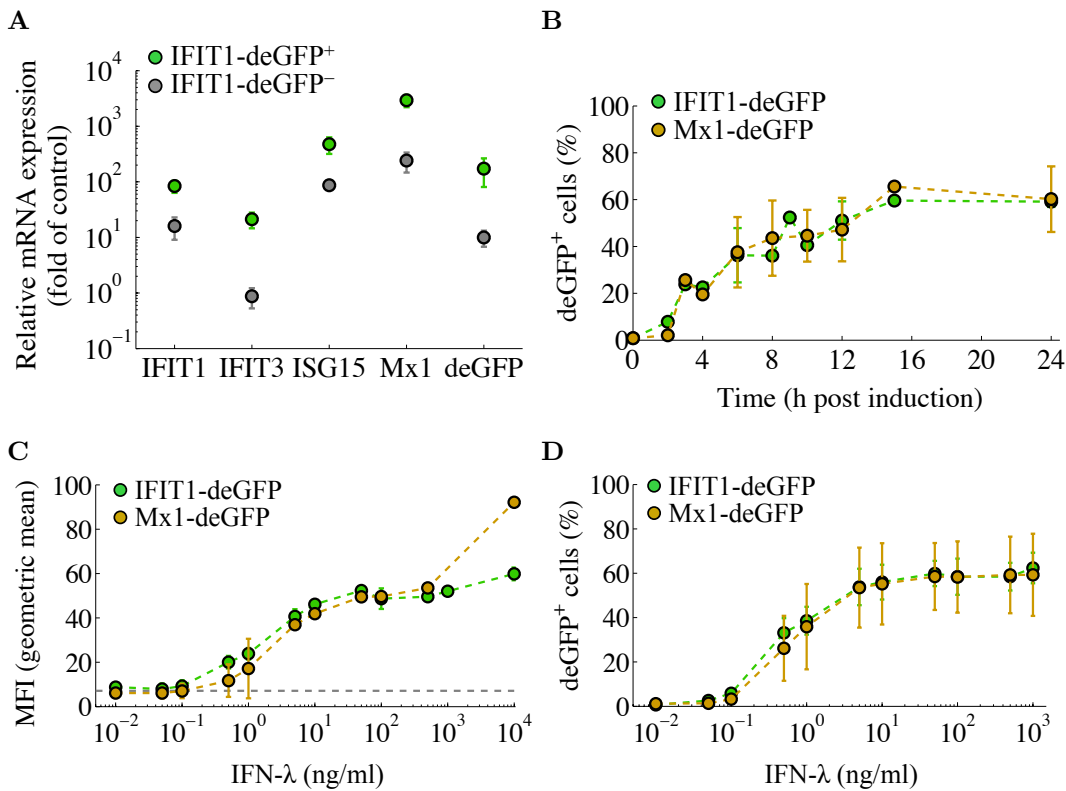


**Figure 3.8.:** Comparable time and dose-dependent IFN response of IFIT1 and Mx1 reporter cells. (A) Expression of different ISGs in IFIT1 positive cells. A549 IFIT1-deGFP reporter cells were stimulated with 10 IU/ml IFN- $\alpha$  for 24 h and subsequently sorted according to deGFP expression by flow cytometry. Immediately after sorting IFIT1-deGFP<sup>+</sup> (green color) and IFIT1-deGFP<sup>-</sup> (gray color) were lysed and total RNA was extracted. Amounts of different ISG mRNAs (x-axis) were quantified using qRT-PCR and normalized to GAPDH mRNA levels (y-axis). (B) Similar induction kinetics of IFIT1 and Mx1 reporter cells after IFN stimulation. A549 IFIT1-deGFP and Mx1-deGFP reporter cells were stimulated with 10 ng/ml IFN- $\lambda$ . At the indicated time points we detected the fraction of IFIT1-deGFP<sup>+</sup> cells (green color) and Mx1-deGFP<sup>+</sup> cells (yellow color) by flow cytometry. (C, D) Dose-dependent IFN response of IFIT1 and Mx1 reporter cells. A549 IFIT1-deGFP and Mx1-deGFP reporter cells were stimulated with various concentrations of IFN- $\lambda$  (x-axis) for 24 h. The mean fluorescence intensity (MFI) (C; dashed gray line indicates the detection limit) and the fraction of deGFP positive cells (D) was determined for IFIT1-deGFP reporter cells (green color) and Mx1-deGFP reporter cells (yellow color) by flow cytometry. The dose-response data regarding IFIT1 represents the mean and standard deviation of three independent experiments. All other values correspond to the mean and standard deviation of two independent measurements. (Experiments by B. Schmid and R. Bartenschlager)

#### 3.1.3. The heterogeneous IFN response in single cells fosters the coexistence of viral spread and antiviral protection

As we are particularly interested in analyzing the immediate interactions between DENV infection and the antiviral IFN system, we utilized the generated DENV reporter construct together with the fluorescent reporter cells for live-cell dual-color imaging (cf. section 3.1.1).

### 3.1. Studying the dynamics of IFN-induced antiviral defense against DENV

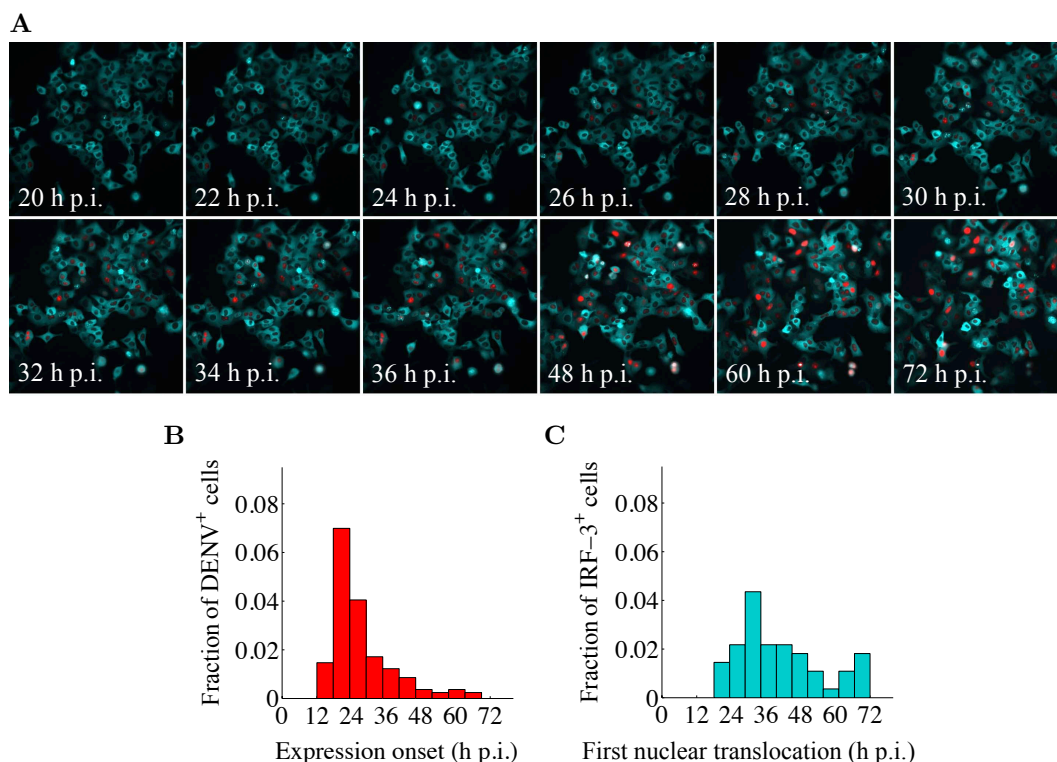


**Figure 3.9.:** Single-cell heterogeneity of DENV replication and IFN induction. (A-C) A549 IRF-3-eGFP reporter cells were infected with DENV-faR-wt at a MOI of 150 and monitored every hour via time-lapse microscopy. Quantification of expression onset of DENV-faR-wt and first nuclear translocation of IRF-3-eGFP was evaluated by manually tracking of single-cell dynamics using the MTrackJ plug-in of the ImageJ software package. Shown are tracking data without daughter cell informations. (A) Representative fluorescence pictures at indicated time post infection (p.i.) visualize the expression of latent transcription factor IRF-3 (cyan cytoplasm), DENV-faR-wt replication (red nucleus) and translocated IRF-3 (cyan nucleus). (B) Quantification of the expression onset of 143 DENV-faR-wt<sup>+</sup> cells in the time period between [12 h p.i.; 69 h p.i.]. (C) Detection of the first nuclear translocation of 51 IRF-3-eGFP<sup>+</sup> cells in the time frame between [18 h p.i.; 72 h p.i.]. (Experiments by B. Schmid and R. Bartenschlager; manual tracking by J. Förster)

First, we studied the induction of IFN after DENV infection through analyzing the virus-induced nuclear translocation of the transcription factor IRF-3. After high-dose infection of the IRF-3-eGFP reporter cells with DENV-faR-wt, we monitored viral replication along with IRF-3-eGFP expression by time-lapse microscopy (Figure 3.9A, viral replication colored in red and IRF-3-eGFP expression in cyan color). Initially, we observed the expression of the latent transcription factor IRF-3 in the cytoplasm of the cells. After a certain delay post infection, the number of virus replicating cells increased over time and nuclear translocation of IRF-3 was detectable in some infected cells. To quantify the expression onset of the viral faR reporter gene and the first nuclear translocation of IRF-3-eGFP, our intern Jonas Förster manually tracked single cells by using the MTrackJ plug-in of the ImageJ software package. The tracking data of individual cells showed a broad distribution of DENV-faR-wt expression onset as well as highly varying initial nuclear translocation of IRF-3 (Figure 3.9B and C). The onset of viral replication started  $\sim 12$  h p.i., whereby IRF-3

### 3. Viral spread is mainly controlled by the autocrine effect of rapidly produced IFN

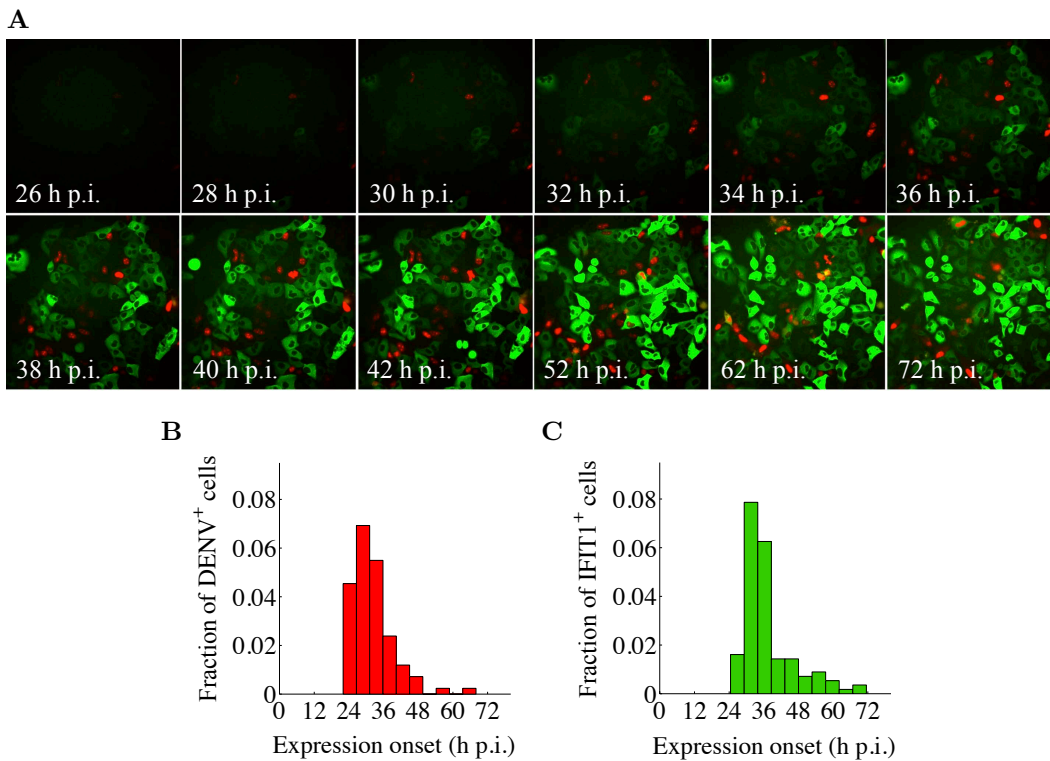


**Figure 3.10.:** Coexistence of viral spread and antiviral IFIT1 expression. (A-C) A549 IFIT1-deGFP reporter cells were infected with DENV-faR-wt at a MOI of 0.2 and monitored every half hour via time-lapse microscopy. Quantification of expression onset was evaluated by manually tracking of single-cell dynamics using the MTrackJ plug-in of the ImageJ software package. Shown are tracking data without daughter cell informations. (A) Representative fluorescence pictures at indicated time post infection (p.i.) demonstrate the expression of DENV-faR-wt (red nucleus) and IFIT1-deGFP (green cytoplasm). (B) Quantification of the expression onset of 91 DENV-faR-wt<sup>+</sup> cells in the time period between [22.0 h p.i.; 68.0 h p.i.]. (C) Detection of 119 IFIT1-deGFP<sup>+</sup> cells in the time frame between [24.5 h p.i.; 71.5 h p.i.]. (Experiments by B. Schmid and R. Bartenschlager; manual tracking by J. Förster)

initially translocated into the nucleus  $\sim 18$  h after infection. While cells became DENV-faR-wt positive between 12 h and approximately 3 days post infection, we tracked IFN induction in 34% of the virus replicating cells. These live-cell imaging data demonstrate a high heterogeneity of viral replication and IFN induction after DENV infection at single-cell level.

In addition to the virus-induced transcription factor activation, we examined the dynamics of DENV replication and spread together with the IFN response in real time. For this purpose we performed live-cell microscopy experiments of IFIT1-deGFP reporter cells (Figure 3.10A) or Mx1-deGFP reporter cells (Figure 3.11A) post infection with DENV-faR-wt at a low MOI to enable viral spread through secondary infection events. The time delay until the initial DENV-faR-wt expression appeared was quite similar in both cell lines with 22 h p.i. for IFIT1-deGFP and 24 h p.i. for Mx1-deGFP reporter cells, respectively (cf. Figure 3.10B and Figure 3.11B). The expression onset of DENV-faR-wt was broadly distributed in both ISG

### 3.1. Studying the dynamics of IFN-induced antiviral defense against DENV

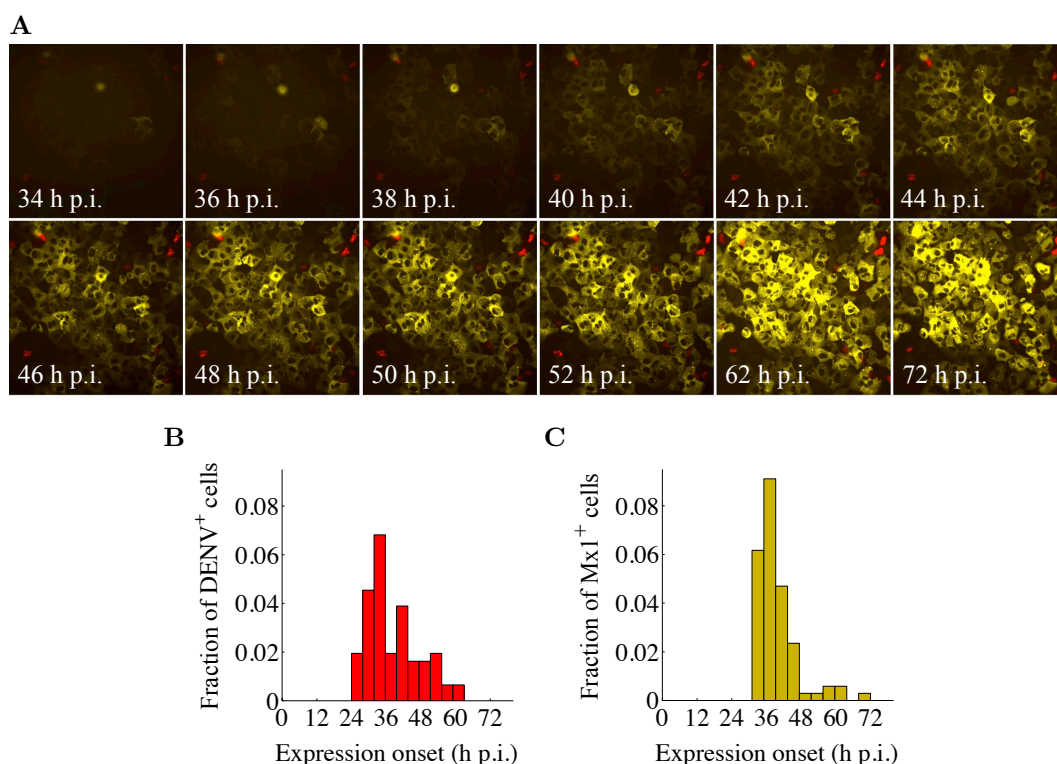


**Figure 3.11.:** Coexistence of viral spread and antiviral Mx1 expression. (A-C) A549 Mx1-deGFP reporter cells were infected with DENV-faR-wt at a MOI of 0.1 and monitored every hour via time-lapse microscopy. Quantification of expression onset was evaluated by manually tracking of single-cell dynamics using the MTrackJ plug-in of the ImageJ software package. Shown are tracking data without daughter cell informations. (A) Representative fluorescence pictures at indicated time post infection (p.i.) visualize the expression of DENV-faR-wt (red nucleus) and Mx1-deGFP (yellow cytoplasm). (B) Quantification of the expression onset of 79 DENV-faR-wt<sup>+</sup> cells in the time period between [24 h p.i.; 63 h p.i.]. (C) Detection of 83 Mx1-deGFP<sup>+</sup> cells in the time frame between [31 h p.i.; 72 h p.i.]. (Experiments by B. Schmid and R. Bartenschlager; manual tracking by J. Förster)

reporter cell lines. Given that the extrapolated time delay for the first appearance of secreted infectious DENV is approximately 14 h p.i. (cf. blue curve in Figure 3.7) and that replication is detectable  $\sim 22 - 24$  h after infection by the faR reporter, the large number of cells becoming DENV-faR-wt positive between 1.5 and 3 days is probably caused by viral spread and secondary infection events.

During the propagation process of DENV, many cells achieve protection against viral infection by induction of antiviral ISGs. The first onset of ISG-reporter expression was delayed relative to the appearance of DENV-faR-wt positive cells by 2.5 h for IFIT1-deGFP and 7 h in the case of Mx1-deGFP. The short time period between the initial DENV-faR-wt and IFIT1-deGFP expression possibly reflects the required time to activate IFIT1 directly by IRF-3 in an IFN-independent manner (cf. Figure 3.2B) (Grandvaux et al. 2002, Diamond and Farzan 2013, Chen et al. 2013). However, only rarely we observed IFIT1-deGFP - DENV-faR-wt double-positive cells, arguing that in our system IFIT1 expression is induced primarily in response to secreted IFN, rather than due to virus-induced signaling. In contrast

### 3. Viral spread is mainly controlled by the autocrine effect of rapidly produced IFN

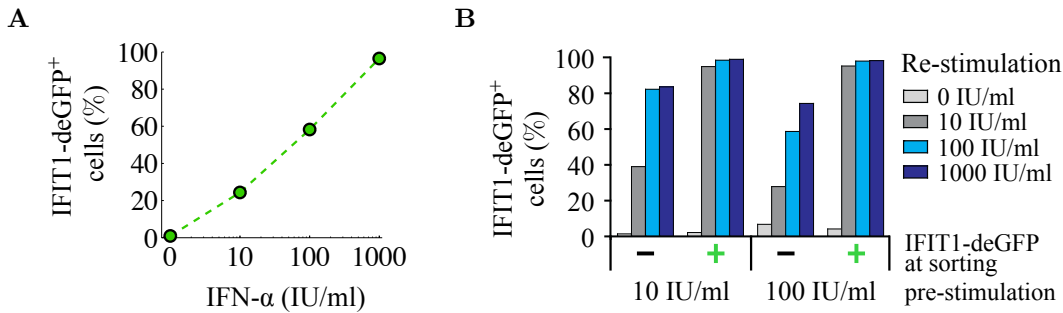


**Figure 3.12.:** Cell-to-cell heterogeneity of the IFN response. (A) A549 IFIT1-deGFP reporter cells were treated with increasing amounts of IFN- $\alpha$  (x-axis) for 24 h. After the stimulation period we determined the fraction of IFIT1-deGFP<sup>+</sup> cells (y-axis) by flow cytometry. (B) A549 IFIT1-deGFP reporter cells stimulated with 10 or 100 IU/ml IFN- $\alpha$  for 24 h from (A) were sorted in IFIT1-deGFP<sup>-</sup> and IFIT1-deGFP<sup>+</sup> cells (x-axis). Separated cell groups were seeded and 24 h later re-stimulated with IFN- $\alpha$  concentrations specified in the legend. After a re-stimulation period of 24 h we measured the fraction of IFIT1-deGFP<sup>+</sup> cells (y-axis) by flow cytometry. (Experiments by B. Schmid and R. Bartenschlager)

to IFIT1, the induction of Mx1 requires the activation of the JAK-STAT signaling pathway by extracellular IFN (Bandyopadhyay et al. 1995). Indeed, the number of Mx1-deGFP - DENV-faR-wt double-positive cells was negligible. In particular, the fact that DENV-faR expressing cells did not induce Mx1-deGFP is consistent with an efficient block of JAK-STAT signaling in DENV-infected cells (cf. Figure 3.6). Although DENV is able to prevent antiviral protection in infected cells and efficiently spreads, the highly heterogeneous onset of IFIT1-deGFP and Mx1-deGFP expression (cf. Figure 3.10C and Figure 3.11C) demonstrate that antiviral protection of naïve cells by IFN coexists with viral spread in unprotected cells.

Additionally, we checked whether the heterogeneous IFN response in single cells is not caused by an insufficiency of cells to respond towards secreted IFN. First, we measured the fraction of IFIT1-deGFP positive cells upon stimulation with different concentrations of IFN- $\alpha$  using flow cytometry (Figure 3.12A). The determined IFN-responding fraction increased continuously with IFN- $\alpha$  dose to nearly 95%. Afterwards, we sorted IFIT1-deGFP reporter cells treated with either 10 or 100 IU/ml IFN- $\alpha$  into deGFP-expressing and non-expressing fractions. Sorted cell fractions were seeded and re-stimulated with the same IFN- $\alpha$  concentrations as in the first treatment (Figure 3.12B). Almost all cells that had responded in the first stimulation experiment expressed IFIT1-deGFP after the second treatment. This high degree of responsiveness is possibly a result of larger amounts of signal-transduction molecules like STAT1/2 as well as IRF-9 and/or the further induction of these proteins during the first IFN treatment (Maiwald et al. 2010). However, cells that did not respond to primary IFN- $\alpha$  stimulation showed practically the same dose response as naïve cells during primary IFN- $\alpha$  treatment. These results indicate that responsiveness to extracellular IFN is a stochastic process in individual cells, which does not depend on the ability of cells to respond towards extracellular IFN.

Overall, the single-cell analysis demonstrates a strong cell-to-cell heterogeneity of viral replication, IFN induction and IFN response. The similar time courses of

### 3.1. Examination of viral fitness by comparing DENV-wt with a DENV mutant

IFIT1-deGFP and Mx1-deGFP induction indicate that secreted IFN is the prime inducer of the antiviral response in our system. Cells expressing either ISG reporter remained DENV-faR-wt negative, showing that IFN produced by DENV-infected cells protected naïve cells against virus infection. Thus, the live-cell imaging data demonstrate that viral spread and protection of cells through IFN response occur in parallel - and compete - after DENV infection.

#### 3.1.4. Examination of viral fitness by comparing DENV-wt with a DENV mutant lacking 2'-O-methyltransferase activity

Our studies of the interactions between DENV and the IFN system revealed that efficient viral spread and IFN-induced antiviral immune defense occur simultaneously in an infected cell population (cf. section 3.1.2 and 3.1.3). To analyze which antiviral factors have the greatest influence on viral fitness, we compare DENV-wt with the DENV-E217A mutant, which is unable to modify the DENV RNA genome by 2'-O-methylation (Egloff et al. 2002, Ray et al. 2006, Dong et al. 2014).

Virus mutants, which lack 2'-O methylation of the viral genome, induce stronger immune responses, are severely attenuated *in vivo*, and thus might serve as vaccine candidates (Li et al. 2013b, Züst et al. 2013). It was suggested that 2'-O-methylation is a mechanism to evade detection of the virus by the intracellular receptor MDA5 (Züst et al. 2011), which in turn impedes the induction of IFN. Another rationale for the attenuated DENV-E217A mutant infection comes from the observation that IFIT1 sequesters 2'-O-unmethylated capped RNA and hence inhibits the translation of viral RNA (Pichlmair et al. 2011, Habjan et al. 2013). Given that IFIT1 can be expressed in an IFN-independent manner (Grandvaux et al. 2002, Diamond and Farzan 2013, Chen et al. 2013) and in response to IFN (cf. Figure 3.2B), the attenuation of the DENV-E217A mutant could result from an IFN-independent and an IFN-dependent antiviral response.

To examine the dynamics of the DENV-E217A mutant in living cells, our cooperation partners generated a replication competent DENV-faR-E217A fluorescent reporter (Schmid 2014). The DENV-faR-E217A mutant was created from the DENV-faR-wt reporter construct through substituting the glutamic acid residue (E) by an alanine residue (A) at the amino acid position 217 of the NS5 protein (Figure 3.13) (Egloff et al. 2002, Züst et al. 2013).

The infection of the IFN-competent IFIT1-deGFP and Mx1-deGFP reporter cells with DENV-faR-wt or DENV-faR-E217A is a suitable reporter system to investigate the differences between wild-type and E217A mutant infections. To directly compare the dynamics of DENV-wt with DENV-E217A mutant, we performed in parallel time-resolved flow cytometry measurements of the ISG reporter cells after infection with DENV-faR-wt or DENV-faR-E217A (Figure 3.14A and B for IFIT1-deGFP reporter cells; similar results for Mx1-deGFP reporter cells, Schmid 2014). Both ISG reporter cell lines were infected with a low viral titer to allow viral spread through secondary infection events. The dynamic flow-cytometric analysis for all experimental combinations was independently repeated and yielded comparable re-

### 3. Viral spread is mainly controlled by the autocrine effect of rapidly produced IFN

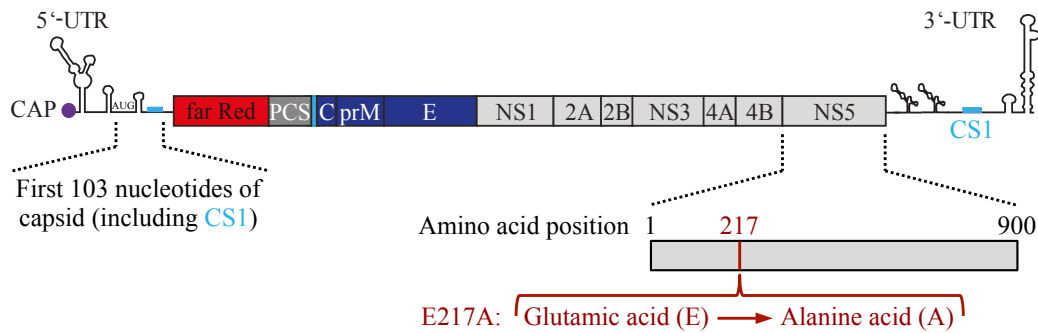


**Figure 3.13.:** Scheme of the established DENV-faR-E217A mutant reporter virus. Based on the DENV-faR-wt reporter construct (cf. Figure 3.2A) a DENV-faR-E217A mutant was generated through substituting the glutamic acid residue (E) by an alanine residue (A) at the amino acid position 217 of the NS5 protein (dark red color). (Graph provided by B. Schmid)

sults (cf. data in Figure 3.21 for IFIT1-deGFP reporter cells). After infection with DENV-faR-wt we detected the first virus replicating cells 36 h p.i. followed by a continuous rise of DENV-faR-wt positive cells over time. Approximately 12 h after the onset of DENV-faR-wt expression cells began to express IFIT1-deGFP and the fraction of responding cells increased in the time frame between 48 and 84 h post infection. In contrast to DENV-faR-wt infection, the DENV-faR-E217A infected cells became IFIT1-deGFP positive much earlier at ~ 24 h p.i. and the fraction of IFIT1-deGFP expressing cells rose strongly until the end of the experiment. The initial DENV-faR-E217A positive cells were visible 36 h p.i. and only a minor increase of DENV-faR-E217A replicating cells could be monitored within the observation period. In agreement with the single-cell analysis by time-lapse microscopy (cf. section 3.1.3 page 67), the fraction of IFIT1-deGFP - DENV-faR double-positive cells was very low. Altogether, the immediate comparison of DENV-wt with DENV-E217A demonstrates that the E217A mutant induces an attenuated infection as well as an earlier and enhanced IFN response.

In addition, we used the cell culture supernatants of the kinetic experiments to quantify the production of IFN by enzyme-linked immunosorbent assay (ELISA). We found that the A549 reporter cells predominantly express IFN- $\lambda$  (Figure 3.15), while the secretion of IFN- $\beta$  was comparatively lower and IFN- $\alpha$  was not detectable (Schmid 2014). After infection with DENV-faR-wt extracellular IFN- $\lambda$  was verifiable together with virus replication from 36 h p.i. onwards (cf. Figure 3.14A). In the DENV-faR-E217A infected cell culture we detected IFN- $\lambda$  already at 24 h after infection, while virus replication of the DENV-faR-E217A mutant was initially determined later at 36 h post infection (cf. Figure 3.14B). The IFN- $\lambda$  production and IFIT1-deGFP expression appeared simultaneously 24 h post DENV-faR-E217A infection (cf. Figure 3.14B), while in the DENV-faR-wt experiment the onset of IFIT1-deGFP expression occurred 12 hours after the initial release of IFN- $\lambda$  (cf. Figure 3.14A). As very low levels of produced IFN lie probably below the detection limit of the ELISA, we have no experimental information about the exact onset time of IFN production. But comparing the shape of the IFN- $\lambda$  release kinetics after DENV-faR-wt or DENV-faR-E217A infection, we assume an earlier secretion

3.1. Examination of viral fitness by comparing DENV-wt with a DENV mutant

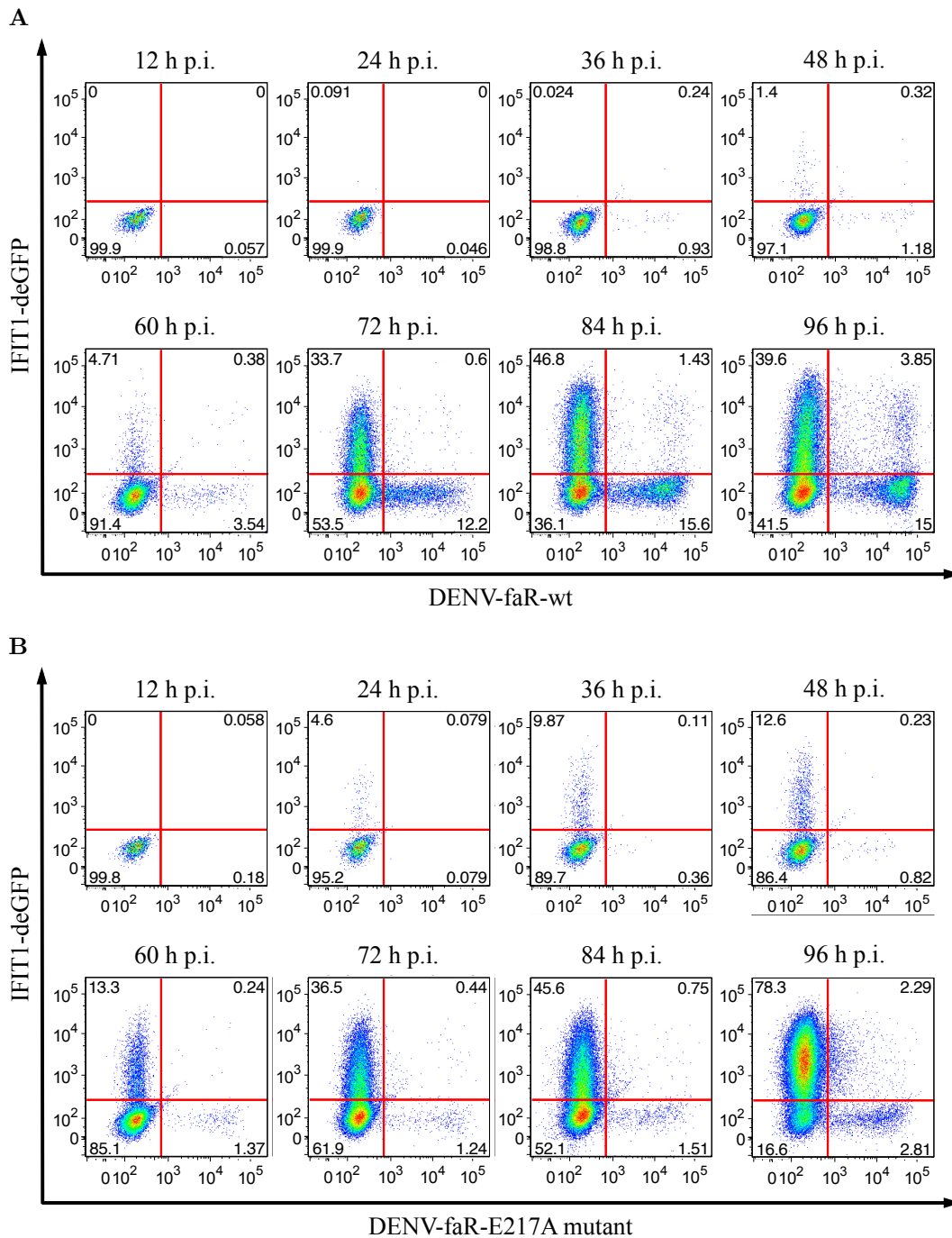


**Figure 3.14.:** In contrast to DENV-wt, the DENV-E217A mutant causes faster IFN response and barely spreads. (A, B) A549 IFIT1-deGFP reporter cells were infected with DENV-faR-wt (A) or DENV-faR-E217A mutant (B) at a MOI of 0.1. At the indicated time points post infection (p.i.), cells were fixed and 100  $\mu$ l of the cell suspension was subjected to flow cytometry. The dot plots illustrate the jointly measured DENV-faR (x-axis) and IFIT1-deGFP (y-axis) fluorescence intensities of individual cells. Shown is one of two independent experiments after infection with DENV-wt or DENV-E217A mutant. (Experiments by B. Schmid and R. Bartenschlager)

3. *Viral spread is mainly controlled by the autocrine effect of rapidly produced IFN*

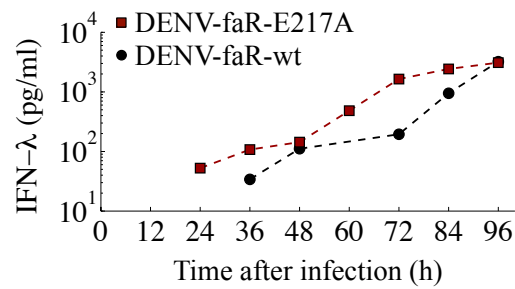


**Figure 3.15.:** The DENV-E217A mutant induces faster IFN production compared to DENV-wt. Cell supernatant of A549 IFIT1-deGFP reporter cells infected with DENV-faR-wt (black color) or DENV-faR-E217A mutant (dark red color) at a MOI of 0.1 from the respective experiment shown in Figure 3.14 were analyzed for IFN-λ expression by ELISA. (Experiments by B. Schmid and R. Bartenschlager)

of IFN-λ through DENV-faR-E217A infected cells.

In summary, compared to DENV-wt, the vaccine candidate DENV-E217A mutant elicits faster IFN production resulting in an earlier onset of the IFN response and barely spreads in IFN-competent cells.

### 3.2. Population-based delay differential equation model of viral spread and IFN-induced antiviral defense

Our research on the competition between spreading DENV and IFN-induced antiviral protection is driven by the question, which components of the IFN system have the greatest influence on viral fitness. The comparison between DENV-wt and attenuated DENV-E217A mutant infections (cf. section 3.1.4), is a perfectly suited experimental tool to detect key factors contributing to the improved antiviral defense against DENV-E217A mutant. To analyze the underlying differences between DENV-wt and DENV-E217A mutant infections by means of mathematical modeling, we first need to select the appropriate type of model to describe the data.

The results of our stochastic model of the IFN response against primary viral infection demonstrate that the heterogeneous single-cell behavior can be translated into predictable cell population dynamics (cf. section 2.2.3 and 2.4). Furthermore, a rapid spread of DENV and IFN over many cell diameters on the relevant time scale of hours is proven by the high diffusion coefficients of DENV and IFN ( $D_{\text{DENV}} = 2.6 \times 10^4 \mu\text{m}^2/\text{h}$ , Chang et al. 2008 and  $D_{\text{IFN}} = 1.1 \times 10^5 \mu\text{m}^2/\text{h}$ , Hu et al. 2011), and spatial gradients are therefore negligible. For these reasons, we decide to use a population-based modeling approach with uniform distribution of secreted IFN and viral spread. The time-resolved data after DENV-wt or DENV-E217A mutant infection (cf. Figure 3.14 and 3.15) suggest that the timing of viral spread as well as IFN release play an important role in the competition between virus and the IFN system. Accordingly, we establish a delay differential equation (DDE) model of viral spread and IFN-induced antiviral defense in a cell population.

In population dynamics, DDE models might be classified between ordinary differential equation (ODE) models and so called structured population models given by first-order hyperbolic partial differential equations (PDEs) (Baker et al. 1999, Bocharov and Rihan 2000). The latter class of models describes the dynamics of age-structured or, more widely, state-structured populations (Charlesworth 1980, Metz and Diekmann 1986, Barbarossa 2013) where the population is characterized by a distribution depending on both time and a property of the individuals like age, mass or any other feature (cf. Bocharov and Haderler 2000, Getto et al. 2008, Gwiazda et al. 2014, for instance). While state-structured population models deal with at least two independent dynamic variables, DDE models only consider temporal dynamics (cf. Bazhan and Belova 1999, Lee et al. 2009, Pawelek et al. 2012, Tan et al. 2012, for example).

In general, DDEs are defined by equations of the form

$$\dot{y} = f(t, y(t), \mathcal{W}(\omega_1(t), y(t)), \mathcal{W}(\omega_2(t), y(t)), \dots, \mathcal{W}(\omega_n(t), y(t))), \quad (3.1)$$

with  $t \in \mathbb{R}$ ,  $n \in \mathbb{N}$ , weighting functions  $\omega_i(t)$  for  $i = 1, \dots, n$  and

$$\mathcal{W}(\omega_i(t), y(t)) = \int_{-\infty}^t \omega_i(t-s)y(s)ds. \quad (3.2)$$

A DDE with discrete delays arises if the weighting factors  $\omega_i(t)$  correspond to delta distributions, also called delta functions,  $\delta(z)$  with  $z = t - \tau_i$  (Murray 2002).

### 3. Viral spread is mainly controlled by the autocrine effect of rapidly produced IFN

One possible definition of the delta distribution  $\delta(z)$  is given by

$$\delta(z) = \begin{cases} 0 & , \text{ for } z \neq 0; \\ \int_{z-\epsilon}^{z+\epsilon} \delta(s) ds = 1 & , \forall \epsilon > 0 \end{cases} \quad (3.3)$$

and results in the following characteristic property:

$$\int_{-\infty}^{\infty} \delta(s-z) f(s) ds = f(z), \quad (3.4)$$

for a continuous function  $f$  on  $\mathbb{R}$ . By applying the property (3.4) as well as setting  $\omega_i(t) = \delta(t - \tau_i)$ , equation (3.2) changes to

$$\mathcal{W}(\delta(t - \tau_i), y(t)) = \int_{-\infty}^t \delta(t - \tau_i - s) y(s) ds = y(t - \tau_i). \quad (3.5)$$

A discrete DDE is defined by the combination of the equation (3.1) and (3.5). If  $\tau_i$  in (3.5) is constant, time-dependent or depending on  $y(t)$ , then the discrete DDE describes a differential equation with constant delay, time-dependent delay or state-dependent delay, respectively (Barbarossa 2013).

Using mathematical modeling, we would like to analyze the timing of virus replication, virus production and IFN secretion. The measured single-step growth curve of these processes after high dose infection with DENV-faR-wt (cf. Figure 3.7) corresponds, from a mathematical point of view, to the integral of the probability density function of the onset time of these events in single cells. As an approximation of these onset time distributions, we decided to create a DDE model with constant time delays for virus replication, virus production and IFN secretion. To consider a differential equation system with constant delays is a good compromise of tractability and detail. In section 3.3 we will show that this model can be parameterized by experimental data and therefore provides a starting point for a full mechanistic understanding of viral propagation and IFN-induced antiviral defense.

In our DDE model with constant delays (Figure 3.16 and DDE system (3.11)) we consider at the initial time  $t_0$  a number of naïve cells  $S_0$  which are susceptible to virus infection, as well as an initial extracellular viral load  $V_0$ . Susceptible cells  $S$  can become infected by extracellular virus  $V$  with infection rate  $r_V$  (cf. blue arrow in Figure 3.16). Depending on the time elapsed since viruses have entered the host cells, infected cells  $I$  can acquire up to three different features in parallel:

- After a time delay  $\tau_R > 0$ , infected but not yet virus replicating cells  $I_{\overline{R}}$  turn into virus replicating cells  $I_R$ . The time delay of virus replication  $\tau_R$  is related to the mean expression onset of virus replication in individual cells monitored after infection with DENV-faR-wt (cf. Figure 3.9 - 3.11 and 3.14A) or DENV-faR-E217A mutant (cf. Figure 3.14B).
- After a time delay  $\tau_V > 0$ , infected but not yet virus releasing cells  $I_{\overline{V}}$  become virus producing cells  $I_V$  and release new generated infectious virus particles

### 3.2. Population-based model of viral spread and IFN-induced antiviral defense

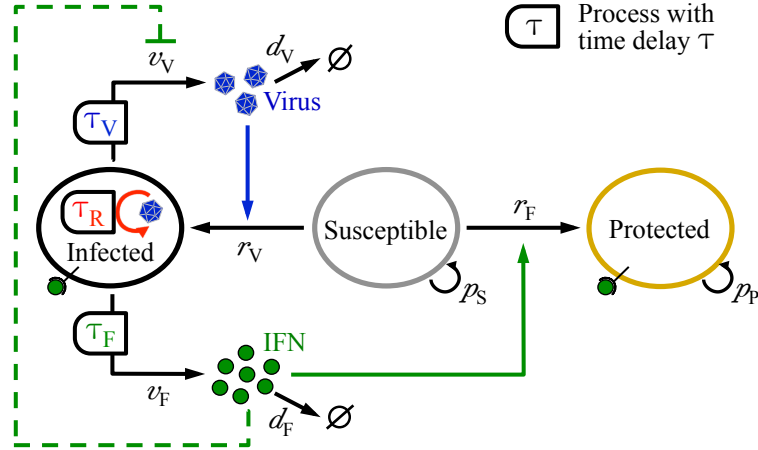


**Figure 3.16.:** Scheme of the mathematical model which describes how naïve and thus susceptible cells can become either infected by extracellular virus or protected by the antiviral effect of secreted IFN. Susceptible cells (gray oval) can become infected by extracellular virus with the infection rate  $r_V$  (blue arrow). Virus replication ( $\odot$ ) arises in infected cells (black oval) at time  $\tau_R$  after viral entry (red color) and results in virus production with the virus production rate  $v_V$  from time  $\tau_V > \tau_R$  onwards. Moreover, infected cells start to express IFN with the secretion rate  $v_F$  at time  $\tau_F$  after viral infestation. Recognition of secreted IFN turn susceptible cells into protected cells (yellow oval) with the protection rate  $r_F$  (solid green arrow). In addition, IFN can indirectly induce antiviral genes in infected cells (dashed green inhibition link). Extracellular virus and IFN are removed ( $\emptyset$ ) by cellular uptake as well as extracellular degradation with the rate constant of virus degradation  $d_V$  and the rate constant of IFN degradation  $d_F$ . While propagation is inhibited in infected cells, susceptible and protected cells proliferate ( $\odot$ ) with the rates  $p_S$  and  $p_P$ , respectively.

with the virus production rate  $v_V$ . The time delay of virus production  $\tau_V$  represents the average time required to replicate, translate viral proteins, assemble and release new virus particles (cf. blue curve in Figure 3.7).

- After a time delay  $\tau_F > 0$ , infected but not yet IFN expressing cells  $I_{\bar{F}}$  turn into IFN secreting cells  $I_F$  and produce IFN  $F$  with the IFN secretion rate  $v_F$ . The time delay of IFN secretion  $\tau_F$  corresponds to the mean onset of IFN expression. It includes the necessary time of viral recognition, downstream signal transduction as well as IFN transcription, translation and secretion (cf. dark green curve in Figure 3.7 and Figure 3.15).

Since the time delay  $\tau_V$  also comprises the duration of virus replication, the condition  $\tau_V > \tau_R$  must be fulfilled, while we do not require any temporal link between  $\tau_F$  and both other time delays. Whether the production of new virus particles takes longer than IFN secretion or vice versa will be determined by the parameter estimation in section 3.3.

According to the experimental study, IFN has two antiviral effects (cf. Figure 3.5):

- Pre-stimulation with IFN demonstrated that extracellular IFN can protect naïve cells against productive DENV infection. To incorporate this paracrine IFN response in our model, we take into account an IFN-induced switch from

### 3. Viral spread is mainly controlled by the autocrine effect of rapidly produced IFN

susceptible cells to protected cells  $P$  with the protection rate  $r_F$  (solid green arrow in Figure 3.16).

- Stimulation of infected cells with IFN in an early phase after viral entry can activate antiviral defense mechanisms, which reduce virus replication and consequently virus production. To keep the model initially simple, so that its parameters can be identified from experimental data, we neglect a direct autocrine impact of IFN in the first instance (dashed green inhibition link in Figure 3.16). After the model parameterization (cf. section 3.3), we will examine the effect of secreted IFN on infected cells explicitly with an extended version of the model (cf. section 3.4 and 3.5).

In order to include the removal of extracellular virus and IFN by cellular uptake and, to a lesser extent, by extracellular degradation, we assume a decrease of virus and IFN with the rate constant of virus degradation  $d_V$  and the rate constant of IFN degradation  $d_F$ , respectively.

Furthermore, we observed that infected cells proliferate less and die faster than non-infected cells. To compensate this propagation difference and, additionally, to keep the number of model parameters low, we suppose an inhibited proliferation in infected cells, whereby susceptible and protected cells proliferate with the rates  $p_S$  and  $p_P$ , respectively.

To establish the DDE system of our model, particular attention must be paid to the formulation of the three features of the infected cells comprising virus replication, virus production and IFN expression, which begin at time  $\tau_R$ ,  $\tau_V$  and  $\tau_F$ , respectively. As the time delays  $\tau_m$  for  $m \in \{R, V, F\}$  are free parameters and only bound to the condition  $\tau_V > \tau_R$ , the properties of the infected cells can arise at different times, overlap each other and take place in parallel. Therefore we consider each feature of the infected cells separately and calculate the number of inactive infected cells  $I_{\bar{m}}(t)$  and active infected cells  $I_m(t)$  for  $m \in \{R, V, F\}$  depending on time  $t \in \mathbb{R}$ . For this purpose we first require the total number of infected cells  $I$  at time  $t$

$$I(t) = I_{\bar{m}}(t) + I_m(t) \quad \forall m \in \{R, V, F\} \quad (3.6)$$

and the corresponding differential equation

$$\dot{I}(t) \stackrel{\substack{\text{page 74} \\ \text{Fig. 3.16}}}{=} r_V V(t) S(t). \quad (3.7)$$

The number of inactive infected cells  $I_{\bar{m}}$  at time  $t$  consists of all cells which become infected in the time period  $[t - \tau_m, t]$ , since after  $\tau_m$  inactive cells  $I_{\bar{m}}$  progress to active cells  $I_m$ . Thus,  $I_{\bar{m}}$  is given by

$$I_{\bar{m}}(t) \stackrel{(3.7)}{=} \int_{t-\tau_m}^t r_V V(s) S(s) ds. \quad (3.8)$$

To obtain the differential equation  $\dot{I}_{\bar{m}}$ , we differentiate both sides of (3.8) with

### 3.2. Population-based model of viral spread and IFN-induced antiviral defense

respect to time  $t$  and apply the fundamental theorem of calculus:

$$\begin{aligned}\dot{I}_{\overline{m}}(t) &= \frac{d}{dt} \int_{t-\tau_m}^t r_V V(s) S(s) ds \\ &= r_V V(t) S(t) - r_V V(t - \tau_m) S(t - \tau_m).\end{aligned}\quad (3.9)$$

Using the preceding equations, the differential equation  $\dot{I}_m$  results from

$$\begin{aligned}\dot{I}_m(t) &\stackrel{(3.6)}{=} \frac{d}{dt} (I(t) - I_{\overline{m}}(t)) \\ &= \dot{I}(t) - \dot{I}_{\overline{m}}(t) \\ &\stackrel{(3.7, 3.9)}{=} r_V V(t - \tau_m) S(t - \tau_m).\end{aligned}\quad (3.10)$$

Taking all considerations together, our model is described by the following DDE system:

$$\begin{aligned}\dot{S}(t) &= -r_V V(t) S(t) - r_F F(t) S(t) + p_S S(t) \\ \dot{I}_{\overline{R}}(t) &= r_V V(t) S(t) - r_V V(t - \tau_R) S(t - \tau_R) \\ \dot{I}_R(t) &= r_V V(t - \tau_R) S(t - \tau_R) \\ \dot{I}_{\overline{V}}(t) &= r_V V(t) S(t) - r_V V(t - \tau_V) S(t - \tau_V) \\ \dot{I}_V(t) &= r_V V(t - \tau_V) S(t - \tau_V) \\ \dot{I}_{\overline{F}}(t) &= r_V V(t) S(t) - r_V V(t - \tau_F) S(t - \tau_F) \\ \dot{I}_F(t) &= r_V V(t - \tau_F) S(t - \tau_F) \\ \dot{P}(t) &= r_F F(t) S(t) + p_P P(t) \\ \dot{F}(t) &= v_F I_F(t) - d_F F(t) \\ \dot{V}(t) &= v_V I_V(t) - d_V V(t).\end{aligned}\quad (3.11)$$

The initial value problem corresponding to our model is defined by the DDE system (3.11) for time  $t \in [t_0, t_{\text{end}}]$  together with initial conditions, which we specify next. As we will use our model to simulate experiments in which naïve cells have been infected with a viral load  $V_0$  at the starting time  $t_0 = 0$ , only two initial values of our DDE system are unequal to zero, namely the number of susceptible cells  $S(0) = S_0$  as well as the extracellular viral load  $V(0) = V_0$ .

In addition, we need to provide a history function for each variable in (3.11) that has a delay argument and therefore refers to the past  $[t_0 - \tau_m, t_0]$  for  $m \in \{R, V, F\}$ . For DDE models with multiple discrete delays, the history functions have to be defined on the time interval  $[t_0 - \tau_{\text{max}}, t_0]$ , where  $\tau_{\text{max}}$  represents the maximum of the positive time delays (Bellen and Zennaro 2003). Since in the experimental setup the initial infection took place at time  $t_0 = 0$ , we must set  $V(t) = 0$  for  $t < 0$ . This implies, however, that the choice of the history function for the number of susceptible cells  $S$  is irrelevant for the solution of the DDE system (3.11), since the delayed variable  $S(t - \tau_m)$  with  $\tau_m > 0$  is always multiplied by  $V(t - \tau_m)$  and  $V(t - \tau_m) = 0$  for  $t < \tau_m$ . For simplicity, we take  $S(t) = 0$  for  $t < 0$ .

### 3. Viral spread is mainly controlled by the autocrine effect of rapidly produced IFN

To reflect the experimental situation, we cannot avoid that the initial condition of the DDE system (3.11) with respect to the extracellular viral load  $V$  is discontinuous due to

$$\lim_{t \rightarrow 0, t < 0} V(t) = 0 \neq V_0 = \lim_{t \rightarrow 0, t > 0} V(t). \quad (3.12)$$

Such a discontinuity in the initial time  $t_0$  propagates along the integration interval and causes subsequent discontinuity points in the first and higher order time derivatives, whereby, however, the solution of the DDE system becomes smoother with increasing integration time (Bellen and Zennaro 2003).

Bellen and Zennaro analyzed the propagation of initial discontinuities in a general  $n_y$ -dimensional DDE system with  $n_\tau$  constant time delays  $\tau_i$ ,  $i = 1, \dots, n_\tau$ , defined by

$$\begin{aligned} \dot{y}(t) &= f(t, y(t), y(t - \tau_1), y(t - \tau_2), \dots, y(t - \tau_{n_\tau})), & t_0 \leq t \leq t_{\text{end}}, \\ y(t_0) &= y_0, \\ y(t) &= h(t), & t_0 - \tau_{\text{max}} \leq t \leq t_0, \end{aligned} \quad (3.13)$$

with the state variable  $y(t) \in \mathbb{R}^{n_y}$ , the right-hand-side function  $f \in \mathbb{R}^{n_y}$ , the initial state  $y_0 \in \mathbb{R}^{n_y}$ , the history function  $h(t) \in \mathbb{R}^{n_y}$  and positive time delays  $\tau_i > 0$  under the conditions that

- (C1)  $f$  is continuous with respect to  $t$ ,
- (C2)  $f$  is Lipschitz continuous with respect to  $y(t)$  and with respect to  $y(t - \tau_i)$  and
- (C3)  $h(t)$  is Lipschitz continuous.

Our 10-dimensional DDE model (3.11) with three strictly positive constant time delays belongs to the class of DDE systems given by the initial value problem (3.13) and fulfills the conditions (C1)–(C3): (C1) The right-hand-side function of (3.11) does not depend on the variable  $t$  explicitly and thus continuity with respect to  $t$  is trivial. (C2) The required Lipschitz continuity of the right-hand-side function  $f$  follows from the continuous differentiability of the right-hand-side function of (3.11) with respect to  $y(t)$  and with respect to  $y(t - \tau_i)$  on an appropriately chosen compact subset of  $\mathbb{R} \times \mathbb{R}^{n_y} \times (\mathbb{R}^{n_y})^{n_\tau}$ . (C3) The Lipschitz continuity of the history function is ensured as we consider the constant zero function as history functions for those variables in our system (3.11) that have a delay argument.

Under these conditions, Bellen and Zennaro demonstrated that in the general DDE system (3.13) a discontinuity in the initial time  $t_0$  causes the discontinuity points

$$\xi_{i,j} = t_0 + j \tau_i \quad \forall j \in \mathbb{N} \text{ and } i = 1, \dots, n_\tau. \quad (3.14)$$

For our DDE system (3.11), this means that the discontinuities in the initial time  $t_0 = 0$  leads to a continuous solution for  $t > 0$ , but with discontinuities in (higher order) derivatives at the time points  $t = j \tau_m \forall j \in \mathbb{N}$  and  $m \in \{R, V, F\}$ .

In spite of the occurrence of discontinuous derivatives, the existence of a unique solution of the DDE system (3.13), and in particular of our DDE system (3.11), can

### 3.2. Population-based model of viral spread and IFN-induced antiviral defense

be proven with the method of steps (Bellen and Zennaro 2003, Smith 2011, Lenz et al. 2014, Lenz 2014). This method is based on the principle of partitioning the integration interval  $[t_0, t_{\text{end}}]$  into subintervals ranging from one discontinuity point to the next. In each subinterval, the DDE system reduces to an ODE system by substituting the delayed terms by known quantities: the history function or the solution at earlier times, respectively. Since this ODE system fulfills the conditions (C1)–(C3) (cf. page 78), the Theorem of Picard and Lindelöf (e.g. Hartman 2002) can be applied, which provides existence and uniqueness of the solution on the subintervals. Thus, by successive integration on the subintervals, a unique solution of the DDE system (3.13) is obtained on the finite time interval  $[t_0, t_{\text{end}}]$ .

As our DDE model (3.11) considers the kinetics of an infected cell population along with the dynamics of extracellular virus and IFN, we must ensure that the solution of our DDE system stays non-negative for positive initial data. For this purpose, we apply a positivity theorem given in the book by Smith (Smith 2011). Smith gives this result for the case of one constant delay using method of steps and employing a theorem about non-negative solutions of ODE initial value problems. This positivity theorem can be extended straightforwardly to DDE systems with multiple constant delays:

The solution  $y(t)$  of a DDE system (3.13) with positive constant time delays  $\tau_i > 0$ ,  $i = 1, \dots, n_\tau$  and a right-hand-side function  $f : \mathbb{R} \times \mathbb{R}_{\geq 0}^{n_y} \times (\mathbb{R}_{\geq 0}^{n_y})^{n_\tau} \rightarrow \mathbb{R}^{n_y}$  satisfies  $y(t) \geq 0 \forall t \in [t_0, t_{\text{end}}]$ , if the following conditions hold:

- (P1)  $f$  is continuous,
- (P2)  $f$  is continuously differentiable with respect to  $y(t)$ ,
- (P3)  $h(t)$  is continuous,
- (P4)  $h(t) \geq 0$  and
- (P5)  $\forall k = 1, \dots, n_y, \forall t, \forall y(t) \in \mathbb{R}_{\geq 0}^{n_y}, \forall y(t - \tau_i) \in \mathbb{R}_{\geq 0}^{n_y}$  for  $i = 1, \dots, n_\tau$  :

$$y_k(t) = 0 \Rightarrow f_k(t, y(t), y(t - \tau_1), y(t - \tau_2), \dots, y(t - \tau_{n_\tau})) \geq 0.$$

In the case of our DDE system (3.11), the requirements (P1) and (P2) are met as the right-hand-side function does not depend on the variable  $t$  explicitly and is continuously differentiable with respect to  $y(t)$  and with respect to  $y(t - \tau_i)$ . Since we use the constant zero history function for  $S$  and  $V$ , the conditions (P3) and (P4) are also fulfilled. To verify (P5), we will first take a closer look at each equation of a subsystem of the DDE model (3.11) concerning the state variable  $\tilde{y} = (S, I_R, I_V, I_F, P, F, V)$ . The reduced system obtained by restricting (3.11) to the state variable  $\tilde{y}$  is still a closed DDE system, since it is independent of the neglected variables  $I_{\bar{m}}$  describing the number of inactive infected cells. Examining it, we verify that for  $t \in [t_0, t_{\text{end}}]$ ,  $\tilde{y}(t) \in \mathbb{R}_{\geq 0}^7$ ,  $\tilde{y}(t - \tau_m) \in \mathbb{R}_{\geq 0}^7 \forall m \in \{R, V, F\}$  and strictly positive constant rates it holds:

### 3. Viral spread is mainly controlled by the autocrine effect of rapidly produced IFN

$$\begin{aligned}
\text{If } S(t) = 0 &\Rightarrow \dot{S}(t) = 0. \\
\text{If } I_m(t) = 0 &\Rightarrow \dot{I}_m(t) = r_V V(t - \tau_m) S(t - \tau_m) \geq 0. \\
\text{If } P(t) = 0 &\Rightarrow \dot{P}(t) = r_F F(t) S(t) \geq 0. \\
\text{If } F(t) = 0 &\Rightarrow \dot{F}(t) = v_F I_F(t) \geq 0. \\
\text{If } V(t) = 0 &\Rightarrow \dot{V}(t) = v_V I_V(t) \geq 0.
\end{aligned}$$

Therefore, the subsystem with the state variable  $\tilde{y}$  satisfies the conditions (P1)–(P5) of the positivity theorem and has a unique non-negative solution. In particular, we obtain a non-negative solution for the number of susceptible cells  $S(t) \geq 0$  and the extracellular viral load  $V(t) \geq 0 \forall t \in [t_0, t_{\text{end}}]$  as required for a meaningful solution to the biological problem. By utilizing these non-negative solutions we can verify that the original DDE system (3.11) with the state variable  $y = (S, I_{\bar{R}}, I_R, I_{\bar{V}}, I_V, I_{\bar{F}}, I_F, P, F, V) \in \mathbb{R}^{10}$  fulfills the requirement (P5). For this purpose, it remains to show that  $I_{\bar{m}}$  for  $m \in \{R, V, F\}$  satisfies (P5). According to equation (3.8),  $I_{\bar{m}}$  for  $m \in \{R, V, F\}$  are integrals over the function  $\dot{I}(t) = r_V V(t) S(t) \geq 0 \forall t \in [t_0, t_{\text{end}}]$  as shown above, and are therefore uniquely defined, continuous and non-negative.

Taken together, the initial value problem of our DDE model (3.11) has a unique positive solution on any finite time interval.

For the simulation of the DDE system (3.11) we utilize Matlab as a programming environment. Using a binary Matlab executable (mex) subroutine, we set up an interface between Matlab and the freely available RADAR5 solver written in ANSI Fortran-90 (Guglielmi and Hairer 2005). The RADAR5 framework comprises an algorithm to calculate numerically the solution of stiff delay differential equations based on an adapted 3-stage Radau IIA collocation method (Hairer and Wanner 1999, Guglielmi and Hairer 2001, Guglielmi and Hairer 2008). This algorithm corresponds to a certain implicit Runge-Kutta method of order 5 in which the Runge-Kutta equations are solved by means of a suitable Newton process (Guglielmi 2005). The Newton iterations require two Jacobian matrices, on the one hand, the standard Jacobian matrix  $\mathcal{J}$  and, on the other hand, the Jacobian matrix with respect to the delayed variables  $\mathcal{J}_\tau$ . These Jacobian matrices are either computed internally or can be provided by the user. In order to increase the accuracy of the numerical solution, we implement the time dependent Jacobian matrices  $\mathcal{J}(t)$  and  $\mathcal{J}_\tau(t)$  of our DDE system (3.11) within the RADAR5 code. An explicit presentation of both Jacobian matrices is given in appendix A.1.

In addition to the RADAR5 solver we also tested Matlab's dde23 solver for delay differential equations with constant delays (Shampine and Thompson 2001, Shampine and Thompson 2009). Although the implementation in Matlab is more convenient and modifications of the model can be achieved with less effort than within the RADAR5 framework, the significantly faster calculation in Fortran makes the RADAR5 solver more suitable for the purpose of parameter estimation, which will be detailed next.

### 3.3. Parameterization of the delay differential equation model

As we are primarily interested in examining the underlying mechanisms of the differences between DENV-wt and attenuated DENV-E217A mutant infections (cf. section 3.1.4), we first parameterize our model (3.11) using DENV-wt infection measurements exclusively (see section 3.3.1). Based on this DENV-wt specific parameter set, we fit the DENV-E217A mutant related data by allowing only four reasonable key parameters to be different (see section 3.3.2).

This approach will enable us to discover two parameters which differ strongly between DENV-wt and DENV-mutant infections: The virus production rate is  $\sim 8$ -fold lower and the delay of IFN secretion is  $\sim 24$  h shorter after DENV-E217A mutant infection compared to DENV-wt. Importantly, IFN release sets in prior to virus production after DENV-E217A mutant infection, whereby the timing of these two events are almost identical in the case of DENV-wt.

#### 3.3.1. Estimation of model parameters by using DENV-wt measurements

In order to analyze the mechanistic differences between DENV-wt and attenuated DENV-E217A mutant infections, we first parameterize our model (3.11) by considering only DENV-wt infection data and, subsequently, utilize these estimates to determine DENV-E217A mutant specific parameter changes. For parameter estimation we focus on the well-suited time-resolved flow cytometry data set along with ELISA quantification of IFN- $\lambda$  after infection of the ISG reporter cells with DENV-faR-wt or DENV-faR-E217A (cf. Figure 3.14 and 3.15). This data set was obtained by measuring a specified proportion of the cell suspensions and thus provides quantitative as well as directly comparable differences between DENV-wt and DENV-E217A mutant infections in terms of absolute cell numbers in a certain volume.

At the beginning of the experiments, the ISG reporter cells were infected at a MOI of 0.1. Based on the definition of MOI given by

$$\text{MOI} = \frac{V_0}{S_0}, \quad (3.15)$$

and the initial number of naïve cells  $S_0 \sim 15000$  in the relevant experiments, we set the initial extracellular viral load  $V_0 \stackrel{(3.15)}{=} 0.1 \times 15000 = 1500$  arbitrary units/ml. This specification implies that the viral load related infection rate  $r_V$  can be determined up to a scaling factor.

In addition, we take advantage of an independent virus stability experiment to obtain an estimate of the virus degradation rate constant  $d_V$  (Figure 3.17). The DENV-faR-wt stability analysis was performed by incubating IFN-incompetent baby hamster kidney cells (BHK-21) with a high number of DENV-faR-wt particles i.e., the BHK-21 cells were infecting and the cell culture medium was not changed. The extracellular amount of virus was identified by TCID<sub>50</sub> assay over time. Since the

### 3. Viral spread is mainly controlled by the autocrine effect of rapidly produced IFN

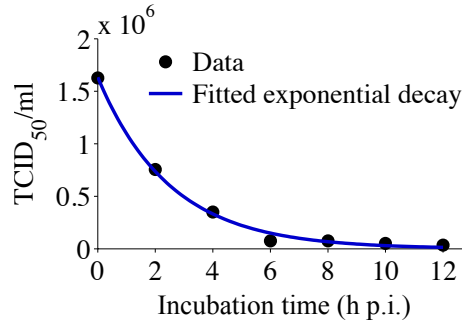


**Figure 3.17.:** Estimation of the rate constant of virus degradation  $d_V$ . The parameter determination of the rate constant of virus degradation  $d_V$  is based on a virus stability experiment, in which naïve BHK-21 cells were incubated with  $1.6 \times 10^6$  DENV-faR-wt particles and virus titers (black dots) were quantified by TCID<sub>50</sub> assay at the indicated time points post infection (p.i.). The data are fitted with an exponential decay equation (blue curve) by applying a trust-region-reflective least-squares algorithm with  $10^4$  different random initial values. The best fit results in  $d_V = 0.4/\text{h}$  together with an initial virus concentration of  $1.6 \times 10^6$  TCID<sub>50</sub>/ml. (Experiments by B. Schmid and R. Bartenschlager)

production of new infectious virus particles in host cells takes approximately 14 h (cf. blue curve in Figure 3.7), the measured extracellular amount of virus decreased continuously between 0 and 12 h after incubation. According to the shape of the observed virus kinetic, we suppose an exponential decay of extracellular virus  $\mathcal{V}$  and consider as objective function

$$\mathcal{V}(t) = \mathcal{V}_0 e^{-d_V t} \quad (3.16)$$

for  $t \in \mathbb{R}$  with the initial condition  $\mathcal{V}(0) = \mathcal{V}_0$ . To fit the parameters of the objective function (3.16) to the virus stability data, we utilize the trust-region-reflective least-squares algorithm of Matlab's optimization toolbox (Coleman and Zhang 2003) and choose for the corresponding chi-squares statistic (2.35) a constant error. After applying the optimization method with  $10^4$  different random initial values, the best fit yields  $d_V = 0.4/\text{h}$  and provides a satisfying match with the data (cf. Figure 3.17, blue curve).

Moreover, we found that fitting of the IFN secretion rate  $v_F$  and the rate constant of IFN degradation  $d_F$  at once would lead to a correlation of both parameters. Thus, we set  $d_F = 0.15/\text{h}$  to the previously determined rate constant of IFN degradation of the stochastic model (cf. Table 2.2 in section 2.2.3).

To determine the remaining model parameters, we use the time-resolved data set consisting of two independent flow cytometry measurements along with ELISA quantifications (cf. Figure 3.14 and 3.15) by comparing the following observed kinetics with the related model readouts (ROs) (Figure 3.18):

- (RO1) The total number of cells  $A$  serves as a control and is described in our model by

$$A(t) = S(t) + I_{\bar{m}}(t) + I_m(t) + P(t), \quad (3.17)$$

at time  $t \in \mathbb{R}$  and  $m \in \{\text{R}, \text{V}, \text{F}\}$ .

### 3.3. Parameterization of the delay differential equation model

- (RO2) The number of experimentally identified IFIT1-deGFP – DENV-faR double-negative cells are represented by  $\tilde{S}(t)$  defined as

$$\tilde{S}(t) = S(t) + I_{\overline{R}}(t). \quad (3.18)$$

$\tilde{S}(t)$  comprises both susceptible cells  $S$  and already infected but not yet virus replicating cells  $I_{\overline{R}}$ , which implies that the DENV-faR fluorescent protein is not yet visible in the host cell.

- (RO3) The observed DENV-faR positive cells corresponds to the calculated number of virus replicating cells  $I_R(t)$ .
- (RO4) The detected ISG expressing IFIT1-deGFP<sup>+</sup> – DENV-faR<sup>-</sup> cells are modeled by the protected cells  $P(t)$ .
- (RO5) Since IFN- $\lambda$  is the most prominent type of IFN in our cell system (Schmid 2014), we equate the measured level of secreted IFN- $\lambda$  with the simulated amount of released IFN  $F(t)$ .

To exploit both independently performed experiments, the model dynamics listed in (RO2)–(RO5) are simultaneously fitted to the related time course data of experiments 1 and 2 by allowing only the initial number of susceptible cells  $S_0$  to vary between experiments, while all other parameters are identical.

As optimization method we use the trust-region-reflective least-squares algorithm of Matlab's optimization toolbox (Coleman and Zhang 2003) by calling the Fortran program of our DDE system with a binary mex subroutine. Since we compare several components of the model with their respective data, the chi-squares statistic  $\chi^2$  of the model parameters  $\theta_k$ ,  $k = 1, \dots, N_p$ , is given by

$$\chi^2(\theta_1, \dots, \theta_{N_p}) = \sum_{j=1}^{N_c} \sum_{i=1}^{N_t} \left( \frac{d_j(t_i) - y_j(t_i | \theta_1, \dots, \theta_{N_p})}{\sigma_j(t_i)} \right)^2, \quad (3.19)$$

where  $N_p$  stands for the number of model parameters and  $N_c$  denotes the number of model components  $y_j(t_i | \theta_1, \dots, \theta_{N_p})$  that describe the associated data set  $(t_i, d_j(t_i))$  with the measurement error  $\sigma_j(t_i)$  for  $i = 1, \dots, N_t$  and  $j = 1, \dots, N_c$  at  $N_t$  observation times. To account for the fact that the data used for fitting were obtained via different measurement techniques and comprise small as well as large values, we assume for the measurement errors a 10% deviation band relative to the measured kinetic data:  $\sigma_j(t_i) = 0.1 d_j(t_i)$ . To find a reliable best fit parameter set of our optimization problem

$$\min_{\{\theta_k | k=1, \dots, N_p\}} (\chi^2(\theta_1, \dots, \theta_{N_p})), \quad (3.20)$$

the least-squares minimization has to be repeated for a large number of different random initial values. Although it turns out that the simulation of the DDE model (3.11) using the RADAR5 solver written in Fortran is considerably less time consuming as our stochastic model based on Gillespie's algorithm (cf. 2.2 - 2.3), the integration of the DDE system (3.11) is still slower than solving comparably large

3. Viral spread is mainly controlled by the autocrine effect of rapidly produced IFN

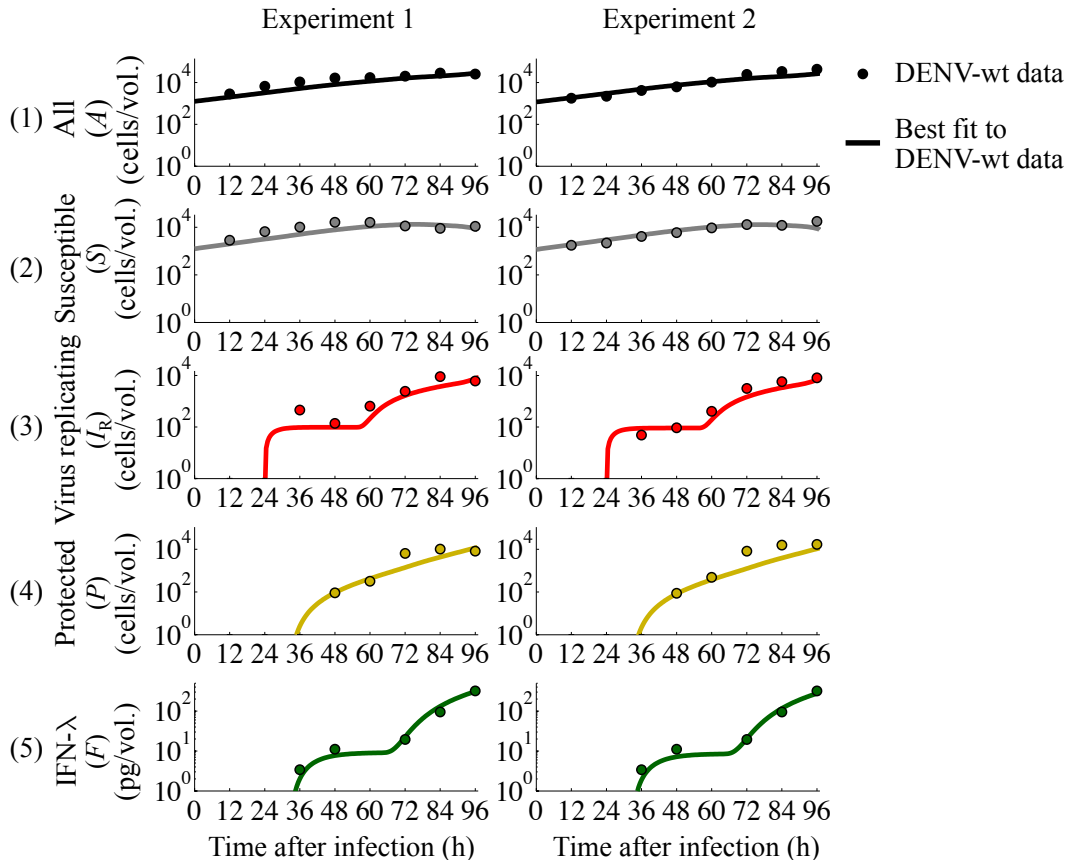


**Figure 3.18.:** Best fit of the mathematical model to two independent experiments concerning DENV-faR-wt infection. For parameter estimation we compare simulated (solid lines) with observed (circles) cell dynamics of (1) all (as control), (2) susceptible IFIT1-deGFP – DENV-faR-wt double-negative, (3) virus replicating DENV-faR-wt positive as well as (4) protected IFIT1-deGFP<sup>+</sup> – DENV-faR-wt<sup>-</sup> cells along with (5) IFN- $\lambda$  release after infection of A549 IFIT1-deGFP reporter cells with DENV-faR-wt at a MOI of 0.1. The data set is based on two independent flow cytometry measurements (cf. Figure 3.14A), while IFN- $\lambda$  was quantified in experiment 2 by ELISA (cf. Figure 3.15, colored in black). Absolute cell numbers can be considered as a volume (vol.) of 100  $\mu$ l was consistently analyzed. We fit the model simultaneously to both experiments by only allowing the initial number of susceptible cells to be specific to each measurement, whereby all other parameters are the same for both experiments. The best fit is obtained by using a trust-region-reflective least-squares algorithm with at least  $10^4$  different random initial values. (Experiments by B. Schmid and R. Bartenschlager)

ODE systems. To speed up calculation, we utilize Matlab’s parallel computing toolbox to run several optimization processes simultaneously on a computer cluster. Since this cluster can execute 240 individual sessions in parallel, we are able to repeat the optimization procedure for more than  $10^4$  different random initial values. The resulting best fit correctly reproduces the observed kinetic data of both experiments (Figure 3.18).

In order to assess the uncertainties of the best fit parameter values, we calculate likelihood-based confidence intervals for the estimated parameters by applying the profile likelihood method (Venzon and Moolgavkar 1988). Likelihood-based confi-

### 3.3. Parameterization of the delay differential equation model

dence regions dependent on a threshold in the likelihoods  $Q_{\chi^2}(1 - \alpha, DF)$ , which represents the  $(1 - \alpha)$  quantile of the  $\chi^2$ -distribution with  $DF$  degrees of freedom. As we aim to compute the confidence bound of each individual parameter, the degree of freedom in this case is equal to 1. The  $(1 - \alpha)$  confidence interval (CI) of a single parameter  $\theta_l$ ,  $l \in \{1, \dots, N_p\}$ , encloses a set of parameter values  $\nu$  and is defined as

$$\text{CI}_{(1-\alpha)}^{\theta_l} = \{\nu \mid \Delta\chi_{\theta_l}^2(\nu) \leq Q_{\chi^2}(1 - \alpha, 1)\}, \quad (3.21)$$

with

$$\begin{aligned} \Delta\chi_{\theta_l}^2(\nu) &= \min_{\{\theta_k \mid k=1, \dots, N_p; k \neq l\}} (\chi^2(\theta_1, \dots, \theta_{l-1}, \nu, \theta_{l+1}, \dots, \theta_{N_p})) \\ &\quad - \min_{\{\theta_k \mid k=1, \dots, N_p\}} (\chi^2(\theta_1, \dots, \theta_{N_p})). \end{aligned} \quad (3.22)$$

To compute

$$\min(\chi_{\theta_l}^2) := \min_{\{\theta_k \mid k=1, \dots, N_p; k \neq l\}} (\chi^2(\theta_1, \dots, \theta_{l-1}, \nu, \theta_{l+1}, \dots, \theta_{N_p})) \quad (3.23)$$

from equation (3.22), we fix the parameter  $\theta_l$ ,  $l \in \{1, \dots, N_p\}$  systematically to different values  $\nu$  around the estimated optimum and solve the minimization problem with respect of the remaining parameters  $\{\theta_k \mid k = 1, \dots, N_p; k \neq l\}$ . Afterwards, the term  $\Delta\chi_{\theta_l}^2(\nu)$  (cf. (3.22)) is obtained by subtracting the fitted  $\chi^2$ -value minimized over all parameters (3.20) from the calculated  $\min(\chi_{\theta_l}^2)$ -value. The most common confidence regions  $\text{CI}_{95\%}$  and  $\text{CI}_{68\%}$  follow from equation (3.21) by taking into account the corresponding quantiles of the  $\chi^2$ -distribution  $Q_{\chi^2}(95\%, 1) = 3.8$  and  $Q_{\chi^2}(68\%, 1) = 1$ , respectively. By plotting  $\Delta\chi_{\theta_l}^2(\nu)$  and detecting those values  $\nu$  for which  $\Delta\chi_{\theta_l}^2$  remain below the respective quantile-based thresholds, the confidence intervals can be determined directly from the graph of the profile likelihood.

The application of the profile likelihood method for our model regarding the parameters that were estimated based on the kinetic DENV-wt data set shown in Figure 3.18, reveals that all these parameters are identifiable within narrow confidence bounds (Figure 3.19 and Table 3.2). Since the model is constrained by experimental DENV-wt data, we can utilize it to make quantitative predictions about the competition between spreading DENV and IFN-induced antiviral protection.

To validate the parameterization, we examine whether key parameter values are consistent with the results of independent measurements. Since we suspect that timing is an important factor in the antiviral immune defense, our focus lies on the estimates of the three time delays.

The determined delay of virus replication  $\tau_R$  of 24 h (cf. Figure 3.19, first profile likelihood in the upper row and Table 3.2) is mainly influenced by fitting the virus replicating cells  $I_R(t)$  to the DENV-faR-wt positive IFIT1 reporter cells after low dose infection (cf. (RO3) on page 83 and Figure 3.18(3)). Thus,  $\tau_R$  should comply with the mean expression onset of virus replication in individual IFIT1-deGFP reporter cells after infection with DENV-faR-wt at a low MOI, which was independently monitored by live-cell imaging (cf. Figure 3.10B). In this time-lapse microscopy experiment DENV-faR-wt<sup>+</sup> reporter cells became visible in the time

### 3. Viral spread is mainly controlled by the autocrine effect of rapidly produced IFN

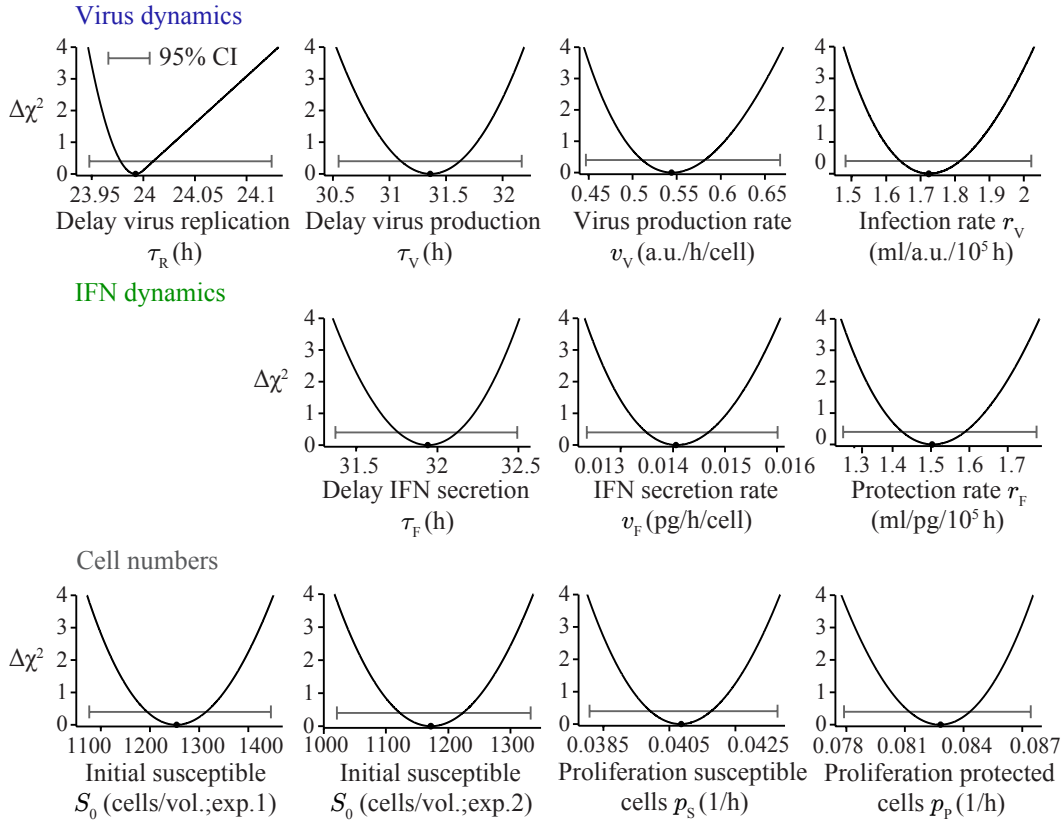


**Figure 3.19.:** Profile likelihoods demonstrate that the model parameters are identified by DENV-wt data. The profile likelihood method is applied to determine the 95% confidence interval (CI) of all model parameters, which are estimated using the kinetic DENV-wt data set shown in Figure 3.18 (cf. Table 3.2). The plots illustrate the change of the  $\chi^2$ -function ( $\Delta\chi^2$ , y-axis) of the indicated parameter (x-axis) calculated according to equation (3.22). Abbreviations: arbitrary units (a.u.), experiment (exp.), hours (h), milliliter (ml), picogram (pg), volume (vol.; 100  $\mu$ l).

period between [22.0 h p.i.; 68.0 h p.i.] with a mean onset of 32.2 h post infection. Hence, the time delay  $\tau_R$  corresponds to the initial rather than the average onset of virus replication in real time at single-cell level.

For testing the estimated delay of virus production  $\tau_V = 31.4$  h (cf. Figure 3.19, second profile likelihood in the upper row and Table 3.2), we relate this time delay to the half-time of DENV particle release after high dose infection quantified at high temporal resolution by TCID<sub>50</sub> assay (cf. blue curve in Figure 3.7). A direct comparison demonstrates that the predicted time delay  $\tau_V$  accurately reflects the measured half-time of  $\sim 32$  h (Figure 3.20A). Moreover, the single-step growth curves in the upper panel of Figure 3.7 enable us to extrapolate the first appearance of replicated viral RNA and released DENV in a heavily infected cell population. Although these approximated values of  $\sim 8$  h and  $\sim 14$  h for the onset of virus replication and DENV production, respectively, are much shorter than the respective model estimates, the time difference of  $\sim 6$  h between the two events agrees with the predicted lag of  $\tau_V - \tau_R = 31.4 - 24 = 7.4$  h. The consistency between the predicted and detected mean latency of virus production post infection as well as after onset of virus repli-

### 3.3. Parameterization of the delay differential equation model

Model parameter	Value [95% CI]	
<b>Virus dynamics</b>		
Initial viral load	$V_0$	1500 a.u./ml
Delay of virus replication	$\tau_R$	24.0[23.9;24.1] h
Delay of virus production	$\tau_V$	31.4[30.6;32.2] h
Virus production rate	$v_V$	0.54[0.45;0.67] a.u./h/cell
Infection rate	$r_V$	$1.7 \times 10^{-5}$ [ $1.5 \times 10^{-5}$ ; $2.0 \times 10^{-5}$ ] ml/a.u./h
Virus degradation rate	$d_V$	0.4/h
<b>IFN dynamics</b>		
Delay of IFN secretion	$\tau_F$	31.9[31.4;32.5] h
IFN secretion rate	$v_F$	0.014[0.012;0.016] pg/h/cell
Protection rate	$r_F$	$1.5 \times 10^{-5}$ [ $1.3 \times 10^{-5}$ ; $1.8 \times 10^{-5}$ ] ml/pg/h
IFN degradation rate	$d_F$	0.15/h
<b>Cell numbers</b>		
Initial susceptible cells (exp. 1)	$S_0$	12540 [10760;14460] cells/ml
Initial susceptible cells (exp. 2)	$S_0$	11720 [10210;13330] cells/ml
Proliferation rate susceptible cells	$p_S$	0.041[0.038;0.044] 1/h
Proliferation rate protected cells	$p_P$	0.083[0.078;0.087] 1/h

**Table 3.2.:** Model parameter estimates of the population-based DDE model. According to the biological meaning of the model parameters (cf. section 3.2), we estimate the parameter values as depicted in section 3.3.1 by considering only experiments regarding DENV-wt infection. Given are the best fit values and the 95% confidence intervals (calculated with the profile likelihood method) after fitting the model to the time-resolved data set shown in Figure 3.18 using a fixed initial viral load along with separately determined values for virus and IFN degradation rates. All model simulations concerning DENV-wt refer to this parameter set. Abbreviations: arbitrary units (a.u.), confidence interval (CI), experiment (exp.), hours (h), milliliter (ml), picogram (pg).

ation is especially noteworthy, since the DDE system as a whole was fitted without using data of extracellular virus dynamics (cf. Figure 3.18).

Furthermore, the single-step growth curve of secreted IFN- $\lambda$  after infection with DENV-faR-wt at a high MOI (cf. dark green curve in Figure 3.7) can serve as a control experiment for the determined delay of IFN secretion  $\tau_F = 31.9$  h (cf. Figure 3.19, first profile likelihood in the second row and Table 3.2). Comparing  $\tau_F$  with the measured halftime of IFN- $\lambda$  release of  $\sim 26.5$  h, we found that the model prediction provides a reasonably close approximation (Figure 3.20B).

As already mentioned in section 3.2, the single-step growth curves in Figure 3.7 illustrate the temporal distribution of heterogeneous single-cell behavior, which we approximated by constant time delays. However, the fact that the fixed time delays of the parameterized model match independently observed delays, confirms the ability of our model to make quantitative predictions of cell population dynamics.

In addition to the time delays, we also examine the parameterized IFN response in the model using a previously described IFN stimulation experiment, in which A549 IFIT1-deGFP reporter cells were treated with IFN- $\lambda$  (cf. green curve in Figure 3.8B).

### 3. Viral spread is mainly controlled by the autocrine effect of rapidly produced IFN

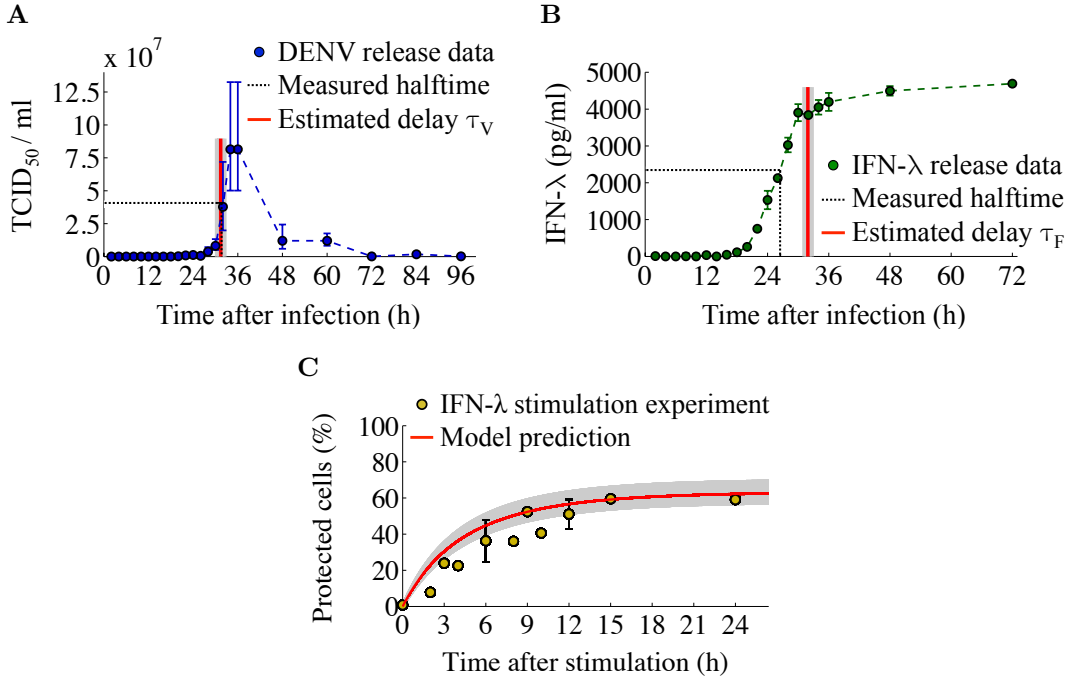


**Figure 3.20.:** The estimated parameter values of virus production time, IFN secretion delay and IFN response agree with independently measured key data. (A, B) IFN-competent A549 cells were infected with DENV-faR-wt at a MOI of 10 and analyzed at the indicated time points post infection. (A) Extracellular virus (blue color) was detected by TCID<sub>50</sub> assay. Highlighted are the observed half-time of ~ 32 h (dashed black line) and the estimated delay of virus production  $\tau_V = 31.4$  h (red line with shaded 95% confidence interval [30.6 h; 32.2 h]; data replotted from Figure 3.7 on linear scale). (B) Extracellular IFN- $\lambda$  (dark green color) was quantified by ELISA. Marked are the observed half-time of ~ 26.5 h (dashed black line) and the estimated delay of IFN secretion  $\tau_F = 31.9$  h (red line with shaded 95% confidence region [31.4 h; 32.5 h]; data replotted from Figure 3.7). (C) A549 IFIT1-deGFP reporter cells were stimulated with 10 ng/ml IFN- $\lambda$  and subjected to flow cytometry at the displayed times after treatment. Plotted are the experimentally observed rise in IFIT1-deGFP<sup>+</sup> cells (yellow dots) and the predicted increase in protected cells (red line with shaded 95% confidence bound) simulated with the submodel (3.24) by assuming an initial stimulation with IFN (data replotted from Figure 3.8B). (Experiments by B. Schmid and R. Bartenschlager)

To imitate the initial conditions of this experiment, we consider a number of susceptible cells  $S_0$  along with the applied extracellular IFN concentration  $F_0 = 10$  ng/ml. When simulating the IFN response, we assume that the recognition of extracellular IFN  $F$  turn susceptible cells  $S$  into protected cells  $P$  with the protection rate  $r_F$ . The removal of IFN by cellular uptake and, to a lesser extent, by extracellular degradation is taken into account through the IFN degradation rate  $d_F$ . The dynamics of this small submodel at time  $t \in \mathbb{R}$  is defined by the following ODE system:

$$\begin{aligned}
 \dot{S}(t) &= -r_F F(t) S(t) & S(0) &= S_0 \\
 \dot{P}(t) &= r_F F(t) S(t) & P(0) &= 0 \\
 \dot{F}(t) &= -d_F F(t) & F(0) &= F_0.
 \end{aligned} \tag{3.24}$$

### 3.3. Parameterization of the delay differential equation model

We fix  $S_0, r_F$  and  $d_F$  to the fitted values given in Table 3.2. The ODE system (3.24) was then solved using a standard ODE solver of Matlab based on explicit Runge-Kutta method (Bogacki and Shampine 1989, Shampine and Reichelt 1997). The direct comparison shows a good agreement between the predicted fraction of protected cells and the observed IFN-responding cells (Figure 3.20C). This test indicates that the parameterized model describes the IFN response correctly and, additionally, underscores the accuracy of the estimated protection rate  $r_F$ .

Taken together, the validity of the model is corroborated by the parameterization within narrow confidence intervals from DENV-wt data and, additionally, by the consistency with key results obtained in independent experiments that were not utilized for model fitting.

#### 3.3.2. Detection of DENV mutant specific model parameters by utilizing the knowledge from DENV-wt fitting

In order to analyze the differences between DENV-wt and attenuated DENV-E217A mutant infections on a quantitative level, we utilize the population-based model parameterized exclusively with DENV-wt data (cf. section 3.3.1) to identify DENV-E217A mutant specific parameters, which are able to describe the observed population dynamics after DENV-faR-E217A mutant infection (cf. Figure 3.14B and 3.15).

Motivated by findings from the literature, we argue that four parameters might vary between DENV-wt and DENV-E217A mutant infections. Since studies demonstrate that IFIT1 inhibits translation of mutant RNA (Pichlmair et al. 2011, Habjan et al. 2013), the generation of new infectious virus particles could take longer or occur at a lower rate after infection with DENV-E217A mutant. Moreover, as other reports show that 2'-O-unmethylated RNA is detected more readily by intracellular pattern recognition receptors (Züst et al. 2011), infected cells might also produce IFN faster or to a larger extent.

For the parameter optimization regarding DENV-E217A mutant infection, we take advantage of the established DENV-wt parameter set (cf. Table 3.2) and estimate only the four just mentioned potentially DENV-E217A mutant specific parameters (MP) in line with the respective constraints:

- (MP1) Delay of mutant virus production  $\tau_{Vmut} > \tau_R$
- (MP2) Mutant virus production rate  $v_{Vmut} \leq v_V$
- (MP3) Delay of IFN secretion after mutant virus infection  $\tau_{Fmut}$
- (MP4) IFN secretion rate after mutant virus infection  $v_{Fmut} \geq v_F$ .

In the same way as in the DENV-wt case, we determine the DENV-E217A mutant specific parameters (MP1)–(MP4), by fitting the model dynamics listed in (RO2)–(RO5) (cf. section 3.3.1 page 82) simultaneously to the related time-resolved data set consisting of two independent flow cytometry measurements along with ELISA

### 3. Viral spread is mainly controlled by the autocrine effect of rapidly produced IFN

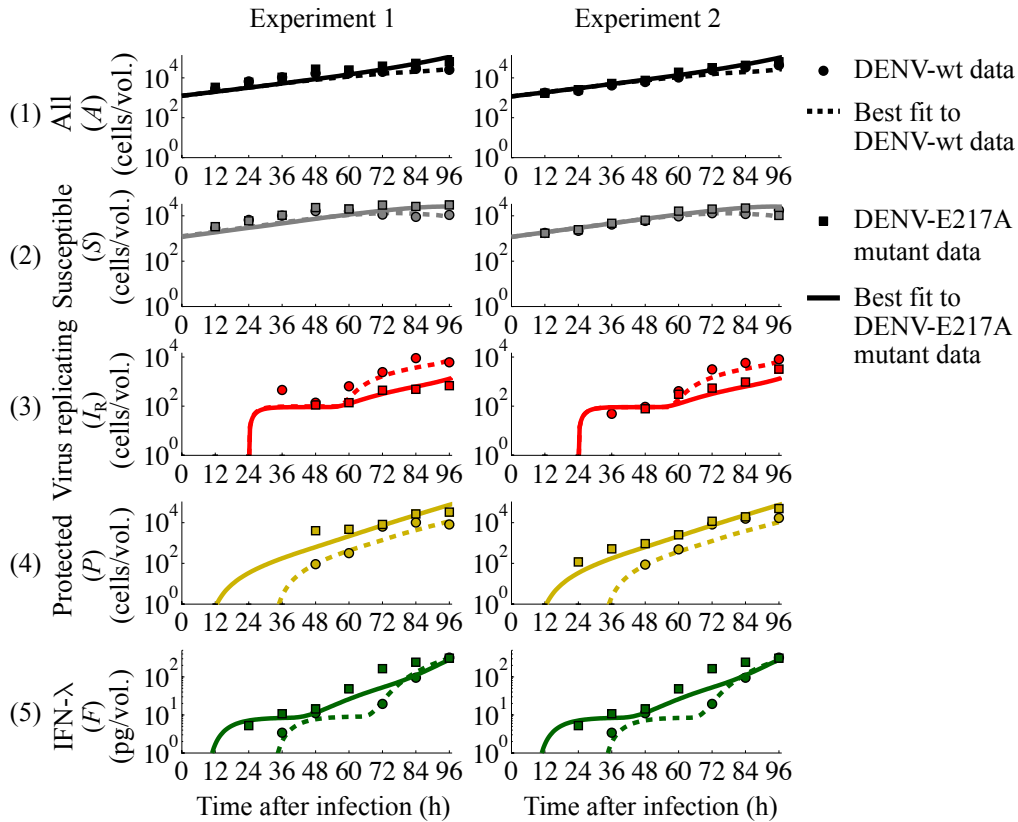


**Figure 3.21.:** Best fit of the mathematical model to two independent experiments concerning DENV-faR-E217A mutant infection by utilizing the DENV-wt parameter estimates. Initially, the model simulations concerning DENV-wt (dashed lines) are fitted to the respective time-resolved DENV-wt data (circles). The resulting DENV-wt parameter estimates (cf. section 3.3.1 and Table 3.2) are used to optimize the DENV-E217A mutant specific parameters (MP1)–(MP4) (cf. page 89) by fitting the model dynamics regarding DENV-E217A mutant (solid lines) simultaneously to the related DENV-E217A mutant kinetics (squares) of both independent experiments. For parameter optimization we compare simulated with observed cell dynamics of (1) all (as control), (2) susceptible IFIT1-deGFP – DENV-faR double-negative, (3) virus replicating DENV-faR positive as well as (4) protected IFIT1-deGFP<sup>+</sup> – DENV-faR<sup>-</sup> cells along with (5) IFN- $\lambda$  release after infection of A549 IFIT1-deGFP reporter cells with DENV-faR at a MOI of 0.1. The best fit is obtained by applying a trust-region-reflective least-squares algorithm with at least  $5 \times 10^3$  different random initial values. The data set is based on two independently performed flow cytometry measurements (cf. Figure 3.14), while IFN- $\lambda$  was quantified in experiment 2 by ELISA (cf. Figure 3.15). Absolute cell numbers can be considered as a volume (vol.) of 100  $\mu$ l was consistently analyzed. (Experiments by B. Schmid and R. Bartenschlager)

quantifications post DENV-faR-E217A mutant infection (Figure 3.21(2)–(5)).

We repeated the optimization procedure for more than  $5 \times 10^3$  different random initial values in the same way as for the data concerning DENV-wt. The obtained best fit provides a good match with the observed kinetics after DENV-faR-E217A mutant infection of both experiments (Figure 3.21).

Again, applying the profile likelihood method, we calculate the 95% confidence in-

### 3.3. Parameterization of the delay differential equation model

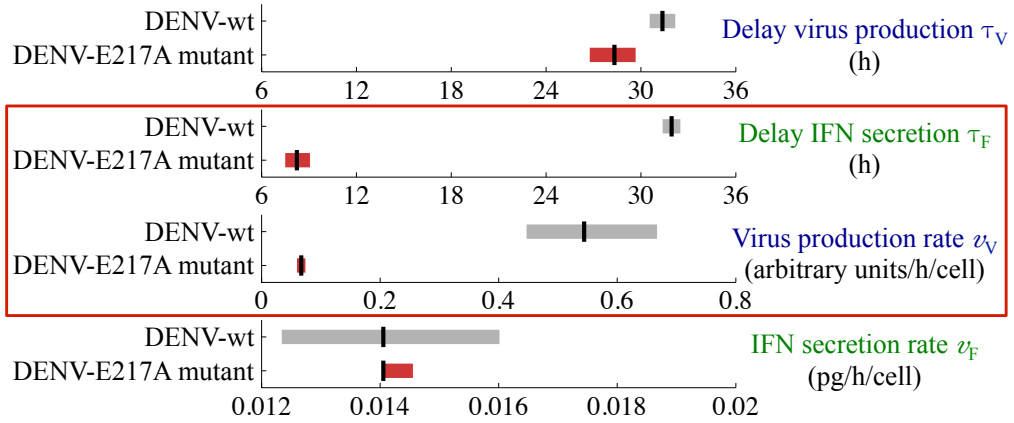


**Figure 3.22.:** The difference between DENV-wt and attenuated DENV-E217A mutant infection is mainly based on an accelerated IFN induction and decreased virus production triggered by the E217A mutant. The direct comparison of the estimated best fit values (vertical black lines) and the corresponding 95% confidence intervals (bands; calculated with the profile likelihood method) of the four model parameters (right y-axis), which have been allowed to differ between DENV-wt and DENV-E217A mutant infection (left y-axis) demonstrates that only the delay of IFN secretion  $\tau_F$  and the virus production rate  $v_V$  differ considerably (framed in dark red color).

tervals of the estimated DENV-E217A mutant specific parameters (MP1)–(MP4) according to (3.21). The resulting narrow confidence bounds confirm the identifiability of all four parameters. More importantly, the comparison of the confidence regions reveals that only two of the four DENV-E217A mutant specific parameters differ strongly from their DENV-wt values: The delay of IFN secretion is  $\sim 24$  h shorter and the virus production rate is  $\sim 8$ -fold lower after DENV-E217A mutant infection in contrast to DENV-wt (Table 3.3 and Figure 3.22). While the estimated delays for virus production and IFN secretion are almost identical after DENV-wt infection, IFN release takes place well before virus production in DENV-E217A mutant infected cells.

Both identified DENV-E217A mutant specific parameters could contribute to the observed attenuated spread of the E217A mutant, but their relative importance is still open. Indeed, the IFN production delay  $\tau_F$  and the virus production rate  $v_V$  might not be independent parameters as virus replication could be inhibited by autocrine IFN in a time-dependent manner (cf. Figure 3.5). To account for this effect, we extend the mathematical model in the following section 3.4. Using this extended version of the model, we will analyze the antiviral effect of  $\tau_F$  and  $v_V$  in detail in section 3.5.

3. *Viral spread is mainly controlled by the autocrine effect of rapidly produced IFN*

Model parameter		Value [95% CI]
<b>Virus dynamics</b>		
Delay of virus production (DENV-wt)	$\tau_V$	31.4[30.6;32.2] h
Delay of virus production (E217A mutant)	$\tau_{Vmut}$	28.3[26.8;29.7] h
Virus production rate (DENV-wt)	$v_V$	0.540[0.45;0.670] a.u./h/cell
Virus production rate (E217A mutant)	$v_{Vmut}$	0.067[0.06;0.074] a.u./h/cell
<b>IFN dynamics</b>		
Delay of IFN secretion (DENV-wt)	$\tau_F$	31.9[31.4;32.5] h
Delay of IFN secretion (E217A mutant)	$\tau_{Fmut}$	8.2[ 7.5; 9.1] h
IFN secretion rate (DENV-wt)	$v_F$	0.014[0.012;0.016] pg/h/cell
IFN secretion rate (E217A mutant)	$v_{Fmut}$	0.014[0.014;0.015] pg/h/cell

**Table 3.3.:** Optimized model parameters of the population-based DDE model which differ between DENV-wt and DENV-E217A mutant infection. After the model parameterization by considering only DENV-wt related experiments (cf. section 3.3.1 and Table 3.2), data concerning DENV-E217A mutant infection are fitted by allowing only four parameters to differ between DENV-wt and DENV-E217A mutant (cf. section 3.3.2). Given are the best fit values and the 95% confidence intervals (calculated with the profile likelihood method) of these four infection specific parameters after fitting the model to the time-resolved data set shown in Figure 3.21. Abbreviations: arbitrary units (a.u.), confidence interval (CI), DENV-E217A mutant (mut), hours (h), picogram (pg).

### 3.4. Extension of the population-based model to elucidate the autocrine and paracrine effects of IFN

The prediction of the data-driven quantitative model that a decreased virus production and accelerated IFN induction make the difference between DENV-wt and the attenuated DENV-E217A mutant (cf. Figure 3.22), raises the questions how much impact either factor individually has on the outcome of infection, or even if the two factors are possibly related to each other. The latter question is prompted by our observation that stimulation of infected cells with IFN in an early phase after infection causes a reduction of virus replication and consequently virus production (cf. Figure 3.5). However, this autocrine effect of IFN must be temporally limited, since stimulation with IFN has no further influence after a certain time period post infection.

To analyze explicitly the impact of IFN on infected cells, we expand our established model (3.11) by assuming that recognition of IFN with the rate  $r_P$ , in the time window of IFN responsiveness  $\tau_P$  after viral entry, inhibits the production of new infectious virus particles (Figure 3.23, solid green inhibition link). Technically, we calculate the probability of infected cells to sense secreted IFN in the time period  $\tau_P$  after viral entry by applying a technique from the field of the survival analysis (Cox and Oakes 1984, Dobson 2001, Rodríguez 2007).

For this purpose we first consider a non-negative, continuous random variable  $T$ , which represents the waiting time until an infected cell recognizes IFN. The cumulative distribution function (CDF) of  $T$  is defined by

$$CDF_T(\tilde{t}) = \mathcal{P}(T \leq \tilde{t}) \quad (3.25)$$

$$\stackrel{\substack{T \text{ continuous} \\ \text{and non-negative}}}{=} \int_0^{\tilde{t}} f_T(x) dx, \quad (3.26)$$

where  $f_T$  is the density function of  $T$ . The  $CDF_T$  describes the probability  $\mathcal{P}$  to recognize IFN within the time span  $\tilde{t} \in \mathbb{R}_{\geq 0}$ .

Accordingly, the complement of  $CDF_T$

$$\mathcal{Z}_T(\tilde{t}) = 1 - CDF_T(\tilde{t}) \quad (3.27)$$

$$\stackrel{(3.25)}{=} \mathcal{P}(T > \tilde{t}) \quad (3.28)$$

$$\stackrel{(3.26)}{=} \int_{\tilde{t}}^{\infty} f_T(x) dx,$$

with the initial condition

$$\mathcal{Z}_T(0) = 1, \quad (3.29)$$

is the probability that IFN was not sensed within the time period  $\tilde{t}$ .  $\mathcal{Z}_T$  is known as the “survival function” and has the derivative

$$\mathcal{Z}'_T(\tilde{t}) = -f_T(\tilde{t}). \quad (3.30)$$

### 3. Viral spread is mainly controlled by the autocrine effect of rapidly produced IFN

In addition, we need the so-called hazard function, which is the time-dependent probability rate of recognizing IFN in an infinitesimally small time interval  $[\tilde{t}; \tilde{t} + d\tilde{t}]$  under the condition that there was no stimulation through IFN up to time  $\tilde{t}$ . The hazard function is generally defined by

$$\begin{aligned}
h(\tilde{t}) &= \lim_{d\tilde{t} \rightarrow 0} \left( \frac{\mathcal{P}(\tilde{t} \leq T < \tilde{t} + d\tilde{t} \mid T \geq \tilde{t})}{d\tilde{t}} \right) \\
&= \lim_{d\tilde{t} \rightarrow 0} \left( \frac{\mathcal{P}(\tilde{t} \leq T < \tilde{t} + d\tilde{t} \cap T \geq \tilde{t})}{d\tilde{t}} \right) \frac{1}{\mathcal{P}(T \geq \tilde{t})} \\
&\stackrel{T \text{ continuous}}{=} \lim_{d\tilde{t} \rightarrow 0} \left( \frac{\mathcal{P}(\tilde{t} \leq T < \tilde{t} + d\tilde{t})}{d\tilde{t}} \right) \frac{1}{\mathcal{Z}_T(\tilde{t})} \\
(3.28) & \\
&\stackrel{T \text{ continuous}}{(3.25)} \lim_{d\tilde{t} \rightarrow 0} \left( \frac{CDF_T(\tilde{t} + d\tilde{t}) - CDF_T(\tilde{t})}{d\tilde{t}} \right) \frac{1}{\mathcal{Z}_T(\tilde{t})} \\
&= \frac{CDF'_T(\tilde{t})}{\mathcal{Z}_T(\tilde{t})} \\
(3.26) & \\
&\stackrel{=}{=} \frac{f_T(\tilde{t})}{\mathcal{Z}_T(\tilde{t})} \\
(3.30) & \\
&\stackrel{=}{=} -\frac{\mathcal{Z}'_T(\tilde{t})}{\mathcal{Z}_T(\tilde{t})}. \tag{3.31}
\end{aligned}$$

In order to obtain a formula of  $\mathcal{Z}_T$  depending on the hazard function we reformulate equation (3.31) by integrating both sides:

$$\begin{aligned}
h(\tilde{t}) &= -\frac{\mathcal{Z}'_T(\tilde{t})}{\mathcal{Z}_T(\tilde{t})} \\
\iff h(\tilde{t}) &= -\frac{d}{d\tilde{t}} \ln(\mathcal{Z}_T(\tilde{t})) \\
\iff \int_0^{\tilde{t}} h(x) dx &= -(\ln(\mathcal{Z}_T(\tilde{t})) - \ln(\mathcal{Z}_T(0))) \\
(3.29) \iff -\int_0^{\tilde{t}} h(x) dx &= \ln(\mathcal{Z}_T(\tilde{t})) \\
\iff \mathcal{Z}_T(\tilde{t}) &= \exp\left(-\int_0^{\tilde{t}} h(x) dx\right). \tag{3.32}
\end{aligned}$$

In our case, the probability rate of recognizing IFN is given by

$$h(t) = r_P F(t), \tag{3.33}$$

where  $r_P$  denotes the rate of IFN-induced inhibition of virus production and  $F(t)$  is the time-dependent amount of extracellular IFN (cf. Figure 3.23, solid green inhibition link).

The distinction whether or not an infected cell is stimulated by IFN within the time window  $\tau_P$  after the time point of infection  $t_I \geq 0$  (Figure 3.24) is relevant at the

### 3.4. Model extension to elucidate the autocrine and paracrine effects of IFN

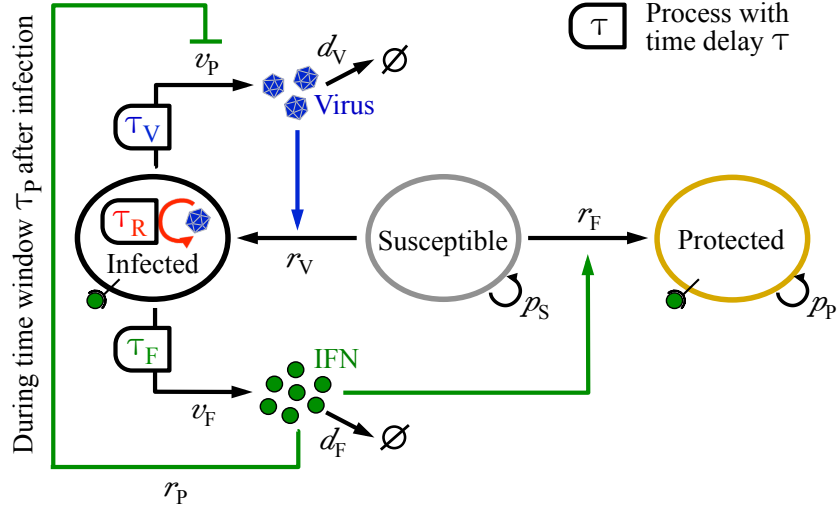


**Figure 3.23.:** Scheme of the full population-based model, which describes the competition between spreading virus and the antiviral immune response induced in a paracrine and temporally limited autocrine manner by secreted IFN. Susceptible cells (gray oval) can become infected by extracellular virus with the infection rate  $r_V$  (blue arrow). Virus replication ( $\odot$ ) arises in infected cells (black oval) at time  $\tau_R$  after viral entry (red color) and results in virus production with the virus production rate  $v_P$  from time  $\tau_V > \tau_R$  onwards. Moreover, infected cells start to express IFN with the secretion rate  $v_F$  at time  $\tau_F$  post viral infection. Recognition of secreted IFN turn susceptible cells into protected cells (yellow oval) with the protection rate  $r_F$  (solid green arrow). In addition, sensing of IFN with the rate  $r_P$  in the time window  $\tau_P$  after viral entry inhibits virus production in infected cells (solid green inhibition link). Extracellular virus and IFN are removed ( $\emptyset$ ) by cellular uptake as well as extracellular degradation with the rate constant of virus degradation  $d_V$  and the rate constant of IFN degradation  $d_F$ . While propagation is inhibited in infected cells, susceptible and protected cells proliferate ( $\odot$ ) with the rates  $p_S$  and  $p_P$ , respectively.

time

$$\begin{aligned} t &= t_I + \tau_V \\ \iff t - \tau_V &= t_I. \end{aligned} \quad (3.34)$$

Therefore, we compute the probability that IFN is not recognized up to the time

$$t_I + \tau_P \stackrel{(3.34)}{=} t - \tau_V + \tau_P \quad (3.35)$$

under the condition that there was no stimulation through IFN before the time point of viral entry. The condition is necessary, since sensing of IFN before infection leads to antiviral protection in our model. The probability of an infected cell to produce virus without antiviral IFN action is thus calculated as

$$\begin{aligned} \mathcal{P}(T > t_I + \tau_P \mid T > t_I) &\stackrel{(3.35)}{=} \mathcal{P}(T > t - \tau_V + \tau_P \mid T > t - \tau_V) \\ &\stackrel{(3.34)}{=} \frac{\mathcal{P}(T > t - \tau_V + \tau_P \cap T > t - \tau_V)}{\mathcal{P}(T > t - \tau_V)} \\ &= \frac{\mathcal{P}(T > t - \tau_V + \tau_P)}{\mathcal{P}(T > t - \tau_V)} \end{aligned}$$

3. Viral spread is mainly controlled by the autocrine effect of rapidly produced IFN

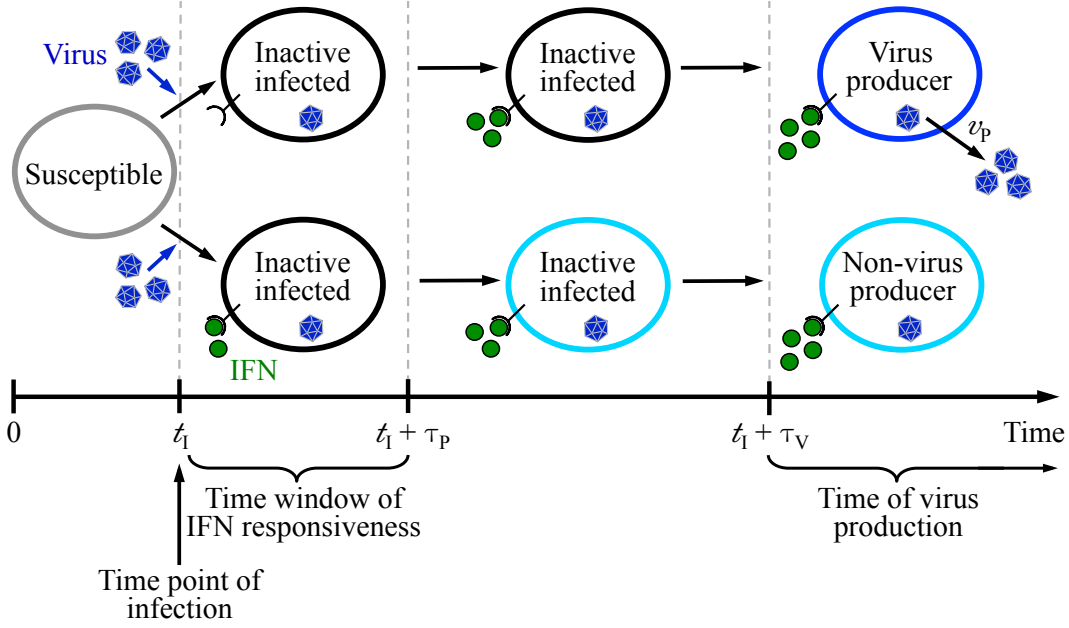


**Figure 3.24.:** Scheme of the modeled antiviral effect of IFN on already infected cells. To incorporate in our model an antiviral impact of IFN on infected cells, we assume after the time point of infection  $t_1$  of susceptible cells (gray oval) an IFN responsive time window  $\tau_P$ . Inactive infected cells (black oval), which receive no IFN stimulus in the time interval  $[t_1; t_1 + \tau_P]$  become at  $t_1 + \tau_V$  virus producing cells (dark blue oval) and release new infectious viral particles with the rate constant  $v_P$  (upper sequence). In contrast, virus production is inhibited in inactive infected cells, which recognize IFN in the time frame  $[t_1; t_1 + \tau_P]$  (light blue oval; lower sequence).

$$\begin{aligned}
 & \stackrel{(3.28)}{=} \frac{\mathcal{Z}_T(t - \tau_V + \tau_P)}{\mathcal{Z}_T(t - \tau_V)} \\
 & \stackrel{(3.32)}{=} \exp\left(-\int_0^{t - \tau_V + \tau_P} h(x) dx\right) \exp\left(\int_0^{t - \tau_V} h(x) dx\right) \\
 & \stackrel{(3.33)}{=} \exp\left(-\int_0^{t - \tau_V + \tau_P} r_P F(x) dx\right) \exp\left(\int_0^{t - \tau_V} r_P F(x) dx\right) \\
 & = \exp\left(-r_P \int_{t - \tau_V}^{t - (\tau_V - \tau_P)} F(x) dx\right) \\
 & = \exp(r_P [\mathcal{F}(t - \tau_V) - \mathcal{F}(t - (\tau_V - \tau_P))]), \quad (3.36)
 \end{aligned}$$

where  $\mathcal{F}$  denotes the antiderivative of  $F$ .

The probability (3.36) enables us to discriminate between infected cells  $I_{V\bar{P}}$ , which receive no IFN stimulus and thus produce virus with the rate constant  $v_P$  after  $\tau_V$ , and infected, non-virus producing cells  $I_{VP}$ , which recognize IFN within the time window  $\tau_P$  (cf. Figure 3.24). Accordingly, we include  $I_{V\bar{P}}$ ,  $I_{VP}$  and  $\mathcal{F}$  in our DDE model (3.11) and obtain the following DDE system with four time delays:

### 3.4. Model extension to elucidate the autocrine and paracrine effects of IFN

$$\begin{aligned}
\dot{S}(t) &= -r_V V(t)S(t) - r_F F(t)S(t) + p_S S(t) \\
\dot{I}_{\bar{R}}(t) &= r_V V(t)S(t) - r_V V(t - \tau_R)S(t - \tau_R) \\
\dot{I}_R(t) &= r_V V(t - \tau_R)S(t - \tau_R) \\
\dot{I}_{\bar{V}}(t) &= r_V V(t)S(t) - r_V V(t - \tau_V)S(t - \tau_V) \\
\dot{I}_{\bar{V}\bar{P}}(t) &= \exp(r_P [\mathcal{F}_1(t) - \mathcal{F}_2(t)]) r_V V(t - \tau_V)S(t - \tau_V) \\
\dot{I}_{VP}(t) &= (1 - \exp(r_P [\mathcal{F}_1(t) - \mathcal{F}_2(t)])) r_V V(t - \tau_V)S(t - \tau_V) \\
\dot{I}_{\bar{F}}(t) &= r_V V(t)S(t) - r_V V(t - \tau_F)S(t - \tau_F) \\
\dot{I}_F(t) &= r_V V(t - \tau_F)S(t - \tau_F) \\
\dot{P}(t) &= r_F F(t)S(t) + p_P P(t) \\
\dot{F}(t) &= v_F I_F(t) - d_F F(t) \\
\dot{\mathcal{F}}_1(t) &= F(t - \tau_V) \\
\dot{\mathcal{F}}_2(t) &= F(t - (\tau_V - \tau_P)) \\
\dot{V}(t) &= v_P I_{\bar{V}\bar{P}}(t) - d_V V(t).
\end{aligned} \tag{3.37}$$

The initial value problem corresponding to the extended model is defined by the DDE system (3.37) for time  $t \in [t_0, t_{\text{end}}]$  together with initial conditions, which we specify in the following. In analogy to the DDE system (3.11), only the initial number of susceptible cells  $S(0) = S_0$  and the initial extracellular viral load  $V(0) = V_0$  are non-zero at the starting time  $t_0 = 0$ . For those variables in (3.37) that have a delay argument, we use as history functions the constant zero function, that is,  $S(t) = 0$ ,  $V(t) = 0$  as well as  $F(t) = 0$  for all  $t < 0$ .

In a manner analogous to the investigation of the original DDE system (3.11), we can show that the initial value problem of the full DDE model (3.37) has a unique positive solution. To see this note that the condition (P5) of the positivity theorem (cf. page 79) can be verified by demonstrating (P5) for a closed subsystem of the extended DDE model (3.37) concerning the state variable  $\tilde{y} = (S, I_R, I_{\bar{V}\bar{P}}, I_{VP}, I_F, P, F, \mathcal{F}_1, \mathcal{F}_2, V)$ . In particular, the right-hand-side function of  $\dot{I}_{\bar{V}\bar{P}}$  fulfills (P5), as the exponential function is positive. To verify (P5) with respect to  $I_{VP}$ , we recall that the term  $\exp(r_P [\mathcal{F}_1(t) - \mathcal{F}_2(t)]) \in (0, 1]$ , as it represents the probability of an infected cell to produce virus without antiviral IFN action (cf. equation (3.36)).

To simulate the full DDE model (3.37), we utilize Matlab as a programming environment and solve the DDE system numerically by calling the RADAR5 solver written in ANSI Fortran-90 (Guglielmi and Hairer 2005) with a binary mex subroutine. For an increased accuracy of the numerical solution, we implement the time-dependent standard Jacobian matrix  $\mathcal{J}_{\text{full}}(t)$  and the Jacobian matrix with respect to the delayed variables  $\mathcal{J}_{\text{full},\tau}(t)$  within the RADAR5 code. Both Jacobian matrices are given in appendix A.2.

The results of the IFN-stimulation experiment depicted in Figure 3.5 indicate an IFN responsive time window  $\tau_P$  of approximately 6 h post infection with DENV-wt

### 3. Viral spread is mainly controlled by the autocrine effect of rapidly produced IFN

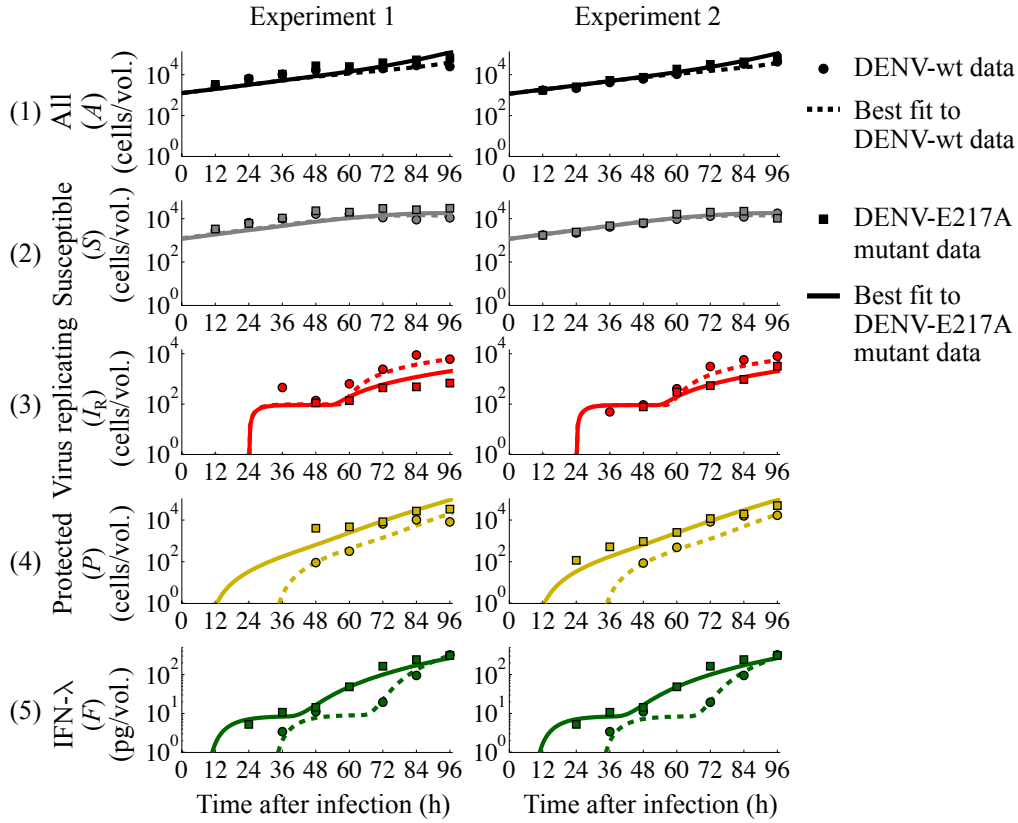


**Figure 3.25.:** The full model reproduces the observed dynamics of both DENV-wt and DENV-E217A mutant infections. The full model (3.37) can describe the data concerning DENV-wt (dashed lines and circles, respectively) and DENV-E217A mutant (solid lines and squares, respectively) infections, which were previously used to parameterize the original model (3.11). We compare simulated with observed cell dynamics of (1) all (as control), (2) susceptible IFIT1-deGFP – DENV-faR double-negative, (3) virus replicating DENV-faR positive as well as (4) protected IFIT1-deGFP<sup>+</sup> – DENV-faR<sup>-</sup> cells along with (5) IFN- $\lambda$  release after infection of A549 IFIT1-deGFP reporter cells with DENV-faR at a MOI of 0.1. The data set is based on two independently performed flow cytometry measurements (cf. Figure 3.14), while IFN- $\lambda$  was quantified in experiment 2 by ELISA (cf. Figure 3.15). Absolute cell numbers can be considered as a volume (vol.) of 100  $\mu$ l was consistently analyzed. The full model (3.37) is simulated with the additional parameter values given in Table 3.4 and the DENV-wt parameter estimates listed in Table 3.2 as well as the established DENV-E217A mutant specific parameter set shown in Table 3.3. (Experiments by B. Schmid and R. Bartenschlager)

at a MOI of 10. The infection with such a high viral dose causes a synchronized infection of the cell population. Since the delay of virus replication after a non-synchronized infection is expected to be delayed, we simulate low dose infections with a time window of IFN responsiveness of  $\tau_P = 8$  h. Additionally, we fix the rate of IFN-induced inhibition of virus production  $r_P = 10^4 r_F$ , as we suspect that restriction of virus replication is achieved faster than antiviral protection.

According to findings from the literature, IFIT1 is one of those ISGs that can be induced directly after viral recognition in an IFN-independent manner (Grandvaux et al. 2002, Diamond and Farzan 2013, Chen et al. 2013). An early IFN-independent

### 3.4. Model extension to elucidate the autocrine and paracrine effects of IFN

Model parameter	Value	
<b>Virus dynamics</b>		
Virus production rate (DENV-wt)	$v_P$	0.54 a.u./h/cell
Virus production rate (E217A mutant)	$v_{P_{mut}}$	0.27 a.u./h/cell
<b>IFN dynamics</b>		
Time window of IFN responsiveness	$\tau_P$	8 h
Rate of IFN-induced inhibition of virus production	$r_P$	0.15 ml/pg/h

**Table 3.4.:** Additional parameters of the full population-based model. The extended model (3.37) is simulated with the given additional parameter values and the DENV-wt parameter estimates listed in Table 3.2 as well as the established DENV-E217A mutant specific parameter set shown in Table 3.3. Abbreviations: arbitrary units (a.u.), DENV-E217A mutant (mut), hours (h), milliliter (ml), picogram (pg).

IFIT1 induction could thus also be contributing to the predicted decreased virus production in IFIT1 reporter cells after DENV-E217A mutant infection. Since we have no available data on the extent to which virus production of the DENV-E217A mutant is influenced by IFN-independent mechanisms in our system, we assume that virus producing cells release new infectious virus particles with the rate  $v_{P_{mut}} = 0.5 v_P$  after infection with the DENV-E217A mutant. Accordingly, the virus production rate of the E217A mutant represents half of the virus production rate  $v_P = v_V$  after infection with DENV-wt.

The simulation of the model (3.37) with the mentioned modifications listed in Table 3.4 shows that the simulated dynamics match the observed kinetics of both DENV-wt and DENV-E217A mutant infections equally well as the original model (3.11) (Figure 3.25).

In summary, the full model allows us to study the competition between spreading DENV and the antiviral immune response induced in an autocrine as well as paracrine manner by secreted IFN. Therefore we will utilize the model (3.37) in the following section 3.5 to analyze the relative importance of decreased virus production and accelerated IFN expression triggered by DENV-E217A mutant, taking into account the antiviral effect of IFN on infected and/or susceptible cells.

### 3.5. Quantitative modeling predicts effective limitation of viral spread by rapid autocrine IFN action on infected cells

The population-based model implies that there are two distinct waves of virus replication after DENV-wt infection (cf. Figure 3.18(3)). While the first wave corresponds to replication in cells that were initially infected, the second wave, starting at  $\sim 60$  h post infection, is most likely due to reinfection by spreading DENV-wt released from primary infected cells. In contrast to DENV-wt, virus replication resulting from secondary infection events of propagating DENV-E217A mutant is considerably weaker (cf. Figure 3.21).

The quantitative model explains the attenuated spread of the DENV-E217A mutant by two effects. First, virus production is reduced, and second, IFN induction is faster after infection with DENV-E217A mutant in comparison to DENV-wt (cf. Figure 3.22). To examine the individual impact of these two factors on viral spread, we simulate the outcome of DENV-wt infections for varying mutant specific parameter values (Figure 3.27) by considering the following three model variations (M1)–(M3) (Figure 3.26):

- (M1) The full model (3.37), which enables the simulation of the interaction between spreading DENV and the antiviral immune defense induced in an autocrine and paracrine way by released IFN (cf. Figure 3.26A and Figure 3.27 left column).
- (M2) A variation of the model to consider only the antiviral effect of autocrine IFN acting on DENV-infected cells. This model is simulated by setting the protection rate  $r_F$  to zero in (3.37) (cf. Figure 3.26B and Figure 3.27 middle column).
- (M3) The original model (3.11), which only regards the antiviral effect of paracrine IFN protecting susceptible cells against DENV infection (cf. Figure 3.26C and Figure 3.27 right column).

After simulating these combinations, we compare the relative change of the population structure consisting of susceptible, virus replicating and protected cells as well as the different amount of IFN and virus (cf. rows in Figure 3.27). For easier comparison, the color scales are normalized so that the result of the full model simulated with the determined DENV-wt parameter values (cf. Table 3.2 and 3.4) have value zero (cf. Figure 3.27, green color).

The simulations of the full model (M1) with varying mutant specific parameter values show that both the delay of IFN secretion  $\tau_F$  and the virus production rate  $v_P$  can independently control the fraction of susceptible as well as virus replicating cells and, consequently, the spread of IFN and virus. Moreover, the relative change of the protected cells implies the existence of a time limit for the delay of IFN secretion of  $\sim 24$  h. For longer latencies of IFN expression, protection is ineffective and the population is separated in susceptible as well as infected cells, depending of the virus

### 3.5. Modeling predicts effective limitation of viral spread by autocrine IFN action

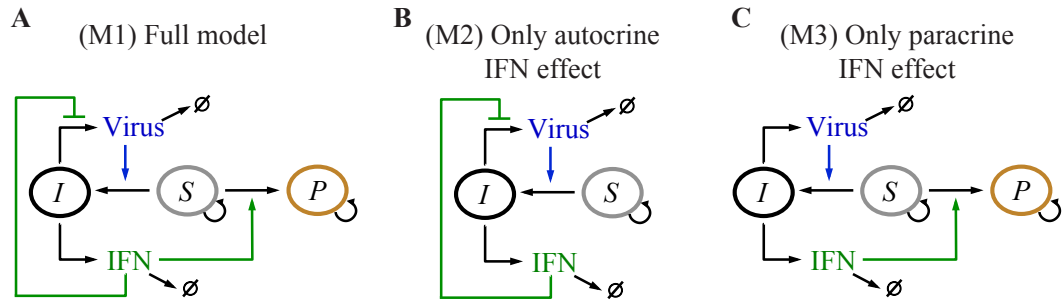


**Figure 3.26.:** Schemes of the three model variations (M1)–(M3). (A) The full model (M1) considers the autocrine and paracrine effect of IFN in an infected cell population: Susceptible cells  $S$  (gray oval) can become infected by extracellular virus (blue arrow). Virus replication in infected cells  $I$  (black oval) results in virus production and expression of IFN. Recognition of secreted IFN turn susceptible cells into protected cells  $P$  (yellow oval) (solid green arrow). In addition, sensing of IFN in an early phase after viral entry inhibits virus production in infected cells (solid green inhibition link). Extracellular virus and IFN are removed ( $\emptyset$ ) by cellular uptake as well as extracellular degradation. While propagation is inhibited in infected cells, susceptible and protected cells proliferate ( $\odot$ ). (B) In comparison to the full model, the model variant (M2) only considers the autocrine effect of IFN on infected cells. (C) Compared to the full model, the model variant (M3) only regards the antiviral effect of paracrine IFN protecting susceptible cells against viral infection.

production rate. Importantly, the IFN-independent reduction of virus production rate attenuates viral spread, but this attenuation is strongly enhanced by the rapid secretion of IFN. The control of the mutant specific parameters  $\tau_F$  and  $v_P$  over the amounts of susceptible cells, virus replicating cells, secreted IFN and extracellular virus still remains intact in the model variant (M2), where a solely autocrine effect of IFN is allowed. It is particularly notable that the simulations of the model (M2) concerning the number of virus replicating cells and the amount of produced virus look practically identical to the full model. The main difference is in the number of protected cells, but interestingly this has no strong effect on viral spread. In contrast to the models (M1) and (M2), the influence of IFN on viral spread largely disappears if IFN has only a paracrine effect. Moreover, the amount of extracellular virus in model (M3) illustrates a very high virus production, which by far exceeds that in the models with autocrine effect of IFN.

According to this analysis, the spread of the DENV-E217A mutant is mainly restricted through an autocrine effect of IFN on infected cells which causes a decreased virus production. Remarkably, the models predict that an increased paracrine effect due to accelerated IFN secretion would have very little effect on viral spread.

The measured population structures after infection with DENV-faR-wt or DENV-faR-E217A mutant illustrate the persistence of a large fraction of susceptible cells throughout the entire 4-day time course (Figure 3.28). The number of naïve cells remained even larger in the DENV-E217A mutant infected cell population, although IFN is induced faster after DENV-E217A mutant infection. This observation confirms the modeling prediction that viral spread is primarily limited by decreased virus production rather than by the effect of IFN to protect as many cells as possible.

3. Viral spread is mainly controlled by the autocrine effect of rapidly produced IFN

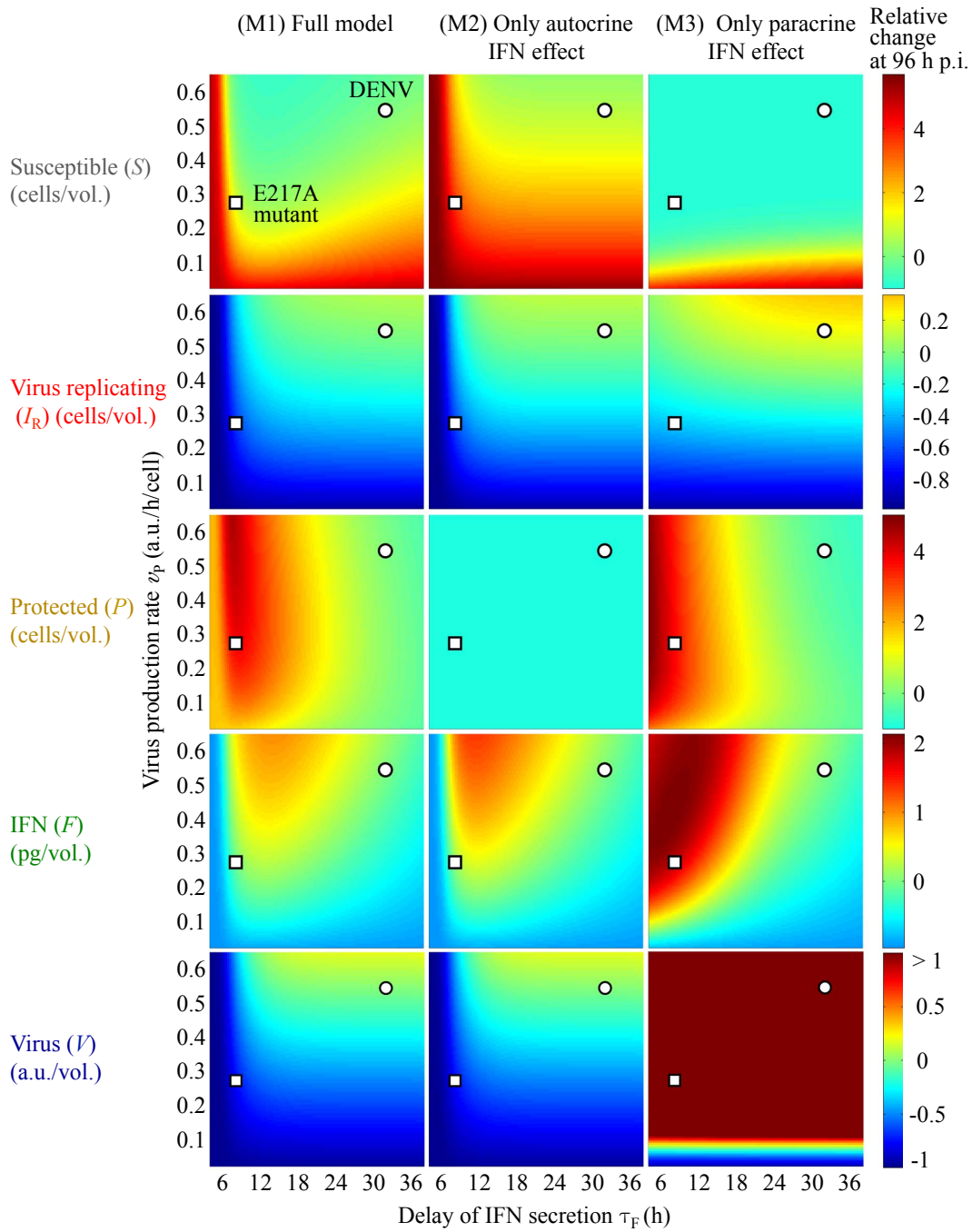


**Figure 3.27.:** Quantitative modeling predicts strong restriction of viral spread by a rapid autocrine effect of IFN on infected cells. DENV-wt infections are simulated with varying parameter values for the delay of IFN secretion  $\tau_F$  (x-axis) and virus production rate  $v_P$  (y-axis) by using the three model variations (M1)–(M3) (cf. page 100 and Figure 3.26). Shown is the relative change of susceptible  $S$ , virus replicating  $I_R$  and protected  $P$  cells as well as extracellular IFN  $F$  and virus  $V$  at 96 h post infection (arranged in rows). The relative values are obtained by scaling to the results of the full model simulated with the determined DENV-wt parameter values (white circles), so that these reference results have always value zero (green color). Values below or above the respective reference value are plotted in cool or warm colors, respectively. For the purpose of comparison, the results of the full model simulated with the DENV-E217A mutant parameter estimates are denoted through the white squares. Abbreviations: arbitrary units (a.u.), picogram (pg), volume (vol.; 100  $\mu$ l).

### 3.5. Modeling predicts effective limitation of viral spread by autocrine IFN action

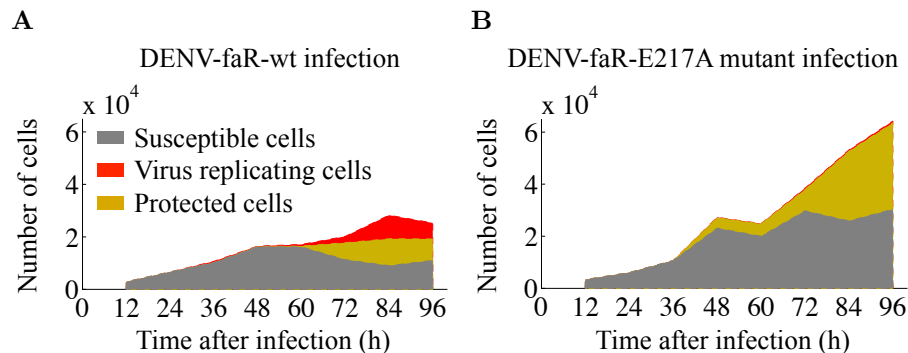


**Figure 3.28.:** A large proportion of the cell population remains susceptible after infection with DENV-wt or DENV-E217A mutant. (A, B) A549 IFIT1-deGFP reporter cells were infected with DENV-faR-wt (A) or DENV-faR-E217A mutant (B) at a MOI of 0.1. At the indicated time points post infection, cells were fixed and 100  $\mu$ l of the cell suspension was subjected to flow cytometry. The area plots represent the distribution of the observed population structure consisting of susceptible IFIT1-deGFP<sup>-</sup> DENV-faR double-negative (gray color), virus replicating DENV-faR positive (red color) and protected IFIT1-deGFP<sup>+</sup> DENV-faR<sup>-</sup> cells (yellow color). Shown is the first of two independent experiments after infection with DENV-wt or DENV-E217A mutant replotted from Figure 3.21. (Experiments by B. Schmid and R. Bartenschlager)

To further examine the ability of autocrine action of IFN to reduce virus production, we electroporated IFN-competent A549 cells and IFN-incompetent BHK-21 cells with DENV-faR-wt or DENV-faR-E217A mutant RNA (Figure 3.29). By using electroporation of the respective viral RNA genome, we hit almost all cells, which enables us to investigate predominantly autocrine IFN effects. In the IFN-competent A549 cell culture, we detected a strong decrease of infectious particle release after electroporation with DENV-faR-E217A mutant in contrast to DENV-faR-wt. A relative small difference between the two types of virus reporter constructs could be found in the electroporated IFN-incompetent BHK-21 cells, which indicates that the DENV-faR-E217A mutant has no general defect in RNA replication. A possible reason for the slightly reduced DENV-faR-E217A mutant virus production in BHK-21 cells compared to DENV-wt might be due to IFN-independent expression of IFIT1 (Grandvaux et al. 2002, Diamond and Farzan 2013, Chen et al. 2013) that in turn inhibits 2'-O-unmethylated RNA translation (Pichlmair et al. 2011, Habjan et al. 2013). The moderate decline of virus production in BHK-21 cells between the two time points could result from an increased cell death of BHK-21 cells. Notably, the lacking strong attenuation of DENV-E217A mutant production in an IFN-incompetent cell line corroborates the modeling prediction that a rapid autocrine effect of IFN on infected cells strongly limits viral spread.

Taken together, our study of the competition between spreading DENV and the antiviral IFN response by means of mathematical modeling and experimental validation demonstrates that the fitness of the DENV-E217A mutant is reduced due to an early IFN effect on already infected cells, which in turn curbs virus production. Since we also consider an IFN-independent inhibition of virus production in the full model (cf. section 3.4 page 99) and our analysis reveals a control of viral spread by both the virus production rate (cf. Figure 3.27, relative change of virus

3. Viral spread is mainly controlled by the autocrine effect of rapidly produced IFN

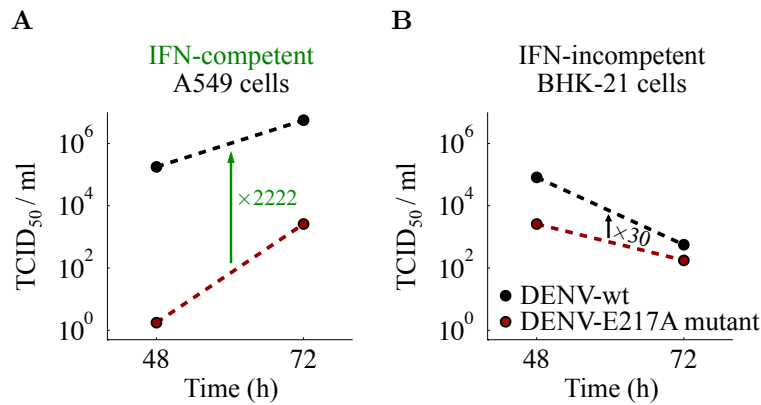


**Figure 3.29.:** The virus production of the DENV-E217A mutant is reduced through the action of autocrine IFN. (A, B) IFN-competent A549 cells (A) and IFN-incompetent BHK-21 cells (B) were electroporated with the RNA genome of DENV-faR-wt (black color) or DENV-faR-E217A mutant (dark red color). Infectious virus release was determined by TCID<sub>50</sub> assay at 48 h and 72 h post electroporation. Arrows and numbers refer to fold difference of virus titers monitored on average in the supernatant of the cell cultures. (Experiments by B. Schmid and R. Bartenschlager)

replicating cells in vertical direction) and the delay of IFN secretion (cf. Figure 3.27, relative change of virus replicating cells in horizontal direction), the reduction in virus production appears to have an IFN-independent component as well as an IFN-dependent component. Importantly, the accelerated secretion of IFN enables a rapid and strong autocrine effect of IFN, which counteracts virus production most likely before DENV prevents an efficient IFN response by inhibition of STAT1 or degradation of STAT2 (cf. Figure 3.1 and 3.6). Our results therefore indicate that the outcome of infection is primarily determined by the relative kinetics of DENV replication and autocrine IFN action on infected cells (Schmid, Rinas et al. submitted).

## 4. Discussion

This thesis consists of two main parts: First, we analyzed the antiviral IFN system after primary infection at single-cell level with a data-based stochastic model (cf. chapter 2). Second, we studied the competition between viral spread and IFN-induced antiviral protection in a cell population by using a parameterized delay differential equation model (cf. chapter 3). In the following we will discuss our findings separately for each model system and subsequently in overall terms.

### 4.1. Stochastic modeling predicts paracrine propagation of the IFN response mediated by individual sentinels

**Live-cell imaging data demonstrate multi-layered stochasticity.** By live-cell imaging, we have examined the dynamics of the antiviral IFN system in single cells after primary infection (cf. section 2.1). We illustrated that signal transduction and IFN gene induction contribute quantitatively to heterogeneous expression of the IFN- $\beta$  gene, and that cell-intrinsic stochasticity prevails in both processes. In addition to heterogeneous IFN induction, we detected a bimodal, all-or-nothing expression of antiviral target genes, in which virus can replicate in the non-responding subpopulation and the responding subpopulation is protected against viral replication. Thus, cell-to-cell variability is a pervasive feature of the IFN network.

**Heterogeneous IFN induction is largely determined by cell-intrinsic noise.** The origin of cell-to-cell variability in IFN expression became the subject of controversial debate. Both host cell-intrinsic causes (Hu et al. 2007, Apostolou and Thanos 2008, Hu et al. 2011) and the ability of viruses to antagonize the IFN system (Chen et al. 2010, Killip et al. 2011) have been considered to be responsible for heterogeneous IFN induction. In section 2.1.2 we addressed the question, whether the stochasticity in IFN expression depends on the infecting virus. We demonstrated that the cell-to-cell heterogeneity in IFN- $\beta$  induction after infection with NDV is not caused by varying infection times, the level of viral replication or the absence of IFN-inducing viral RNA. On that basis, we conclude that the stochastic IFN- $\beta$  expression is predominantly of cellular origin in our experimental system. However, viruses have developed multiple mechanisms to interfere with the expression of IFN (Haller et al. 2006, Versteeg and García-Sastre 2010). Thus, it is possible that antagonizing effects triggered by other types of viruses could contribute to heterogeneous IFN induction.

Using live-cell imaging, we could demonstrate that the heterogeneity in IFN expres-

#### 4. Discussion

sion is largely due to cell-intrinsic stochasticity. Imaging IFN expression in sister cells after viral infection or transfection with the viral-surrogate poly I:C indicates that cell-intrinsic mechanisms generate high variability in antiviral signaling as well as IFN- $\beta$  gene expression (cf. Figure 2.5). Therefore, host cell intrinsic noise plays an important role in heterogeneous IFN induction.

**The decision to express IFN is primarily taken upstream of transcription factor activation.** By live-cell microscopy, we analyzed the sources of cell-intrinsic stochasticity in IFN expression and quantified their relative contributions (cf. Figure 2.4 and Figure 2.5). Our findings revealed that both signal transduction activating the key transcription factors of IFN and IFN- $\beta$  gene expression have strong stochastic components. Previous reports described stochastic gene regulation as the main source of heterogeneous IFN- $\beta$  expression (Hu et al. 2007, Apostolou and Thanos 2008). We rather observed that the majority of cells (91% after high dose infection) that activated transcription factor IRF-7 also expressed IFN shortly after. Therefore, we conclude that, the decision to express IFN- $\beta$  is primarily taken upstream of transcription factor activation. Heterogeneity at the level of signal transduction could result from limiting amounts of RIG-I pathway components like RIG-I, MAVS, IRF-3 or IRF-7 (cf. Figure 1.2) as proposed by other studies (Zhao et al. 2012). Depending on the expression levels of pathway components, the relative contribution of transcription factor activation and IFN- $\beta$  gene induction to cell-to-cell heterogeneity could be cell-type specific.

**Data-based stochastic modeling transforms heterogeneous single-cell behavior into predictable cell population dynamics.** To link intracellular heterogeneous single-cell decisions with the IFN-induced antiviral protection of the cell population, we established a multi-scale stochastic model. This stochastic model combines the heterogeneous IFN signaling in individual cells with the cell-to-cell communication through released IFN. Based on experimental data we determined the model parameters and found that stochastic switching in individual cells translates into predictable dynamics of IFN-secreting and IFN-responding cell fractions at the population level.

**Parameter determination reveals cooperative RIG-I signaling.** From the parameter estimation of our stochastic model, we were able to draw two mechanistically relevant conclusions characterizing IFN induction. Concerning viral signaling, we found that the activation of RIG-I-mediated signaling by virus is cooperative (cf. section 2.3.1). This result is supported by the fact that RIG-I cooperatively multi-merizes along viral dsRNA (Binder et al. 2011). In this earlier work it was concluded that the strength of the viral signal in terms of initiation efficiency and viral dsRNA length is transmitted through the RIG-I pathway to induce an adjusted antiviral response. After detection of viral infection in a cell, RIG-I activates MAVS (cf. Figure 1.2), which leads to the formation of a MAVS-associated signaling complex (Onoguchi et al. 2010, West et al. 2011). The formation of large macromolecular complexes is linked to slow stochastic processes (Luijsterburg et al. 2010) that could influence both frequency and temporal heterogeneity of IFN- $\beta$  expression.

**IFN gene induction needs to be modeled as a slow multi-step process.** Similar to RIG-I activation, IFN- $\beta$  gene induction requires the step-wise assembly

#### 4.1. Stochastic modeling predicts paracrine propagation of the IFN response

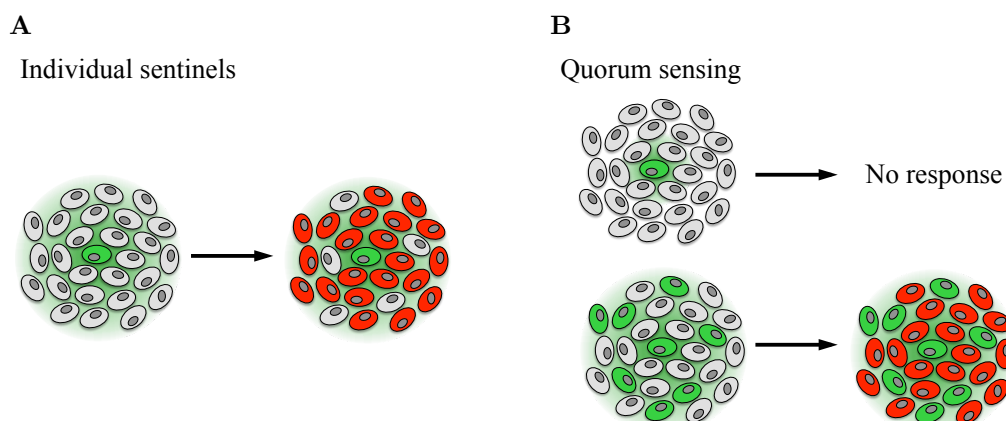


**Figure 4.1.:** Stochastic modeling predicts that IFN expressing cells act as individual sentinels of viral infection to protect a large fraction of naïve cells. (A) Stochastic modeling and validation experiments (cf. section 2.4) indicate that an individual IFN- $\beta$  expressing cell (green cell) can trigger an antiviral immune response (red cells) in a large number of naïve cells (gray cells). (B) Quorum sensing is a communication mechanism according to which a single signal-producing cell (green cell) is unable to induce a response in inactive cells (gray cells) (upper scheme). A response in terms of target gene expression (red cells) only occurs if a critical number of signal-producing cells exceed an extracellular signal threshold (lower scheme).

of a multi-protein complex known as the IFN- $\beta$  enhanceosome (Hu et al. 2007, Ford and Thanos 2010). The proposed step-wise assembly of the IFN- $\beta$  enhanceosome agrees well with our fitting result, namely that the observed distribution of IFN- $\beta$  expression onset in single cells must be described as a slow multi-step process (cf. section 2.3.2). In addition to the assembly of large protein structures, varying expression levels of signaling molecules, transcription factors etc. may further contribute to the detected cell-to-cell heterogeneity (Feinerman et al. 2008, Tay et al. 2010).

**Stochastic modeling predicts paracrine amplification of the IFN response.** Despite strong cell-to-cell variability in IFN induction and response, the corresponding behavior of the cell population is remarkably predictable. The stochastic model demonstrates that simulated stochastic single-cell decisions were able to reproduce the observed reliable, non-stochastic population dynamics (cf. Figure 2.11). Importantly, mathematical modeling and experimental validation show that this reliable population level response is mediated by paracrine propagation of the IFN signal, which compensates the strong heterogeneity in IFN induction. In this way, individual IFN-secreting cells can act as sentinels of viral infection to protect a large number of naïve cells (Figure 4.1A). This protective warning system allows a fast antiviral response initiated by few early sentinels with up to 40 times as many IFN responding cells than IFN-secreting cells (cf. Figure 2.15B). Since the IFN system functions as a first line of defense against viral infections, a rapid action is generally required to limit viral propagation.

Our prediction that paracrine propagation of the IFN signal can translate stochastic single-cell decisions into reliable antiviral protection of the cell population (Rand,

#### 4. Discussion

Rinas et al. 2012) has been confirmed by a subsequent study (Shalek et al. 2014). In this recent paper, individual bacteria-stimulated cells were isolated in sealed chambers to prevent cell-to-cell communication. The expression of core antiviral genes in isolated cells was substantially decreased compared to the control experiment where cell-to-cell communication was unhindered, while cell-to-cell variability was detectable in both cases. This result confirms our finding that paracrine signaling enhances antiviral response.

**Sentinel mechanism versus quorum sensing.** The predicted sentinel mechanism of paracrine signal propagation can be contrasted with another mode of cell-to-cell communication known as quorum sensing. In quorum sensing, a critical number of signal-producing cells is necessary to exceed an extracellular signal threshold, which is then sufficient to induce a target gene program in inactive cells (Figure 4.1B). Quorum sensing was found to be a communication behavior of certain T cells during an immune response (Burroughs et al. 2006, Busse et al. 2010, Feinerman et al. 2010, Butler et al. 2013). In comparison with the individual sentinel system, quorum sensing may result in a delayed reaction against pathogens. However, such a cooperative activation can act as a control system to prevent autoimmunity, which is a misdirected immune response of an organism against its own cells and tissues (Burroughs et al. 2006). Autoimmune diseases are the third most common cause of morbidity as well as mortality in industrialized countries (Kivity et al. 2009). Infectious agents like viruses can trigger autoimmune disorders and many studies assume that a dysregulated IFN system plays a role in the development of autoimmune diseases (Hall and Rosen 2010, Ivashkiv and Donlin 2014).

**Interpretation of heterogeneous IFN expression.** How exactly heterogeneous IFN expression should be interpreted is not fully clear. Stochastic IFN induction could arise from mechanistic limitations of the host cells (as has been suggested for other cytokines; Mariani et al. 2010) that are compensated by paracrine response amplification. Alternatively, cell-to-cell variability may have functional benefits. In particular, the widely distributed onset times of IFN expression in single cells could sustain signaling if the IFN production period per cell is restricted, for example, due to temporally limited presence of transcription factors in the cell nucleus, viral countermeasures or cell death.

**Summary remarks.** Taken together, our findings demonstrate that the key steps of the antiviral IFN signaling pathway are stochastic events in individual cells, which can be described by a stochastic mathematical model. Based on single-cell data after primary infection, mathematical modeling and validation experiments indicate that the paracrine amplification of the IFN signal can mediate reliable antiviral protection at the cell-population level. The prediction of paracrine cell-to-cell communication as an efficient mechanism for averaging single-cell heterogeneity will likely be relevant also for other systems.

## 4.2. Population-based modeling predicts strong reduction of viral spread by the autocrine effect of rapidly produced IFN

**Studying the immediate interactions between viral spread and IFN-induced antiviral defense.** Above, using our stochastic model and a virus capable of primary infections only, we showed that paracrine propagation of the IFN signal is an efficient mechanism to transmit stochastic single-cell decisions into reliable antiviral protection of the cell population. Driven by the question which components of the IFN system are essential for limiting viral spread due to secondary infections, we investigated the dynamics of the antiviral IFN network after infection with spreading DENV (cf. chapter 3).

The outcome of virus infections, either rapid containment or spreading, depends closely on the relative kinetics of viral propagation and the activation of the antiviral IFN system. Some earlier reports showed that IFN-induced ISG expression protects cultured cells against subsequent DENV infection (Diamond et al. 2000, Brass et al. 2009, Li et al. 2013a). However, the kinetics of the antiviral IFN response in relation to virus replication and spread have not been quantified in a single system based on live-cell imaging data.

**The observed characteristics of the competition between spreading DENV and the antiviral IFN response.** To study the underlying dynamics of viral replication and spread versus IFN-induced antiviral defense at the single-cell level, we used a fully viable DENV reporter construct and host cells with authentic fluorescence reporters for IFN-stimulated antiviral genes. We found that IFN has two antiviral effects. First, stimulation with IFN before infection efficiently protects naïve cells against productive DENV infection and, second, stimulation of infected cells with IFN in an early phase after infection reduces viral replication and consequently viral spread (cf. Figure 3.5). In accordance with the results regarding primary infection with NDV in chapter 2, we observed strong cell-to-cell heterogeneity in IFN induction and in IFN response (cf. section 3.1.3). The heterogeneous expression of antiviral genes leads to a coexistence of antiviral protection of naïve cells by IFN and viral spread in non-protected cells. To identify which antiviral components are able to control viral spread, we compare DENV-wt with the vaccine candidate DENV-E217A mutant. This mutant fails to counteract the IFN system by 2'-O-methylation of the viral RNA. In contrast to DENV-wt, we detected that the DENV-E217A mutant elicits faster IFN expression and barely spreads at all (cf. Figure 3.14 and 3.15).

**Parameter optimization of the DDE model identifies DENV-E217A mutant specific parameters.** In order to analyze the underlying differences between DENV-wt and DENV-E217A mutant infections, we established a differential equation model with constant time delays for viral replication, virus production and IFN secretion (cf. Figure 3.16). Our delay differential equation (DDE) model of viral spread and IFN-induced protection was initially parameterized using a consistent set of experimental data based on DENV-wt infection of IFN-competent human cells.

#### 4. Discussion

By utilizing the DENV-wt related parameter set and time-course data concerning DENV-E217A mutant infection, we identified E217A mutant specific parameters. The profile likelihood analysis revealed that only two mutant specific parameters differed strongly from the corresponding DENV-wt values: The virus production rate  $v_V$  is  $\sim 8$ -fold lower, and the delay of IFN secretion  $\tau_F$  is  $\sim 24$  h shorter after DENV-E217A mutant infection, compared to DENV-wt. Importantly, IFN secretion takes place *prior* to virus production after DENV-E217A mutant infection, whereas the production of IFN and virus occurs almost *simultaneously* in the case of DENV-wt.

**Data-driven modeling predicts limitation of DENV spread by rapid autocrine IFN action.** As a faster expression of IFN results in more rapid IFN response and an accelerated autocrine effect of IFN on infected cells can inhibit virus replication in a time-dependent manner (cf. Figure 3.5), the two mutant specific parameters  $\tau_F$  and  $v_V$  could be related, with shorter  $\tau_F$  causing lower  $v_V$ . We therefore extended our model to elucidate the autocrine and paracrine effects of IFN. By means of mathematical modeling and validation experiments, we arrived at the prediction that rapid autocrine IFN action curbing virus production in infected cells is essential for the attenuation of the DENV-E217A mutant, whereas faster paracrine IFN action on naïve cells has only a low impact on the spread of DENV.

The result that paracrine IFN response contributes only marginally to the limitation of spreading DENV is quite surprising, as a small fraction of DENV-E217A mutant infected cells does protect a larger number of naïve cells by paracrine IFN action (cf. Figure 3.28B). But at the same time, a large number of cells remained susceptible throughout the entire 4-day observation period illustrating that lack of available host cells is not a limiting factor for viral spread in our system. These data indicate that fast-acting autocrine IFN signaling is able to contain viral spread quickly, while an accelerated paracrine IFN response could serve as an additional protective measure, which is, however, limited due to high cell-to-cell heterogeneity.

Our model prediction that the autocrine action of IFN on infected cells is decisive in controlling the spread of DENV is supported by a seminal mathematical model of hepatitis C virus (HCV) kinetics (Neumann et al. 1998). This earlier model describes the dynamics of uninfected target cells, infected cells and extracellular HCV, informed by time course data of patients after treatment with IFN. While considering the antiviral effect of IFN only indirectly with an effectiveness rate, this standard model of HCV kinetic demonstrated that the major effect of IFN treatment is to inhibit HCV production or release rather than blocking new infections.

**Reported reasons for the attenuation of viruses with 2'-O-unmethylated RNA.** The attenuated spread of viruses lacking 2'-O-methyltransferase activity of the viral genome has been widely discussed in the literature. It was proposed that in wild-type the 2'-O-methylation of the viral genome prevents the recognition of the virus by the RNA sensor MDA5 and thus inhibits IFN induction (Züst et al. 2011). Furthermore, it was demonstrated that viruses with 2'-O-methylation largely evade antiviral IFN response mediated by IFIT1 (Daffis et al. 2010, Züst et al. 2011, Kimura et al. 2013, Szretter et al. 2012). A restriction of viral replication through IFIT1 can be explained through the sequestration of 2'-O-unmethylated

#### 4.2. Modeling predicts strong reduction of viral spread by rapid autocrine IFN action

RNA by IFIT1, thereby impeding translation of viral RNA (Pichlmair et al. 2011, Habjan et al. 2013). IFIT1 is an ISG, which can be induced directly after viral sensing by IRF-3 independent from IFN (Grandvaux et al. 2002, Diamond and Farzan 2013, Chen et al. 2013). Additionally, IFIT1 can also be induced in response to secreted IFN (cf. Figure 3.2B and Figure 3.12). Therefore, the attenuation of the DENV-E217A mutant might result from an IFN-independent and an IFN-dependent antiviral response.

**Accelerated IFN secretion is a critical determinant for the attenuation of the DENV-E217A mutant.** The slight decline of DENV-E217A mutant virus production in IFN-incompetent BHK-21 cells compared to DENV-wt (cf. Figure 3.29B) could indeed arise from an IFN-independent decrease of the virus production rate. However, in IFN-competent A549 cells we detected a much larger difference between DENV-wt and E217A mutant virus production compared to IFN-incompetent BHK-21 cells (cf. Figure 3.29). In our full DDE model we also take into account that the virus replication of the DENV-E217A mutant can be restricted in an IFN-independent manner. Since we have no available data on the extent to which virus production of the E217A mutant is influenced by IFN-independent mechanisms in the A549 reporter cell line, we assumed that the DENV-E217A mutant produces half as much virus as DENV-wt. With this assumption the model matched the kinetics of both DENV-wt and E217A mutant replication and IFN response as before the extension of the model (cf. Figure 3.25 and Figure 3.21). The model analysis of the relative importance of decreased virus production and accelerated IFN expression (cf. Figure 3.27) revealed that the IFN-independent reduction of virus production rate attenuates viral spread (cf. Figure 3.27, relative change of virus replicating cells in vertical direction), but this attenuation was strongly enhanced for shorter delays of IFN secretion (cf. Figure 3.27, relative change of virus replicating cells in horizontal direction). Therefore, the timing of IFN induction is an important factor of viral spread and critically determines the attenuation of the E217A mutant.

Further insight on the antiviral effects of IFN-independent mechanisms would be gained by accurately quantifying the IFN-independent reduction on the virus production rate. The contribution of IFN-independent antiviral signaling on the virus production rate could be detected experimentally by infecting A549 cells, in which the IFN- $\alpha$  and IFN- $\lambda$  receptors are knocked down, for instance through a small-interfering RNA (siRNA) approach. The determination of the virus production in such knockout cells after infection with DENV-wt and DENV-E217A mutant might be used to fit the IFN-independent decrease of the virus production rate of the DENV-E217A mutant.

**Effective autocrine IFN action on infected cells during the initial stage of viral replication.** According to the results of the parameter estimation, DENV-E217A mutant infected cells secrete IFN  $\sim 8$  h after infection and thus much earlier than DENV-wt infected cells, which express IFN  $\sim 32$  h post infection (cf. Figure 3.22). A rapid IFN signal can activate the JAK-STAT signaling pathway, most likely before DENV is able to counteract an efficient IFN response in infected cells. For example, DENV-induced degradation of STAT2 (cf. Figure 3.6) requires a sufficient expression level of viral proteins (Acosta et al. 2014). Therefore, DENV-E217A mutant infected cells receive an autocrine IFN stimulus during the initial phase of viral

#### 4. Discussion

replication, in which infected cells may still be IFN responsive, and IFN-mediated expression of ISGs can then lead to a strong reduction of the virus production rate. In contrast, DENV-wt infected cells express IFN in later stages of viral replication when high amounts of non-structural viral proteins are present and probably already disturb the JAK-STAT signaling pathway. An autocrine IFN signal at such a late phase of viral replication would not be able to inhibit virus production in these already IFN unresponsive DENV-wt infected cells. This could explain the observed stronger increase in the number of virus replicating cells due to secondary infection events starting  $\sim 60$  h post infection after DENV-wt compared to E217A mutant infection (cf. Figure 3.21(3)).

**The parameter estimates reveal a temporal advantage of IFN secretion over E217A mutant spread.** In the case of DENV-E217A mutant infections, our model predicts a temporal advantage of IFN secretion which takes place  $\sim 20$  h prior to virus production. During this time window, IFN signaling can initiate an antiviral gene program in susceptible cells before new infectious virus particles are released. Additionally, extracellular IFN produced as a result of the initial infection is immediately available in the early stages of all secondary infection events and will lead to an efficient decrease of the virus production rate in susceptible cells, which become newly infected by viral spread. In such case, a further wave of virus production would be minimal. In contrast to the DENV-E217A mutant, the estimated delays of IFN secretion and virus production after infection with DENV-wt are almost identical and last  $\sim 31 - 32$  h. Therefore, the antiviral IFN response has to compete against spreading DENV-wt without a temporal advantage of IFN expression, and the primary DENV-wt infected cells may already be IFN unresponsive. If this is the case, IFN produced by primary infected cells may influence only those infected cells that are subject to secondary DENV-wt infections during viral spread.

**Summarizing remarks.** In summary, our study of the interactions between spreading DENV and the antiviral IFN defense reveals an early “window of opportunity” during which the IFN response can curb viral replication by acting on already infected cells. Thus, our results demonstrate that the relative dynamics of virus replication and the antiviral impact of autocrine IFN primarily determine the outcome of DENV infections.

### 4.3. Using mathematical modeling to gain insight into virus-host competitions

**Integrating data and mechanisms from the molecular to the cell-population level by means of mathematical modeling.** In this work we established two complementary mathematical models to examine the dynamics of the IFN response against viral infections. While the first model focuses on stochastic single-cell decisions, the second one classifies the cell population in different subpopulations according to their infection state. Finding the right balance between the detailed simulation of the observed molecular as well as population-based virus-host dynamics (Figure 4.2) and the computational feasibility of mathematical models is a challenging task.

Our stochastic model links the virus-induced IFN signaling in individual cells with the extracellular cell-to-cell communication via secreted IFN in a cell population after primary infection with NDV (cf. Figure 2.9). The stochastic state transitions of the single cells with respect to virus replication, IFN induction and IFN response are generated using Gillespie's stochastic simulation algorithm and only the intercellular communication via released IFN is calculated deterministically. The simulation of such an almost entirely stochastic model with a large number of heterogeneous individuals on timescales of several hours is very time consuming and practically excludes straightforward parameter optimization approaches (Gillespie 2007, Cao and Samuels 2009, Banks et al. 2011). Thus, it is necessary to reduce model complexity in some way.

We here took the approach of a differential equation model with constant time delays for viral replication, virus production, IFN secretion and autocrine IFN responsiveness to analyze the dynamics of viral spread and IFN-induced antiviral protection at the population level (cf. Figure 4.2B and Figure 3.23). This model type describes multi-step processes with a single delay equal for all individual cells. While our stochastic model is constructed to directly reflect the observed heterogeneous events in individual cells, the DDE model also accounts for the stochastic onset of the IFN response in individual cells due to the slow protection rate (cf. Figure 3.21(4) and Figure 3.20C). This population-based estimate of a slow protection will appear stochastic at the single-cell level. In order to incorporate more directly the observed single-cell heterogeneity of viral replication, viral release and IFN expression (cf. Figure 3.7) into the DDE model, one could replace constant delays by temporally distributed delays (MacDonald 1989, Rateitschak and Wolkenhauer 2007). Since the results of our stochastic model demonstrate that cell-to-cell variability can be translated into predictable cell population dynamics, the use of temporally distributed delays would probably only lead to smoother simulated kinetics of the number of virus replicating cells and the extracellular concentration of IFN (cf. Figure 3.21(3) and (5)).

**Data-driven modeling provides insight into the competition between spreading DENV and IFN-induced antiviral protection.** Our study of the antiviral IFN response after infection with non-spreading NDV and spreading DENV-E217A mutant revealed a strong paracrine propagation of the IFN signal

#### 4. Discussion

according to which one IFN-secreting cell protects a large number of naïve cells by IFN-induced expression of antiviral genes (cf. Figure 2.15B and Figure 3.28B). This protective warning system was severely impaired after infection with DENV-wt (cf. Figure 3.28A). In addition, the determination of predominantly autocrine IFN action using electroporation revealed that the ability of DENV-wt to modify its RNA genome by 2'-O-methylation also disturbs the autocrine IFN response (cf. Figure 3.29). Although both modes of action of IFN are more powerful after infection with the DENV-E217A mutant than post DENV-wt infection, we demonstrated by mathematical modeling that a rapid autocrine action of IFN on infected cells is essential for the attenuation of the E217A mutant (cf. Figure 3.27). In contrast, accelerated protection of naïve cells by paracrine IFN action has only a minor impact on the spread of DENV (cf. Figure 3.27 right column).

Our experimental data and modeling results indicate that the timing of IFN sensing by DENV-infected cells is crucial for an efficient autocrine effect in our system. The stimulation of infected cells with IFN in an early phase after DENV-wt infection resulted in a reduction of virus replication and consequently virus production (cf. Figure 3.5). However, the time window during which treatment with IFN post infection had an impact on virus replication was limited. On the basis of our model simulations, an IFN signal at the earliest possible stage of viral replication strongly enhanced the attenuation of viral spread (cf. Figure 3.27, varying parameter values for the delay of IFN secretion  $\tau_F$  in horizontal direction). Therefore it seems that DENV is most prone to antiviral response in the very initial stages of viral replication, where therapeutic interventions against DENV should prove to be most effective.

**The interference strategies of viruses could influence the dynamics of the antiviral IFN system.** The narrow “window of opportunity”, during which IFN treatment has an antiviral effect on DENV-infected cells, could be explained by the ability of DENV to disturb the JAK-STAT signaling pathway (cf. Figure 3.1). An IFN signal during the initial phase of DENV replication might induce an IFN response before a sufficiently high amount of non-structural viral proteins has been generated to inhibit STAT1 (Muñoz-Jordán et al. 2003, Muñoz-Jordán et al. 2005) or degrade STAT2 (cf. Figure 3.6). On the one hand, such an IFN-responsive time window could be longer after infection of a cell with a different type of virus, which does not counteract the IFN response such as HIV or hepatitis A virus (Versteeg and García-Sastre 2010). But on the other hand, the IFN-responsive time slot might also be shorter if a cell become infected with a virus, which is able to antagonize the IFN response right after infection. An example for this is the Rift Valley fever virus, which expresses the nonstructural protein NSs immediately after infection (Ikegami et al. 2005) and, subsequently, the NSs protein is able to antagonize both IFN induction and ISG expression (Haller et al. 2006, Ikegami and Makino 2011). In a case where viral infection inhibits ISG expression in the host before viral replication can be restricted, protection of naïve cells by paracrine sensing of IFN could be crucial to limit viral spread. We thus expect that various interference strategies of pathogenic viruses inhibiting IFN induction and/or IFN response (Versteeg and García-Sastre 2010) will have different effects on the dynamics of the IFN system.

**Options for further work.** To examine more precisely how an early autocrine IFN

4.3. Using mathematical modeling to gain insight into virus-host competitions

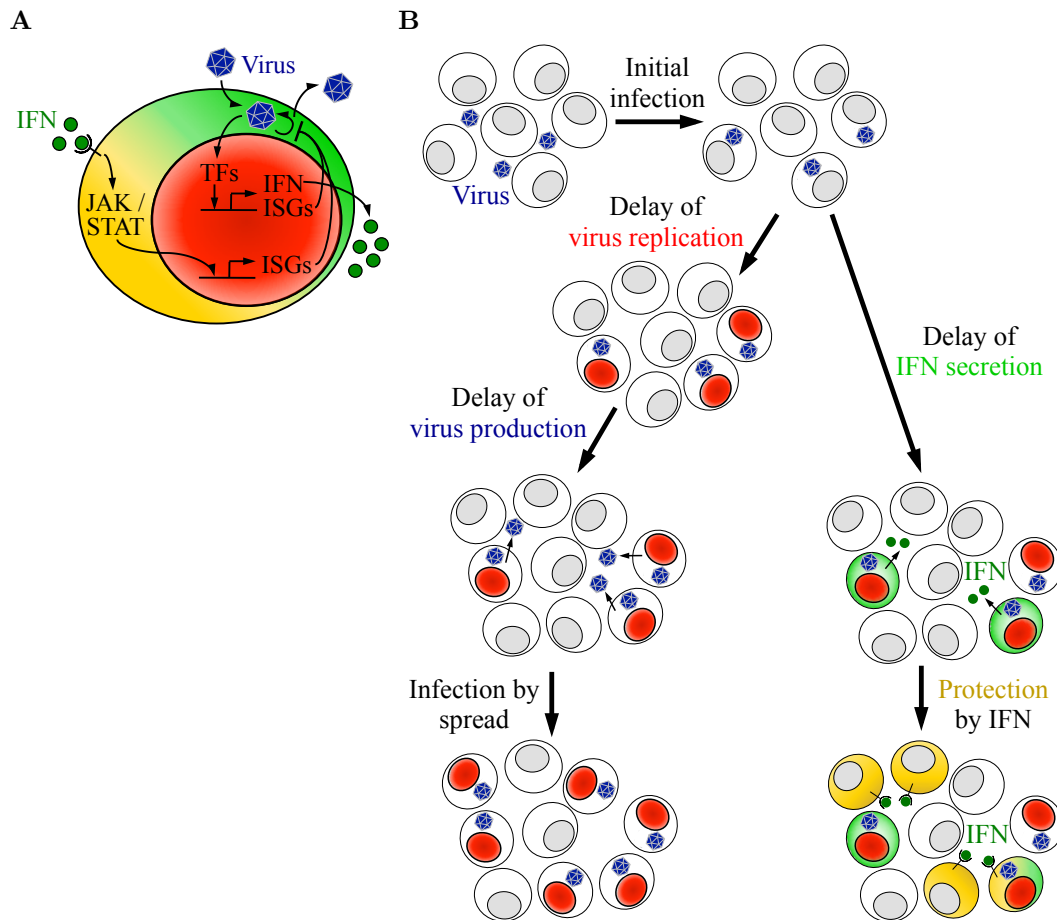


**Figure 4.2.:** Scheme of the molecular and population-based virus-host interactions of the antiviral IFN response. (A) Virus-host interactions at the single-cell level. After infection of a cell, viruses use the host machinery for their replication ( $\odot$ ). The recognition of viruses by specific receptors induces a signaling cascade, which activates the transcription factors (TFs) of IFN. The nuclear translocation of the transcription factors leads to the expression of IFN and antiviral ISGs (green cytoplasm). The ISGs can prevent further viral entry and inhibit viral replication in the infected cell. Moreover, secreted IFN stimulates the JAK/STAT signaling pathway, which in turn results in the expression of further ISGs (yellow cytoplasm). (B) Virus-host interactions at the population level. After the initial viral infection of a cell population, viruses require a certain amount of time for their replication (red nucleus) and the production of new infectious virus particles. The release of newly generated virus causes further infections of host cells by viral spread. Parallel to the viral propagation, the cellular recognition of viral pathogens evokes the secretion of IFN (green cytoplasm) after a certain delay post infection. Sensing of IFN leads to the expression of antiviral genes which block viral activity in infected cells and trigger an antiviral protective state in naïve cells (yellow cytoplasm).

effect interferes with the production of DENV, it would be advisable to incorporate intracellular steps of DENV replication into the DDE model. Moreover, a possible alternative modeling approach for such an extension might be an infection-age structured PDE model (Hethcote 2000, Nelson et al. 2004, Getto et al. 2008, Guedj et al. 2013). This type of model offers more flexibility by allowing to describe viral

#### 4. Discussion

replication, virus production and antiviral response depending on the time a cell has been infected. While age-structured PDE models are valuable tools to analyze the interactions between intracellular and extracellular processes, PDE models are, in general, more computationally demanding than DDE models (Kim et al. 2009). Time-resolved data of viral RNA as well as virus production kinetics after infection with DENV-wt and DENV-E217A mutant could provide the experimental basis for such models. A deeper mechanistic understanding of the stages of the DENV replication cycle, which are most sensitive to the antiviral IFN response and/or most amenable to antiviral treatment could guide the design of novel antiviral therapies to combat DENV infections.

In both models, spatial effects of viral spread and cell responses have not been considered explicitly as on the relevant time scale for virus replication and host gene expression, all cells in the culture are likely to see spatially averaged virus and IFN concentrations (Chang et al. 2008, Hu et al. 2011). This might change in dense tissues (Funk et al. 2005, Graw et al. 2014) or focal infections (Haseltine et al. 2008, Labadie and Marciniak-Czochra 2011, Bertolusso and Kimmel 2012) where viral spread and IFN diffusion could cause, at least initially, more localized infections and IFN responses. It would be interesting to investigate how DENV spreads in a non-well-mixed system, and whether spatial heterogeneity can be observed. A reaction-diffusion model based on spatio-temporal data might be used to analyze whether a rapid autocrine effect of IFN is still the key determinant for the attenuation of the E217A mutant in a spatially distributed system. The parameterization of such a PDE model could be facilitated by utilizing the estimates of the cell-intrinsic parameters of our DDE model as a starting point to determine the remaining spatially dependent parameters from the spatio-temporal data.

**Final remarks.** In conclusion, our work emphasizes that mathematical modeling plays an important role in integrating data and mechanisms from the molecular to the cell-population level. The research on understanding which molecular mechanisms of the antiviral IFN response are able to control the spread of a certain virus can help to develop novel antiviral therapies and vaccines.

# A. Appendix

## A.1. Jacobian matrices of the delay differential equation model

The population-based delay differential equation model (3.11) is numerically solved by using the RADAR5 solver written in ANSI Fortran-90 (Guglielmi and Hairer 2005). To ensure a high accuracy of the solution, we implement within the RADAR5 code the following sparse standard Jacobian matrix  $\mathcal{J}(t)$  and the Jacobian matrix with respect to the delayed variables  $\mathcal{J}_\tau(t)$  for time  $t \in \mathbb{R}$ :

$$\mathcal{J}(t) = \begin{pmatrix} -r_V V(t) - r_F F(t) + p_S & 0 & 0 & 0 & 0 & 0 & 0 & 0 & -r_F S(t) & -r_V S(t) \\ r_V V(t) & 0 & 0 & 0 & 0 & 0 & 0 & 0 & 0 & r_V S(t) \\ 0 & 0 & 0 & 0 & 0 & 0 & 0 & 0 & 0 & 0 \\ r_V V(t) & 0 & 0 & 0 & 0 & 0 & 0 & 0 & 0 & r_V S(t) \\ 0 & 0 & 0 & 0 & 0 & 0 & 0 & 0 & 0 & 0 \\ r_V V(t) & 0 & 0 & 0 & 0 & 0 & 0 & 0 & 0 & r_V S(t) \\ 0 & 0 & 0 & 0 & 0 & 0 & 0 & 0 & 0 & 0 \\ r_F F(t) & 0 & 0 & 0 & 0 & 0 & 0 & p_P & r_F S(t) & 0 \\ 0 & 0 & 0 & 0 & 0 & 0 & v_F & 0 & -d_F & 0 \\ 0 & 0 & 0 & 0 & v_V & 0 & 0 & 0 & 0 & -d_V \end{pmatrix}$$

$$\mathcal{J}_\tau(t) = \begin{pmatrix} 0 & 0 & 0 & 0 & 0 & 0 & 0 & 0 & 0 & 0 \\ -r_V V(t - \tau_R) & 0 & 0 & 0 & 0 & 0 & 0 & 0 & 0 & -r_V S(t - \tau_R) \\ r_V V(t - \tau_R) & 0 & 0 & 0 & 0 & 0 & 0 & 0 & 0 & r_V S(t - \tau_R) \\ -r_V V(t - \tau_V) & 0 & 0 & 0 & 0 & 0 & 0 & 0 & 0 & -r_V S(t - \tau_V) \\ r_V V(t - \tau_V) & 0 & 0 & 0 & 0 & 0 & 0 & 0 & 0 & r_V S(t - \tau_V) \\ -r_V V(t - \tau_F) & 0 & 0 & 0 & 0 & 0 & 0 & 0 & 0 & -r_V S(t - \tau_F) \\ r_V V(t - \tau_F) & 0 & 0 & 0 & 0 & 0 & 0 & 0 & 0 & r_V S(t - \tau_F) \\ 0 & 0 & 0 & 0 & 0 & 0 & 0 & 0 & 0 & 0 \\ 0 & 0 & 0 & 0 & 0 & 0 & 0 & 0 & 0 & 0 \\ 0 & 0 & 0 & 0 & 0 & 0 & 0 & 0 & 0 & 0 \end{pmatrix}.$$

## A.2. Jacobian matrices of the full delay differential equation model

A numerical solution of the full population-based delay differential equation model (3.37) is obtained by utilizing the RADAR5 solver written in ANSI Fortran-90 (Guglielmi and Hairer 2005). For an increased accuracy of the solution, we provide within the RADAR5 code the following sparse standard Jacobian matrix  $\mathcal{J}_{\text{full}}(t)$  and the Jacobian matrix with respect to the delayed variables  $\mathcal{J}_{\text{full},\tau}(t)$  for time  $t \in \mathbb{R}$ :

$$\mathcal{J}_{\text{full}}(t) = \begin{pmatrix} j_1 & 0 & 0 & 0 & 0 & 0 & 0 & 0 & 0 & -r_{\text{F}}S(t) & 0 & 0 & -r_{\text{V}}S(t) \\ r_{\text{V}}V(t) & 0 & 0 & 0 & 0 & 0 & 0 & 0 & 0 & 0 & 0 & 0 & r_{\text{V}}S(t) \\ 0 & 0 & 0 & 0 & 0 & 0 & 0 & 0 & 0 & 0 & 0 & 0 & 0 \\ r_{\text{V}}V(t) & 0 & 0 & 0 & 0 & 0 & 0 & 0 & 0 & 0 & 0 & 0 & r_{\text{V}}S(t) \\ 0 & 0 & 0 & 0 & 0 & 0 & 0 & 0 & 0 & 0 & j_{\mathcal{F}} & -j_{\mathcal{F}} & 0 \\ 0 & 0 & 0 & 0 & 0 & 0 & 0 & 0 & 0 & 0 & -j_{\mathcal{F}} & j_{\mathcal{F}} & 0 \\ r_{\text{V}}V(t) & 0 & 0 & 0 & 0 & 0 & 0 & 0 & 0 & 0 & 0 & 0 & r_{\text{V}}S(t) \\ 0 & 0 & 0 & 0 & 0 & 0 & 0 & 0 & 0 & 0 & 0 & 0 & 0 \\ r_{\text{F}}F(t) & 0 & 0 & 0 & 0 & 0 & 0 & 0 & p_{\text{P}} & r_{\text{F}}S(t) & 0 & 0 & 0 \\ 0 & 0 & 0 & 0 & 0 & 0 & 0 & v_{\text{F}} & 0 & -d_{\text{F}} & 0 & 0 & 0 \\ 0 & 0 & 0 & 0 & 0 & 0 & 0 & 0 & 0 & 0 & 0 & 0 & 0 \\ 0 & 0 & 0 & 0 & 0 & 0 & 0 & 0 & 0 & 0 & 0 & 0 & 0 \\ 0 & 0 & 0 & 0 & v_{\text{P}} & 0 & 0 & 0 & 0 & 0 & 0 & 0 & -d_{\text{V}} \end{pmatrix}$$

$$\mathcal{J}_{\text{full},\tau}(t) = \begin{pmatrix} 0 & 0 & 0 & 0 & 0 & 0 & 0 & 0 & 0 & 0 & 0 & 0 & 0 \\ -r_{\text{V}}V(t - \tau_{\text{R}}) & 0 & 0 & 0 & 0 & 0 & 0 & 0 & 0 & 0 & 0 & 0 & -r_{\text{V}}S(t - \tau_{\text{R}}) \\ r_{\text{V}}V(t - \tau_{\text{R}}) & 0 & 0 & 0 & 0 & 0 & 0 & 0 & 0 & 0 & 0 & 0 & r_{\text{V}}S(t - \tau_{\text{R}}) \\ -r_{\text{V}}V(t - \tau_{\text{V}}) & 0 & 0 & 0 & 0 & 0 & 0 & 0 & 0 & 0 & 0 & 0 & -r_{\text{V}}S(t - \tau_{\text{V}}) \\ j_{\tau,(5,1)} & 0 & 0 & 0 & 0 & 0 & 0 & 0 & 0 & 0 & 0 & 0 & j_{\tau,(5,13)} \\ j_{\tau,(6,1)} & 0 & 0 & 0 & 0 & 0 & 0 & 0 & 0 & 0 & 0 & 0 & j_{\tau,(6,13)} \\ -r_{\text{V}}V(t - \tau_{\text{F}}) & 0 & 0 & 0 & 0 & 0 & 0 & 0 & 0 & 0 & 0 & 0 & -r_{\text{V}}S(t - \tau_{\text{F}}) \\ r_{\text{V}}V(t - \tau_{\text{F}}) & 0 & 0 & 0 & 0 & 0 & 0 & 0 & 0 & 0 & 0 & 0 & r_{\text{V}}S(t - \tau_{\text{F}}) \\ 0 & 0 & 0 & 0 & 0 & 0 & 0 & 0 & 0 & 0 & 0 & 0 & 0 \\ 0 & 0 & 0 & 0 & 0 & 0 & 0 & 0 & 0 & 0 & 0 & 0 & 0 \\ 0 & 0 & 0 & 0 & 0 & 0 & 0 & 0 & 0 & 1 & 0 & 0 & 0 \\ 0 & 0 & 0 & 0 & 0 & 0 & 0 & 0 & 0 & 1 & 0 & 0 & 0 \\ 0 & 0 & 0 & 0 & 0 & 0 & 0 & 0 & 0 & 0 & 0 & 0 & 0 \end{pmatrix}$$

with

$$\begin{aligned} j_1 &= -r_{\text{V}}V(t) - r_{\text{F}}F(t) + p_{\text{S}} \\ j_{\mathcal{F}} &= r_{\text{P}} \exp(r_{\text{P}} [\mathcal{F}_1(t) - \mathcal{F}_2(t)]) r_{\text{V}}V(t - \tau_{\text{V}})S(t - \tau_{\text{V}}) \\ j_{\tau,(5,1)} &= \exp(r_{\text{P}} [\mathcal{F}_1(t) - \mathcal{F}_2(t)]) r_{\text{V}}V(t - \tau_{\text{V}}) \\ j_{\tau,(5,13)} &= \exp(r_{\text{P}} [\mathcal{F}_1(t) - \mathcal{F}_2(t)]) r_{\text{V}}S(t - \tau_{\text{V}}) \\ j_{\tau,(6,1)} &= (1 - \exp(r_{\text{P}} [\mathcal{F}_1(t) - \mathcal{F}_2(t)])) r_{\text{V}}V(t - \tau_{\text{V}}) \\ j_{\tau,(6,13)} &= (1 - \exp(r_{\text{P}} [\mathcal{F}_1(t) - \mathcal{F}_2(t)])) r_{\text{V}}S(t - \tau_{\text{V}}). \end{aligned}$$

# Bibliography

- Ackermann, H.-W. The first phage electron micrographs. *Bacteriophage*, 1(4):225, 2011.
- Acosta, E. G., Kumar, A., and Bartenschlager, R. Revisiting Dengue virus-host cell interaction: new insights into molecular and cellular virology. *Advances in Virus Research*, 88:1–109, 2014.
- Adiwijaya, B. S., Herrmann, E., Hare, B., Kieffer, T., Lin, C., Kwong, A. D., Garg, V., Randle, J. C., Sarrazin, C., Zeuzem, S., and Caron, P. R. A multi-variant, viral dynamic model of genotype 1 HCV to assess the in vivo evolution of protease-inhibitor resistant variants. *PLoS Computational Biology*, 6(4):e1000745, 2010.
- Aguirre, S., Maestre, A. M., Pagni, S., Patel, J. R., Savage, T., Gutman, D., Maringer, K., Bernal-Rubio, D., Shabman, R. S., Simon, V., Rodriguez-Madoz, J. R., Mulder, L. C. F., Barber, G. N., and Fernandez-Sesma, A. DENV inhibits type I IFN production in infected cells by cleaving human STING. *PLoS Pathogens*, 8(10):e1002934, 2012.
- Alexopoulou, L., Holt, A. C., Medzhitov, R., and Flavell, R. A. Recognition of double-stranded RNA and activation of NF- $\kappa$ B by Toll-like receptor 3. *Nature*, 413(6857):732–738, 2001.
- Alon, U. An introduction to systems biology: design principles of biological circuits. CRC Press, 2006.
- Anderson, R. M. and May, R. M. Infectious diseases of humans, vol. 1. Oxford University Press, Oxford, 1991.
- Apostolou, E. and Thanos, D. Virus infection induces NF- $\kappa$ B-dependent inter-chromosomal associations mediating monoallelic IFN- $\beta$  gene expression. *Cell*, 134(1):85–96, 2008.
- Artenstein, A. W. Vaccines: a biography. Springer New York, 2010.
- Ashour, J., Laurent-Rolle, M., Shi, P.-Y., and García-Sastre, A. NS5 of Dengue virus mediates STAT2 binding and degradation. *Journal of Virology*, 83(11):5408–5418, 2009.
- Baker, C. T., Bocharov, G. A., and Rihan, F. A. A report on the use of delay differential equations in numerical modelling in the biosciences. *Manchester Centre for Computational Mathematics, Numerical Analysis Report*, (343), 1999.
- Baker, S. and Cousins, R. D. Clarification of the use of chi-square and likelihood functions in fits to histograms. *Nuclear Instruments and Methods in Physics Research*, 221(2):437–442, 1984.

## Bibliography

- Bandyopadhyay, S. K., Leonard, G. T., Bandyopadhyay, T., Stark, G. R., and Sen, G. C. Transcriptional induction by double-stranded RNA is mediated by interferon-stimulated response elements without activation of interferon-stimulated gene factor 3. *Journal of Biological Chemistry*, 270(33):19624–19629, 1995.
- Banks, H. T., Broido, A., Canter, B., Gayvert, K., Hu, S., Joyner, M., and Link, K. Simulation algorithms for continuous time markov chain models. *Proceedings of SiMCRT*, 2011.
- Barbarossa, M. V. On a class of neutral equations with state-dependent delay in population dynamics. PhD Thesis, Technische Universität München, 2013.
- Bartenschlager, R. and Miller, S. Molecular aspects of Dengue virus replication. *Future Medicine*, (3):155–165, 2008.
- Bauhofer, O., Ruggieri, A., Schmid, B., Schirmacher, P., and Bartenschlager, R. Persistence of HCV in quiescent hepatic cells under conditions of an interferon-induced antiviral response. *Gastroenterology*, 143(2):429–438, 2012.
- Bazhan, S. and Belova, O. Interferon-induced antiviral resistance. A mathematical model of regulation of Mx1 protein induction and action. *Journal of Theoretical Biology*, 198(3):375–393, 1999.
- Beijerinck, M. Concerning a contagium vivum fluidum as a cause of the spot-disease of tobacco leaves. *Verhandelingen der Koninklijke akademie Wetenschappen te Amsterdam*, (65):3–21, 1898.
- Bellen, A. and Zennaro, M. Numerical methods for delay differential equations. Oxford University Press, Oxford, 2003.
- Bertolusso, R. and Kimmel, M. Spatial and stochastic effects in a model of viral infection. *Fundamenta Informaticae*, 118(4):327–343, 2012.
- Bhatt, S., Gething, P. W., Brady, O. J., Messina, J. P., Farlow, A. W., Moyes, C. L., Drake, J. M., Brownstein, J. S., Hoen, A. G., Sankoh, O., Myers, M. F., George, D. B., Jaenisch, T., Wint, G. R. W., Simmons, C. P., Scott, T. W., Farrar, J. J., and Hay, S. I. The global distribution and burden of Dengue. *Nature*, 2013.
- Binder, M., Eberle, F., Seitz, S., Mücke, N., Hüber, C. M., Kiani, N., Kaderali, L., Lohmann, V., Dalpke, A., and Bartenschlager, R. Molecular mechanism of signal perception and integration by the innate immune sensor retinoic acid-inducible gene-I (RIG-I). *Journal of Biological Chemistry*, 286(31):27278–27287, 2011.
- Binder, M., Sulaimanov, N., Clausznitzer, D., Schulze, M., Hüber, C. M., Lenz, S. M., Schlöder, J. P., Trippler, M., Bartenschlager, R., Lohmann, V., and Kaderali, L. Replication vesicles are load-and choke-points in the hepatitis C virus lifecycle. *PLoS Pathogens*, 9(8):e1003561, 2013.
- Bocharov, G. and Haderler, K. Structured population models, conservation laws, and delay equations. *Journal of Differential Equations*, 168(1):212–237, 2000.

- Bocharov, G. A. and Rihan, F. A. Numerical modelling in biosciences using delay differential equations. *Journal of Computational and Applied Mathematics*, 125(1):183–199, 2000.
- Bogacki, P. and Shampine, L. F. A 3(2) pair of Runge-Kutta formulas. *Applied Mathematics Letters*, 2(4):321–325, 1989.
- Brass, A. L., Huang, I.-C., Benita, Y., John, S. P., Krishnan, M. N., Feeley, E. M., Ryan, B. J., Weyer, J. L., Van Der Weyden, L., Fikrig, E., Adams, D. J., Xavier, R. J., Farzan, M., and Elledge, S. J. The IFITM proteins mediate cellular resistance to influenza A H1N1 virus, West Nile virus, and Dengue virus. *Cell*, 139(7):1243–1254, 2009.
- Brennan, K. and Bowie, A. G. Activation of host pattern recognition receptors by viruses. *Current Opinion in Microbiology*, 13(4):503–507, 2010.
- Burroughs, N., Miguel Paz Mendes de Oliveira, B., and Adrego Pinto, A. Regulatory T cell adjustment of quorum growth thresholds and the control of local immune responses. *Journal of Theoretical Biology*, 241(1):134–141, 2006.
- Busse, D., de la Rosa, M., Hobiger, K., Thurley, K., Flossdorf, M., Scheffold, A., and Höfer, T. Competing feedback loops shape IL-2 signaling between helper and regulatory T lymphocytes in cellular microenvironments. *Proceedings of the National Academy of Sciences*, 107(7):3058–3063, 2010.
- Bustos-Arriaga, J., García-Machorro, J., León-Juárez, M., García-Cordero, J., Santos-Argumedo, L., Flores-Romo, L., Méndez-Cruz, A. R., Juárez-Delgado, F. J., and Cedillo-Barrón, L. Activation of the innate immune response against DENV in normal non-transformed human fibroblasts. *PLoS Neglected Tropical Diseases*, 5(12):e1420, 2011.
- Butler, T. C., Kardar, M., and Chakraborty, A. K. Quorum sensing allows T cells to discriminate between self and nonself. *Proceedings of the National Academy of Sciences*, 110(29):11833–11838, 2013.
- Cann, A. Principles of molecular virology, vol. 1. Academic Press, 2005.
- Cao, Y. and Samuels, D. C. Discrete stochastic simulation methods for chemically reacting systems. *Methods in Enzymology*, 454:115–140, 2009.
- Capua, I. and Alexander, D. Human health implications of avian influenza viruses and paramyxoviruses. *European Journal of Clinical Microbiology and Infectious Diseases*, 23(1):1–6, 2004.
- Chambers, T. and Rice, C. Molecular biology of the flaviviruses. *Microbiological Sciences*, 4(7):219–223, 1987.
- Chan, Y. K., Huang, I.-C., and Farzan, M. IFITM proteins restrict antibody-dependent enhancement of Dengue virus infection. *PloS One*, 7(3):e34508, 2012.
- Chang, W.-S., Shang, H., Perera, R. M., Lok, S.-m., Sedlak, D., Kuhn, R. J., and Lee, G. U. Rapid detection of Dengue virus in serum using magnetic separation and fluorescence detection. *Analyst*, 133(2):233–240, 2008.

## Bibliography

- Charlesworth, B. Evolution in age-structured populations, vol. 1. Cambridge University Press, Cambridge, 1980.
- Chatterjee, A., Guedj, J., and Perelson, A. S. Mathematical modeling of HCV infection: what can it teach us in the era of direct antiviral agents? *Antiviral Therapy*, 17(6 0 0):1171, 2012.
- Chen, H.-W., King, K., Tu, J., Sanchez, M., Luster, A. D., and Shresta, S. The roles of IRF-3 and IRF-7 in innate antiviral immunity against Dengue virus. *The Journal of Immunology*, 191(8):4194–4201, 2013.
- Chen, S., Short, J., Young, D., Killip, M., Schneider, M., Goodbourn, S., and Randall, R. Heterocellular induction of interferon by negative-sense RNA viruses. *Virology*, 407(2):247–255, 2010.
- Cheng, C. S., Feldman, K. E., Lee, J., Verma, S., Huang, D.-B., Huynh, K., Chang, M., Ponomarenko, J. V., Sun, S.-C., Benedict, C. A., Ghosh, G., and Hoffmann, A. The specificity of innate immune responses is enforced by repression of interferon response elements by NF- $\kappa$ B p50. *Science Signaling*, 4(161):ra11, 2011.
- Childs, K., Stock, N., Ross, C., Andrejeva, J., Hilton, L., Skinner, M., Randall, R., and Goodbourn, S. mda-5, but not RIG-I, is a common target for paramyxovirus V proteins. *Virology*, 359(1):190–200, 2007.
- Coffin, J. M. HIV population dynamics in vivo: implications for genetic variation, pathogenesis, and therapy. *Science*, 267(5197):483–489, 1995.
- Coleman, T. and Zhang, Y. Optimization toolbox for use with Matlab. *The Math-Works Inc.*, 2003.
- Cox, D. R. and Oakes, D. Analysis of survival data, vol. 21. CRC Press, 1984.
- da Conceição, T. M., Rust, N. M., Berbel, A. C. E. R., Martins, N. B., do Nascimento Santos, C. A., Da Poian, A. T., and de Arruda, L. B. Essential role of RIG-I in the activation of endothelial cells by Dengue virus. *Virology*, 435(2):281–292, 2013.
- Daffis, S., Szretter, K. J., Schriewer, J., Li, J., Youn, S., Errett, J., Lin, T.-Y., Schneller, S., Züst, R., Dong, H., Thiel, V., Pierson, T. C., Buller, R. M., Gale Jr, M., Shi, P.-Y., and Diamond, M. S. 2'-O methylation of the viral mRNA cap evades host restriction by IFIT family members. *Nature*, 468(7322):452–456, 2010.
- Dahari, H., Ribeiro, R. M., Rice, C. M., and Perelson, A. S. Mathematical modeling of subgenomic hepatitis C virus replication in Huh-7 cells. *Journal of Virology*, 81(2):750–760, 2007.
- Darnell, J. E., Kerr, I. M., and Stark, G. R. Jak-STAT pathways and transcriptional activation in response to IFNs and other extracellular signaling proteins. *Science*, 264(5164):1415–1421, 1994.
- Diamond, M. S. and Farzan, M. The broad-spectrum antiviral functions of IFIT and IFITM proteins. *Nature Reviews Immunology*, 13(1):46–57, 2013.

- Diamond, M. S. and Harris, E. Interferon inhibits Dengue virus infection by preventing translation of viral RNA through a PKR-independent mechanism. *Virology*, 289(2):297–311, 2001.
- Diamond, M. S., Roberts, T. G., Edgil, D., Lu, B., Ernst, J., and Harris, E. Modulation of Dengue virus infection in human cells by alpha, beta, and gamma interferons. *Journal of Virology*, 74(11):4957–4966, 2000.
- Díaz, A., Kouri, G. P., Guzmán, M. G., Lobaina, L., Bravo, J. R., Ruiz, A., Ramos, A., and Martínez, R. Description of the clinical picture of Dengue hemorrhagic fever/Dengue shock syndrome (DHF/DSS) in adults. *Bulletin of the Pan American Health Organization (PAHO)*, 22(2):133–44, 1988.
- Dobson, A. J. An introduction to generalized linear models. CRC Press, 2001.
- Dong, H., Fink, K., Züst, R., Lim, S. P., Qin, C.-F., and Shi, P.-Y. Flavivirus RNA methylation. *Journal of General Virology*, 95(Pt 4):763–778, 2014.
- Egloff, M.-P., Benarroch, D., Selisko, B., Romette, J.-L., and Canard, B. An RNA cap (nucleoside-2'-O-)-methyltransferase in the flavivirus RNA polymerase NS5: crystal structure and functional characterization. *The EMBO Journal*, 21(11):2757–2768, 2002.
- Ehrlich, P. R. and Himmelweit, F. The collected papers of Paul Ehrlich, vol. 1. Pergamon, 1956.
- Ellis, E. L. and Delbrück, M. The growth of bacteriophage. *The Journal of General Physiology*, 22(3):365–384, 1939.
- Elowitz, M. B., Levine, A. J., Siggia, E. D., and Swain, P. S. Stochastic gene expression in a single cell. *Science*, 297(5584):1183–1186, 2002.
- Feinerman, O., Jentsch, G., Tkach, K. E., Coward, J. W., Hathorn, M. M., Sneddon, M. W., Emonet, T., Smith, K. A., and Altan-Bonnet, G. Single-cell quantification of IL-2 response by effector and regulatory T cells reveals critical plasticity in immune response. *Molecular Systems Biology*, 6(1), 2010.
- Feinerman, O., Veiga, J., Dorfman, J. R., Germain, R. N., and Altan-Bonnet, G. Variability and robustness in T cell activation from regulated heterogeneity in protein levels. *Science*, 321(5892):1081–1084, 2008.
- Feldmann, H., Czub, M., Jones, S., Dick, D., Garbutt, M., Grolla, A., and Artsock, H. Emerging and re-emerging infectious diseases. *Medical Microbiology and Immunology*, 191(2):63–74, 2002.
- Fischl, W. and Bartenschlager, R. High-throughput screening using Dengue virus reporter genomes. In *Antiviral methods and protocols*, Springer, 205–219. 2013.
- Ford, E. and Thanos, D. The transcriptional code of human IFN- $\beta$  gene expression. *Biochimica et Biophysica Acta*, 1799(3):328–336, 2010.
- Funk, G. A., Jansen, V. A., Bonhoeffer, S., and Killingback, T. Spatial models of virus-immune dynamics. *Journal of Theoretical Biology*, 233(2):221–236, 2005.

## Bibliography

- Gelderblom, H. R. Structure and classification of viruses. *Medical Microbiology*, 4th, 1996.
- Getto, P., Kimmel, M., and Marciniak-Czochra, A. Modelling and analysis of dynamics of viral infection of cells and of interferon resistance. *Journal of Mathematical Analysis and Applications*, 344(2):821–850, 2008.
- Gilbert, M. T. P., Rambaut, A., Wlasiuk, G., Spira, T. J., Pitchenik, A. E., and Worobey, M. The emergence of HIV/AIDS in the Americas and beyond. *Proceedings of the National Academy of Sciences*, 104(47):18566–18570, 2007.
- Gillespie, D. T. A general method for numerically simulating the stochastic time evolution of coupled chemical reactions. *Journal of Computational Physics*, 22(4):403–434, 1976.
- Gillespie, D. T. Exact stochastic simulation of coupled chemical reactions. *The Journal of Physical Chemistry*, 81(25):2340–2361, 1977.
- Gillespie, D. T. Stochastic simulation of chemical kinetics. *Annual Review of Physical Chemistry*, 58:35–55, 2007.
- Gong, Y., Trowbridge, R., Macnaughton, T. B., Westaway, E. G., Shannon, A. D., and Gowans, E. J. Characterization of RNA synthesis during a one-step growth curve and of the replication mechanism of bovine viral diarrhoea virus. *Journal of General Virology*, 77(11):2729–2736, 1996.
- Gordon, M. Virus bodies. John Buist and the elementary bodies of vaccinia. *Edinburgh Medical Journal*, 44:65–71, 1937.
- Gottschalk, R. A., Martins, A. J., Sjoelund, V. H., Angermann, B. R., Lin, B., and Germain, R. N. Recent progress using systems biology approaches to better understand molecular mechanisms of immunity. *Seminars in Immunology*, 25(3):201–208, 2013.
- Grandvaux, N., Servant, M. J., tenOever B, Sen, G. C., Balachandran, S., Barber, G. N., Lin, R., and Hiscott, J. Transcriptional profiling of interferon regulatory factor 3 target genes: direct involvement in the regulation of interferon-stimulated genes. *Journal of Virology*, 76(11):5532–5539, 2002.
- Graw, F., Balagopal, A., Kandathil, A. J., Ray, S. C., Thomas, D. L., Ribeiro, R. M., and Perelson, A. S. Inferring viral dynamics in chronically HCV infected patients from the spatial distribution of infected hepatocytes. *PLoS Computational Biology*, 10(11):e1003934, 2014.
- Gross, C. P. and Sepkowitz, K. A. The myth of the medical breakthrough: smallpox, vaccination, and Jenner reconsidered. *International Journal of Infectious Diseases*, 3(1):54–60, 1998.
- Guedj, J., Dahari, H., Rong, L., Sansone, N. D., Nettles, R. E., Cotler, S. J., Layden, T. J., Uprichard, S. L., and Perelson, A. S. Modeling shows that the NS5A inhibitor daclatasvir has two modes of action and yields a shorter estimate of the hepatitis C virus half-life. *Proceedings of the National Academy of Sciences*, 110(10):3991–3996, 2013.

- Guedj, J. and Neumann, A. Understanding hepatitis C viral dynamics with direct-acting antiviral agents due to the interplay between intracellular replication and cellular infection dynamics. *Journal of Theoretical Biology*, 267(3):330–340, 2010.
- Guglielmi, N. On the Newton iteration in the application of collocation methods to implicit delay equations. *Applied Numerical Mathematics*, 53(2):281–297, 2005.
- Guglielmi, N. and Hairer, E. Implementing Radau IIA methods for stiff delay differential equations. *Computing*, 67(1):1–12, 2001.
- Guglielmi, N. and Hairer, E. Users’ guide for the code RADAR5 - version 2.1. *Università dell’ Aquila, Italy, Technical Report*, 2005.
- Guglielmi, N. and Hairer, E. Computing breaking points in implicit delay differential equations. *Advances in Computational Mathematics*, 29(3):229–247, 2008.
- Gwiazda, P., Jablonski, J., Marciniak-Czochra, A., and Ulikowska, A. Analysis of particle methods for structured population models with nonlocal boundary term in the framework of bounded Lipschitz distance. *Numerical Methods for Partial Differential Equations*, 2014.
- Habjan, M., Hubel, P., Lacerda, L., Benda, C., Holze, C., Eberl, C. H., Mann, A., Kindler, E., Gil-Cruz, C., Ziebuhr, J., Thiel, V., and Pichlmair, A. Sequestration by IFIT1 impairs translation of 2’O-unmethylated capped RNA. *PLoS Pathogens*, 9(10):e1003663, 2013.
- Hairer, E. and Wanner, G. Stiff differential equations solved by Radau methods. *Journal of Computational and Applied Mathematics*, 111(1):93–111, 1999.
- Hall, J. C. and Rosen, A. Type I interferons: crucial participants in disease amplification in autoimmunity. *Nature Reviews Rheumatology*, 6(1):40–49, 2010.
- Haller, O., Kochs, G., and Weber, F. The interferon response circuit: induction and suppression by pathogenic viruses. *Virology*, 344(1):119–130, 2006.
- Hamer, W. H. The Milroy lectures on epidemic disease in England: the evidence of variability and of persistency of type. Bedford Press, 1906.
- Hartman, P. Ordinary differential equations. SIAM Classics in Applied Mathematics, Philadelphia, 2002.
- Haseltine, E. L., Lam, V., Yin, J., and Rawlings, J. B. Image-guided modeling of virus growth and spread. *Bulletin of Mathematical Biology*, 70(6):1730–1748, 2008.
- Heesterbeek, H. The Law of Mass-Action in Epidemiology: A Historical Perspective. In *Ecological paradigms lost: routes of theory change*, Elsevier Academic Press, vol. 2, 81. 2005.
- Hethcote, H. W. Three basic epidemiological models. In *Applied mathematical ecology*, Springer, 119–144. 1989.
- Hethcote, H. W. The mathematics of infectious diseases. *SIAM Review*, 42(4):599–653, 2000.

## Bibliography

- Hierholzer, J. and Killington, R. Virus isolation and quantitation. In *Virology methods manual*, Academic Press. 1996.
- Hilleman, M. R. Vaccines in historic evolution and perspective: a narrative of vaccine discoveries. *Vaccine*, 18(15):1436–1447, 2000.
- Ho, D. D., Neumann, A. U., Perelson, A. S., Chen, W., Leonard, J. M., and Markowitz, M. Rapid turnover of plasma virions and CD4 lymphocytes in HIV-1 infection. *Nature*, 373(6510):123–126, 1995.
- Honda, K., Yanai, H., Negishi, H., Asagiri, M., Sato, M., Mizutani, T., Shimada, N., Ohba, Y., Takaoka, A., Yoshida, N., and Taniguchi, T. IRF-7 is the master regulator of type-I interferon-dependent immune responses. *Nature*, 434(7034):772–777, 2005.
- Hu, J., Nudelman, G., Shimoni, Y., Kumar, M., Ding, Y., López, C., Hayot, F., Wetmur, J. G., and Sealfon, S. C. Role of cell-to-cell variability in activating a positive feedback antiviral response in human dendritic cells. *PloS One*, 6(2):e16614, 2011.
- Hu, J., Sealfon, S. C., Hayot, F., Jayaprakash, C., Kumar, M., Pendleton, A. C., Ganee, A., Fernandez-Sesma, A., Moran, T. M., and Wetmur, J. G. Chromosome-specific and noisy IFNB1 transcription in individual virus-infected human primary dendritic cells. *Nucleic Acids Research*, 35(15):5232–5241, 2007.
- Ikegami, T. and Makino, S. The pathogenesis of Rift Valley fever. *Viruses*, 3(5):493–519, 2011.
- Ikegami, T., Won, S., Peters, C., and Makino, S. Rift Valley fever virus NSs mRNA is transcribed from an incoming anti-viral-sense S RNA segment. *Journal of Virology*, 79(18):12106–12111, 2005.
- Ishikawa, H. and Barber, G. N. STING is an endoplasmic reticulum adaptor that facilitates innate immune signalling. *Nature*, 455(7213):674–678, 2008.
- Ivanowski, D. Concerning the mosaic disease of the tobacco plant. *St. Petersburg Academy of Imperial Science Bulletin*, 35:67–70, 1892.
- Ivashkiv, L. B. and Donlin, L. T. Regulation of type I interferon responses. *Nature Reviews Immunology*, 14(1):36–49, 2014.
- Jenner, E. The origin of the vaccine inoculation, 1801. *London: DN Shury*, 12, 1801.
- Jiang, D., Weidner, J. M., Qing, M., Pan, X.-B., Guo, H., Xu, C., Zhang, X., Birk, A., Chang, J., Shi, P.-Y., Block, T. M., and Guo, J.-T. Identification of five interferon-induced cellular proteins that inhibit West Nile virus and Dengue virus infections. *Journal of Virology*, 84(16):8332–8341, 2010.
- Jones, M., Davidson, A., Hibbert, L., Gruenwald, P., Schlaak, J., Ball, S., Foster, G. R., and Jacobs, M. Dengue virus inhibits alpha interferon signaling by reducing STAT2 expression. *Journal of Virology*, 79(9):5414–5420, 2005.
- Kærn, M., Elston, T. C., Blake, W. J., and Collins, J. J. Stochasticity in gene expression: from theories to phenotypes. *Nature Reviews Genetics*, 6(6):451–464, 2005.

- Kato, H., Sato, S., Yoneyama, M., Yamamoto, M., Uematsu, S., Matsui, K., Tsujimura, T., Takeda, K., Fujita, T., Takeuchi, O., and Akira, S. Cell type-specific involvement of RIG-I in antiviral response. *Immunity*, 23(1):19–28, 2005.
- Kato, H., Takeuchi, O., Sato, S., Yoneyama, M., Yamamoto, M., Matsui, K., Uematsu, S., Jung, A., Kawai, T., Ishii, K. J., Yamaguchi, O., Otsu, K., Tsujimura, T., Koh, C., Reis e Sousa, C., Matsuura, Y., Fujita, T., and Akira, S. Differential roles of MDA5 and RIG-I helicases in the recognition of RNA viruses. *Nature*, 441(7089):101–105, 2006.
- Kaufmann, S. H. Immunology’s foundation: the 100-year anniversary of the Nobel Prize to Paul Ehrlich and Elie Metchnikoff. *Nature Immunology*, 9(7):705–712, 2008.
- Kendall, D. G. Stochastic processes and population growth. *Journal of the Royal Statistical Society. Series B (Methodological)*, 11(2):230–282, 1949.
- Kermack, W. O. and McKendrick, A. G. A contribution to the mathematical theory of epidemics. *Proceedings of the Royal society of London. Series A*, 115:700–721, 1927.
- Killip, M., Young, D., Ross, C., Chen, S., Goodbourn, S., and Randall, R. Failure to activate the IFN- $\beta$  promoter by a paramyxovirus lacking an interferon antagonist. *Virology*, 415(1):39–46, 2011.
- Kim, P. S., Levy, D., and Lee, P. P. Modeling and simulation of the immune system as a self-regulating network. *Methods in Enzymology*, 467:79–109, 2009.
- Kimura, T., Katoh, H., Kayama, H., Saiga, H., Okuyama, M., Okamoto, T., Umemoto, E., Matsuura, Y., Yamamoto, M., and Takeda, K. Ifit1 inhibits Japanese encephalitis virus replication through binding to 5’ capped 2’-O unmethylated RNA. *Journal of Virology*, 87(18):9997–10003, 2013.
- Kirkpatrick, S., Gelatt, C. D., and Vecchi, M. P. Optimization by simulated annealing. *Science*, 220(4598):671–680, 1983.
- Kivity, S., Agmon-Levin, N., Blank, M., and Shoenfeld, Y. Infections and autoimmunity – friends or foes? *Trends in Immunology*, 30(8):409–414, 2009.
- Kreuz, L. E. and Levy, A. H. Physical properties of chick interferon. *Journal of Bacteriology*, 89(2):462–469, 1965.
- Kumagai, Y., Kumar, H., Koyama, S., Kawai, T., Takeuchi, O., and Akira, S. Cutting Edge: TLR-dependent viral recognition along with type I IFN positive feedback signaling masks the requirement of viral replication for IFN- $\alpha$  production in plasmacytoid dendritic cells. *The Journal of Immunology*, 182(7):3960–3964, 2009.
- Kumar, A., Bühler, S., Selisko, B., Davidson, A., Mulder, K., Canard, B., Miller, S., and Bartenschlager, R. Nuclear localization of Dengue virus nonstructural protein 5 does not strictly correlate with efficient viral RNA replication and inhibition of type I interferon signaling. *Journal of Virology*, 87(8):4545–4557, 2013.

## Bibliography

- Kunzi, M. S. and Pitha, P. M. Interferon targeted genes in host defense. *Autoimmunity*, 36(8):457–461, 2003.
- Kurane, I. and Ennis, F. A. Induction of interferon alpha from human lymphocytes by autologous, Dengue virus-infected monocytes. *The Journal of Experimental Medicine*, 166(4):999–1010, 1987.
- Labadie, M. and Marciniak-Czochra, A. A reaction-diffusion model for viral infection and immune response. *hal-00546034v2*, 2011.
- Lai, C.-Y., Hu, H.-P., King, C.-C., and Wang, W.-K. Incorporation of Dengue virus replicon into virus-like particles by a cell line stably expressing precursor membrane and envelope proteins of Dengue virus type 2. *Journal of Biomedical Science*, 15(1):15–27, 2008.
- Lauer, G. M. and Walker, B. D. Hepatitis C virus infection. *New England Journal of Medicine*, 345(1):41–52, 2001.
- Lee, H. Y., Topham, D. J., Park, S. Y., Hollenbaugh, J., Treanor, J., Mosmann, T. R., Jin, X., Ward, B. M., Miao, H., Holden-Wiltse, J., Perelson, A. S., Zand, M., and Wu, H. Simulation and prediction of the adaptive immune response to influenza A virus infection. *Journal of Virology*, 83(14):7151–7165, 2009.
- Lenz, S. M. Impulsive hybrid discrete-continuous delay differential equations. PhD Thesis, University of Heidelberg, 2014.
- Lenz, S. M., Schlöder, J. P., and Bock, H. G. Numerical computation of derivatives in systems of delay differential equations. *Mathematics and Computers in Simulation*, 96:124–156, 2014.
- Leung, A. K. C. Variolation and vaccination in late imperial China, ca 1570–1911. In *History of vaccine development*, Springer, 5–12. 2011.
- Li, K., Markosyan, R. M., Zheng, Y.-M., Golfetto, O., Bungart, B., Li, M., Ding, S., He, Y., Liang, C., Lee, J. C., Gratton, E., Cohen, F. S., and Liu, S.-L. IFITM proteins restrict viral membrane hemifusion. *PLoS Pathogens*, 9(1):e1003124, 2013a.
- Li, S.-H., Dong, H., Li, X.-F., Xie, X., Zhao, H., Deng, Y.-Q., Wang, X.-Y., Ye, Q., Zhu, S.-Y., Wang, H.-J., Zhang, B., Leng, Q.-B., Zuest, R., Qin, E.-D., Qin, C.-F., and Shi, P.-Y. Rational design of a flavivirus vaccine by abolishing viral RNA 2'-O methylation. *Journal of Virology*, 87(10):5812–5819, 2013b.
- Lillemeier, B. F., Köster, M., and Kerr, I. M. STAT1 from the cell membrane to the DNA. *The EMBO Journal*, 20(10):2508–2517, 2001.
- Lindenbach, B. D., Evans, M. J., Syder, A. J., Wölk, B., Tellinghuisen, T. L., Liu, C. C., Maruyama, T., Hynes, R. O., Burton, D. R., McKeating, J. A., and Rice, C. M. Complete replication of hepatitis C virus in cell culture. *Science*, 309(5734):623–626, 2005.
- Lindenbach, B. D., Thiel, H.-J., and Rice, C. M. *Flaviviridae: the viruses and their replication*. In *Fields virology*, Lippincott Williams & Wilkins, New York. 2006.

- Liu, L., Oza, S., Hogan, D., Perin, J., Rudan, I., Lawn, J. E., Cousens, S., Mathers, C., and Black, R. E. Global, regional, and national causes of child mortality in 2000–13, with projections to inform post-2015 priorities: an updated systematic analysis. *The Lancet*, 2014.
- Luijsterburg, M. S., von Bornstaedt, G., Gourdin, A. M., Politi, A. Z., Moné, M. J., Warmerdam, D. O., Goedhart, J., Vermeulen, W., Van Driel, R., and Höfer, T. Stochastic and reversible assembly of a multiprotein DNA repair complex ensures accurate target site recognition and efficient repair. *The Journal of Cell Biology*, 189(3):445–463, 2010.
- MacDonald, N. Biological delay systems: linear stability theory. Cambridge University Press, 1989.
- Maheshri, N. and O’Shea, E. K. Living with noisy genes: how cells function reliably with inherent variability in gene expression. *Annual Review of Biophysics and Biomolecular Structure*, 36:413–434, 2007.
- Maiwald, T., Schneider, A., Busch, H., Sahle, S., Gretz, N., Weiss, T. S., Kummer, U., and Klingmüller, U. Combining theoretical analysis and experimental data generation reveals IRF9 as a crucial factor for accelerating interferon  $\alpha$ -induced early antiviral signalling. *FEBS Journal*, 277(22):4741–4754, 2010.
- Mariani, L., Schulz, E. G., Lexberg, M. H., Helmstetter, C., Radbruch, A., Löhning, M., and Höfer, T. Short-term memory in gene induction reveals the regulatory principle behind stochastic IL-4 expression. *Molecular Systems Biology*, 6(1), 2010.
- Matheson, I., Walls, D., and Gardiner, C. Stochastic models of first-order nonequilibrium phase transitions in chemical reactions. *Journal of Statistical Physics*, 12(1):21–34, 1975.
- Mayer, A. Concerning the mosaic disease of tobacco. *Die Landwirtschaftliche Versuchsstationen*, (32):451–467, 1886.
- Mazzon, M., Jones, M., Davidson, A., Chain, B., and Jacobs, M. Dengue virus NS5 inhibits interferon- $\alpha$  signaling by blocking signal transducer and activator of transcription 2 phosphorylation. *Journal of Infectious Diseases*, 200(8):1261–1270, 2009.
- McQuarrie, D. A. Stochastic approach to chemical kinetics. *Journal of Applied Probability*, 4(3):413–478, 1967.
- Metz, J. A. and Diekmann, O. The dynamics of physiologically structured populations. *Lecture Notes in Biomathematics*, 68, 1986.
- Mishra, A. Smallpox: forgotten by public, remains a concern for public health. *Proceedings of the National Academy of Sciences, India Section B: Biological Sciences*, 82(1):23–29, 2012.
- Moghadas, S. M. Gaining insights into human viral diseases through mathematics. *European Journal of Epidemiology*, 21(5):337–342, 2006.

## Bibliography

- Montagnier, L. 25 years after HIV discovery: prospects for cure and vaccine. *Virology*, 397(2):248–254, 2010.
- Morrison, J., Laurent-Rolle, M., Maestre, A. M., Rajsbaum, R., Pisanelli, G., Simon, V., Mulder, L. C., Fernandez-Sesma, A., and García-Sastre, A. Dengue virus coopts UBR4 to degrade STAT2 and antagonize type I interferon signaling. *PLoS Pathogens*, 9(3):e1003265, 2013.
- Muñoz-Jordán, J. L., Laurent-Rolle, M., Ashour, J., Martínez-Sobrido, L., Ashok, M., Lipkin, W. I., and García-Sastre, A. Inhibition of alpha/beta interferon signaling by the NS4B protein of flaviviruses. *Journal of Virology*, 79(13):8004–8013, 2005.
- Muñoz-Jordán, J. L., Sánchez-Burgos, G. G., Laurent-Rolle, M., and García-Sastre, A. Inhibition of interferon signaling by Dengue virus. *Proceedings of the National Academy of Sciences*, 100(24):14333–14338, 2003.
- Murphy, B. R. and Whitehead, S. S. Immune response to Dengue virus and prospects for a vaccine. *Annual Review of Immunology*, 29:587–619, 2011.
- Murray, J. D. *Mathematical biology: I. An introduction (Interdisciplinary Applied Mathematics) (Pt. 1)*. Springer, 2002.
- Murray, N. E. A., Quam, M. B., and Wilder-Smith, A. Epidemiology of Dengue: past, present and future prospects. *Clinical Epidemiology*, 5:299, 2013.
- Myung, I. J. Tutorial on maximum likelihood estimation. *Journal of Mathematical Psychology*, 47(1):90–100, 2003.
- Nasirudeen, A., Wong, H. H., Thien, P., Xu, S., Lam, K.-P., and Liu, D. X. RIG-I, MDA5 and TLR3 synergistically play an important role in restriction of Dengue virus infection. *PLoS Neglected Tropical Diseases*, 5(1):e926, 2011.
- Nelson, P. W., Gilchrist, M. A., Coombs, D., Hyman, J. M., and Perelson, A. S. An age-structured model of HIV infection that allows for variations in the production rate of viral particles and the death rate of productively infected cells. *Mathematical Biosciences and Engineering*, 1:267–288, 2004.
- Neumann, A. U., Lam, N. P., Dahari, H., Gretch, D. R., Wiley, T. E., Layden, T. J., and Perelson, A. S. Hepatitis C viral dynamics in vivo and the antiviral efficacy of interferon- $\alpha$  therapy. *Science*, 282(5386):103–107, 1998.
- Normile, D. Surprising new Dengue virus throws a spanner in disease control efforts. *Science*, 342(6157):415–415, 2013.
- Nowak, M. and May, R. M. *Virus dynamics: mathematical principles of immunology and virology*. Oxford University Press, 2000.
- Onoguchi, K., Onomoto, K., Takamatsu, S., Jogi, M., Takemura, A., Morimoto, S., Julkunen, I., Namiki, H., Yoneyama, M., and Fujita, T. Virus-infection or 5'ppp-RNA activates antiviral signal through redistribution of IPS-1 mediated by MFN1. *PLoS Pathogens*, 6(7):e1001012, 2010.

- Onoguchi, K., Yoneyama, M., Takemura, A., Akira, S., Taniguchi, T., Namiki, H., and Fujita, T. Viral infections activate types I and III interferon genes through a common mechanism. *Journal of Biological Chemistry*, 282(10):7576–7581, 2007.
- Pan, X.-B., Han, J.-C., Cong, X., and Wei, L. BST2/tetherin inhibits Dengue virus release from human hepatoma cells. *PloS One*, 7(12):e51033, 2012.
- Pawelek, K. A., Liu, S., Pahlevani, F., and Rong, L. A model of HIV-1 infection with two time delays: mathematical analysis and comparison with patient data. *Mathematical Biosciences*, 235(1):98–109, 2012.
- Peña, J. and Harris, E. Early Dengue virus protein synthesis induces extensive rearrangement of the endoplasmic reticulum independent of the UPR and SREBP-2 pathway. *PloS One*, 7(6):e38202, 2012.
- Perelson, A., Essunger, P., and Ho, D. Dynamics of HIV-1 and CD4+ lymphocytes in vivo. *AIDS*, 11:Suppl A:S17–24, 1997.
- Perelson, A. S. Modelling viral and immune system dynamics. *Nature Reviews Immunology*, 2(1):28–36, 2002.
- Pichlmair, A., Lassnig, C., Eberle, C.-A., Górna, M. W., Baumann, C. L., Burkard, T. R., Bürckstümmer, T., Stefanovic, A., Krieger, S., Bennett, K. L., Rüllicke, T., Weber, F., Colinge, J., Müller, M., and Superti-Furga, G. IFIT1 is an antiviral protein that recognizes 5'-triphosphate RNA. *Nature Immunology*, 12(7):624–630, 2011.
- Pichlmair, A. and Reis e Sousa, C. Innate recognition of viruses. *Immunity*, 27(3):370–383, 2007.
- Pierson, T. C. and Diamond, M. S. Vaccine development as a means to control Dengue virus pathogenesis: do we know enough? *Annual Review of Virology*, 2014.
- Press, W. H., Teukolsky, S. A., Vetterling, W. T., and Flannery, B. P. Numerical recipes 3rd edition: the art of scientific computing. Cambridge University Press, 2007.
- Prokunina-Olsson, L., Muchmore, B., Tang, W., Pfeiffer, R. M., Park, H., Dickensheets, H., Hergott, D., Porter-Gill, P., Mumy, A., Kohaar, I., Chen, S., Brand, N., Tarway, M., Liu, L., Sheikh, F., Astemborski, J., Bonkovsky, H. L., Edlin, B. R., Howell, C. D., Morgan, T. R., Thomas, D. L., Rehermann, B., Donnelly, R. P., and O'Brien, T. R. A variant upstream of IFNL3 (IL28B) creating a new interferon gene IFNL4 is associated with impaired clearance of hepatitis C virus. *Nature Genetics*, 45(2):164–171, 2013.
- Pulendran, B. and Ahmed, R. Immunological mechanisms of vaccination. *Nature Immunology*, 12(6):509–517, 2011.
- Raj, A. and van Oudenaarden, A. Nature, nurture, or chance: stochastic gene expression and its consequences. *Cell*, 135(2):216–226, 2008.

## Bibliography

- Rand, U. Dynamics of type I interferon induction and action. PhD Thesis, Medical School Hannover, 2010.
- Rand, U., Rinas, M., Schwerk, J., Nöhren, G., Linnes, M., Kröger, A., Flossdorf, M., Kály-Kullai, K., Hauser, H., Höfer, T., and Köster, M. Multi-layered stochasticity and paracrine signal propagation shape the type-I interferon response. *Molecular Systems Biology*, 8:584, 2012.
- Rantala, M. and Van de Laar, M. Surveillance and epidemiology of hepatitis B and C in Europe - a review. *Eurosurveillance*, 13(21):717–727, 2008.
- Raser, J. M. and O’Shea, E. K. Noise in gene expression: origins, consequences, and control. *Science*, 309(5743):2010–2013, 2005.
- Rateitschak, K. and Wolkenhauer, O. Intracellular delay limits cyclic changes in gene expression. *Mathematical Biosciences*, 205(2):163–179, 2007.
- Ray, D., Shah, A., Tilgner, M., Guo, Y., Zhao, Y., Dong, H., Deas, T. S., Zhou, Y., Li, H., and Shi, P.-Y. West Nile virus 5’-cap structure is formed by sequential guanine N-7 and ribose 2’-O methylations by nonstructural protein 5. *Journal of Virology*, 80(17):8362–8370, 2006.
- Rehwinkel, J., Tan, C. P., Goubau, D., Schulz, O., Pichlmair, A., Bier, K., Robb, N., Vreede, F., Barclay, W., Fodor, E., , and Reis e Sousa, C. RIG-I detects viral genomic RNA during negative-strand RNA virus infection. *Cell*, 140(3):397–408, 2010.
- Roberts, R. M., Liu, L., Guo, Q., Leaman, D., and Bixby, J. The evolution of the type I interferons. *Journal of Interferon & Cytokine Research*, 18(10):805–816, 1998.
- Rodríguez, G. Lecture notes on generalized linear models. Princeton University, 2007.
- Rong, L., Dahari, H., Ribeiro, R. M., and Perelson, A. S. Rapid emergence of protease inhibitor resistance in hepatitis C virus. *Science Translational Medicine*, 2(30):30ra32–30ra32, 2010.
- Ronni, T., Melen, K., Malygin, A., and Julkunen, I. Control of IFN-inducible MxA gene expression in human cells. *The Journal of Immunology*, 150(5):1715–1726, 1993.
- Rott, R. Molecular basis of infectivity and pathogenicity of myxovirus. *Archives of Virology*, 59(4):285–298, 1979.
- Sadler, A. J. and Williams, B. R. Interferon-inducible antiviral effectors. *Nature Reviews Immunology*, 8(7):559–568, 2008.
- Schirmacher, V. and Fournier, P. Newcastle disease virus: a promising vector for viral therapy, immune therapy, and gene therapy of cancer. In *Gene therapy of cancer*, Springer, 565–605. 2009.

- Schmid, B. Dynamics of hepatitis C virus and Dengue virus-induced innate immune responses. PhD Thesis, University of Heidelberg, 2014.
- Schneider, J. J. and Kirkpatrick, S. Stochastic optimization. Springer, 2006.
- Schoggins, J. W., Dorner, M., Feulner, M., Imanaka, N., Murphy, M. Y., Ploss, A., and Rice, C. M. Dengue reporter viruses reveal viral dynamics in interferon receptor-deficient mice and sensitivity to interferon effectors in vitro. *Proceedings of the National Academy of Sciences*, 109(36):14610–14615, 2012.
- Seal, B. S. and King, D. J. Newcastle disease virus. *Encyclopedia for Life Sciences*, 2005.
- Shalek, A. K., Satija, R., Shuga, J., Trombetta, J. J., Gennert, D., Lu, D., Chen, P., Gertner, R. S., Gaublot, J. T., Yosef, N., Schwartz, S., Fowler, B., Weaver, S., Wang, J., Wang, X., Ding, R., Raychowdhury, R., Friedman, N., Hacohen, N., Park, H., May, A. P., and Regev, A. Single-cell RNA-seq reveals dynamic paracrine control of cellular variation. *Nature*, 2014.
- Shampine, L. F. and Reichelt, M. W. The Matlab ODE suite. *SIAM Journal on Scientific Computing*, 18(1):1–22, 1997.
- Shampine, L. F. and Thompson, S. Solving DDEs in Matlab. *Applied Numerical Mathematics*, 37(4):441–458, 2001.
- Shampine, L. F. and Thompson, S. Numerical solution of delay differential equations. In *Delay differential equations*, Springer, 1–27. 2009.
- Smieja, J., Jamaluddin, M., Brasier, A. R., and Kimmel, M. Model-based analysis of interferon- $\beta$  induced signaling pathway. *Bioinformatics*, 24(20):2363–2369, 2008.
- Smith, H. L. An introduction to delay differential equations with applications to the life sciences. Springer New York, 2011.
- Snijder, B. and Pelkmans, L. Origins of regulated cell-to-cell variability. *Nature Reviews Molecular Cell Biology*, 12(2):119–125, 2011.
- Spencer, S. L., Gaudet, S., Albeck, J. G., Burke, J. M., and Sorger, P. K. Non-genetic origins of cell-to-cell variability in TRAIL-induced apoptosis. *Nature*, 459(7245):428–432, 2009.
- Spiller, D. G., Wood, C. D., Rand, D. A., and White, M. R. Measurement of single-cell dynamics. *Nature*, 465(7299):736–745, 2010.
- Stark, G. R. and Darnell Jr., J. E. The JAK-STAT pathway at twenty. *Immunity*, 36(4):503–514, 2012.
- Swain, P. S., Elowitz, M. B., and Siggia, E. D. Intrinsic and extrinsic contributions to stochasticity in gene expression. *Proceedings of the National Academy of Sciences*, 99(20):12795–12800, 2002.
- Szretter, K. J., Daniels, B. P., Cho, H., Gainey, M. D., Yokoyama, W. M., Gale Jr, M., Virgin, H. W., Klein, R. S., Sen, G. C., and Diamond, M. S. 2'-O methylation of the viral mRNA cap by West Nile virus evades Ifit1-dependent and -independent mechanisms of host restriction in vivo. *PLoS Pathogens*, 8(5):e1002698, 2012.

## Bibliography

- Takaoka, A. and Yanai, H. Interferon signalling network in innate defence. *Cellular Microbiology*, 8(6):907–922, 2006.
- Takeuchi, O. and Akira, S. Innate immunity to virus infection. *Immunological Reviews*, 227(1):75–86, 2009.
- Tan, J., Pan, R., Qiao, L., Zou, X., and Pan, Z. Modeling and dynamical analysis of virus-triggered innate immune signaling pathways. *PloS One*, 7(10):e48114, 2012.
- Tay, S., Hughey, J. J., Lee, T. K., Lipniacki, T., Quake, S. R., and Covert, M. W. Single-cell NF- $\kappa$ B dynamics reveal digital activation and analogue information processing. *Nature*, 466(7303):267–271, 2010.
- Taylor, R. Interpretation of the correlation coefficient: a basic review. *Journal of Diagnostic Medical Sonography*, 6(1):35–39, 1990.
- Theofilopoulos, A. N., Baccala, R., Beutler, B., and Kono, D. H. Type I interferons ( $\alpha/\beta$ ) in immunity and autoimmunity. *Annual Review of Immunology*, 23:307–335, 2005.
- Thompson, A. J. and Locarnini, S. A. Toll-like receptors, RIG-I-like RNA helicases and the antiviral innate immune response. *Immunology and Cell Biology*, 85(6):435–445, 2007.
- Thompson, M. R., Kaminski, J. J., Kurt-Jones, E. A., and Fitzgerald, K. A. Pattern recognition receptors and the innate immune response to viral infection. *Viruses*, 3(6):920–940, 2011.
- Venzon, D. and Moolgavkar, S. A method for computing profile-likelihood-based confidence intervals. *Applied Statistics*, 87–94, 1988.
- Versteeg, G. A. and García-Sastre, A. Viral tricks to grid-lock the type I interferon system. *Current Opinion in Microbiology*, 13(4):508–516, 2010.
- Vinkemeier, U. Getting the message across, STAT! Design principles of a molecular signaling circuit. *The Journal of Cell Biology*, 167(2):197–201, 2004.
- Waldmann, K.-H. and Stocker, U. M. Stochastische Modelle: Eine anwendungsorientierte Einführung, EMILeA-stat. 2004.
- Wathelet, M. G., Berr, P. M., and Huez, G. A. Regulation of gene expression by cytokines and virus in human cells lacking the type-I interferon locus. *European Journal of Biochemistry*, 206(3):901–910, 1992.
- Wei, X., Ghosh, S. K., Taylor, M. E., Johnson, V. A., Emini, E. A., Deutsch, P., Lifson, J. D., Bonhoeffer, S., Nowak, M. A., Hahn, B. H., Saag, M. S., and Shaw, G. M. Viral dynamics in human immunodeficiency virus type 1 infection. *Nature*, 373(6510):117–122, 1995.
- Welsch, S., Miller, S., Romero-Brey, I., Merz, A., Bleck, C. K., Walther, P., Fuller, S. D., Antony, C., Krijnse-Locker, J., and Bartenschlager, R. Composition and three-dimensional architecture of the Dengue virus replication and assembly sites. *Cell Host & Microbe*, 5(4):365–375, 2009.

- West, A. P., Shadel, G. S., and Ghosh, S. Mitochondria in innate immune responses. *Nature Reviews Immunology*, 11(6):389–402, 2011.
- WHO, W. H. O. World health statistics 2014. *WHO Press, World Health Organization*, 2014.
- Wilder-Smith, A., Renhorn, K.-E., Tissera, H., Bakar, S. A., Alphey, L., Kitayapong, P., Lindsay, S., Logan, J., Hatz, C., Reiter, P., Rocklöv, J., Byass, P., Louis, V. R., Tozan, Y., Massad, E., Tenorio, A., Lagneau, C., L’Ambert, G., Brooks, D., Wegerdt, J., and Gubler, D. DengueTools: innovative tools and strategies for the surveillance and control of Dengue. *Global Health Action*, 5, 2012.
- Yoneyama, M., Kikuchi, M., Natsukawa, T., Shinobu, N., Imaizumi, T., Miyagishi, M., Taira, K., Akira, S., and Fujita, T. The RNA helicase RIG-I has an essential function in double-stranded RNA-induced innate antiviral responses. *Nature Immunology*, 5(7):730–737, 2004.
- Yu, C.-Y., Chang, T.-H., Liang, J.-J., Chiang, R.-L., Lee, Y.-L., Liao, C.-L., and Lin, Y.-L. Dengue virus targets the adaptor protein MITA to subvert host innate immunity. *PLoS Pathogens*, 8(6):e1002780, 2012.
- Zawatzky, R., De Maeyer, E., and De Maeyer-Guignard, J. Identification of individual interferon-producing cells by in situ hybridization. *Proceedings of the National Academy of Sciences*, 82(4):1136–1140, 1985.
- Zhao, M., Zhang, J., Phatnani, H., Scheu, S., and Maniatis, T. Stochastic expression of the interferon- $\beta$  gene. *PLoS Biology*, 10(1):e1001249, 2012.
- Zhong, B., Yang, Y., Li, S., Wang, Y.-Y., Li, Y., Diao, F., Lei, C., He, X., Zhang, L., Tien, P., and Shu, H.-B. The adaptor protein MITA links virus-sensing receptors to IRF3 transcription factor activation. *Immunity*, 29(4):538–550, 2008.
- Zou, X., Xiang, X., Chen, Y., Peng, T., Luo, X., and Pan, Z. Understanding inhibition of viral proteins on type I IFN signaling pathways with modeling and optimization. *Journal of Theoretical Biology*, 265(4):691–703, 2010.
- Zuniga, J., Whiteside, A., and Ghaziani, A. A decade of HAART: the development and global impact of highly active antiretroviral therapy. Oxford University Press, USA, 2008.
- Züst, R., Cervantes-Barragan, L., Habjan, M., Maier, R., Neuman, B. W., Ziebuhr, J., Szretter, K. J., Baker, S. C., Barchet, W., Diamond, M. S., Siddell, S. G., Ludewig, B., and Thiel, V. Ribose 2'-O-methylation provides a molecular signature for the distinction of self and non-self mRNA dependent on the RNA sensor Mda5. *Nature Immunology*, 12(2):137–143, 2011.
- Züst, R., Dong, H., Li, X.-F., Chang, D. C., Zhang, B., Balakrishnan, T., Toh, Y.-X., Jiang, T., Li, S.-H., Deng, Y.-Q., Ellis, B. R., Ellis, E. M., Poidinger, M., Zolezzi, F., Qin, C.-F., Shi, P.-Y., and Fink, K. Rational design of a live attenuated Dengue vaccine: 2'-O-methyltransferase mutants are highly attenuated and immunogenic in mice and macaques. *PLoS Pathogens*, 9(8):e1003521, 2013.



# Abbreviations and symbols

$\mathbb{1}_A$  characteristic function of the set  $A$ , p. 43

$\cong$  corresponds to

$\emptyset$  degradation

$\dot{f}(t) = \frac{d}{dt}f(t)$  derivative of the function  $f(t)$  with respect to time  $t$

$\in$  element of

$:=$  equal by definition

$A \cap B$  intersection of the sets  $A$  and  $B$

$\oslash$  replication

$\forall$  universal quantifier; for all

$\alpha$  alpha

**A549** carcinomic human alveolar epithelial cell line, p. 56

**AIDS** acquired immunodeficiency syndrome, p. 13

**a.u.** arbitrary units, p. 86

$\beta$  beta

**BAC** bacterial artificial chromosome, p. 21, 56

**BHK-21** baby hamster kidney cell line, p. 81

**C** capsid protein of DENV, p. 7, 55

**CDF** cumulative distribution function, p. 43, 93

**CFP** cyan fluorescent protein, p. 21

$\chi^2$  chi-squares statistic, p. 43, 49, 83

**CI** confidence interval, p. 85

**CS1** circularization sequence 1, p. 57

## *Abbreviations and symbols*

- CV*** coefficient of variation, p. 22
- $\delta(\boldsymbol{x})$  delta distribution also known as delta function, p. 73
- $\Delta T_{\text{gen}}$  time difference between sister cells regarding IFN- $\beta$ -tGFP expression, p. 26
- $\Delta T_{\text{sig}}$  time difference between sister cells regarding IRF-7 signaling, p. 26
- DAPI** 4',6-diamidino-2-phenylindole fluorescent stain, p. 61
- DDE** delay differential equation, p. 3, 73
- deGFP** destabilized version of enhanced green fluorescent protein, p. 56
- DENV** Dengue virus, p. 6, 6, 53
- DF*** degree of freedom, p. 44, 85
- DKFZ** German Cancer Research Center, p. 143
- DNA** deoxyribonucleic acid, p. 5
- ds** double-stranded, p. 5, 57
- E** envelope protein of DENV, p. 7, 55
- $\epsilon$  epsilon
- E217A mutant** DENV mutant, which differ from the DENV-wt due to a single substitution of the glutamic acid residue (E) by an alanine residue (A) at the amino acid position 217 of the NS5 protein, p. 11, 16, 54, 69
- eGFP** enhanced green fluorescent protein, p. 56
- ELISA** enzyme-linked immunosorbent assay, p. 63, 70
- exp.** experiment, p. 86
- FACS** fluorescence-activated cell sorting, p. 30
- faR** far red fluorescent protein, p. 55
- $\gamma$  gamma
- $\gamma(m, z)$  gamma distribution with the positive parameters  $m$  and  $z$ , p. 46
- $\Gamma$  Gamma
- $\Gamma(m)$  gamma function with the positive parameter  $m$ , p. 46
- g** gram
- GAPDH** glyceraldehyde 3-phosphate dehydrogenase, p. 63
- GFP** green fluorescent protein, p. 21

- h** hours
- $\mathcal{H}$**  Heaviside step function, p. 36
- HAART** highly active antiretroviral therapy, p. 13
- HAU** haemagglutinating unit, p. 22
- HCV** hepatitis C virus, p. 13, 110
- HIV** human immunodeficiency virus, p. 13
- HN** hemagglutinin-neuraminidase, p. 6, 23
- HZI** Helmholtz Centre for Infection Research, p. 19
- IFIT1** interferon-induced protein with tetratricopeptide repeats 1 also known as ISG56, p. 56
- IFIT3** interferon-induced protein with tetratricopeptide repeats 3, p. 64
- IFN** interferons, p. 1, 9, 19
- i.i.d.** independent and identically distributed, p. 46
- IRF** interferon regulatory factor, p. 9, 21
- ISG** interferon stimulated gene, p. 9, 19
- ISG56** interferon stimulated gene 56, also known as IFIT1, p. 56
- ISGF3** IFN-stimulated gene factor 3, p. 9
- IU** international units, p. 61
- JAK** janus activated kinase, p. 9
- $\kappa$**  kappa
- kDa** kilodalton, p. 62
- $\lambda$**  lambda
- $L$**  likelihood function, p. 46
- $\mathcal{L}$**  log-likelihood function, p. 46
- ln** natural logarithm
- log** logarithm
- $\mu\text{g}$**  microgram
- $\mu\text{l}$**  microliter

*Abbreviations and symbols*

**μm** micrometer

**MAVS** mitochondrial antiviral-signaling protein, p. 9

**mCherry** monomeric cherry (red fluorescent protein), p. 21

**MDA5** melanoma differentiation-associated protein 5, p. 9, 55

**mex subroutine** Matlab executable subroutine, p. 4, 80

**MFI** mean fluorescence intensity, p. 24, 62

**min** minutes

**ml** milliliter

**MOI** multiplicity of infection, p. 24

**MP** potentially DENV-E217A mutant specific model parameter, p. 89

**mRNA** messenger RNA, p. 5

**Mx** MX dynamin-like GTPase, p. 56

**N** set of natural numbers  $\{1, 2, 3, \dots\}$

**$N_0$**  set of non-negative integer numbers  $\{0, 1, 2, 3, \dots\}$

**NDV** Newcastle disease virus, p. 6, 22

**NF-κB** nuclear factor kappa B, p. 9, 21

**ng** nanogram

**NIH3T3** mouse embryonic fibroblast cell line, p. 22

**NLS** nuclear localization signal, p. 55

**NS** non-structural protein of DENV, p. 7, 55

**ODE** ordinary differential equation, p. 73

**$\mathcal{P}(A)$**  probability of  $A$ , p. 93

**$\mathcal{P}(A | B)$**  conditional probability of  $A$  under the condition  $B$ , p. 32

**p50** protein involved in nuclear factor kappa B heterodimer formation, p. 9

**p65** protein involved in nuclear factor kappa B heterodimer formation, p. 9, 21

**PAMP** pathogen-associated molecular pattern, p. 8

**PCS** sequence encoding for the 2A cleavage factor of the *Thosea asigna* virus, p.

- PDE** partial differential equation, p. 73
- pg** picogram
- p.i.** post infection, p. 23
- poly I:C** polyinosinic-polycytidylic acid, p. 22
- prM** premembrane protein of DENV, p. 7, 55
- PRR** pattern-recognition receptor, p. 8
- qPCR** quantitative polymerase chain reaction, p. 30
- qRT-PCR** quantitative real time reverse polymerase chain reaction, p. 63
- $r$  correlation coefficient, p. 26
- $r^2$  coefficient of determination, p. 26
- $\mathbb{R}$  set of real numbers
- $\mathbb{R}_{\geq 0}$  set of nonnegative real numbers
- RIG-I** retinoic acid-inducible gene I, p. 9, 19
- RLR** RIG-I-like receptor, p. 9
- RNA** ribonucleic acid, p. 5
- RO** readout, p. 38, 82
- RPS9** 40S ribosomal protein S9, p. 30
- RSAD2** radical S-adenosyl methionine domain containing 2, p. 30
- siRNA** small-interfering RNA, p. 111
- ss** single-stranded, p. 5, 22, 55
- SSA** stochastic simulation algorithm, p. 32
- STAT** signal transducer and activator of transcription, p. 9
- STING** stimulator of interferon genes also known as MITA, p. 9, 53
- TagRFP** red fluorescent protein tag, p. 28
- TCID<sub>50</sub>** tissue culture infectious dose 50, p. 58
- TCP** trans-complementation particle, p. 58
- $T_{\text{div}}$  time of cell division, p. 26
- TF** transcription factor, p. 9

## *Abbreviations and symbols*

- $T_{\text{gen}}$  time delay between nuclear translocation of NF- $\kappa$ B/IRF-7 and onset of IFN- $\beta$  expression, p. 26
- $\overline{T}_{\text{gen}}$  mean value of  $T_{\text{gen}}$ , p. 26
- $\mathcal{T}_{\text{gen}}$  simulated time delay between nuclear translocation of NF- $\kappa$ B/IRF-7 and onset of IFN- $\beta$  expression, p. 39
- tGFP** turbo green fluorescent protein, p. 21
- TLR** Toll-like receptor, p. 9, 55
- TMV** tobacco mosaic virus, p. 5
- $T_{\text{sig}}$  signaling delay from viral infection to nuclear translocation of the transcription factors NF- $\kappa$ B and IRF-7, p. 26
- $\overline{T}_{\text{sig}}$  mean value of  $T_{\text{sig}}$ , p. 26
- $\mathcal{T}_{\text{sig}}$  simulated signaling delay from viral infection to nuclear translocation of the transcription factors NF- $\kappa$ B and IRF-7, p. 39
- TYK** tyrosine kinase, p. 9
- U** unit, p. 28
- USP18** ubiquitin specific peptidase 18, p. 30
- UTR** untranslated region, p. 57, 70
- vol.** volume, p. 84
- WHO** World Health Organization, p. 12
- wt** wild-type, p. 16, 53
- YFP** yellow fluorescent protein, p. 21

# Publications and presentations

## First author publications

- 2015      Bianca Schmid\*, Melanie Rinas\*, Alessia Ruggieri, Antje Reuter, Wolfgang Fischl, Nathalie Harder, Jan-Philip Bergeest, Michael Flossdorf, Karl Rohr, Thomas Höfer# and Ralf Bartenschlager#  
Live cell analysis and modeling identify determinants of attenuation of Dengue virus 2'-O-methylation mutant  
*Manuscript submitted for publication*
- 2012      Ulfert Rand\*, Melanie Rinas\*, Johannes Schwerk, Gesa Nöhren, Melanie Linnes, Andrea Kröger, Michael Flossdorf, Kristóf Kály-Kullai, Hansjörg Hauser, Thomas Höfer# and Mario Köster#  
Multi-layered stochasticity and paracrine signal propagation shape the type-I interferon response  
*Molecular Systems Biology*, 8:584, 2012

(\* first authors, # corresponding authors)

## Oral presentations

- 07/2013      Lightning talk at the 1st Workshop on Virus Dynamics in Frankfurt am Main, Germany
- 11/2012      Selected talk at the RECOMB Conference on Regulatory and Systems Genomics with DREAM Challenges in San Francisco, United States
- 05/2012      Selected lightning talk at the International Conference on Systems Biology of Human Disease (SBHD) in Heidelberg, Germany
- 2010 – 2013      Talks at four German Cancer Research Center (DKFZ) hosted scientific retreats in Germany

## Poster presentations

- 09/2014      Status Seminar of the e:Bio Innovation Competition in Systems Biology in Berlin, Germany
- 07/2013      1st Workshop on Virus Dynamics in Frankfurt am Main, Germany

*Publications and presentations*

- 05/2012 International Conference on Systems Biology of Human Disease (SBHD) in Heidelberg, Germany
- 09/2011 International Conference on Systems Biology (ICSB) in Heidelberg and Mannheim, Germany
- 07/2011 DKFZ PhD Retreat in Weil der Stadt, Germany
- 02/2011 FORSYS Status Seminar in Heidelberg, Germany
- 12/2010 DKFZ PhD Poster Presentation in Heidelberg, Germany
- 06/2010 International Conference on Systems Biology of Human Disease (SBHD) in Boston, United States
- 01/2010 Mid-Term Review of the Helmholtz Alliance on Systems Biology in Heidelberg, Germany
- 10/2009 Second Status Seminar and Meeting of the Scientific Advisory Board of the Helmholtz Alliance on Systems Biology in Heidelberg, Germany

# Acknowledgments

The present thesis was carried out in the Division of Theoretical Systems Biology headed by Prof. Thomas Höfer at the German Cancer Research Center (DKFZ) and BioQuant Center, University of Heidelberg. At this point I would like to thank everyone who has made this work possible and who has directly or indirectly supported me during my PhD study at the combined faculty for the Natural Sciences and Mathematics, University of Heidelberg.

Mein größter Dank gilt Prof. Thomas Höfer für die Annahme als Doktorandin in seiner Arbeitsgruppe, die Bereitstellung dieses faszinierenden Themas und insbesondere für seine umfangreiche Betreuung. Durch sein enormes Fachwissen, seine Diskussionsfreudigkeit und seine unschätzbar wertvollen Ideen war er mir eine große Hilfe und ich durfte sehr viel von ihm lernen.

Ganz besonders möchte ich mich bei Prof. Anna Marciniak-Czochra dafür bedanken, dass sie meine Arbeit mitbetreut hat. Ihre hilfreichen Anregungen und Ratschläge waren stets eine fachliche Bereicherung. Darüber hinaus danke ich ihr für ihre Bereitschaft, das Erstgutachten zu übernehmen.

Ein herzlicher Dank geht an Prof. Ursula Klingmüller für ihr konstruktives Engagement in meinem PhD-Komitee. Ihre gezielten Fragestellungen und wertvollen Kommentare haben unsere Diskussionen wesentlich vorangebracht. Zudem möchte ich mich bei ihr dafür bedanken, dass sie sich dazu bereit erklärt hat, bei meiner Verteidigung als Prüferin zu agieren.

Besonders danke ich Prof. Hans Georg Bock für seine Bereitschaft, in meiner Prüfungskommission mitzuwirken. Seine Begeisterung für die angewandte Mathematik hat mich bereits zu Beginn meiner Doktorandenzeit motiviert.

In ganz besonderem Maße möchte ich mich bei meinem Kollegen Dr. Michael Floßdorf bedanken, welcher mich insbesondere in der Anfangszeit mitbetreut hat und meine Arbeit durch viele wertvolle Ideen voranbrachte. Speziell danke ich ihm, dass er sich für meine Fragen stets Zeit nahm und mir durch sein enormes Wissen sehr viel beibrachte.

Ein großes Dankeschön geht an unsere experimentellen Kooperationspartner Dr. Ulfert Rand, Dr. Mario Köster und Dr. Hansjörg Hauser. Vor allem danke ich ihnen, dass sie mir ihre Resultate anvertraut haben und mich mit viel Geduld dabei unterstützten, die Biologie hinter den Daten zu verstehen.

Darüber hinaus danke ich Dr. Bianca Schmid und Prof. Ralf Bartenschlager für eine spannende Zusammenarbeit, bei welcher ich mittels ihrer Daten und hilfreichen Diskussionen in das faszinierende Gebiet der Ausbreitung von Dengue Viren ein-

## *Acknowledgments*

tauchen durfte. An dieser Stelle möchte ich Bianca ganz besonders dafür danken, dass sie sich wissenschaftlich und auch privat immer für mich Zeit nahm.

Ganz herzlich bedanke ich mich bei Tim Heinemann, welcher in stürmischen Zeiten mein Fels in der Brandung war und dessen empathische Fähigkeiten meist zu milderem Klima führten. Außerdem danke ich ihm, dass er bei kleinen sowie großen Schwierigkeiten stets mit Rat und Tat an meiner rechten Seite saß.

Ein besonderes Dankeschön geht an Dr. Erika Kuchen für die schätzenswerten wissenschaftlichen und persönlichen Gespräche, welche wir vor allem in unseren Abendstunden führen konnten. Daneben danke ich ihr, dass ihre Energie, ihr Optimismus und ihre Begeisterungsfähigkeit so wunderbar ansteckend sind.

Darüber hinaus möchte ich mich bei Dr. Nils Becker für die vielen lehrreichen Diskussionen bedanken, bei denen ich immer das Gefühl hatte, jede Frage ohne Bedenken stellen zu dürfen.

Ein großer Dank geht an Diana Haendly, deren Unterstützung weit über eine kompetente administrative Hilfe hinausging.

Bedanken möchte ich mich bei Michael Nemetz sowie Dr. Nick Kepper, dass sie mir bei jedem noch so skurrilen Computerproblem hilfsbereit beistanden.

Ein Dankeschön richtet sich an Dr. Anne Weiser für die vielen aufbauenden Gespräche und ihre Fähigkeit die Dinge präzise auf den Punkt zu bringen.

Many thanks to Dr. Anneke Brümmer, Dr. Michael Floßdorf, Dr. Anna Matveeva, Tim Heinemann, Dr. Erika Kuchen and Melania Barile for a great office atmosphere, which made it easier and more fun to work.

Special thanks go to Dr. Kristóf Kály-Kullai for his expert assistance during the initial phase of my PhD study.

I am very thankful to the current and former members of the Höfer group for the pleasant working atmosphere, which has given me solid support and encouragement.

Daneben bedanke ich mich bei Jonas Förster, dass er mit viel Ausdauer die Mikroskopie-Daten zur Einzelzell-Analyse manuell getrackt hat.

Vielen lieben Dank an Dr. Nils Becker, Tim Heinemann, Dr. Ludwig Gauckler, Gabriele Gauckler, Dr. Erika Kuchen, Dr. Anna Schulze sowie Dr. Michael Floßdorf für das kritische Lesen meiner Doktorarbeit und die hieraus entstandenen konstruktiven Diskussionen.

Ganz besonders danke ich meiner wundervollen Freundin Gabriele Gauckler, dass ich mit ihr über alles reden kann und sie immer für mich da ist.

Von Herzen danke ich meiner Mutter Antonie Rinas, dass sie mich bei allen meinen Entscheidungen unterstützt und mir mit ihrer Liebe in jeder Situation sicheren Rückhalt bietet. Daneben danke ich vielmals meiner Großmutter Emilie Rinas, welche mich stets ermutigt hat, meinen eigenen Weg zu gehen.